

Imperial College London  
Department of Computing

# Moisture Estimation for Precision Agriculture through RF Sensing

Youssef N Altherwy

Submitted in part fulfilment of the requirements for the degree of  
Doctor of Philosophy in Computing of Imperial College London, March 2022





# Abstract

Convenient, non-obtrusive, low-cost, and accurate sensing of fruit moisture content is crucial for the scientific studies of Pomology and Viticulture and their associated agriculture. It can provide early indicators of yield estimation and crop health as well as providing data for food production and precision farming systems. With a focus on grapes, we introduce SING, a scheme that senses grape moisture content by utilizing RF signals but without physical contact with the fruit. In this thesis, we extend the investigation of the theoretical relationship between the dielectric properties and the moisture content of agricultural products to establish a sensing model in the 5 GHz band. To make the work practical, we are first to measure the dielectric properties of grape bunches (not individually as that would be destructive), presenting a unique measurement challenge as internal grapes are hidden. In doing so, we demonstrate that our technique precisely estimates moisture content to a high degree of accuracy (90%). Current RF sensing models to estimate moisture are destructive; they require samples to be constrained in containers. Our work is first to dispense with such impracticalities, and, without contact with the object, accurately measures non-uniform grape clusters in open space. We demonstrate that SING is superior to existing work in its ability to accurately measure the dielectric properties of non-uniform fruit objects and test this through both lab-based experimentation and preliminary outdoor vineyard tests. We also examine the transferability of SING’s approach to real-world scenarios.



## **Declaration of Originality**

I hereby declare that the intellectual content of this Thesis is the product of my own work except where explicitly stated otherwise.



## Copyright Declaration

The copyright of this Thesis rests with the author. Unless otherwise indicated, its contents are licensed under a Creative Commons Attribution-Non Commercial 4.0 International Licence (CC BY-NC). Under this licence, you may copy and redistribute the material in any medium or format. You may also create and distribute modified versions of the work. This is on the condition that: you credit the author and do not use it, or any derivative works, for a commercial purpose. When reusing or sharing this work, ensure you make the licence terms clear to others by naming the licence and linking to the licence text. Where a work has been adapted, you should indicate that the work has been changed and describe those changes. Please seek permission from the copyright holder for uses of this work that are not included in this licence or permitted under UK Copyright Law.



## Acknowledgements

I would like to express my deepest gratitude to my supervisor Prof. Julie A. McCann for her constant guidance and support during the whole PhD. journey. I also would like to extend my gratitude to my family and the former and current members of the AESE group for their help and support.





## Dedication

To my beautiful wife and two daughters, thank you.

‘And these examples We present to the people, but none will understand them except those of knowledge’

*Al-’Ankabut, Verse 43*

# Contents

<b>Abstract</b>	<b>i</b>
<b>Declaration</b>	<b>iii</b>
<b>Copyright Declaration</b>	<b>v</b>
<b>Acknowledgements</b>	<b>vii</b>
<b>1 Introduction</b>	<b>1</b>
1.1 Motivation . . . . .	1
1.2 Objectives and Contributions . . . . .	2
1.3 Publications . . . . .	3
1.4 Thesis Organization . . . . .	3
<b>2 Background</b>	<b>4</b>
2.1 Overview of Dielectric Properties . . . . .	4
2.2 Related Work . . . . .	7
2.2.1 Agricultural Sensing . . . . .	9
2.2.2 RF Sensing for General Applications . . . . .	14
2.2.3 RF Sensing for Agricultural Applications . . . . .	21

2.2.4	Grape Moisture Sensing . . . . .	26
<b>3</b>	<b>SING: Free Space SensING of Grape Moisture using RF Sensing</b>	<b>38</b>
3.1	Feasibility of Moisture Estimation through RF Sensing . . . . .	39
3.1.1	The Relationship between the Moisture Content and $\kappa$ . . . . .	41
3.1.2	The Relationship between the Sugar and $\kappa$ . . . . .	46
3.1.3	The Relationship between the Frequency and $\kappa$ . . . . .	50
3.1.4	SING Frequencies . . . . .	51
3.2	SING Methodology . . . . .	54
3.2.1	SING Experiment and Simulation Setup . . . . .	55
3.2.2	The Predictive Model . . . . .	59
3.2.3	SING's Free Space Transmission Technique . . . . .	60
3.2.4	Calculating $\varepsilon^*$ and $\kappa$ . . . . .	62
3.2.5	Calculating $\rho$ . . . . .	65
3.2.6	The impact of diffraction on SING accuracy . . . . .	67
3.2.7	The impact of foliage on SING accuracy . . . . .	70
<b>4</b>	<b>SING Results</b>	<b>79</b>
4.1	Results and Discussion . . . . .	79
4.1.1	Moisture and Thickness Regression Models . . . . .	79
4.1.2	SING's Angle Combinations . . . . .	87
4.1.3	SING's Performance . . . . .	88
4.1.4	Multiple-Segment . . . . .	97
4.1.5	Initial Vineyard testing . . . . .	105

4.2	Conclusion . . . . .	107
<b>5</b>	<b>Outdoor SING</b>	<b>108</b>
5.1	Outdoor SING Constraints . . . . .	108
5.1.1	The distance between the transmitter and receiver. . . . .	108
5.1.2	The placement of the antenna. . . . .	110
5.1.3	Multiple vs. Rotating antennas. . . . .	111
5.2	Outdoor SING Design . . . . .	112
5.2.1	Deployment options . . . . .	112
5.2.2	Measurement devices . . . . .	113
5.2.3	Host Computer . . . . .	119
5.3	Power Consumption and Overall Cost . . . . .	120
<b>6</b>	<b>Conclusion and Beyond</b>	<b>127</b>
6.1	Thesis Summary . . . . .	127
6.2	Future of SING . . . . .	130
	<b>Bibliography</b>	<b>131</b>
<b>A</b>	<b>SING: Supplementary Figures</b>	<b>146</b>
A.1	The relationship between $\varepsilon^*$ and the Moisture Content . . . . .	146
A.2	Radiation Directivity and Pattern . . . . .	147
A.3	Attenuation and Phase shift at multiple angles . . . . .	150
A.4	The impact of foliage on SING accuracy . . . . .	154

**B SING Results: Supplementary Figures** **159**

B.1 Minimum against Maximum number of angles . . . . . 159

# List of Tables

2.1	The dielectric properties of pure Water, different fruits, and different chemical compounds at 5 GHz and room temperature $\approx 25\text{ }^{\circ}\text{C}$ . The values are obtained from [75, 91, 60]. . . . .	6
2.2	Summary of key papers and SING . . . . .	37
4.1	Different Statistical measures of the $R^2$ value for the 3-Fold and 5-Fold CVs. The values are obtained from figures 4.1 and 4.2. . . . .	83
4.2	The moisture regression model information (equations 3.10, §3.2.2). . . . .	83
4.3	The training set clusters information . . . . .	84
4.4	The validation set clusters information . . . . .	84
4.5	Different Statistical measures of the $R^2$ value for the 3-Fold and 5-Fold CVs. The values are obtained from figures 4.3 and 4.4. . . . .	85
4.6	The thickness regression model information (Eq.3.32, §3.2.5). . . . .	87
4.7	All and eligible segments in each segment category . . . . .	99
5.1	Deployment Options . . . . .	113
5.2	Comparison between three different types of SDRs. The values are obtained from [9, 6, 15]. . . . .	117
5.3	Comparison between different host machines. The values are obtained from [20, 21, 22, 4]. . . . .	120

5.4	The {SDR, Host Computer} configurations . . . . .	122
5.5	Typical power consumption and weight of the active components in figures 5.4 and 5.5, and the servo motor required to rotate the antennas. The values are obtained from [10, 7, 17, 23, 5, 26, 11, 1] . . . . .	122
5.6	The typical current and power consumption for each configuration. . . . .	123
5.7	The cost of the 12 configurations. . . . .	125
5.8	The approximate weight of the 12 configurations . . . . .	126



# List of Figures

2.1	Summary of $\varepsilon^*$ measuring techniques. Specifically, (a) the resonant cavity, (b) the transmission line, (c) the free space transmission, and (d) the coaxial probe measuring techniques. . . . .	8
3.1	$\kappa$ against different moisture concentration (%) in sugar solutions at 11 frequencies {5.0,5.1,5.2,...,6.0 GHz}. . . . .	43
3.2	$\kappa$ of variable moisture content concentration {40% to 90 %} at 50 frequencies in the 5 GHz band. . . . .	45
3.3	$\varepsilon'$ of variable moisture content concentration {40% to 90 %} at 50 frequencies in the 5 GHz band. . . . .	45
3.4	$\varepsilon'$ of different moisture volumes at 50 frequencies in the 5 GHz band. . . . .	47
3.5	$\varepsilon''$ of different moisture contents at 50 frequencies in the 5 GHz band. . . . .	47
3.6	$\varepsilon'$ of the same water-sugar concentration at 50 frequencies in the 5 GHz band. . . . .	48
3.7	$\varepsilon''$ of the same water-sugar concentration at 50 frequencies in the 5 GHz band. . . . .	48
3.8	$\kappa$ of variable sugar concentrations {10% to 60%} at 50 frequencies in the 5 GHz band. . . . .	49
3.9	$\varepsilon'$ of variable sugar concentrations {10% to 60%} at 50 frequencies in the 5 GHz band. . . . .	50

3.10	The EM waves intensity as dBm at frequencies between 1 GHz and 8 GHz. The horizontal line in the figure corresponds to the noise floor of the N5244B VNA [14]. The values are <b>computed</b> through equation 3.9. . . . .	53
3.11	The EM waves intensity as % at frequencies between 1 GHz and 8 GHz. . . . .	54
3.12	SING . . . . .	56
3.13	A grape cluster with leaves and different sizes of grapes designed through CST Microwave Studio . . . . .	57
3.14	The Pyramidal Horn Antenna . . . . .	58
3.15	Radiation directivity at 5.5 GHz. The red curve represents the main lobe direction, whereas the other lines/curves represent the main lobe width and the side lobe amplitude with auxiliary lines. . . . .	58
3.16	The 3D radiation pattern at 5.5 GHz. . . . .	59
3.17	The attenuation $\{A\}$ in dB at $\{5.1, 5.2, 5.3, \dots, \text{and } 5.9 \text{ GHz}\}$ for a cluster with moisture content = 380 ml at 30 equidistant angles between 0 and $2\pi$ . . . . .	61
3.18	The phase shift $\{\phi\}$ in degree at $\{5.1, 5.2, 5.3, \dots, \text{and } 5.9 \text{ GHz}\}$ for a cluster with moisture content = 380 ml at 30 equidistant angles between 0 and $2\pi$ . . . . .	61
3.19	Summary of SING Procedure . . . . .	72
3.20	An illustration of the potential diffracted waves around the edges of a grape cluster. . . . .	73
3.21	Clear Line of Sight (CLoS) simulation setup . . . . .	73
3.22	Small container simulation setup. . . . .	73
3.23	Large container simulation setup. . . . .	74
3.24	The grapes simulation through CST Microwave studio. . . . .	74
3.25	Impulse - normalized - simulation signal . . . . .	75

3.26	The received time-domain signal at $R_x$ for CLoS, Small container, and Large container simulations. The x-axis is time in ns and the y-axis is the amplitude normalized to the input impulse signal. . . . .	75
3.27	The received time-domain signal at $R_x$ for the clear line of sight (CLoS) and a grape cluster simulations. The x-axis is time in ns and the y-axis is the amplitude normalized to the input impulse signal. . . . .	76
3.28	CST simulation of a cluster with leaves . . . . .	76
3.29	The $S_{11}$ and $S_{21}$ measurements with leaves (i.e., w Leaves) and without leaves at angle 0. . . . .	77
3.30	The $S_{11}$ and $S_{21}$ measurements with leaves (i.e., w Leaves) and without leaves at angle $\frac{\pi}{2}$ . . . . .	77
3.31	The $S_{11}$ and $S_{21}$ measurements with leaves (i.e., w Leaves) and without leaves at angle $\pi$ . . . . .	78
3.32	The $S_{11}$ and $S_{21}$ measurements with leaves (i.e., w Leaves) and without leaves at angle $\frac{3\pi}{2}$ . . . . .	78
4.1	The $R^2$ value for each moisture regression model employed in the 3-Fold CV. The x-axis shows the $R^2$ values, and the y-axis shows the number of regression models at each $R^2$ value. . . . .	81
4.2	The $R^2$ value for each moisture regression model employed in the 5-Fold CV. The x-axis shows the $R^2$ values, and the y-axis shows the number of regression models at each $R^2$ value. . . . .	82
4.3	The $R^2$ value for each thickness regression model employed in the 3-Fold CV. The x-axis shows the $R^2$ values, and the y-axis shows the number of regression models at each $R^2$ value. . . . .	85
4.4	The $R^2$ value for each thickness regression model employed in the 5-Fold CV. The x-axis shows the $R^2$ values, and the y-axis shows the number of regression models at each $R^2$ value. . . . .	86

4.5	The mean offset value (%) for each category set. . . . .	90
4.6	The median offset value (%) for each category set. . . . .	91
4.7	The standard deviation value for each category set. . . . .	91
4.8	The mean offset values (%) for equidistant against random scanned angles for each angle set category. . . . .	93
4.9	The median offset values (%) for equidistant against random scanned angles for each angle set category at the <i>all</i> frequency set. . . . .	93
4.10	The mean offset values of the single-segment and multiple-segment. . . . .	95
4.11	The median offset values of the single-segment and multiple-segment. . . . .	96
4.12	The total number of angle sets at each angle set category for each segment category in the single-segment group. . . . .	97
4.13	The total number of angle sets at each angle set category for each segment category in the multiple-segment group. . . . .	98
4.14	The mean offset of the two-segment <i>Min</i> against <i>Max</i> for the <i>All</i> frequency set.	100
4.15	The mean offset of the three-segment <i>Min</i> against <i>Max</i> for the <i>All</i> frequency set.	100
4.16	The mean offset of the five-segment <i>Min</i> against <i>Max</i> for the <i>All</i> frequency set.	101
4.17	The mean offset of the six-segment <i>Min</i> against <i>Max</i> for the <i>All</i> frequency set. .	101
4.18	The mean offset of the ten-segment <i>Min</i> against <i>Max</i> for the <i>All</i> frequency set. .	102
4.19	The mean offset of the fifteen-segment <i>Min</i> against <i>Max</i> for the <i>All</i> frequency set.	102
4.20	The wins (%) for each segment category. . . . .	103
4.21	The difference in the number of angles between <i>Min</i> and <i>Max</i> and the occurrence (%) of such difference across all segments in each segment category. . . . .	104
4.22	Attenuation of the signal between the transmitter and receiver in the presence of cluster of grapes against the clear line-of-sight (CLoS) in a Vineyard. . . . .	106

5.1	Two scenarios to illustrate the relationship between $D_{\text{far-field}}$ and the inter-distance between a vineyard's rows. . . . .	109
5.2	A cluster between two antennas. The preferable setup for SING. . . . .	110
5.3	(a) Illustration of outdoor SING as a handheld device, and (b) illustration of outdoor SING as an aerial device . . . . .	111
5.4	A proposed design of outdoor SING using HackRF One. . . . .	116
5.5	A proposed design of outdoor SING using BladeRF 2.0/LimeSDR. . . . .	118
5.6	Operation flowchart of outdoor SING. . . . .	121
5.7	Maximum scanned clusters for each {SDR, Host Computer} configuration. . . .	124
A.1	$\kappa$ against different moisture concentration (%) at 50 frequencies in {5.0,5.1,5.2,...,6.0 GHz}. . . . .	147
A.2	Radiation directivity at 5 GHz. The red curve represents the main lobe direction, whereas the other lines/curves represent the main lobe width and the side lobe amplitude with auxiliary lines. . . . .	148
A.3	The 3D radiation pattern at 5 GHz. . . . .	148
A.4	Radiation directivity at 6 GHz. The red curve represents the main lobe direction, whereas the other lines/curves represent the main lobe width and the side lobe amplitude with auxiliary lines. . . . .	149
A.5	The 3D radiation pattern at 6 GHz. . . . .	149
A.6	The attenuation $\{A\}$ in dB at {5.1, 5.2, 5.3, ..., and 5.9 GHz} for a cluster with moisture content = 233 ml at 30 equidistant angles between 0 and $2\pi$ . . . . .	150
A.7	The phase shift $\{\phi\}$ in degree at {5.1, 5.2, 5.3, ..., and 5.9 GHz} for a cluster with moisture content = 233 ml at 30 equidistant angles between 0 and $2\pi$ . . . .	151
A.8	The attenuation $\{A\}$ in dB at {5.1, 5.2, 5.3, ..., and 5.9 GHz} for a cluster with moisture content = 157 ml at 30 equidistant angles between 0 and $2\pi$ . . . . .	152

A.9	The phase shift $\{\phi\}$ in degree at $\{5.1, 5.2, 5.3, \dots, \text{and } 5.9 \text{ GHz}\}$ for a cluster with moisture content = 157 ml at 30 equidistant angles between 0 and $2\pi$ . . . .	152
A.10	The attenuation $\{A\}$ in dB at $\{5.1, 5.2, 5.3, \dots, \text{and } 5.9 \text{ GHz}\}$ for a cluster with moisture content = 95 ml at 30 equidistant angles between 0 and $2\pi$ . . . . .	153
A.11	The phase shift $\{\phi\}$ in degree at $\{5.1, 5.2, 5.3, \dots, \text{and } 5.9 \text{ GHz}\}$ for a cluster with moisture content = 95 ml at 30 equidistant angles between 0 and $2\pi$ . . . .	154
A.12	The $S_{11}$ and $S_{21}$ measurements with leaves (i.e., w Leaves) and without leaves at angle $\frac{\pi}{4}$ . . . . .	155
A.13	The $S_{11}$ and $S_{21}$ measurements with leaves (i.e., w Leaves) and without leaves at angle $\frac{3\pi}{4}$ . . . . .	156
A.14	The $S_{11}$ and $S_{21}$ measurements with leaves (i.e., w Leaves) and without leaves at angle $\frac{5\pi}{4}$ . . . . .	157
A.15	The $S_{11}$ and $S_{21}$ measurements with leaves (i.e., w Leaves) and without leaves at angle $\frac{7\pi}{4}$ . . . . .	158
B.1	The median offset of the two-segment <i>Min</i> against <i>Max</i> . . . . .	159
B.2	The median offset of the three-segment <i>Min</i> against <i>Max</i> . . . . .	160
B.3	The median offset of the five-segment <i>Min</i> against <i>Max</i> . . . . .	161
B.4	The median offset of the six-segment <i>Min</i> against <i>Max</i> . . . . .	162
B.5	The median offset of the ten-segment <i>Min</i> against <i>Max</i> . . . . .	163
B.6	The median offset of the fifteen-segment <i>Min</i> against <i>Max</i> . . . . .	164

# Chapter 1

## Introduction

### 1.1 Motivation

The sensing of objects in a convenient, low-cost, non-invasive manner facilitates understanding different phenomena and exploiting new features in many applications. In health, non-invasive sensing has been exploited to monitor respiratory rate, heartbeats, and blood glucose levels without direct contact with the patients [28, 65, 82, 133, 134, 135, 141]. In industry, non-invasive sensing has been used for machine identification, localisation, and health monitoring [127, 72, 92, 136, 126]. Not only that but this notion of sensing had been extended to Precision Agriculture as well [48, 111, 130, 131].

*Precision Agriculture* can be defined as the study of agriculture on a much finer resolution through the application of information technology [100]. Agricultural practices such as harvesting and yield production can benefit immensely from precision agriculture. Generally speaking, agricultural fields such as farms and vineyards do not exhibit uniformity with respect to growth and crop production. Different parts in a field have different characteristics in terms of soil and plants [100]. Even expert farmers with years of experience and knowledge about their farms can still benefit from precision agriculture as ambient factors such as temperature and wind affect yield production significantly, yet they can be unpredictable to some extent.

Precision agriculture can be realised through different technologies. This thesis aims to approach precision agriculture through the interaction between electromagnetic waves, specifically Radio Frequencies (RF), and different agricultural products. We label this interaction as *RF Sensing*. RF Sensing is a terminology describing how RF signals interact with and monitor surrounding phenomena in a non-invasive manner. RF Sensing is a general concept, and in this thesis, we realise precision agriculture through RF Sensing. Specifically, we investigate the applicability of RF Sensing to estimate moisture content in agricultural products such as grapes. **SING** is the terminology we use to describe the sensing of grape moisture content through RF Sensing. Thus, **SING** is a perfect example of realising precision agriculture through RF Sensing.

**SING** importance stems from the fact that understanding the moisture level in grapes is vital for the scientific investigation in Pomology (the study of cultivation of fruits) and Oenology/Viticulture (the studies of grape agriculture). It provides valuable data about the health status of the crop as well as reliable yield estimation [93, 94]. Information about crop health can highlight deviations in growth behaviours that may indicate a problem in the vineyard, which can be dealt with promptly. Reliable yield estimation, on the other hand, enable viticulturists, for example, to make informed decisions about the labour and other materials (e.g., bottles) needed ahead of harvest season as well as feeding into precision agriculture systems [122].

## 1.2 Objectives and Contributions

Previously, we have emphasized the importance of estimating the moisture content in agricultural products such as grapes. Thus, this thesis presents **SING**. **SING** is a scheme that senses grape moisture content through RF Sensing without physical contact with the fruit. In **SING**, we extend the investigation of the theoretical relationship between the dielectric properties and the moisture content of grapes to establish a sensing model in the 5 GHz band. To make the work practical, we are first to measure the dielectric properties of grape bunches (not individually as that would be destructive), presenting a unique measurement challenge as internal



grapes are hidden. In doing so, we demonstrate in Chapters 3 and 4 that our technique precisely estimates moisture content to a high degree of accuracy (90%). Current RF Sensing models to estimate moisture are destructive and require samples to be constrained in containers. SING is first to dispense with such impracticalities, and, without contact with the fruit, accurately measures the geometrically non-uniform grape clusters in open space. Also, we demonstrate SING's superiority to existing work in its ability to accurately measure the dielectric properties of non-uniform fruit objects and test this through both lab-based experimentation and preliminary outdoor vineyard tests.

## 1.3 Publications

- Y. N. Altherwy and J. A. McCann, "SING: Free Space SensING of Grape Moisture using RF Shadowing," in IEEE Transactions on Instrumentation and Measurement, doi: 10.1109/TIM.2020.3027928.

## 1.4 Thesis Organization

Based on the described objectives and contributions, this thesis is organized as follows: Chapter 2 presents the background and related work in the realm of RF Sensing as well as a primer on the dielectric properties and their measuring techniques. Chapters 3 and 4 are dedicated to SING. The former lays out the foundation and methodology behind SING, and the latter presents the results. While working on SING, COVID-19 emerged as a global pandemic. The restrictions applied by governments due to the spread of COVID-19 prevented us from employing SING in a real-world environment such as vineyards. Thus, we dedicate Chapter 5 to discuss the requirements needed to develop SING into an exploitable technology appropriate for real-world scenarios. We present the final remarks and conclude the thesis in Chapter 6.

# Chapter 2

## Background

This chapter presents an overview of the work related to our research. Specifically, we start by presenting related work in agricultural sensing. Afterwards, we discuss previous work that adopt the notion of RF Sensing. Then, we discuss previous work that combine both RF Sensing and agricultural sensing, to introduce the general theme of our work; RF Sensing for agricultural applications. Finally, we review work related to grape moisture sensing to emphasize the research opportunity we investigate in this thesis. But first, we present a primer on dielectric properties, and how to measure them. Measuring the dielectric properties is a cornerstone in moisture estimation through RF Sensing, as we shall emphasize throughout the thesis. Thus, it is essential to explain what the dielectric properties represent and how to measure them before explaining their role in our work.

### 2.1 Overview of Dielectric Properties

The dielectric properties (in other words, the Complex Relative Permittivity ( $\varepsilon^*$ )) describe a dielectric material's (e.g. a grape cluster) behaviour when subjected to an electric field. In general, the dielectric properties are described in terms of two factors, the Relative Permittivity ( $\varepsilon'$ ) and the Loss Factor ( $\varepsilon''$ ). The former represents a material's ability to store electrical energy and polarize with the electric field. The latter represents the electrical energy loss (usually as

heat) of the electric field inside the material [115]. Mathematically,  $\varepsilon^*$  is a complex number and is defined as

$$\varepsilon^* = \varepsilon' - j\varepsilon'' \quad (2.1)$$

For a dielectric material such as a grape cluster,  $\varepsilon'$  and  $\varepsilon''$  values, and by extension  $\varepsilon^*$ , depend on many factors, especially, the frequency of the electric field, the ambient temperature, and the different components of the material such as moisture [115]. When the other factors are known, the grape cluster moisture content can be realised through its dielectric properties ( $\varepsilon^*$ ). Thus, we dedicate this part of the thesis to review different techniques used to measure  $\varepsilon^*$ , especially in the microwave range of frequencies (i.e.  $f \in [1 \text{ GHz} - 300 \text{ GHz}]$ ). We are mainly interested in microwave frequencies because water is the primary absorbent of the electromagnetic waves at those frequencies [115]; this is also why we choose a microwave frequency in our research. Table 2.1 presents the dielectric properties of common materials at 5 GHz such as pure Water. In the table, we present the dielectric properties of different agricultural products since the main focus of this thesis is precision agriculture. Also, the table includes the dielectric properties of common chemical compounds, which are usually used to calibrate dielectric properties measuring devices [104]. The values are presented at the 5 GHz for reasons mentioned later in §3.1.4.

According to [120, 70], there are four main techniques to measure  $\varepsilon^*$  of materials at microwave frequencies: the resonant cavity, the transmission-line, the coaxial probe, and the free-space technique (figure 2.1). The *resonant cavity* (figure 2.1a) is a technique that employs a metal-enclosed structure (i.e. cavity) that resonates highly at specific frequencies; the cavity's resonant frequencies [87]. A dielectric material inserted inside the cavity causes changes to the resonant frequencies, from which the dielectric properties of the material are measured [114]. Note that the cavities' dimensions are comparable to the resonant frequencies' wavelengths; for practical reasons, the resonant cavity technique is mainly used at microwave frequencies due to the small wavelength of such frequencies [87].

The *transmission-line* (figure 2.1b) technique works by physically inserting a dielectric material inside a transmission line, typically, coaxial cables or waveguides [114, 104]. The *free-space*

Material	Relative Permittivity	Loss Factor
Pure Water	73.1000	18.7000
Apple, <i>Malus domestica</i> (Golden Delicious)	52.9125	16.4250
Apple, <i>Malus domestica</i> (Granny Smith)	49.6250	15.3375
Apple, <i>Malus domestica</i> (Red Delicious)	49.0875	15.3500
Avocado, <i>Persea americana</i>	41.6000	14.6250
Banana, <i>Musa x paradisiaca</i>	52.3250	21.5875
Cantaloupe, <i>Cucumis melo</i>	61.3250	18.4625
Carrot, <i>Daucus carota</i> subsp. <i>sativus</i>	51.0000	19.3625
Cucumber, <i>Cucumis sativus</i>	65.2875	17.9125
Grape, <i>Vitis amurensis</i>	58.2875	21.8625
Grapefruit, <i>Citrus x paradisi</i>	66.9000	20.6750
Honeydew, <i>Cucumis melo</i>	63.1250	21.2625
Kiwi fruit, <i>Actinidia chinensis</i>	60.3125	21.4000
Lemon, <i>Citrus limon</i>	65.6125	19.6750
Lime, <i>Citrus aurantiifolia</i>	64.4000	20.1250
Mango, <i>Mangifera indica</i>	56.2125	18.4875
Onion, <i>Allium cepa</i> (Red)	60.0125	19.7375
Onion, <i>Allium cepa</i> (White)	58.5250	18.7000
Onion, <i>Allium cepa</i> (Yellow)	62.1125	18.8750
Orange, <i>Citrus aurantium</i>	61.8875	21.7125
Papaya, <i>Carica papaya</i>	60.8375	20.0250
Pear, <i>Pyrus communis</i>	58.4500	19.5250
Potato, <i>Solanum tuberosum</i>	51.8125	19.3875
Radish, <i>Raphanus sativus</i>	62.9250	18.5125
Squash, <i>Cucurbita mixta</i>	58.1750	16.4125
Strawberry, <i>Fragaria chiloensis</i>	65.3000	19.6125
Sweet potato, <i>Ipomoea batatas</i>	47.1375	16.7750
Turnip, <i>Brassica rapa</i>	56.6000	17.4250
Ethanol	5.2200	3.9800
Methanol	13.2300	12.2100
Ethanediol	8.9000	9.3600

Table 2.1: The dielectric properties of pure Water, different fruits, and different chemical compounds at 5 GHz and room temperature  $\approx 25\text{ }^{\circ}\text{C}$ . The values are obtained from [75, 91, 60].

*transmission* (2.1c) technique uses air as a transmission line and employs holder/fixture to contain the material [114, 104]. The *coaxial probe* (figure 2.1d) technique immerses a probe connected to a coaxial cable inside the material [114, 104]. The three methods mentioned above employ a signal generator/analyzer to analyze signals interacting with the material to measure the dielectric properties. An example of a signal generator/analyzer commonly used in those techniques is a Vector Network Analyzer (VNA); a device used to record changes that occur to signals reflected off and/or transmitted through a material [114, 104]. Those reflected and transmitted signals are commonly referred to as scattering parameters (i.e. S-parameters), where the former represents the Reflection Coefficient ( $\Gamma$ ), and the latter represents the Transmission Coefficient ( $\tau$ ).

In the transmission-line and the free-space transmission techniques, both coefficients ( $\Gamma$  and  $\tau$ ) are used to calculate the dielectric properties, whereas, in the coaxial probe technique, only the reflection coefficient ( $\Gamma$ ) is used. Several methods are discussed in the literature to calculate the dielectric properties from  $\Gamma$  and  $\tau$ . We refer to [115, 116, 47, 104] for a more in-depth analysis of those methods, and postpone the discussion about our method to calculate the dielectric properties to chapter 3.

Now that we have finished presenting the primer for the dielectric properties and their measuring techniques, we move into discussing related work.

## 2.2 Related Work

In this section, we review work related to our research. We start with general work geared towards sensing different phenomena for agricultural applications (§2.2.1). Then, we introduce RF Sensing in more details by presenting work that employ RF Sensing in different sensing applications such as human and machine sensing (§2.2.2). Following that, we focus on work that utilize RF Sensing for agricultural applications (§2.2.3). Then, we discuss work on a particular agricultural application, grape yield estimation (§2.2.4), which represents the objective of our

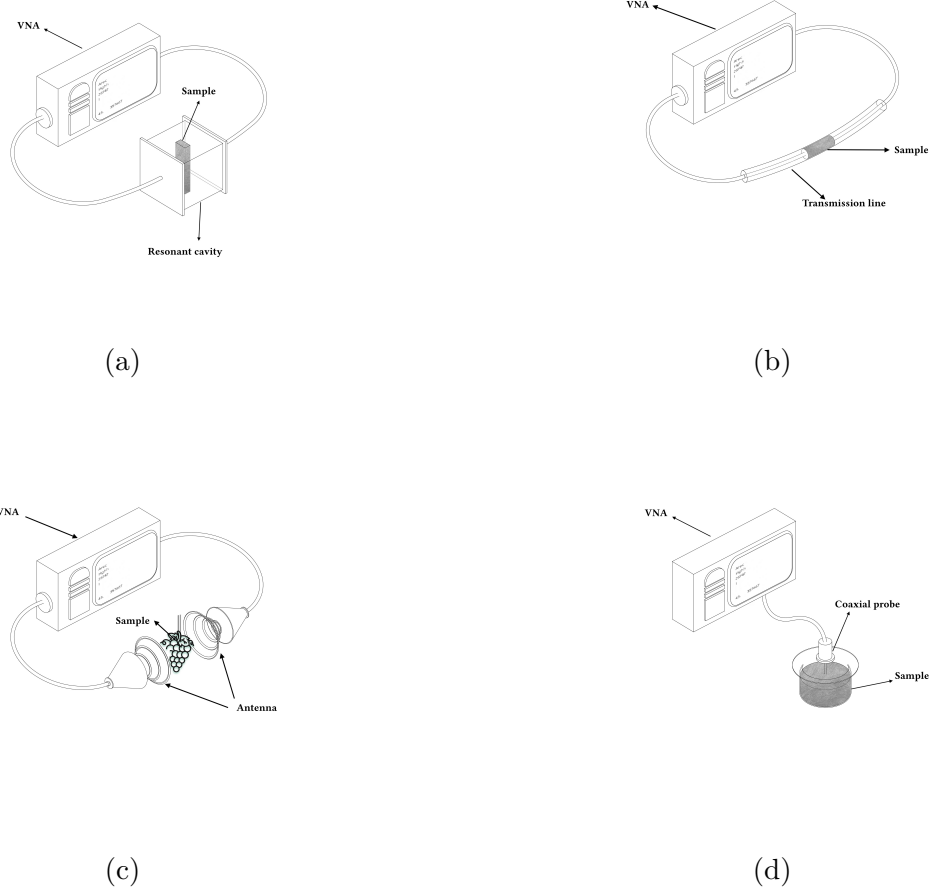


Figure 2.1: Summary of  $\epsilon^*$  measuring techniques. Specifically, (a) the resonant cavity, (b) the transmission line, (c) the free space transmission, and (d) the coaxial probe measuring techniques.

thesis. Finally, we conclude this section by presenting a table 2.2 that summarizes the key papers presented in each of the sections below and our work (i.e., SING). For each paper in the table, we show the objective and the key features that the authors utilize to fulfil the objective. We also show the employed methodology and whether or not the solution is invasive. By an invasive solution, we mean a solution that requires any form of disturbance or direct contact with the target/subject. For example, a solution that requires fruits to be removed from their natural habitat is an invasive solution. Note that most of the work reviewed here have been published in recent years, thus, constituting the state-of-the-art in their respective domains.

### 2.2.1 Agricultural Sensing

Here we discuss recent work in agricultural sensing [74, 36, 90, 129, 121, 53, 43, 81, 137, 80, 31, 106, 117, 115, 116, 57, 79, 54, 139, 140, 88, 69]. We start with general work in agricultural sensing [74, 36, 90, 129, 43], then we discuss work that deals specifically with moisture estimation in agricultural applications [81, 137, 80, 31, 106, 117, 115, 116, 57, 79, 54, 139, 140, 88, 69, 121, 53].

In [74], the authors attempt to detect the presence of unwanted materials mixed with peanuts. Specifically, they try to sense unwanted materials (e.g., sticks and stones) that may exist along with the peanuts by measuring their dielectric properties. The authors employ the free-space transmission technique to measure the dielectric properties; the peanuts are mixed with one of five unwanted materials and poured into a polycarbonate fixture placed between four antenna arrays, divided equally between the transmitter and receiver sides. Each antenna array consists of four yagi antennas operating at 10 GHz and connected to a VNA. The authors conducted two main experiments; the first is to determine the antenna arrays' sensitivity to minute changes in the attenuation and phase; the second is to measure the dielectric properties. According to the results, the system can distinguish between unwanted materials and the peanuts given that the peanuts' characteristics (i.e., attenuation and phase shift) are known beforehand. Thus, this system can alert to the presence of unwanted materials; however, it cannot report the dielectric properties of the unwanted materials and the peanuts individually. The authors did not report the system's performance when multiple unwanted materials are mixed with the peanuts simultaneously.

In [36], the authors discuss the possibility of detecting the ripeness state of oranges without physically cutting them. The authors observed a correlation between sugar concentration and the ripeness state of oranges. Thus, they designed experiments to measure the capacitance value of oranges in a capacitance system. In a capacitance system, the capacitance value (in farads) changes according to changes in the dielectric material between two conductive plates if and only if the area of the plates and the distance between them are fixed [76]. The authors

observed an inversely proportional relationship between the sugar concentration inside oranges and the capacitance value from the experiments. However, this work is a mere indication of the relationship between the sugar concentration and the capacitance value; it does not provide a model to relate the ripeness state to the sugar concentration through the capacitance value. Similarly, the authors in [90] relate the ripeness state of mangoes to the sugar concentration. However, they measure the dielectric properties instead of the capacitance value to define such a relationship. They employ the resonant cavity technique to measure the dielectric properties. Similar to the previous work, this work does not introduce a specific model to estimate the ripeness level of mangoes through the sugar concentration.

In [43], the authors also investigate the ripeness state of fruits (i.e., bananas in this work); but they employ the Electrical Impedance Spectroscopy method to do so. Electrical Impedance Spectroscopy works by measuring the impedance between two electrodes attached to the object under test. This work is motivated to prove that the physiological and biochemical changes resulting from fruit's ripening introduce electrical impedance changes. Thus, the authors attached electrodes to bananas in various ripening states and measured the impedance. They concluded that the real and imaginary parts of impedance do increase as bananas continue to ripe. This work serves as a proof-of-concept but lacks the methodology to estimate bananas' ripeness from electrical impedance.

In a similar vein, the authors in [129] assess the ripeness state of yellow peaches, but through the peaches' colour. They employ hyperspectral imaging to infer the colour, from which the firmness and the sugar concentration can be derived and the ripeness estimated. Hyperspectral imaging works by breaking a single pixel in an image into a broad spectrum of frequencies instead of the primary Red, Green, and Blue. Each spectrum is called a spectral band, and it is a continuous set of frequencies [41]. The authors construct a 11 X 11 brightness map for 45 spectral bands for each yellow peach, and feed this into a 3D-CNN and Multi-task learning models to estimate the firmness and sugar concentrations. Although firmness and sugar concentration are assessed in this work, the moisture content is not; moisture content



is an important factor in determining the ripeness state of fruits, including yellow peaches [129].

We now move to discuss recent work targeted towards moisture estimation in agricultural applications [81, 137, 80, 31, 106, 117, 115, 116, 57, 79, 54, 139, 140, 88, 69, 121, 53]. We start with the work in [81] where the authors measure the moisture content in peanuts through the Near-InfraRed (NIR) spectroscopy. NIR spectroscopy is a type of vibrational spectroscopy that utilizes photon energy in the wavelength range of 750 to 2500 nm (the near infra-red spectrum) to promote molecules in a material to vibrational excitation state [96]. In doing so, different organic components of the material such as moisture can be estimated as a result of the interaction between the photons and the molecules inside the material. Typically, an NIR machine consists of a radiant energy source, a wavelength discrimination device, a sample holder, and a detector [81]. Quartz tungsten halogen lamp is usually considered as a radiant energy source. The wavelength discrimination device is used to split the incoming wave into the different frequency components constituting the wave. The sample holder is where the object under test is placed, and the detector is used to convert the radiant energy into an electrical signal for further processing. In this work (i.e., [81]) the authors employ the NIR machine to estimate the moisture content of peanuts. Specifically, they measure the absorbed and reflected signals from peanuts with different moisture contents to establish a regression model. The regression model takes as inputs the absorbed/reflected signals and outputs the moisture content. One of the NIR machine's main drawbacks is that it cannot penetrate thick samples; thus, it can only be used for physically small samples such as peanuts. Also, the near infra-red spectrum is highly absorbent when exposed to fats, oil, and proteins, along with water. Therefore, agricultural products rich in those components may hinder the NIR machine ability to estimate moisture content.

In [137], the authors estimate the moisture content in sweet corn by measuring their dielectric properties. The free-space transmission technique is employed to measure the dielectric properties. The authors pour the kernels into a sample holder, which resides inside an RF chamber. The RF chamber is a structure where the walls are covered with radiation-absorbing materials

to minimize (if not eliminate) the multi-path effect. The authors feed the dielectric properties measurements to a deep neural network to map the dielectric properties to moisture content. In [80], the authors investigate moisture estimations for grain and nuts through the capacitive sensing approach. The capacitive sensing works by placing dielectric materials (grain and nuts in this work) between two conductive plates and measuring the capacitance value. From the capacitance value, the authors adopt a well-defined method of mapping the capacitance value to dielectric properties (specifically, the relative permittivity) at two frequencies [77, 78]. From there, the authors developed a regression model to obtain the moisture content. One primary requirement of the capacitive sensing approach is that air between the samples should be minimized (if not eliminated). The reason being is that air is a dielectric material; thus, air can alter the capacitance value.

We now move from fruits and vegetables moisture sensing, to moisture sensing in soil [121, 53, 31]. In [121], the authors investigate moisture estimation in the soil through Radio Frequency Identification (RFID). RFID consists of a reader (interrogator) and tags, each with a unique ID number to enable communication with the reader [58]. A tag is essentially an IC and an antenna and is activated by the reader. The tag communicates with the reader through backscattering communication [58]. The work (i.e., [121]) is motivated by the authors' observation, which states that a coupling effect occurs between soil and RFID tag's antenna attached to the soil due to the soil's moisture content. Also, they claim that the amount of coupling is directly related to the moisture level in the soil. As a result, three of the signal's features are affected by the coupling; the signal's phase, the Received Signal Strength (RSS), and the minimum power required to activate the tag (MRT). The authors discard the first two features and focus on the last. Regarding the phase, the authors discard it because several moisture levels could have the same wrapped phase (i.e., the phase between  $-\pi$  and  $\pi$ ). For the RSS, the authors choose MRT over RSS because the latter is more susceptible to environment's noise than the former as RSS represents the round-trip channel from the reader to the tag and back to the tag. In contrast, MRT represents the channel between the reader and the tag only.

To estimate the moisture content, the authors attach two tags to a pot filled with soil with different moisture contents and measure MRT. Then, a regression model is established to map between the moisture content and MRT values. Two tags are chosen to be robust against changes to pot's location. The idea is that two spatially close tags should experience similar environment effect despite pot's location, and that can be utilized to cancel out environment effect on the signal. Low pass filter is used to remove environment noise as environment noise (e.g., people moving, for example) is more frequent than changes in soil's moisture. In this work, parameters like tag's type, tag's location on the pot, and tag's orientation with respect to the reader are derived from experimentation rather than theoretical analysis; this may hinder the system's scalability.

Escriva et al. [53] rely on capacitive sensing to estimate moisture and salinity of the soil. The moisture content is related to the capacitive value (as discussed earlier), and the salinity is related to the electrical conductivity. This work is focused more on designing the capacitive sensor than on establishing an enhanced theoretical model to map the above-mentioned parameters to capacitive and electrical conductivity values. Balaghi et al. [31] discuss the moisture estimation in the soil through the neutron probe device. The neutron probe is a device placed into the soil (similar to a capacitive sensor) that emits fast neutrons, which slow down as they interact with the hydrogen bond in water and reflect back to the probe. Depending on the amount of returned neutrons, the moisture in soil is estimated. Significant drawbacks with this device are cost, complexity, and the need for a licensed operator to operate the device [34].

A common theme for all the reviewed work in this section is the invasiveness of the solutions proposed, whether by removing the agricultural products from their natural habitat (e.g., [137, 36]) or inserting/attaching sensors directly on them (e.g., [53, 31]). An optimal solution is a solution that remotely senses phenomena without disturbing the growth of agricultural products. From this, we introduce the concept of *RF Sensing*: the utilization of the interaction between signals and the environment to perform sensing in a non-destructive and a non-invasive fashion. Thus, the next two sections discuss recent works that adopt RF Sensing for general

applications (§2.2.2) and agricultural applications (§2.2.3), respectively.

### 2.2.2 RF Sensing for General Applications

In this section, we discuss recent work that utilizes RF Sensing for different sensing applications. Specifically, we focus on human, machine, and material sensing through RF Sensing. By doing so, we want to emphasize the applicability of RF Sensing to different domains. We start with human sensing. In [29], the authors proposed SafeDrive-Fi, a system that utilizes the Channel State Information (CSI) to differentiate between safe and dangerous driving behaviours. The authors establish an activity database to map CSI measurements to different driver's movements that reflect a specific behaviour such as angry or sleepy. From that, SafeDrive-Fi record CSI measurements and employs k-Nearest Neighbor (kNN) and Support Vector Machine (SVM) classifiers to match the readings to the behaviour stored in the database. The authors in this work do not report how factors like the distance between the driver and the transceiver affect the results or how CSI measurements will differ depending on the driver's physical appearance. Also, establishing an activity database is a non-trivial task, especially with many variables (including the two variables mentioned above) that may affect the CSI measurements inside a moving car.

BodyCompass is a work published by Yue et al. [133] to estimate a person's posture while sleeping through RF Sensing. BodyCompass employs the Frequency Modulated Continuous Wave (FMCW) radar. FMCW works by emitting continuous waves that are frequency modulated and can detect the speed and the distance between the radar and objects in the environment [133]. BodyCompass works by capturing continuous RF snapshots of the environment and dividing them into specific periods; each period represents a single posture. An RF snapshot is a grid that represents RF reflections off the environment at a given time. In a series of RF snapshots, BodyCompass differentiate between reflections off a person and the environment by monitoring a recurring pattern in the signal's phase resulted from a person's chest movement; a characteristic of breathing. To recover the posture from a series of RF snapshots,

BodyCompass employs a fully connected neural network. In this work, BodyCompass requires training when exposed to a new environment. Also, the authors do not discuss BodyCompass performance when multiple persons are inside the room, or when the system faces a person's back; this may hinder BodyCompass's ability to monitor chest movements. The authors in [82] proposed RFWash, a system that monitors the nine hand movements recommended by the World Health Organization for hand hygiene. RFWash uses a millimetre wave radar to recognize hand gestures. Millimetre-wave radars can detect micro hand gestures thanks to the radar's small wavelength. RFWash works by predicting a sequence of hand hygiene gestures rather than individual gestures; the reason being that a person washing his/her hand usually performs a sequence of gestures rather than a single one. Thus, RFWash is trained on a labelled sequence of gestures to estimate the most likely gesture sequence during run-time. RFWash employs deep neural network for the learning process. A main requirement of RFWash is that users have to remain stationary throughout the whole process.

WiFace [42] is another example of human sensing through RF Sensing. WiFace adopts RF Sensing to build non-invasive facial expressions detection system. WiFace utilizes CSI streams (i.e., readings) to accomplish the task. Specifically, WiFace records CSI streams and separate the weak facial expressions footprint on the signal from the dominating noise by applying Hampel identifier and Butterworth low-pass filter. The former is applied to to remove bursty noise in the signal and the latter to remove high frequency components corresponding to noise. The two filters are applied because, according to the authors, noise in the signal has sudden spikes (i.e., bursty) and higher frequencies. Since WiFace is applied in an indoor environment, the system has to be robust to the multi-path effect. To do so, the authors transform the CSI measurements back to the time-domain, and discard signals delayed more than a specific threshold before transforming CSI back to the frequency-domain; the threshold is derived from a previous paper [73]. Due to the high number of CSI streams, the authors employ Principle Component Analysis (PCA) to reduce the dimensions of the data. After applying PCA, the authors observed that the first principle components contain flat and steep slope regions correspond to non-facial and facial expressions, respectively. Thus, WiFace focuses on the steep slope regions,

and applies a classifier to detect six facial expressions (i.e., happy, fearful, surprised, happily surprised, angrily surprised, and fearfully surprised). In this work, the user has to be in a close proximity to both the transmitter and receiver; all non multi-path communications between the transmitter and the receiver have to pass through the user. Finally, we believe that systems with higher frequencies, such as Google Soli at 57 - 64 GHz [19], may be better equipped to detect micro facial expressions than WiFi based systems due to the former short wavelengths.

Other examples of human sensing include FarSense [135], which utilizes CSI measurements to estimate a person's respiration rate, and MultiSense [134] an extension of FarSense to include multiple persons. In [28], the authors introduced Vital Radio, a system that estimates the respiration and heart-rate of multiple targets in an indoor environment. Vital Radio leverages FMCW ability to capture and store the reflection off different spatially-separated targets into different frequency buckets. This allows Vital Radio to estimate the vital signs of each target individually. In [141], the authors extended Vital Radio to recognize a person's emotions. The extended model - called EQ-Radio - extracts the electrocardiogram (ECG) signal of the heart, from which a classification model is used to recognize different emotions. RF-SCG [65], a system that employs FMCW to capture the minute vibrations generated by the heart's mechanical activities before using deep learning to reconstruct the seismocardiogram (SCG) waveform. HARNN [49], a system that employs the deep recurrent neural network to establish a connection between the WiFi CSI and human activities. WiDrive [30] aims at recognizing drivers activity through CSI measurements by building a real-time recognition system based on Hidden Markov Model (HMM). MultiTrack [110], a WiFi-based system to localize, track, and identify multiple targets' activities by reconstructing a signal profile for each target and compare the profile to a pre-existing activity profile database. Widar3.0 [142], a system that identifies gestures by building a velocity profile for each gesture that represents the power distribution over different speeds. Widar3.0 leverages WiFi CST to build such a profile.

For machine sensing through RF Sensing, we discuss the following work [127, 72, 92, 136, 126]. In [127], the authors introduce TagSMM, a non-invasive vibration detection system through

RFID. In this work, the RFID tags are not attached directly on the machines, thus, promoting the non-invasive sensing. The main challenge in designing TagSMM is to amplify the target machine's frequency amplitude (i.e., the frequency of the vibration). In other words, the target machine's frequency amplitude will be buried in environment noises and need to be amplified. To overcome this, the authors present the following observations: signals backscattered from the tags to the reader represent either static path or dynamic path signals. The former represent signals that do not interact with the target machine (i.e., line of sight and reflections off static objects, such as walls, signals). The latter represents signals that interact with the target machine before reaching the reader. Three vectors are created from the two path signals; a static vector, a dynamic vector, and a composite vector representing the first two vectors combined. Each vector represents the amplitude and phase of their corresponding paths. According to the authors, if the phase shift of the composite vector (i.e., between the static and dynamic vectors) is  $180^\circ$ , then the target machine's frequency amplitude is amplified. Furthermore, if the composite vector's amplitude (i.e., the ratio between the static and dynamic vectors) is minimized, then the target machine's frequency amplitude is also amplified. From these observations, the authors note that three parameters affect the target machine's frequency amplitude: the phase difference between the two vibration ends (i.e., the highest and lowest points of vibration), the amplitude of the vibration (assuming it is constant during vibration), and finally the composite vector's amplitude. The first two parameters are machine-related and cannot be modified, whereas the last one can be changed; hence, TagSMM utilizes the last parameter.

To obtain a  $180^\circ$  phase shift, the path length between the static and dynamic vectors must be  $n\frac{\pi}{2}$  where  $n$  is an odd number; this formula is obtained courtesy of the Fresnel Zone theory. To reduce the amplitude ratio, TagSMM employs two tags that are  $< \frac{\lambda}{2}$  apart; this introduces capacitive coupling between the two tags' antennas. The capacitive coupling interferes destructively with the static path signals, thus reducing the static vector's amplitude and, consequently, the amplitude ratio. To prevent the capacitive coupling from interfering with the dynamic paths signal, TagSMM reduces the RFID's reader transmission power to the point where the dynamic path coupling signals are faded before reaching the reader and interfering

with the original dynamic path signals. In this work, the vibration must be apparent clearly on the surface of the target machine, and any vibrations inside a machine cannot be detected. Also, only a single target machine can exist within the vicinity of the RFID's reader and tags; multiple vibration inducing machines may negatively affect the detection accuracy. Finally, finding the optimal transmission power to prevent dynamic path signals coupling must adhere to the following requirements: the static and dynamic path signals are received, the static path coupling signals are received, the dynamic path signals are not received, and finally the distance between tags must be small to introduce coupling effect. All these requirements, coupled with the fact that the transmission power is a function of different factors such as antennas' gain, renders the task of finding the optimal transmission power complicated.

Similar to [127], the authors in [72] measure machines' vibrations. Specifically, the authors address two challenges: first, how to isolate a machine's vibrations from the multi-path signals. Second, how to amplify the phase changes due to vibrations when they are much weaker than the dominating noise. To this extent, the authors introduce mmVib, a system that employs a Millimetre-wave radar to detect non-invasively micrometer-level vibrations. mmVib consists of three components: vibration detection, robust vibration extraction, and vibration refinement. In vibration detection, mmVib focuses on frequency bins that may contain a vibration activity by analyzing the range-doppler spectrum. The spectrum shows the distance and the speed of a moving object (e.g., machine induced vibrations). The robust vibration extraction is accomplished by combining vibration signals from multiple chirps. A chirp is a signal that increases/decreases in frequency with time. Finally, the vibration refinement is accomplished by utilizing the radar's antenna array to calculate the Angle-of-Arrival (AoA) and refine the vibration measurements. In this work, a Millimetre-wave radar operating at the 77 GHz is employed. Because of the radar short wavelength, mmVib cannot detect vibrations inside highly conductive materials (e.g., metals). Actually, mmVib works effectively when it is close and has a line-of-sight communication with the target machine. Thus, mmVib cannot be easily adopted in factories full of metallic machines.



DroneScale [92] is a system designed to estimate external load carried by commercial (unmodified) drones. The main intuition behind DroneScale is that the load's weight will affect the force needed to fly the drone, and such a force will alter the drone's body vibration. To this extent, DroneScale presents two main contributions: estimating the drone's model and the load's weight by inferring the drone's vibration. Unlike the work reviewed earlier (i.e., [127]), DroneScale utilizes the Doppler shift to infer the drone's vibration. According to the authors, current RF systems cannot capture a 1Hz frequency shift. Thus, DroneScale is equipped with a specialized down-converter and a low noise Analog to Digital Converter (ADC); both chips are different from what exists in current RF systems. The authors note that vibration's frequency is affected by three factors: drone's vibration speed and peak to peak drone's displacement resulted from vibrations. The latter is fixed to 5mm (derived from experimentation), and the former is obtained from the Doppler shift. After obtaining the drone's vibration frequency, DroneScale employs Support Vector Machine (SVM) classifier to infer the drone's model and the load's weight. The classifier is trained using five drone models. DroneScale works at the 2.4 GHz and is a passive system; it only listens to signals. Since DroneScale does not transmit signals and the 2.4 GHz spectrum is busy, the authors do not discuss how DroneScale avoids interference from other RF systems. Also, DroneScale is able to detect drones, and estimate their load, from 200 meters away; this is accomplished thanks to the DroneScale's antenna high gain (19 dBi). However, such a narrow beamwidth may complicate the Doppler shift measurements because drones leave the antenna's field of view almost instantly.

IntuWition [136] tries to answer a specific question: can commodity RF radios sense an object's location and type? IntuWition is a system mounted on a drone that sense objects' locations and types by analyzing the reflected waves' polarization. IntuWition is based on the fact that different objects affect waves' polarization in different ways [136]. For example, a perfectly smooth metallic surface will reflect waves while removing their polarization; whereas a perfectly smooth non-metallic surface will reflect waves and retain their polarization. IntuWition measures polarization by receiving the signals at three vertically-polarized antennas; these antennas are perpendicular to each other. A key challenge in designing IntuWition is to "retrieve"

the correct polarization when the reflected waves bounce off multiple objects before reaching the antennas. To address this challenge, IntuWition separates objects based on their distance from the system. Then, it marks each object as legitimate if and only if its phase shift is not the sum of other legitimate objects' phase shifts. In other words, the waves did not interact with other objects before reaching the current object. Clock synchronization between the transmitter and receivers is enabled by connecting a wire between the transmitter and receivers to ensure correct phase shift measurements. After retrieving the correct polarization, IntuWition employs a Multi-Layer Perception model to infer the correct material. The model classifies five different materials: copper, aluminium, plywood, birch, and human. Intuition performance suffers when objects are small, moving fast, or well-shielded. It also cannot differentiate between objects with similar polarization characteristics.

We conclude this section by discussing RIM [126], an RF-based inertial measurement system that measures a device's speed, direction, and rotating angle. RIM is an RF version of Inertial Measurement Unit (IMU), which usually consists of an accelerometer, a gyroscope, and a magnetometer [124]. RIM works by creating "virtual" antennas; each represents CSI measurements of a physical antenna at a specific time and location. For example, when a physical antenna records CSI measurement at location  $l_i$  and time  $t_i$ , RIM creates a virtual antenna  $v_i$ , which represents the CSI measurements at the mentioned location and time. Thus, two physical antennas are "aligned", if one of them resides at a virtual antenna created by the other physical antenna. RIM decides if a physical antenna resides at a virtual antenna's location by comparing their CSI measurements. To compare two CSI measurements, RIM employs the Time-reversal resonating strength, which is a metric based on the Time-reversal focusing effects. Time reversal is a physics phenomenon dictating that the transmitted signal's energy will be focused temporospatially when combined with its time-reversed and conjugated counterpart [40]. Because CSI changes according to changes in the environment, virtual antennas last for a short time where CSI measurements are most likely unchanged. The device's speed - a task accomplished conventionally by accelerometers - is obtained by searching for two aligned antennas and measures the time it takes for the trailing antenna to reside at a virtual antenna

created by the proceeding antenna; since the distance between the physical antennas is fixed, the speed can be obtained. The device's heading direction - a task accomplished conventionally by magnetometers - is obtained by finding two aligned antennas such that one of them is leading and the other is trailing; the heading direction is the direction of the leading antenna. Finally, the device's rotation - a task accomplished conventionally by gyroscopes - is obtained when all physical antennas are aligned; this occurs only when a device is rotating. Note that RIM can detect only yaw movements, and cannot detect roll or pitch movements.

### 2.2.3 RF Sensing for Agricultural Applications

This section aims to connect the two previous sections together to present agricultural sensing through RF Sensing. As mentioned earlier, agricultural sensing through RF Sensing is the scope of this thesis. Thus, we dedicate this section to discuss related work in that domain.

We start with the work presented in [132], where the authors investigate soluble sugar content estimation in fruits. Specifically, they aim at utilizing RF signals to estimate Brix values. Brix ( $^{\circ}Bx$ ) is a metric to measure soluble solid content in an aqueous solution. 1  $^{\circ}Bx$  refers to 1 gram of sucrose in 100 grams of aqueous solution [132]. The proposed system is a millimetre-wave radio operating at the 60 GHz frequency. The system transmits and receives signals through directional horn antennas, which contact the fruit directly. In detail, the authors investigate the impact of fruit's diameter, fruit's surface roughness, fruit's flesh density, and antennas' location on the Received Signal Strength (RSS). After examining the factors mentioned above, the measured RSS values are used to extract three features: the maximum amplitude value, the peak-to-peak amplitude value, and the channel power spectrum. The first two features are obtained from the time-domain signals, whereas the last one is obtained from the frequency-domain. The system utilizes the RSS values along with the three features to calculate, for each feature, first, second and higher-order statistics such as mean, median, variance, and standard deviation. The resulted statistical values, and RSS values, construct feature vectors. For each feature vector, the system employs the correlation-based feature selection (CFS) to determine

the vector's usefulness. CFS works by selecting features based on the correlation's score against an objective. In here, CFS obtains correlation scores, and consequently features, by employing three feature-searching algorithms: Greedy Forward search, Genetic search, and Firefly search. Each search algorithm outputs a subset of features. Each subset is fed into three regression models: Linear regression, Random Forest regression, and Support Vector regression. The regression models output Brix values; the objective of this work.

In this work [132], the authors assume a direct contact between antennas and fruits; this is to ensure that all waves travel directly from the antennas to the fruit without encountering a medium between them. Any medium in-between will alter the waves properties before reaching the fruits, which reduces the proposed system's accuracy substantially. Thus, the proposed system cannot work efficiently on fruits that are smaller than the antennas' aperture as some waves will travel directly from the transmitter to the receiver without interacting with the fruits. Also, a consequence of the direct contact between antennas and fruits, the signal propagation occurs in the near-field region rather than the well-defined far-field region [33]. The authors mention briefly that the signal propagation occurs in the near-field region, but they do not elaborate on how operating in this region may affect the results. With respect to the proposed models, they are based on the RSS values. However, many research works in agricultural sensing - as discussed in section 2.2.1 - rely on measuring the dielectric properties to estimate organic components such as sugar and moisture content. Contrary to RSS, the dielectric properties are a characteristic of the organic components themselves; a change in the component's value is translated into a change in the dielectric properties value. Thus, we believe that measuring the dielectric properties directly is more efficient to estimate organic components than merely measuring the RSS.

FruitSense [111] detects the ripeness state of fruits through the WiFi signals at the 5 GHz band. FruitSense focuses on climacteric fruits, which continue to ripen even after leaving the plant. Thus, FruitSense is targeted towards end-users to determine if a fruit is edible based on its ripeness. FruitSense utilizes CSI measurements to sense fruits' physiological changes.

A key challenge in designing FruitSense is to separate signals travelling through a fruit from multi-path signals. To resolve this, the authors leverage the power delay profile, which records received signals' power intensity as a function of propagation delay (i.e., time). Intuitively, signals travelling through a fruit will appear earlier than multi-path signals because the former experience the shortest path between the antennas. FruitSense "stitches" all channels in the 5 GHz band to construct 600 MHz bandwidth, which translates to 1.5 ns resolution. The authors claim that such resolution is enough to separate the direct signal from the multi-path. However, channels in the 5 GHz band are non-uniformly spaced due to regulations; thus, applying the Inverse Fast Fourier Transform (IFFT) to obtain the power delay profile is inaccurate as IFFT works with uniformly spaced frequency spectrum. To overcome this issue, FruitSense applies the Inverse non-uniform Discrete Fourier Transform (NDFT) instead of IFFT. After recovering the signals that travelled through the fruit, NDFT is applied to transform the signal back to the frequency-domain. Then, FruitSense extracts features from the CSI measurements through Maximal Overlap Discrete Wavelet Transform (MODWT). Contrary to Discrete Fourier Transform, Discrete Wavelet Transform decomposes the signals based on wavelets rather than sine waves. After features' extraction, FruitSense cross-correlates the features against features in a profile library. The library contains four ripeness states: Unripen, Half Ripen, Ripen, and Over Ripen, for two fruits, Kiwi and Avocado. The ripeness ground truth is measured through a spectrometer, which emits light signals and measures absorbed/scattered signals to infer the ripeness level.

As mentioned earlier, FruitSense is geared towards end-users; however, FruitSense's current design is inefficient. To explain, WiFi Access Points (APs) are installed usually in high locations to provide the best coverage [97]; thus, they tend to be relatively far from receivers such as laptops. However, for FruitSense to work efficiently, the user should place the fruit under test between the WiFi APs and a receiver, which should only be 20 cm apart. This is an unrealistic requirement and undermines a main contribution of the work; the removal of multi-path signals. Intuitively, the multi-path effect is more prominent when the distance between communication devices increases because the signals will bounce off more objects. Therefore, the

short distance between the transmitter and receiver is enough reason to ignore the multi-path effect. A better approach is to examine how changing the distance between transmitters and receivers may affect the multi-path profile, and consequently, the system's accuracy. Also, because of the short distance, the signal propagation most likely occurs in the near-field region; the authors do not discuss how FruitSense copes with that. Finally, similar to the previous work (i.e., [132]) FruitSense does not rely on the dielectric properties to estimate physiological changes. As explained earlier, the dielectric properties are highly-sensitive to those changes, which makes them more useful to consider than CSI measurements alone.

The authors in [130] present Wi-Wheat, a system to estimate moisture content in wheat through RF Sensing. Wi-Wheat utilizes the CSI measurements at the WiFi 5 GHz band to estimate moisture content. Wi-Wheat consists of three components: Data Preprocessing, Feature Extraction, and Classification. In Data Preprocessing, Wi-Wheat “cleans” the raw CSI measurements by performing outlier detection, data normalization, and noise removal. The outlier detection removes spikes and abnormal values in CSI measurements through the Pauta criterion method [86], which swaps the outliers with the data mean value. The data normalization is performed to enhance the classifier's detection accuracy by limiting the input's data range to  $(0,1)$ . The noise removal applies the Chebyshev Type II filter to remove environment noise from the data. After the Data Preprocessing step is finished, Wi-Wheat performs Feature Extraction step by applying Principle Component Analysis (PCA) [27] to highlight the data's main characteristics. Afterwards, Wi-Wheat employs the support vector machine (SVM) classifier to estimate the moisture content based on features extracted from the last step.

Wi-Wheat is based on CSI measurements. However, the authors do not consider the fact that CSI measurements on commercial WiFi APs are well-known to contain phase offset, carrier frequency offset, sampling frequency offset, and symbol timing offset because of unsynchronized transmitters and receivers [134]. Without compensating for the offsets mentioned above, the CSI measurements are highly error-prone. Also, the authors do not discuss experiments parameters such as the distance between transmitters, receivers, and wheat as well as the

weight/volume of wheat; we suspect that those parameters should affect Wi-Wheat performance significantly. Finally, in the Data Preprocessing step, Wi-Wheat applies the Chebyshev type II filter to remove “environment noise”; however, the authors do not define environment noise properly nor explain the motivation behind choosing Chebyshev filter.

We conclude this section by discussing Strobe [48]. Strobe senses soil moisture through RF signals. Strobe utilizes the fact that RF waves travel slower in soil due to the soil’s higher permittivity compared to air. Strobe estimates soil moisture content and soil salinity through permittivity and conductivity, respectively. The permittivity and conductivity are calculated by measuring the apparent permittivity and the apparent conductivity, respectively. According to the authors, the apparent permittivity - different from the real permittivity - is the soil permittivity in **situ** and it is a function of the waves’ velocity and frequency. The apparent conductivity - different from the real electrical conductivity - is the soil electrical conductivity in **situ** and it is a function of the apparent permittivity and attenuation coefficient. The latter measures signals attenuation as they pass through a material [48]. To obtain waves’ velocity, Strobe employs multiple antennas to measure the relative ToF, from which, waves’ velocity is obtained [83, 128]. To obtain the apparent conductivity, Strobe utilizes the amplitude ratio between the three antennas to compute the attenuation coefficient; the attenuation coefficient and the apparent permittivity are used to compute the apparent conductivity. To correctly compute the apparent permittivity and conductivity, Strobe assumes that the moisture content and salinity are the same around the three antennas. Also, the transmission path is the same between the transmitter and the three receivers; the only difference is the extra distance travelled by the signals between the three receivers. The authors cannot control the first assumption; thus, the authors focus on satisfying the second assumption. To do so, the authors install the antennas inside the soil in vertical positions; one antenna nearly above the other. After calculating the apparent permittivity and conductivity, Strobe obtains the real permittivity and conductivity by approximating the apparent permittivity to the former, and using linear regression on the apparent conductivity to compute the latter. Strobe converts the permittivity and conductivity to the moisture content and salinity through exploiting well-defined models used by soil sensors.

Strobe is based on WiFi signals, specifically, the 2.4 GHz band because - according to the authors - the 5 GHz band is highly attenuated in soil. Since WiFi signals suffer from the multi-path effect due to signals propagating in “every” direction, Strobe employs the Multiple Signal Classification (MUSIC) algorithm to recover the direct path from the transmitter to the receivers. As mentioned earlier, Strobe installs multiple antennas as receivers inside the soil. The distance between the antennas is derived from experimentation on the soil where Strobe is installed. Since soil is different in different locations [105], Strobe may require re-calibration when installed in a new environment. Although this work uses RF signals to estimate soil’s moisture and salinity in a non-invasive fashion without installing special sensors in soil, the authors do install antennas inside the soil. Thus, Strobe is not entirely non-invasive, and it can only sense moisture/salinity as deep as 30 cm inside the soil. Existing conductive soil sensors, for example, can accomplish the same job as Strobe by installing a single sensor in soil rather than three antennas [35].

#### 2.2.4 Grape Moisture Sensing

In the previous sections, we reviewed recent work in human/machine/material sensing through RF Sensing (§2.2.2), and agricultural sensing through RF Sensing (2.2.3). By doing so, we want to illustrate what *RF Sensing* means by providing examples of recent work that adopt RF Sensing in different applications, especially agricultural applications. Following that, we conclude this chapter by presenting recent work in grapes yield estimation through non-invasive sensing. Grapes yield estimation is an agricultural application, and non-invasive sensing is a by-product of RF Sensing. Thus, combining both represents the main objective of this thesis.

Before reviewing recent work, we discuss the current practise for yield estimation. Currently, yield estimation is based on measuring cluster’s weight manually to estimate the moisture content, and eventually the yield [107, 125]. This is a laborious and invasive process as sparse samples are cut from the vineyard to extrapolate the overall yield at harvest time. The samples



are taken to predict the yield for the current growing season and/or subsequent seasons [44]. For the current season, samples are taken in the *lag phase* period, which is the time when the seeds begin to harden and the cluster's weight reaches around 50% of their final weight. Then, the final weight is computed through multiplying the estimation from the lag phase period by a constant value; the constant value is typically determined from past growing seasons [44]. This approach is problematic as such predictions do not incorporate the new year's environmental factors that impact the grape growth such as diseases and climate change [45]. Following the current practise, the inaccuracy in yield estimation could reach as high as 40% [122]. Thus, the ideal is a mechanism that can estimate grapes moisture content non-invasively in a more granular and continuous way to observe the diversities of the field; this makes the grape products more sustainable and cost-effective.

Non-invasive alternatives to the current practise can be categorized into measuring grapes weight [84, 67, 113, 39, 112] or counting grapes [45, 93, 94, 56, 51, 102, 62]. We start with the former and discuss the work in [84]. The authors in [84] investigate RGB cameras' ability to estimate clusters size through a single frame. The authors mount an RGB camera on top of a robot that moves between vineyard rows. The authors conduct two main experiments, a controlled experiment and a vineyard experiment. In the controlled experiment, vine plants are placed into pots with a black background behind the pots to enhance images clarity. The vineyard experiment is an uncontrolled experiment where the robot moves between vineyard rows. In both experiments, the camera records videos of the target scenes. Frames are extracted from the videos and parsed into RGB images and point clouds. A Point cloud is a set of sampled points from space representing a shape. In the vineyard experiment, images are treated with different filters to enhance the clarity of those images. Afterwards, clusters in the images are labelled manually or by a detection algorithm based on grapes colour. Finally, different estimation methods are applied to the clusters to obtain the clusters' width and height. The estimation methods work by fitting a shape on a cluster and computing the shape's dimension. For example, the Ellipsoid fitting algorithm works by fitting an ellipsoid on a cluster and computing the ellipsoid's dimension. A key concern for this work is the au-

tomated labelling of clusters with similar colours to the foliage (i.e., leaves). In this case, the labelling algorithm may identify a cluster as leaves and vice versa. To overcome this, manual labelling is applied. However, manually labelling thousands of images is impractical. Thus, the authors choose vines where the colour of grapes is different from the colour of foliage; red in the controlled experiment and blue in the vineyard experiment, whereas the colour of the foliage is green.

The authors in [67] proposed a system to estimate yield by measuring clusters' mass through FMCW radars. This is different from yield estimation from optical imaging (e.g., [84]) because EM waves can interact with hidden grapes, work at night, and are not affected by the luminosity of the scene and the colour of grapes. The proposed system works by constructing 3D radiation images, which can be further exploited to estimate the mass of grape clusters. In detail, the system starts by scanning vine plants and recording the echos (i.e., reflections) from the plant. The echos are recorded for different waves' polarization configurations such as a vertically polarized transmitter and horizontally polarized receivers. The echos are transformed to isosurfaces, representing the power spectrum of the echos in space (i.e., vine plant's location). The isosurfaces are transformed to contours, where each contour is wrapped around a high power echo (i.e., an echo peak). Each contour represents a volume of strong reflections, which may indicate a cluster. After defining the contours, the system employs linear regression to calculate clusters' mass from the contours. The regression model is trained by measuring the mass of harvested clusters. The authors employ three FMCW radars operating at 24, 77, and 122 GHz, respectively. Each radar is placed opposite to vine plants and is moved parallel to the vineyard's row to scan consequent plants. The antennas mounted on the radars are rotated in elevation and azimuth angles, to measure the plants from different angles.

In this work, other materials that co-exist with clusters such as leaves and trunks affect the system's accuracy as evident by empty vines experiment. In the experiment, the authors examine the system's performance on empty vines with everything intact except clusters. Ideally, the system's should report zero mass as no clusters exist, however, the system reported non-zero

mass measurements. This indicates the system inability to distinguish between clusters and other vegetation materials. As mentioned earlier, the antennas are rotated to scan vines from different angles. The rotation's angles - both elevation and azimuth - are dependant on vines' structure. In this work, the angles are defined manually. However, in a vineyard with thousands of vines, manual angle determination is infeasible. Since the system employs radars with high frequencies (i.e., 24, 77, and 122 GHz), the penetration depth - according to Beer-Lambert law [61] - is in the order of millimetres. Thus, we believe the system cannot scan all grapes, especially those at the back of the clusters. One possible solution is to scan the clusters from the front and the back. However, this introduce another problem where measurements overlap and some grapes are scanned more than once such as the middle grapes. In any case, the authors do not discuss the penetration depth nor how to solve this issue.

Another method for yield estimation through weight measurements is the trellis tension wires [113, 39]. The trellis wires are installed along vineyard rows, and the tension is measured continuously. As clusters grow, the tension on wires increases, which is used to estimate clusters' mass. In [113], the authors install 12 tension wires; each wire covers three rows. The data is collected over three years. To estimate the yield, the authors use the tension to yield ratio obtained from the previous two years to estimate the current year's yield. Similarly, the authors in [39] installed trellis tension wires in ten vineyards at different locations. The methodology followed in here is similar to that of the previous work, where tension to yield ratio from last years are used to estimate current year yield. A primary drawback of trellis tension systems is the need to install wires permanently in vineyards and that wires can be affected by environmental factors such as wind and ambient temperature.

For yield estimation by counting grapes, we start with GBCNet [45]. GBCNet is a yield estimation model based on counting the number of grapes in clusters. GBCNet is an imaging system, where a smartphone is used to capture vine plants and deep learning algorithms are applied on the images to obtain the number of grapes. The system follows two approaches to estimate the yield. The first approach is to compute the average number of grapes in a

cluster then multiply this by the average grape's weight, the average number of clusters in a vine plant, and the average number of vine plants in the vineyard. The second approach is to estimate the number of grapes in all photographed scenes in the vineyard and multiply this by the average grape's weight. According to the authors, the second approach is encouraged due to published reports stating that a grape's weight is more stable throughout the years than a cluster's weight. GBCNet applies convolution neural networks on the images to generate density maps. The sum of the pixel values in the density map is the number of grapes. The system is trained and validated on two sets, each containing images collected for different vine plants. In the first set, each image represents a single cluster where the grapes are small and separated from each other. The second set contains images of scenes where each scene contains multiple clusters with different grape sizes. Since GBCNet is an imaging based system, the scenes lighting conditions affect the system's accuracy significantly. In some cases, the system reports foliage as clusters, and cannot detect hidden grapes. The system may require multiple training steps/phases as grapes grow and change colours.

The authors in [93] proposed a system to estimate yield by counting grapes. The system mounts a camera and a light on a vehicle that travels between the vineyard rows. The camera captures images of vine plants, and the light enhances the lighting condition of the captured scene. The system aims at detecting grapes, then counting them. It consists of three components: 1) Detecting possible grape locations, 2) Classifying detected locations as grapes or not, and 3) Grouping adjacent grapes into clusters. For the first component, the system applies the radial symmetry transform to search for candidate grape centers. The radial symmetry transform works by finding points in an image with high symmetry around the points' radial axis. Those points represent possible grape locations. Afterwards, the system applies the K-Nearest Neighbor (K-NN) algorithm to determine if a candidate location is a grape or not. K-NN algorithm calculates the distance from every point in the training set's feature space for each candidate location. Based on the calculated distance, a location is labelled either as grape or not grape. Note that K-NN may generate false-positive results. Thus, the system's last component removes the false-positive results by removing any point that is not close physically to at least

five other points. In other words, the last component keeps clustered points as they represent grapes in a cluster and discard the rest. The system estimates the yield by counting the grapes and multiply the results by a grape’s average mass. Since this work uses a camera to count the grapes, hidden grapes cannot be counted because they are invisible to the camera.

The work presented in [94] extends the previous work ([93]) and introduces the following additions: First, to detect grapes in an image, the authors apply the radial transform symmetry and the invariant maximal detector algorithms. The invariant maximal detector algorithm works by detecting light peaks surrounded by gradually fading light. This occurs as a consequence of illuminating circular objects such as grapes. The peaks represent the grape centers. Second, the authors map the detected grapes to their location on vines to avoid double counting. To accomplish this, they stamp the vehicle’s location opposite to a vine on the taken images of that vine. The vehicle’s location is obtained by mounting a second camera at the back of the vehicle and applying the visual odometry algorithm. If multiple images are captured in the same location, the image with the most detection is retained while the rest is discarded. We believe this solution may leave some grapes undetected because they belong to the discarded images. The last addition to this work is to estimate the hidden grapes number. The authors solve this by deducing a cluster’s dimension from the number of detected grapes. The dimension is obtained either by retrieving the convex hull formed by detected grapes or by fitting a 3D ellipsoid model to each grouped grapes. After obtaining the cluster’s dimension, visible spaces inside the cluster may indicate partially hidden grapes. A grape obscured partially by two visible grapes will translate into a space between the two detected grapes in an image. Thus, we believe the approach to estimate hidden grapes may not work on entirely obscured grapes since they are not represented by spaces in images.

As discussed at the beginning of this section, the current practise for grape yield estimation is invasive, laborious, and highly inaccurate. However, the alternatives reviewed above suffer from different drawbacks that render them error-prone and unscalable. On the one hand, the weight based methods cannot distinguish between weight changes caused by grapes or other

vegetation components such as trunks (e.g., [67]), are affected by environmental factors such as ambient temperature (e.g., [39]), or are unscalable (e.g., [39]). On the other hand, the counting based methods cannot detect hidden grapes (e.g., [94]), cannot distinguish between grapes and foliage with similar colour (e.g., [45]), or are affected significantly by poor illumination in captured images (e.g., [45]). We believe, however, that the key concerns for all the alternatives are how dependant they are on information from past growing seasons and how they estimate yield through mass and not volume. Regarding the former, the proposed systems above still resort to information from past growing seasons such as grapes weight or the number of vines in a row to estimate yields. This leads to inaccurate estimations as vineyards may change from one year to another due to environmental factors [45]. Regarding the latter, both the weight and counting based methods try to estimate the weight of grapes or clusters to estimate yields. Yields are a function of volume and not mass, thus, those methods estimate yields indirectly. Thus, the optimal is a solution that estimates grapes moisture content directly, independent of past seasons information, non-invasive, and scalable. Inspired by RF Sensing solutions for agricultural sensing, the next chapter introduces our solution for accurate, non-invasive, and scalable yield estimation through RF Sensing: SING.

Paper	Objective	Key features	Methodology	Model	Output	Invasiveness
[129]	Assess ripeness state of yellow peaches	Images	Hyperspectral imaging	3D-CNN Classifier and Multi-task learning models	degree of ripeness	yes
[81]	Estimate moisture content in peanuts	Reflected signals	NIR Spectroscopy	Regression model	moisture content value	yes

Paper	Objective	Key features	Methodology	Model	Output	Invasiveness
[138]	Estimate moisture content in sweet corn	Dielectric Properties	Free Space Transmission technique	DNN Classifier	moisture content value	yes
[80]	Estimate moisture content in grain and nuts	Capacitance value	Capacitive Sensing	Regression model	moisture content value	yes
[121]	Estimate moisture content in soil	Minimum power to activate tag (MRT)	RFID	Regression model	moisture content value	yes
[29]	Differentiate between Safe and Dangerous driving	CSI	RF Sensing (Wi-Fi)	kNN and SVM classifiers	Safe vs. Dangerous driving	no
[133]	Estimate a person's posture while sleeping	RF snapshots (i.e., reflections off environment at a given time)	RF Sensing (FMCW Radar)	CNN classifier	Posture as a function of angles	no

Paper	Objective	Key features	Methodology	Model	Output	Invasiveness
[82]	Detect hand movements while washing	RF snapshots	RF Sensing (mm-wave Radar)	DNN classifier	nine hand movements	no
[42]	Detect facial expressions	CSI	RF Sensing (Wi-Fi)	Tree-based machine learning method, SVM, and kNN	six facial expressions	no
[28]	Detect Breathing rate and Heartbeats	RF snapshots	RF Sensing (FMCW Radar)	Mathematical model	Breathing rate and Heartbeats	no
[127]	Detect machine vibration	Amplitude and Phase shifts of reflected signals	RFID	Mathematical model	vibration frequency	no
[72]	Detect machine vibration	range-doppler spectrum	RF Sensing (mm-wave Radar)	Mathematical model	vibration frequency	no



Paper	Objective	Key features	Methodology	Model	Output	Invasiveness
[92]	Detect drone's model and carried load weight	Doppler shift	RF Sensing	SVM classifier	Drone's model and load weight up to a distance of 200 m	no
[136]	Detect object's location and type	Reflected waves polarization	RF Sensing (Wi-Fi)	Multi-Layer Perception classifier	five materials	no
[126]	Build an RF-based Inertial measurement system	Time-reversal resonating strength	RF Sensing (Wi-Fi)	Mathematical model	device's speed, direction, and rotating angles (yaw only)	no
[132]	Estimate Brix value in fruits	RSS	RF Sensing (mm-wave)	Regression models	Brix value	yes

Paper	Objective	Key features	Methodology	Model	Output	Invasiveness
[111]	Assess ripeness state of fruits	CSI	RF Sensing (Wi-Fi)	Cross-correlation against a profile library	Four ripeness states of Kiwi and Avocado	no
[130]	Estimate moisture content in wheat	CSI	RF Sensing (Wi-Fi)	SVM classifier	moisture content value	no
[48]	Estimate moisture content in soil	Permittivity and Conductivity	RF Sensing (Wi-Fi)	Mathematical model	moisture content value	yes
[84]	Estimate grape clusters dimension	images	Optical imaging	Mathematical model	grape cluster's dimension	no
[67]	Estimate grape clusters mass	3D radiation images	RF imaging	Regression model	grape cluster's mass	no
[113]	Estimate a vineyard's yield	weight measurements	Trellis tension wires	Mathematical model	a vineyard's yield	no
[45]	Count the number of grapes	images	Optical imaging	Deep learning and CNN classifier	the number of grapes in an image	no

Paper	Objective	Key features	Methodology	Model	Output	Invasiveness
[93, 94]	Count the number of grapes	images	Optical imaging	Radial transform symmetry, kNN classifier	the number of grapes in an image	no
SING	Estimate moisture content in grapes	Dielectric Properties	RF Sensing	Regression model	moisture content value	no

Table 2.2: Summary of key papers and SING

## Chapter 3

# SING: Free Space SensING of Grape Moisture using RF Sensing

In this chapter, we present SING, a scheme that senses grape moisture through RF Sensing by utilizing the interaction between the RF signals and the dielectric properties of grapes. It is well-known that RF signals interact directly with the water inside materials [115]; this interaction can be utilized to infer the dielectric properties of agricultural products. Previous research has proven the possibility of estimating the moisture content by relying on their dielectric properties [115, 116]. For grapes, this possibility is supported by the notably high amount of water content [118]. We believe the interaction between RF signals and moisture inside grapes can provide a precise estimation of the moisture content in grapes. To this end, this work makes the following contributions:

- a non-intrusive technique that measures fruit moisture content using grapes as a proof-of-concept.
- a technique to account for the non-uniform shape of the grape cluster when estimating the moisture content.
- a technique that is first to demonstrate RF Sensing moisture sensing that does not require contact with the fruit, nor does it require that the fruit is enveloped in any form of

container. Our technique does not assume any prior knowledge of the fruit's thickness as well, thus making the technique practical.

- through extensive experimentation in a lab environment, we verify our theoretical hypotheses and demonstrate that SING measures moisture content that is 90% accurate. SING's accuracy is emphasized when compared to the current practise, which is only 60% accurate in some scenarios [122].
- through vineyard experiments, we provide early indications of SING's viability for practical agricultural management.

The rest of the chapter is organized as follows: in section 3.1, we discuss why exploiting the relationship between RF signals and the dielectric properties is a viable approach to precisely estimate grape moisture content. Compared with, say apples, grape clusters provide a particularly challenging scenario due to their non-uniform geometries. Thus, we investigate how to account for cluster non-uniformity and how to compute their dielectric properties in section 3.2. We postpone the discussion about SING's performance to the next chapter, Chapter 4. It is worth noting that throughout this chapter and the next chapter, the word *water* and *moisture* are used interchangeably, as well as *sugar* and *sucrose*.

### 3.1 Feasibility of Moisture Estimation through RF Sensing

In this section we investigate the possibility of estimating the moisture content of agricultural products through RF Sensing. To do so, first we need to define a real number to facilitate the analysis of the relationship between the moisture content and  $\varepsilon^*$  because  $\varepsilon^*$  is a complex number. We start by referring to the transmission coefficient ( $\tau$ ) in equation 3.1. The transmission coefficient ( $\tau$ ) is the ratio of the Electrical Field of the Transmitted wave ( $E_t$ ) to the Electrical

Field of the Incident wave ( $E_i$ ) as in equation 3.1[61].

$$\tau = \frac{E_t}{E_i} = e^{-\gamma d} \quad (3.1)$$

Where  $d$  is the distance between the source of  $E_t$  and any arbitrary point in space, and  $\gamma$  is the Complex Propagation Constant. According to [116], equation 3.1 can be rewritten to become equation 3.2, where  $\lambda$  is the Transmission Frequency Wavelength.

$$\tau = e^{-j\frac{2\pi}{\lambda}\sqrt{\varepsilon^*}d} \quad (3.2)$$

From equation 3.2, we define the real number discussed earlier as in equations 3.3.

$$\begin{aligned} \varepsilon^* &= \varepsilon' - j\varepsilon'' \\ \sqrt{\varepsilon^*} &= a - jb \\ \sqrt{\varepsilon^*} &= |\sqrt{\varepsilon^*}| \cos(\tan^{-1}(\frac{\varepsilon''}{\varepsilon'})) + j(|\sqrt{\varepsilon^*}| \sin(\tan^{-1}(\frac{\varepsilon''}{\varepsilon'}))) \quad \text{using Euler's formula [95]} \\ -jb &= j \left[ |\sqrt{\varepsilon^*}| \sin(\frac{\tan^{-1}(\frac{\varepsilon''}{\varepsilon'})}{2}) \right] \quad \text{using De Moivre's theroem [95]} \\ b &= -|\sqrt{\varepsilon^*}| \sin(\frac{\tan^{-1}(\frac{\varepsilon''}{\varepsilon'})}{2}) \end{aligned} \quad (3.3)$$

$b$  is the real number we are looking for, and it is refereed to as the *Extinction Coefficient* ( $\kappa$ ) [38].  $\kappa$  quantifies the attenuation of electromagnetic waves when passing through materials [61], and it is related to  $\varepsilon^*$  as in equation 3.4. In the equation,  $\eta^*$  is the Complex Refractive

Index, and  $\eta$  is the Real Refractive Index [64].

$$\begin{aligned}
\varepsilon^* &= \varepsilon' - \varepsilon'' \\
\eta^* &= \eta - j\kappa \\
\varepsilon^* &= \eta^{*2} \\
\sqrt{\varepsilon^*} &= \eta^* \\
\sqrt{\varepsilon^*} &= \eta - j\kappa \\
\sqrt{\varepsilon^*} &= a - jb \text{ from equation 3.3} \\
\kappa &= b
\end{aligned} \tag{3.4}$$

After discussing the relationship between  $\varepsilon^*$  and the extinction coefficient ( $\kappa$ ), we discuss the possibility of estimating the moisture content through RF Sensing by investigating the following,

**Hypothesis 3.1.**  *$\kappa$  is sensitive to changes in the moisture content, and the relationship between the two is monotonic.*

$\kappa$  sensitivity to changes in the moisture content is important because otherwise, we cannot employ the former to estimate the latter. The pursuit of a monotonic relationship between  $\kappa$  and the moisture content is also important because it facilitates the formalization of the moisture content predictive model (Eq. 3.10) discussed in §3.2.2. From the moisture content predictive model, the parameters are the moisture content, sugar, and frequency. In the next sections, we discuss in details hypothesis 3.1 and how the other two parameters - namely, sugar and frequency - are related to that analysis.

### 3.1.1 The Relationship between the Moisture Content and $\kappa$

To address the first part of hypothesis 3.1, we refer to past research including [115, 116, 118] that state that the dielectric properties of a material are dependant on the internal components of that material such as moisture. Moisture is a key factor in affecting the dielectric properties

in the microwave range of electromagnetic waves due to the water dipole effect [118]. Because of the dipole effect, increasing or decreasing moisture content will increase or decrease the number of water molecules that interact with an incident electric field, hence, changing  $\kappa$  value. Figure 3.1 shows how  $\kappa$  reacts to changes in the moisture content in sucrose solutions. The sucrose solution is a mixture of water and sugar. We choose sucrose solutions because the dielectric properties of sucrose solutions and grape clusters are similar under two conditions: i) They have the same moisture-sugar concentration and, ii) they have been exposed to an electric field with the same frequency [89]. The similarity stems from the fact that grapes are composed mainly of water and sugar [118], and that other components in grapes are not affected by RF signals [89]. Another reason for choosing sucrose solutions is related to measurement efficiency. Contrary to grapes, sucrose solutions allow us to control precisely the concentration of moisture and sugar; this enables us to present a meaningful investigation of the relationship between moisture and sugar against  $\kappa$ .

Figure 3.1 is obtained by employing the coaxial probe technique (explained in §2.1) through the Agilent 85070E Dielectric Probe Kit [2]. The dielectric probe kit measures the dielectric properties of liquids by immersing a coaxial probe into the liquids. The probe is connected to a Vector Network Analyzer (VNA) to process the measurements [2]. To obtain the results in figure 3.1, we prepared six sucrose solutions by varying the moisture concentration from 40% to 90% at room temperature (i.e., 25°C). The minimum moisture concentration is 40% because this is the minimum value where sugar dissolves completely into water. The maximum moisture concentration is 90% because increasing the water will diminish the effect of sugar and the solution starts to resemble pure water. We configure the VNA, which is connected to the probe, to measure the dielectric properties at 50 uniformly spaced frequencies between 5.0 and 6.0 GHz, which henceforth we refer to as the 5 GHz band. We explain the choice of the 5 GHz band in §3.1.4. The error bars in the figure represent the 5% inaccuracy of the dielectric probe kit [2]. For the sake of the figure's clarity, we plot the results in figure 3.1 for 11 frequencies {5.0, 5.1, 5.2, ..., and 6.0 GHz}. The remaining frequencies report similar results to the 11 frequencies, and we plot the results for all 50 frequencies in appendix A, §A.1.



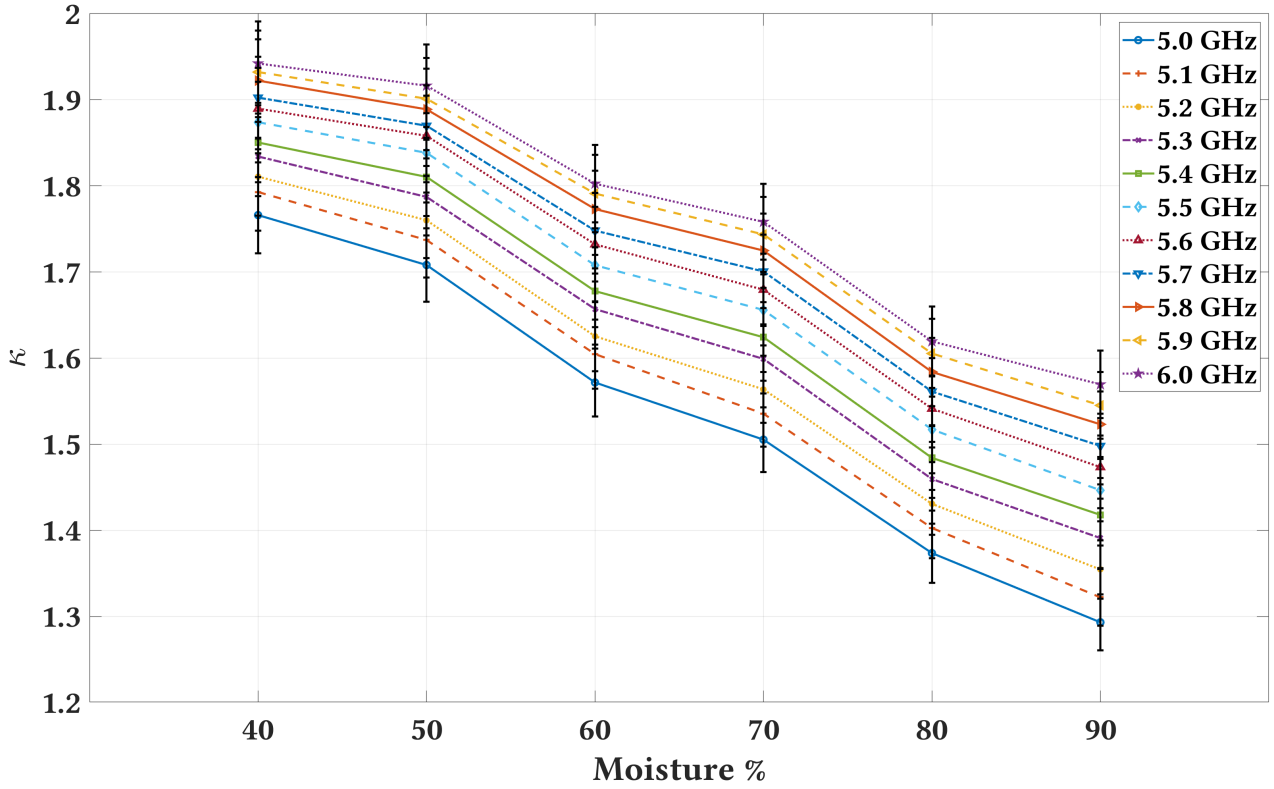


Figure 3.1:  $\kappa$  against different moisture concentration (%) in sugar solutions at 11 frequencies {5.0, 5.1, 5.2, ..., 6.0 GHz}.

To address the monotonic relationship between moisture content and  $\kappa$  (i.e., the second part of hypothesis 3.1), first, we show that moisture content has a monotonic relationship with attenuation ( $A$ ); then we show that the same relationship exists between  $A$  and  $\kappa$ . To address the former, we discuss the outcome of the interaction between the electric field of incident waves ( $E_i$ ) and a dielectric material such as water. When  $E_i$  interacts with water,  $E_i$  undergoes different physical phenomena including reflection and transmission [61]. The transmitted field represents the transmission coefficient ( $\tau$ ) [61]. As more water molecules interact with  $E_i$ ,  $\tau$ 's attenuation ( $A$ ) increases because water is a strong absorbent of electric fields, especially at the microwave frequencies [118]. Thus, a monotonic relationship exists between  $A$  and water's volume (i.e., moisture content). To show that  $A$  has a monotonic relationship with  $\kappa$ , we refer

to equation 3.5.

$$\begin{aligned}
\sqrt{\varepsilon^*} &= a - jb && \text{from Eq.3.3} \\
\tau &= e^{-j\frac{2\pi}{\lambda}\sqrt{\varepsilon^*}d} && \text{from Eq.3.2} \\
\tau &= e^{-j\frac{2\pi}{\lambda}(a-jb)d} && \text{substituting } \sqrt{\varepsilon^*} \text{ by } (a - jb) \\
\tau &= e^{-j\frac{2\pi}{\lambda}ad} \cdot e^{-j\frac{2\pi}{\lambda}(-jb)d} && (3.5) \\
\tau &= e^{-j\frac{2\pi}{\lambda}ad} \cdot e^{-\frac{2\pi}{\lambda}bd} && \text{since } j = \sqrt{-1} \\
A &= e^{-\frac{2\pi}{\lambda}bd} && A \text{ is } \tau\text{'s attenuation} \\
A &= e^{-\frac{2\pi}{\lambda}\kappa d} && \text{since } \kappa = b \text{ from Eq.3.4}
\end{aligned}$$

From equations 3.5, there exist a monotonic relationship between  $A$  and  $\kappa$ . This leads to conclude that a monotonic relationship between moisture content and  $\kappa$  also exist.

To verify the above mentioned analysis empirically, we perform experiments on six sucrose solutions at the 5 GHz band. The solutions have a fixed sugar weight and variable water concentrations from 40% to 90%. Those concentrations are chosen for reasons mentioned earlier. The solutions are tested with the Agilent 85070E Dielectric Probe Kit [2], and experiments on each solution are repeated multiple times at room temperature (i.e., 25°C). The purpose of the experiments is to emphasize the monotonic relationship between the moisture content and  $\kappa$ . Figure 3.2 reports the results for the solutions. In the figure, a monotonic - inverse - relationship between moisture content and  $\kappa$  exists. This is in line with the theoretical analysis mentioned above. The inverse part of the relationship is explained through figure 3.3 and equation 3.3. In figure 3.3,  $\varepsilon'$  and moisture content have a monotonic relationship, which is similar to the findings in [118]. Similarly, in equation 3.3, specifically  $\text{Arg}(\varepsilon^*) = \tan^{-1}(\frac{\varepsilon''}{\varepsilon'})$ ,  $\varepsilon'$  is the denominator and is  $\gg \varepsilon''$  [118]. Thus, as moisture content increases,  $\varepsilon'$  increases and  $\kappa$  is decreased. Hence, a monotonic inverse relationship between moisture content and  $\kappa$ .

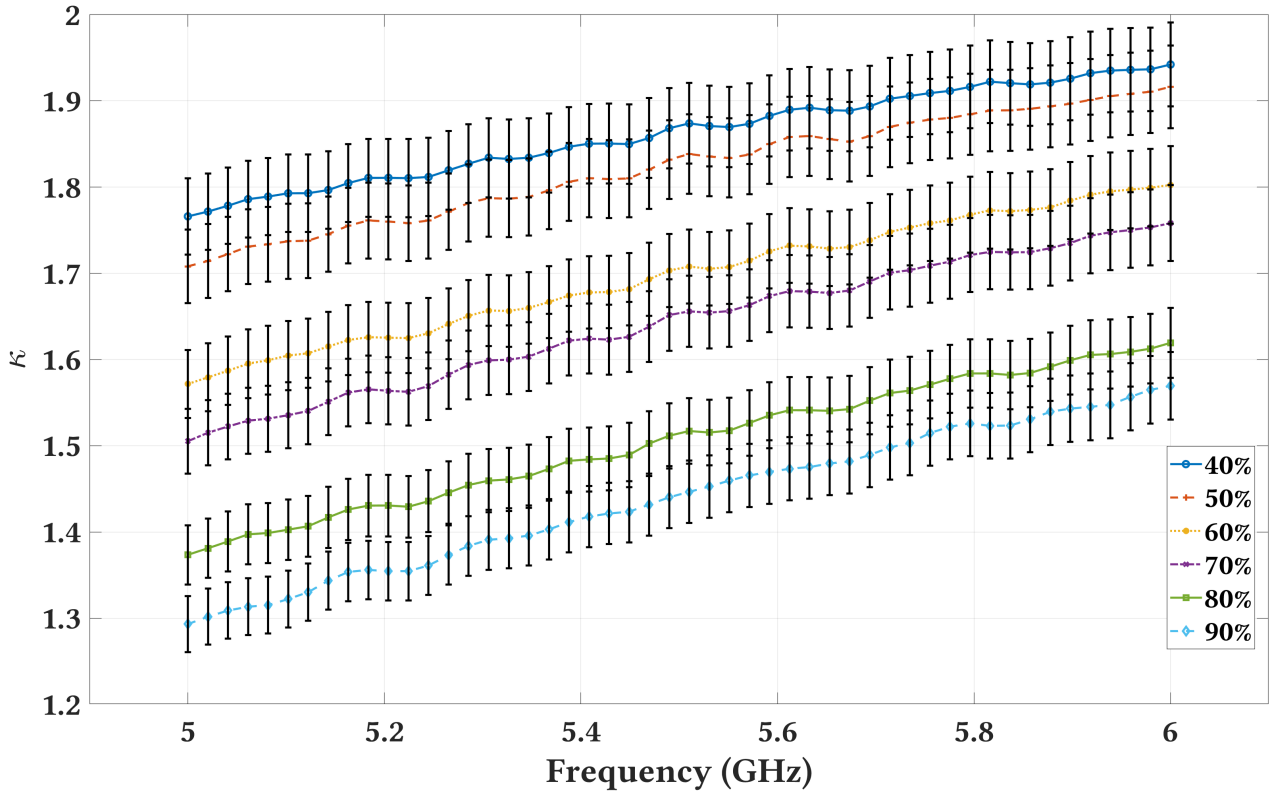


Figure 3.2:  $\kappa$  of variable moisture content concentration {40% to 90 %} at 50 frequencies in the 5 GHz band.

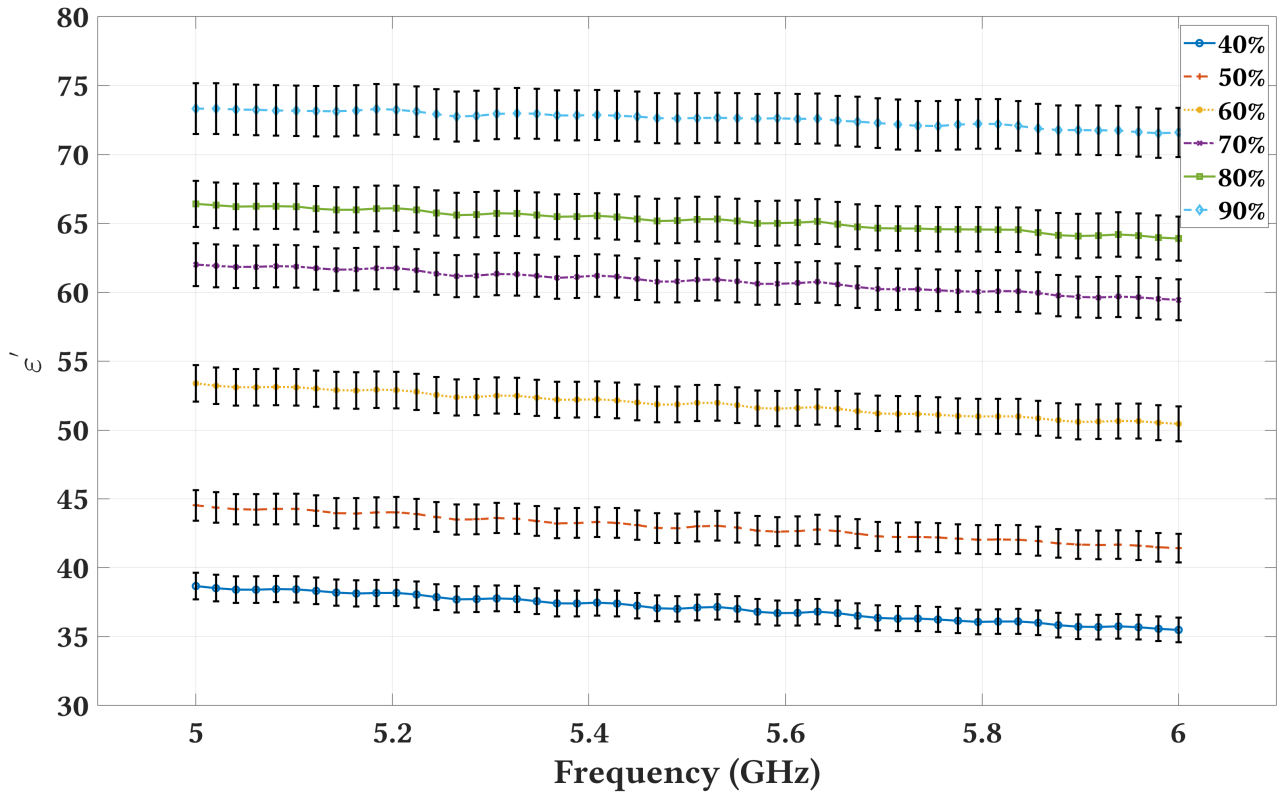


Figure 3.3:  $\varepsilon'$  of variable moisture content concentration {40% to 90 %} at 50 frequencies in the 5 GHz band.

### 3.1.2 The Relationship between the Sugar and $\kappa$

We consider sugar in the analysis because the dielectric properties of sucrose solutions (and equivalently grapes) are defined in terms of three factors: the water molecules, the bound hydration around sugar molecules, and the sugar molecules themselves [98]. Not only that, but analyzing the sugar's effect on RF signals is important for a correct moisture content estimation. To illustrate, in SING we rely on  $\varepsilon^*$  to estimate moisture content;  $\varepsilon^*$  is the same for a solution regardless of the solution's volume, as we explain in the next paragraph. Therefore, for a sucrose solution with fixed water-sugar concentration,  $\varepsilon^*$  is indifferent to changes in the solution's volume. As a result and in order to obtain a correct moisture content estimation, we include the effect of sugar on the RF signals in SING.

To verify that  $\varepsilon^*$  remains the same for a solution despite the solution's volume, we have performed experiments on water only and same-concentration sucrose solutions through the Agilent 85070E Dielectric Probe Kit mentioned earlier [2]. In the water only experiments, we tested six water solutions with the following volumes: {100, 150, 200, 250, 300, and 350 ml}. The results are plotted for both the relative permittivity ( $\varepsilon'$ ) and the loss factor ( $\varepsilon''$ ) at the 50 frequencies in the 5 GHz band in figures 3.4 and 3.5, respectively. Similarly, we performed experiments on seven sucrose solutions (i.e., I, II, III, ..., VII) where the water(%)-sugar(%) concentration is 80%-20%. The results for  $\varepsilon'$  and  $\varepsilon''$  are plotted in figures 3.6 and 3.7, respectively. The four figures emphasize the similarity in both  $\varepsilon'$  and  $\varepsilon''$  between the different water volumes (figures 3.4 and 3.5) and the same-concentration sucrose solutions (figures 3.6 and 3.7). In fact, the small difference in  $\varepsilon'$  and  $\varepsilon''$  measurements is due to the 5% inaccuracy of the measuring kit [2]. Thus,  $\varepsilon^*$  is indifferent to changes in volumes for the same solution. As a result, a correct moisture content estimation cannot be obtained without considering the effect of the RF signals on all of the internal components of a product; for grapes, those components are water and sugar as other components are unaffected by RF signals [89].

Now to emphasize the monotonic relationship between sugar and  $\kappa$ , we prepare six solutions

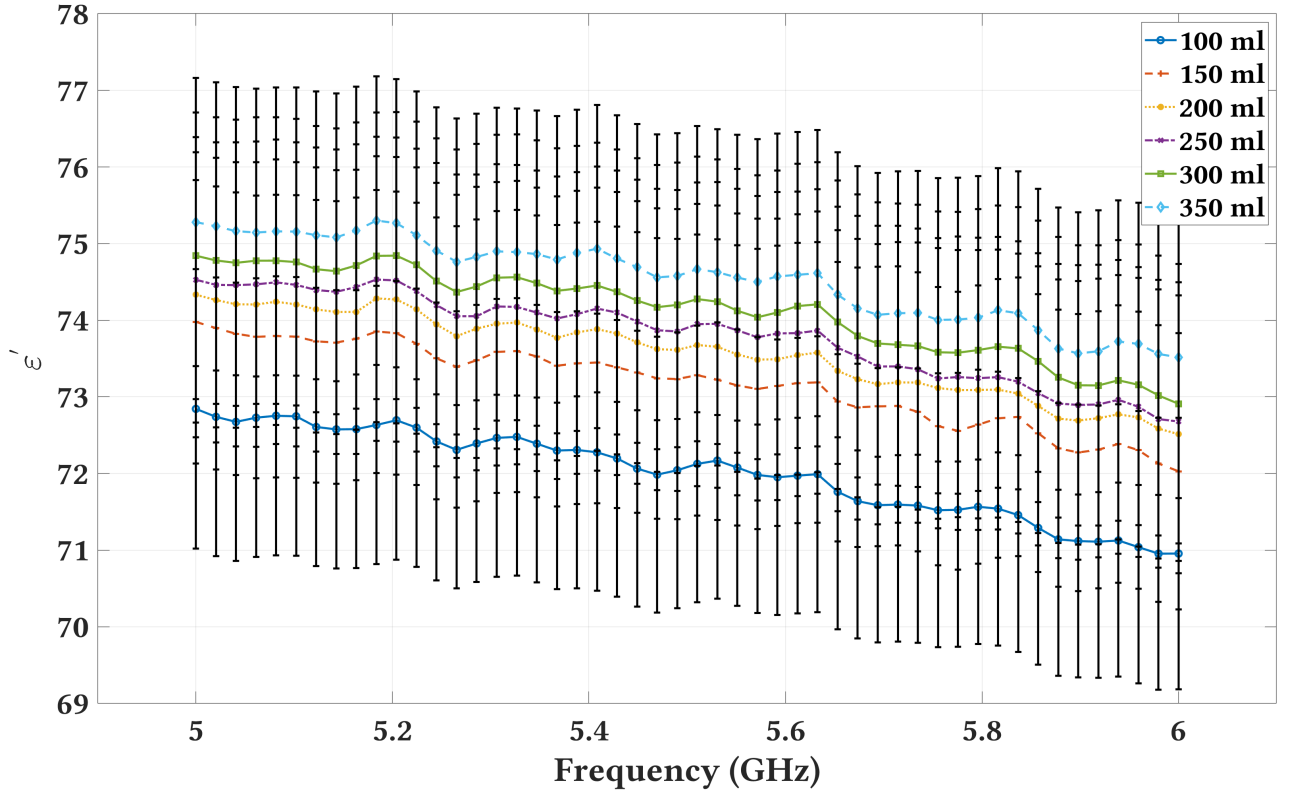


Figure 3.4:  $\epsilon'$  of different moisture volumes at 50 frequencies in the 5 GHz band.

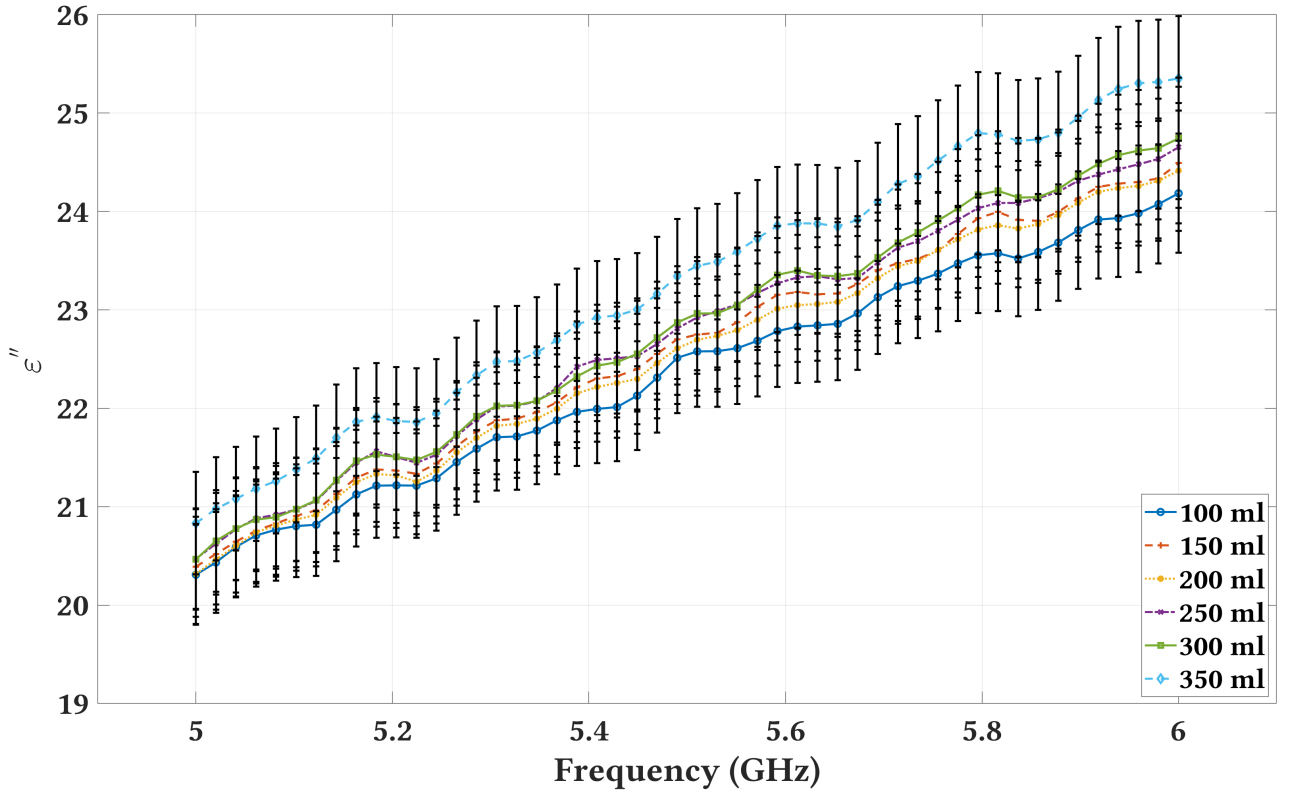


Figure 3.5:  $\epsilon''$  of different moisture contents at 50 frequencies in the 5 GHz band.

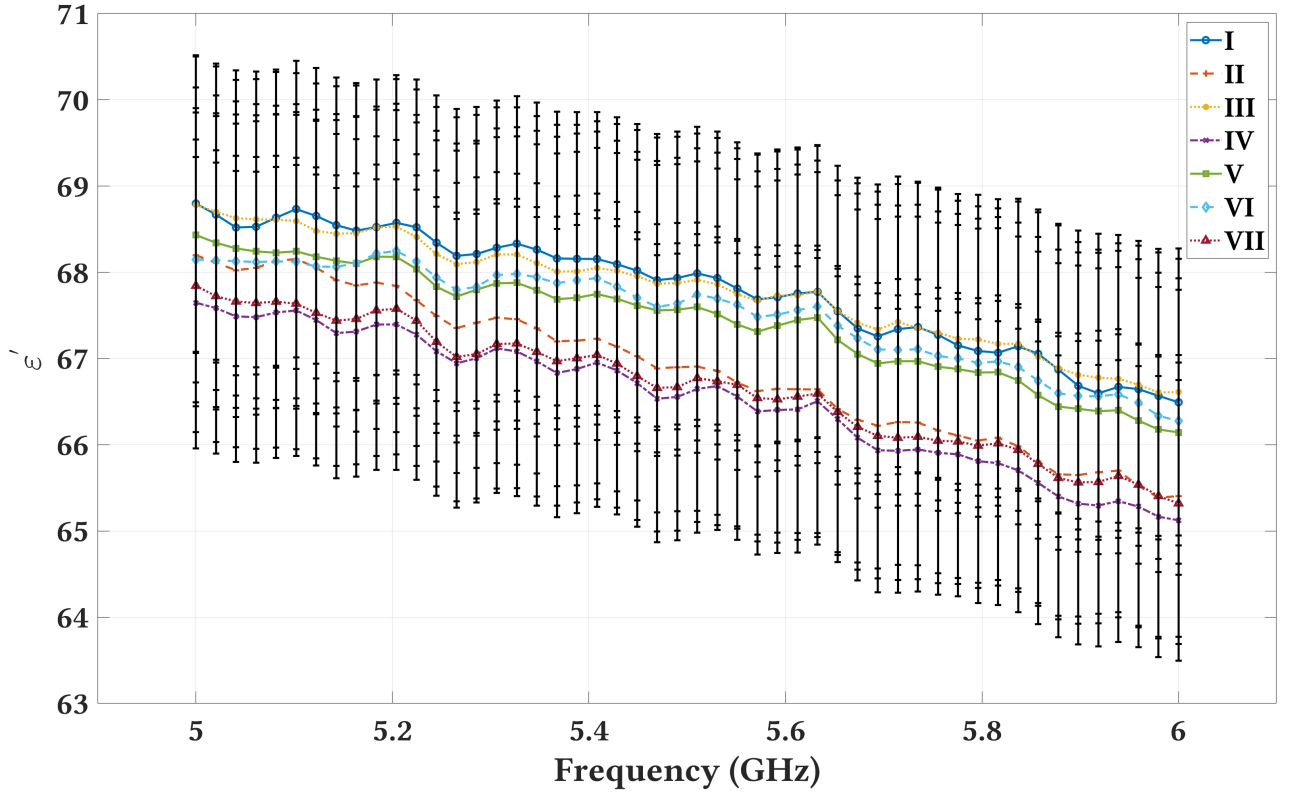


Figure 3.6:  $\varepsilon'$  of the same water-sugar concentration at 50 frequencies in the 5 GHz band.

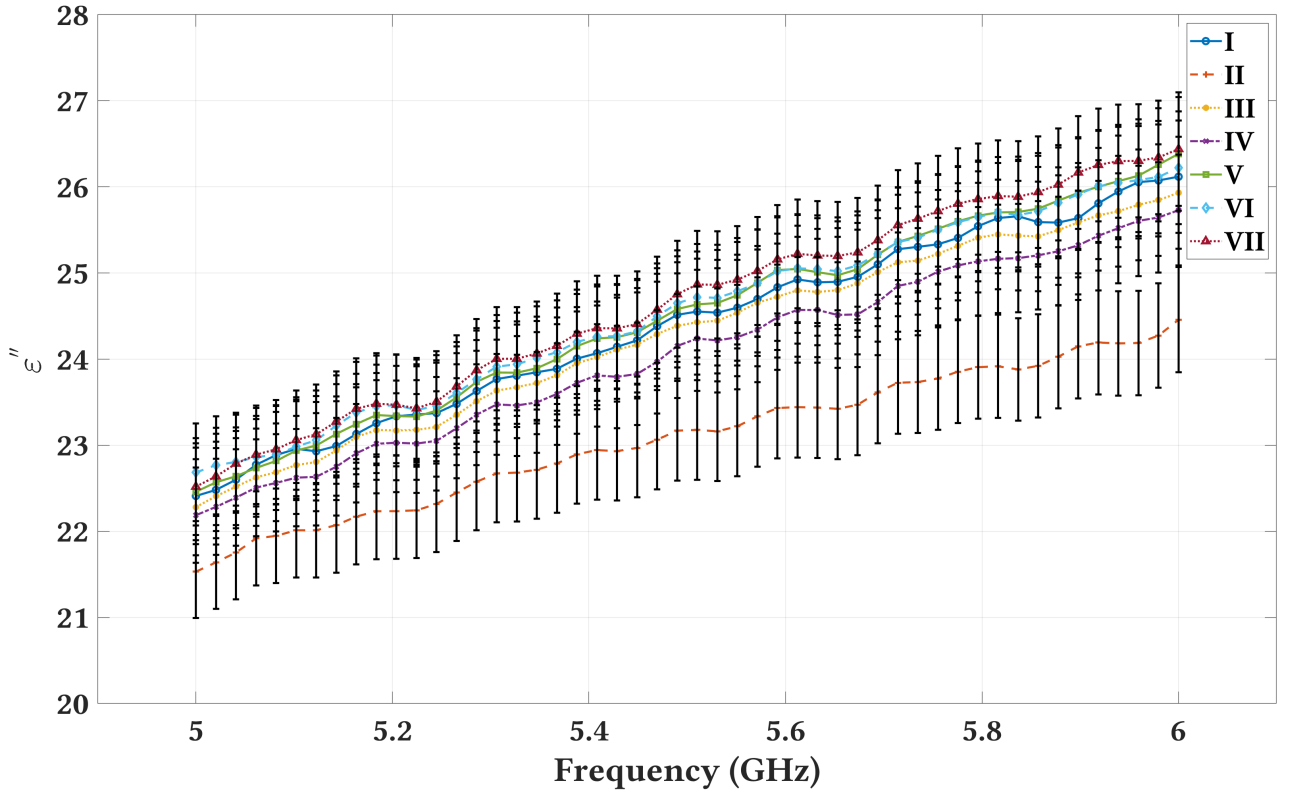


Figure 3.7:  $\varepsilon''$  of the same water-sugar concentration at 50 frequencies in the 5 GHz band.

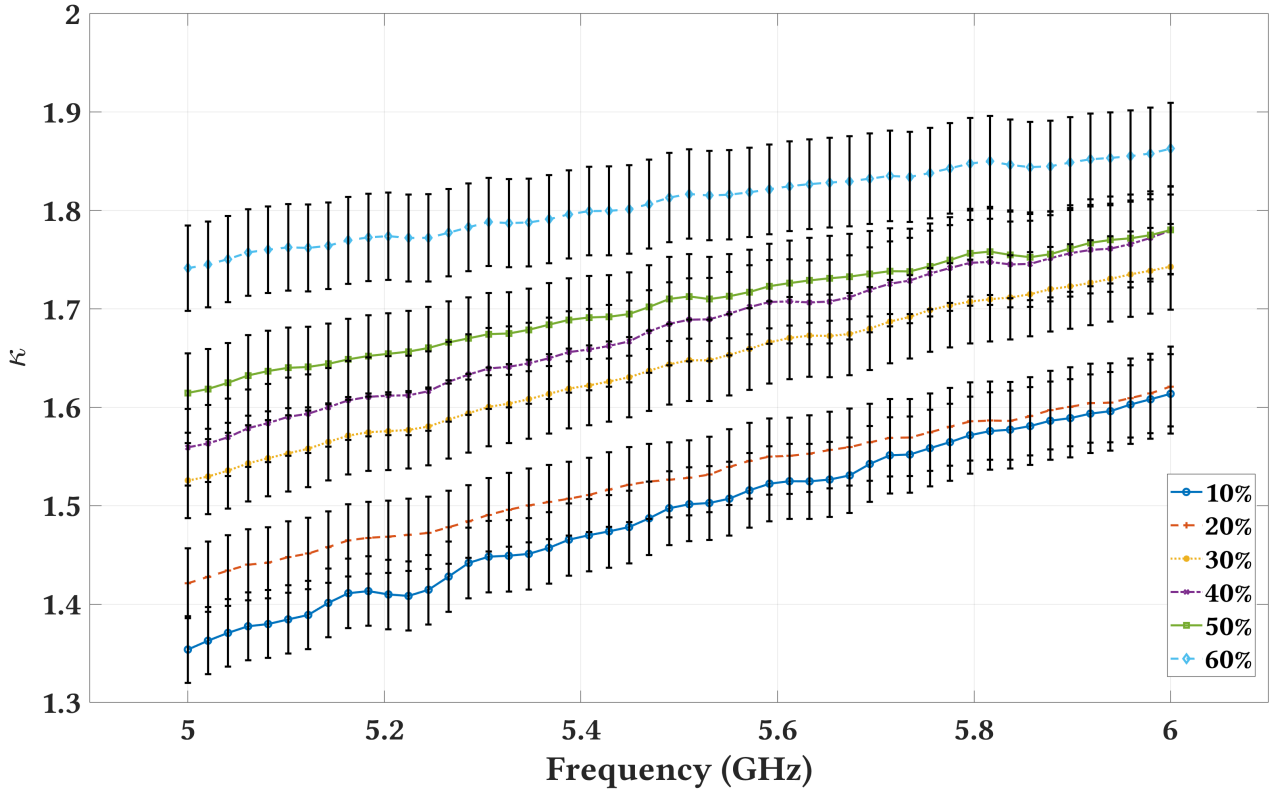


Figure 3.8:  $\kappa$  of variable sugar concentrations  $\{10\% \text{ to } 60\%\}$  at 50 frequencies in the 5 GHz band.

that have a fixed water volume and variable sugar weight, where the sugar concentration is from 10% to 60%. We choose those concentrations because a sucrose solution with sugar concentration less than 10% resembles pure water, and more than 60% prevents sugar from dissolving completely into water. Similar to previous experiments in §3.1.1, the frequency is set to 50 frequencies at the 5 GHz band and the experiments are conducted multiple times at room temperature (i.e.,  $25\text{ }^{\circ}\text{C}$ ). Figure 3.8 presents the results for the solutions. The figure emphasizes the monotonic relationship between sugar and  $\kappa$ . Contrary to figure 3.3 in §3.1.1, an increase in sugar is accompanied by a decrease in  $\varepsilon'$  as presented in figure 3.9. This decrease in  $\varepsilon'$  is the result of more water molecules being bound with sugar molecules, thus, reducing the number of free water molecules that interact with the incident E-field [98].

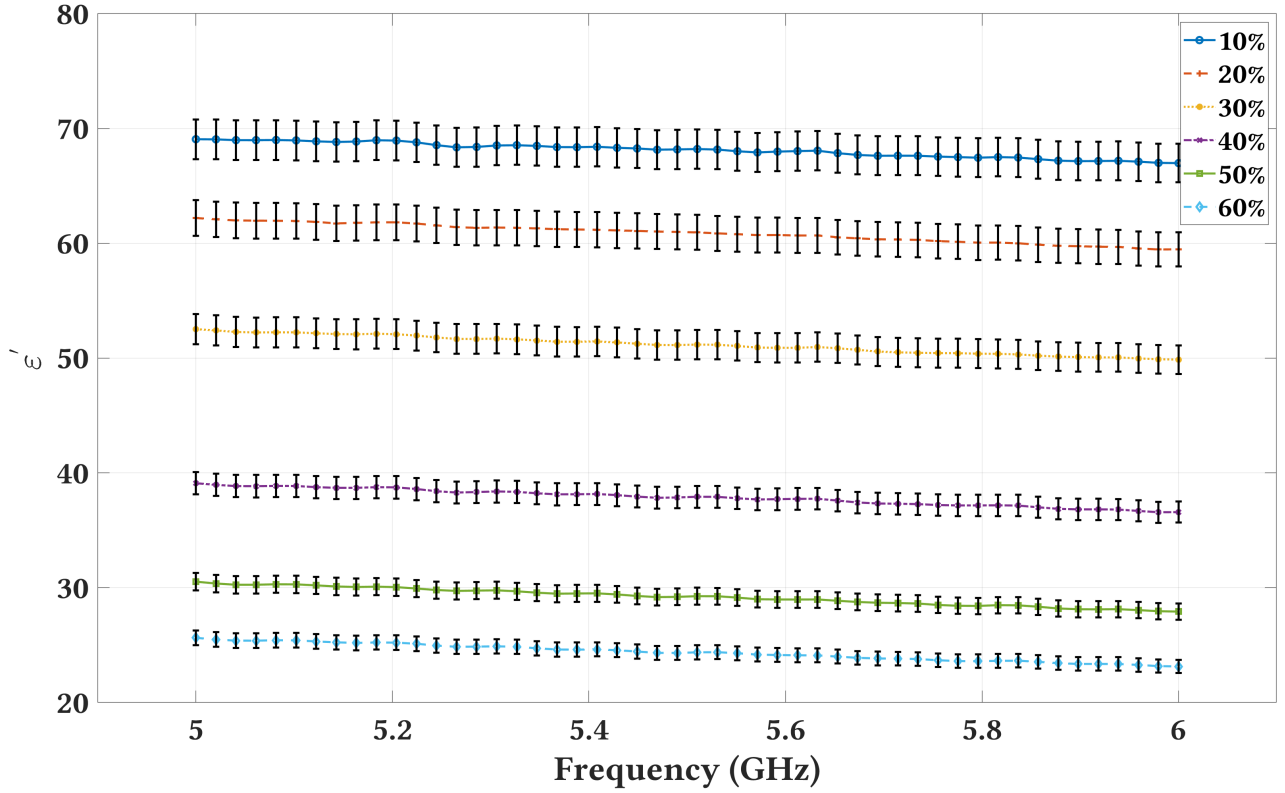


Figure 3.9:  $\varepsilon'_{\omega}$  of variable sugar concentrations  $\{10\% \text{ to } 60\%\}$  at 50 frequencies in the 5 GHz band.

### 3.1.3 The Relationship between the Frequency and $\kappa$

After discussing the relationship between the first two parameters (i.e., moisture and sugar) of the moisture predictive model (i.e., Eq.3.10, §3.2.2) against  $\kappa$ , we investigate now the relationship between  $\kappa$  and the frequency ( $f$ ). The relationship between  $f$  and  $\kappa$  is best explained through figures 3.2 and 3.8. In the figures, we notice how  $\kappa$  increases with  $f$ . Thus, a monotonic relationship also exist between  $f$  and  $\kappa$ .

This concludes the discussion of the relationship between the moisture predictive model parameters and  $\kappa$ . From the discussion we emphasized the monotonic relationship between the three parameters and  $\kappa$ . In the next section, we investigate the reasons behind choosing the 5 GHz band as the operation frequency of SING.



### 3.1.4 SING Frequencies

As mentioned before, we configure the VNA to record measurements at the 5 GHz band (i.e., from 5 to 6 GHz). In fact, SING operates at the 5 GHz band as well. To explain why we choose this band, we refer to the Beer-Lambert law [109]. The Beer-Lambert law computes EM wave intensity ( $I$ ) based on the travelled distance ( $d$ ) and the medium that the EM waves travel through [71]. Thus, we can relate the absorption characteristics of a non-reflective medium based on the intensity of the EM waves travelling through that medium. For example, suppose for a distance  $d$ , the EM waves' intensity travelling through a non-reflective material  $x$  is lower than the intensity through another non-reflective material  $y$ . In that case, we can say that material  $x$  has more absorption characteristics than material  $y$ . This is useful for us as we can decide at which frequencies the EM waves are more absorbed by the moisture inside grapes. In other words, we rely on the EM waves intensity computed by the Beer-Lambert law to find the range of frequencies (i.e. SING frequencies) at which the EM waves are partially, but not fully, absorbed by grapes moisture. We emphasize that the EM waves should be partially but not fully absorbed by grapes to ensure that part of the EM waves should travel through the grapes and reach the receiving end of SING setup - discussed in more details in §3.2.1 -.

Equation 3.6 illustrates the Beer-Lambert law [61] [71].

$$I(d) = I_o e^{-2\alpha d} \quad (3.6)$$

In equation 3.6,  $I_o$  is the EM waves Intensity at the surface of the medium, and  $\alpha$  is the attenuation constant.  $I_o$  is computed through equation 3.7 [99], where  $P$  is the EM waves power and  $A$  is the medium's area.

$$I_o = \frac{P}{A} \quad (3.7)$$

$\alpha$  is computed through equation 3.8, where  $\varepsilon'$  and  $\varepsilon''$  are the medium's relative permittivity

and loss factor, respectively, and  $\lambda$  is the EM waves frequency.

$$\alpha = \frac{\pi(\frac{\epsilon''}{\epsilon'})^2 \sqrt{\epsilon'}}{\lambda} \quad (3.8)$$

To find SING frequencies, we employ as a medium sucrose solutions. We choose sucrose solutions instead of grapes for reasons mentioned earlier in this chapter. We prepare 28 sucrose solutions where the moisture concentration is between 67% and 77%. To compute  $\alpha$  (equation 3.8) we need to measure  $\epsilon'$  and  $\epsilon''$  of the sucrose solutions. To do so, we employ the dielectric probe kit and configure the VNA to operate at 80 frequencies from 1 GHz to 8 GHz [2]. 1 GHz is the start of the microwave range of frequencies and - for practicality - we limit the frequency testing range to 8 GHz because it is infeasible to test all frequencies in the microwave range. However, we note that this range (i.e., from 1 to 8 GHz) is sufficient to find SING frequencies as we explain afterwards.

To find  $I$ , we compute  $I_o$  by setting the power ( $P$ ) according to Ofcom regulations [12], and the area ( $A$ ) according to [84]. Figure 3.10 shows the intensity of the EM waves ( $I$ ) at frequencies {1 GHz, 2 GHz, ..., 8 GHz} for distances up to 14 cm.  $I$  values in the figure are plotted as dBm using equation 3.9.

$$I(\text{dBm}) = 10 * \log_{10}(I) + 30 \quad (3.9)$$

From the figure, we notice that frequencies lower than 5 GHz are not highly absorbed by the sucrose solutions. To illustrate, we show the results from figure 3.10 as percentage in figure 3.11. The latter figure shows the intensity of EM waves ( $I$ ) are more than 50% for frequencies {1 GHz, 2 GHz, 3 GHz, 4 GHz} at a distance of 14 cm. On the contrary,  $I$  at {5 GHz, 6 GHz, 7 GHz, 8 GHz} drops below 30%. The EM waves high degree of absorption at the latter range of frequencies is a vital requirement for SING accuracy. Thus, {5 GHz, 6 GHz, 7 GHz, 8 GHz} are eligible candidates to serve as SING frequencies. Another observation from figure 3.10 are related to the horizontal line at -123 dBm. This line represents the noise floor, which defines

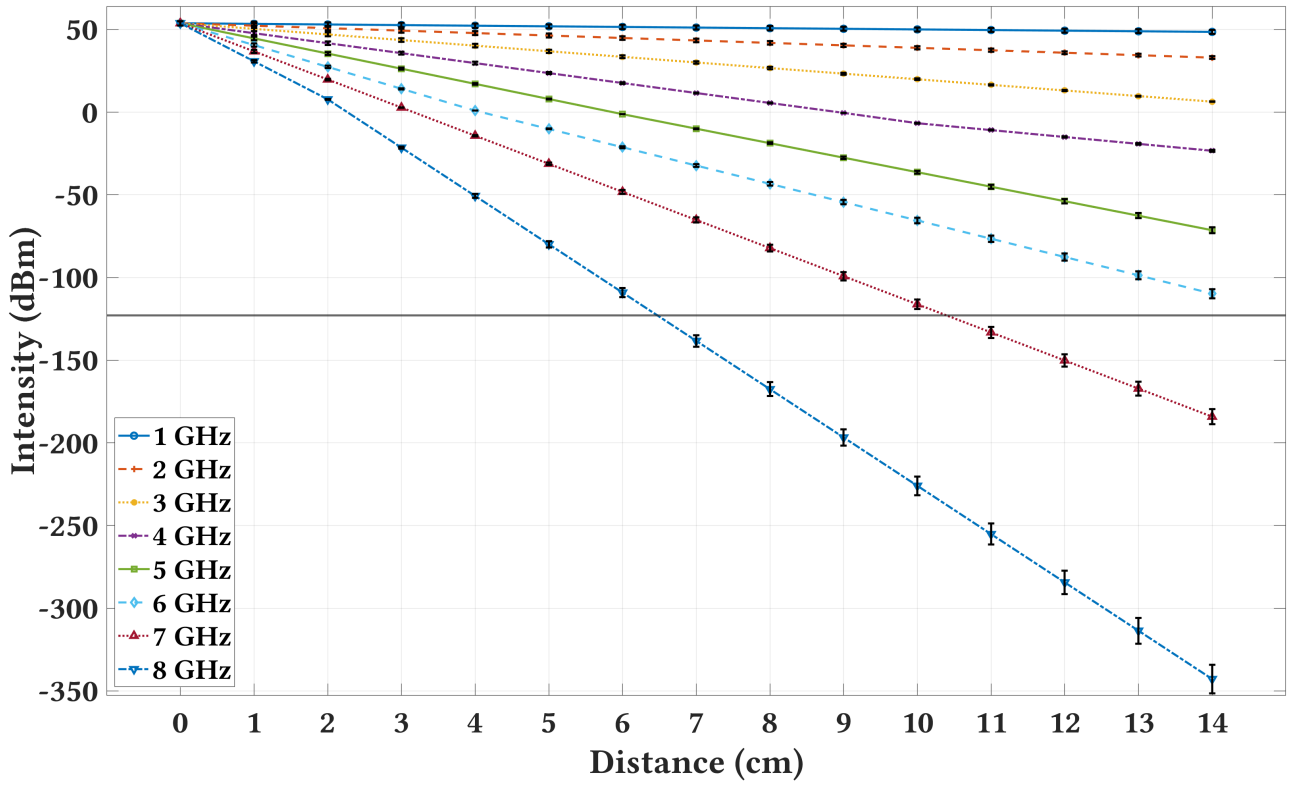


Figure 3.10: The EM waves intensity as dBm at frequencies between 1 GHz and 8 GHz. The horizontal line in the figure corresponds to the noise floor of the N5244B VNA [14]. The values are **computed** through equation 3.9.

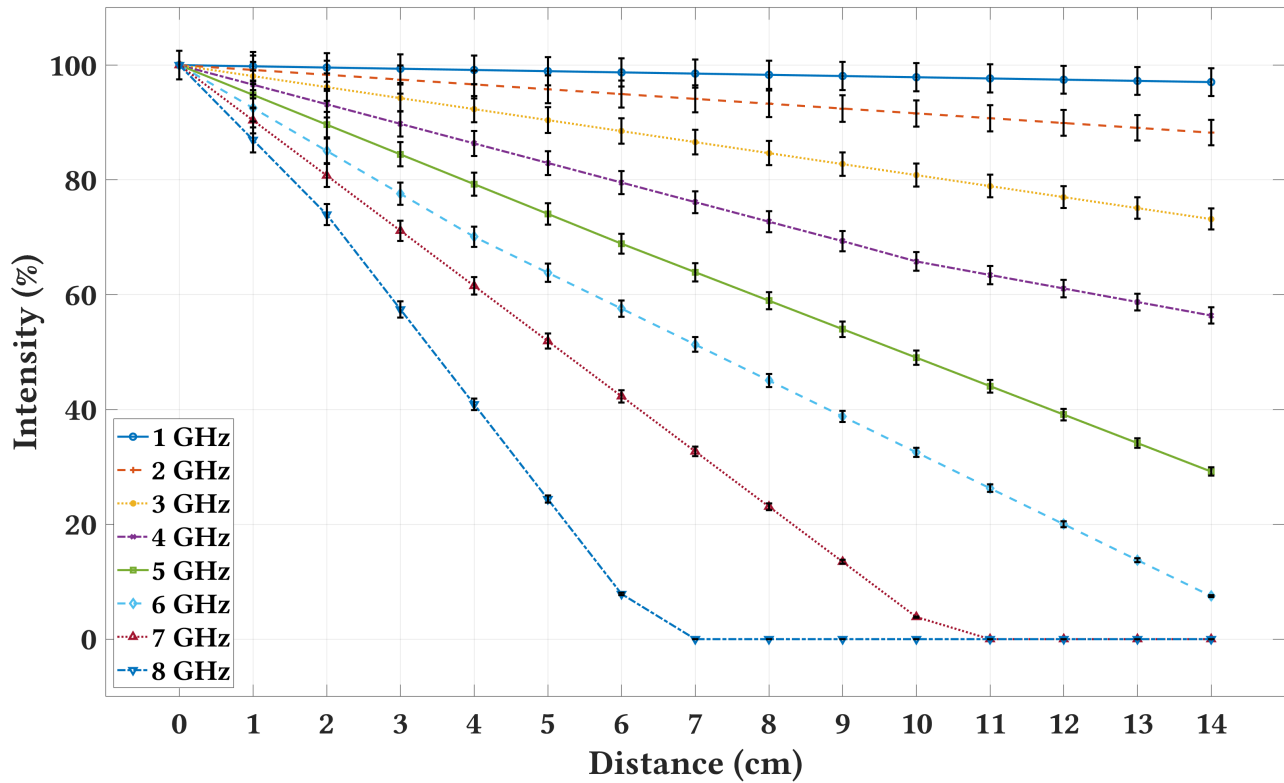


Figure 3.11: The EM waves intensity as % at frequencies between 1 GHz and 8 GHz.

the minimum dBm value at which a receiver can distinguish between a real signal and noise [52]. The -123 dBm value corresponds to the noise floor of one of the most advanced VNA in the market today [14]. For frequencies larger than 6 GHz, for examples 7 GHz and 8 GHz,  $I$  drops below the noise floor after 10 and 6 cm, respectively. This result renders frequencies larger than 6 GHz unsuitable for SING as EM waves will not reach the receiving end of SING setup. Therefore, we choose the 5 GHz band (i.e. 5 to 6 GHz) as SING frequencies. Another reason to support the choice of the 5 GHz band is that this band is a Wi-Fi band. This is important for SING future deployment as it facilitates the integration of SING into existing Wi-Fi infrastructure.

## 3.2 SING Methodology

In this section, we introduce the moisture predictive model (§3.2.2). Then, we present our approach to estimate moisture in grapes through RF Sensing (§3.2.3, §3.2.4, and §3.2.5). Finally,

we investigate factors that may affect SING's performance (§3.2.6 and §3.2.7). But first, we discuss SING experiments and simulations setup (§3.2.1).

### 3.2.1 SING Experiment and Simulation Setup

To analyze and evaluate SING performance, we conduct both experiments and simulations. The former is useful to investigate real-life scenarios, whereas the latter is useful to control factors that cannot be controlled in real-life experiments. The experiment setup (i.e., SING setup) is similar to that of the free-space transmission method with the major difference of computing  $\varepsilon^*$  from multiple angles and being able to do so without a container to envelope the grape's cluster. SING consists of two directional antennas (Huber+Suhner Sencity®Spot-S WiFi Antenna [25]) operating at the 5 GHz band (specifically from 5.1 to 5.9 GHz). The antennas have a 14 dBi gain, and the horizontal and vertical *Half Power Beam Width* are  $40^\circ$  and  $35^\circ$ , respectively [25]. The antennas are connected to a Vector Network Analyzer (E8361A PNA Network Analyzer [8]) that operates between 10 MHz and 67 GHz. As mentioned in §2.1, the Vector Network Analyser (VNA) measures the S-parameters at two ports ( $S_{11}$  and  $S_{21}$ ). The reflection ( $\Gamma$ ) and transmission ( $\tau$ ) coefficients are computed from  $S_{11}$  and  $S_{21}$ , which we discuss in detail in §3.2.4. The two antennas, namely  $T_x$  and  $R_x$ , are vertically polarized, facing each other, and are separated by  $\approx 40cm$ . The distance between the antennas is chosen with respect to the start of the far-field according to [33], which states that the far-field starts at  $\frac{2D^2}{\lambda}$  where  $D$  is the largest antenna dimension, and  $\lambda$  is the transmission's wavelength. The grape's cluster is placed between  $T_x$  and  $R_x$ , and suspended from a wooden rod, which is rotated mechanically using a DC motor controlled by an Arduino board (Arduino Uno [3]). From the rotation, we were able to measure 30 - equally separated - angles for each cluster. The 30 angles are measured in 37 seconds. Therefore, measuring an angle takes  $\approx 1.23$  seconds. Figure 3.12 shows an actual deployment of SING in the lab.

For the simulations, we employ CST Microwave Studio [108]; a 3D electromagnetic solver to simulate electromagnetic applications [108]. We recreate the experiment setup in the simula-

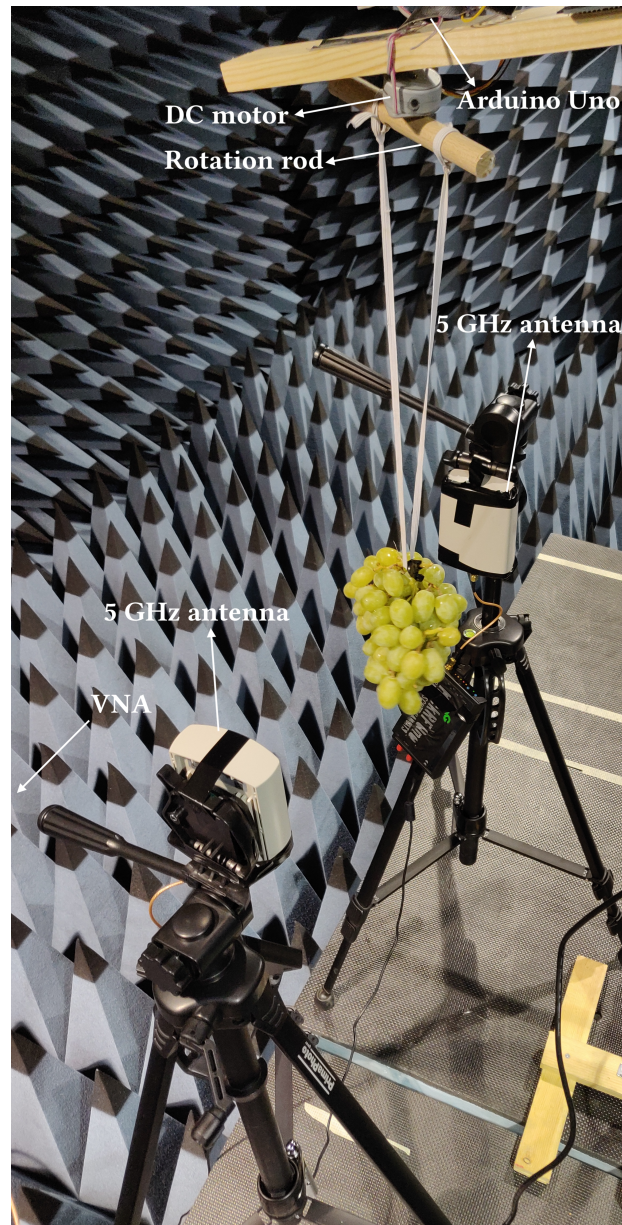


Figure 3.12: SING

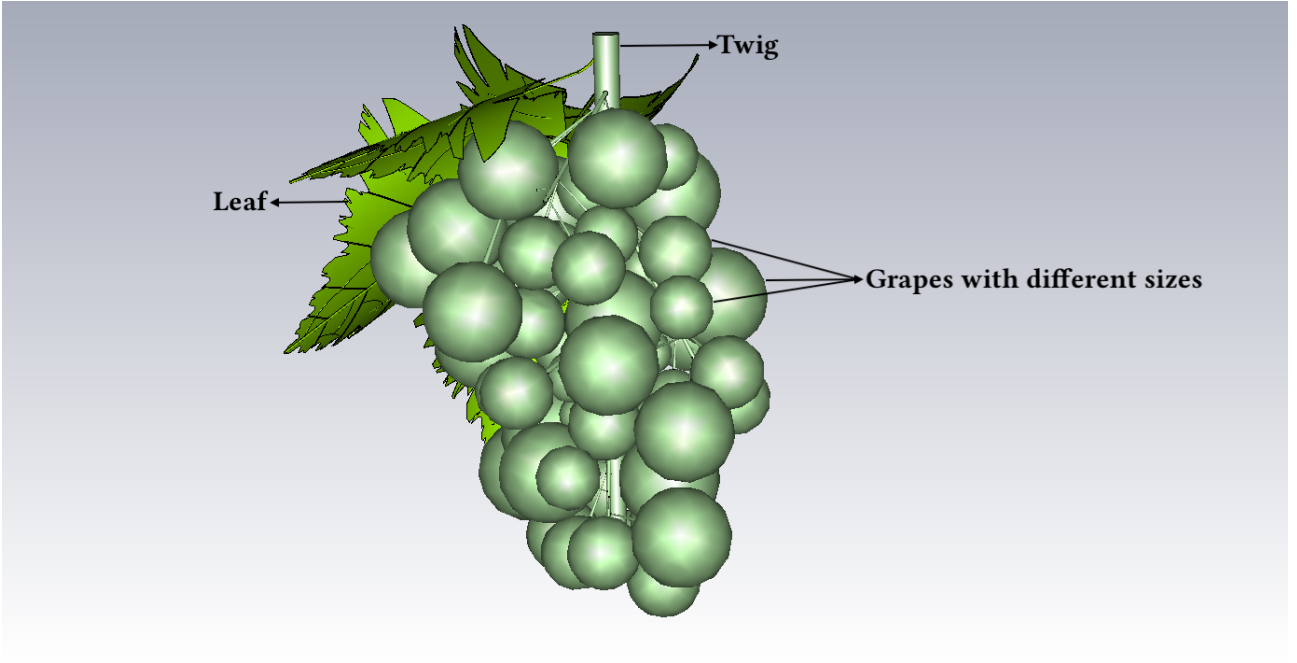


Figure 3.13: A grape cluster with leaves and different sizes of grapes designed through CST Microwave Studio

[108]

tions for consistency purposes. Specifically, we design and place a grape cluster between two directional antennas with a similar gain to the antennas in the experiments. Also, the distance between the antennas and between the antennas and the clusters are the same as the experiments. The grapes are designed as spherical shapes connected to sticks (i.e. stems). We design multiple grape clusters by varying the number and size of grapes. We also design foliage (i.e. leaves) where the thicknesses  $< 1$  mm [101]. Figure 3.13 shows a grape cluster composed of multiple grapes with various sizes and covered by leaves from one side. Finally, the antennas are wide-band Pyramidal Horn antennas operating at the 5 GHz band. We design the antennas by following the mathematical model presented in [33], Chapter 13. The horn antenna - depicted in figure 3.14 - has  $\approx 14$  dBi gain at 5.1 to 5.9 GHz, similar to the antennas in the experiments. Figures 3.15 and 3.16 show the radiation directivity and the radiation pattern at 5.5 GHz, respectively. In appendix A, §A.2, we show both the radiation directivity and pattern at 5 and 6 GHz. All the simulations are run through the Time Domain Solver, which is supported by the CST Microwave Studio (more information about the solver can be found here [108]).

We discuss later in §4.1.1, the grape clusters we employ for both the experiments and simulations

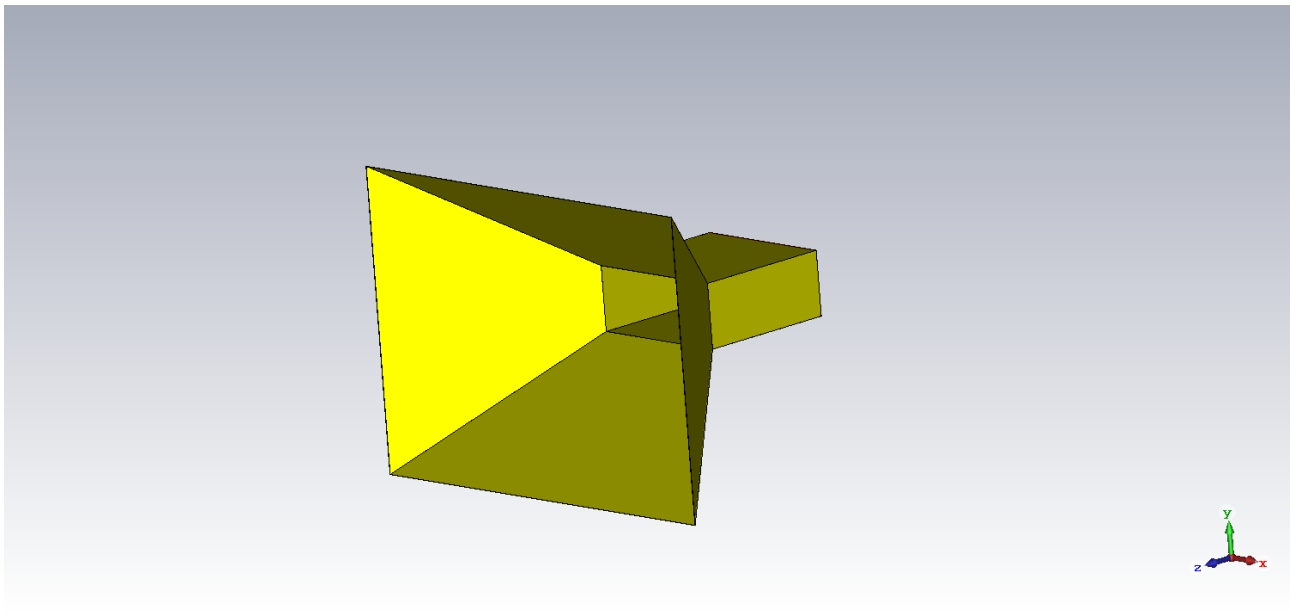


Figure 3.14: The Pyramidal Horn Antenna

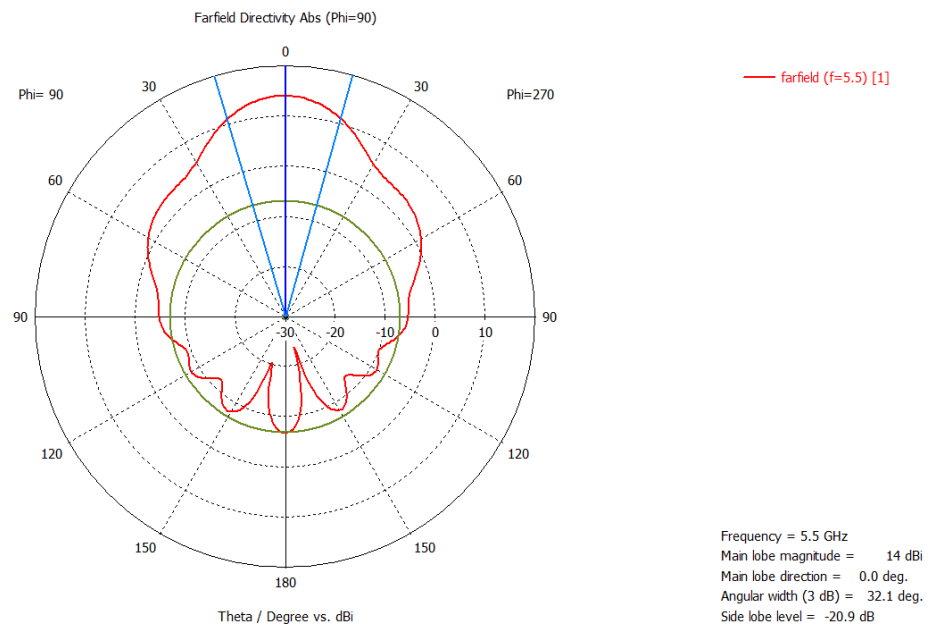


Figure 3.15: Radiation directivity at 5.5 GHz. The red curve represents the main lobe direction, whereas the other lines/curves represent the main lobe width and the side lobe amplitude with auxiliary lines.



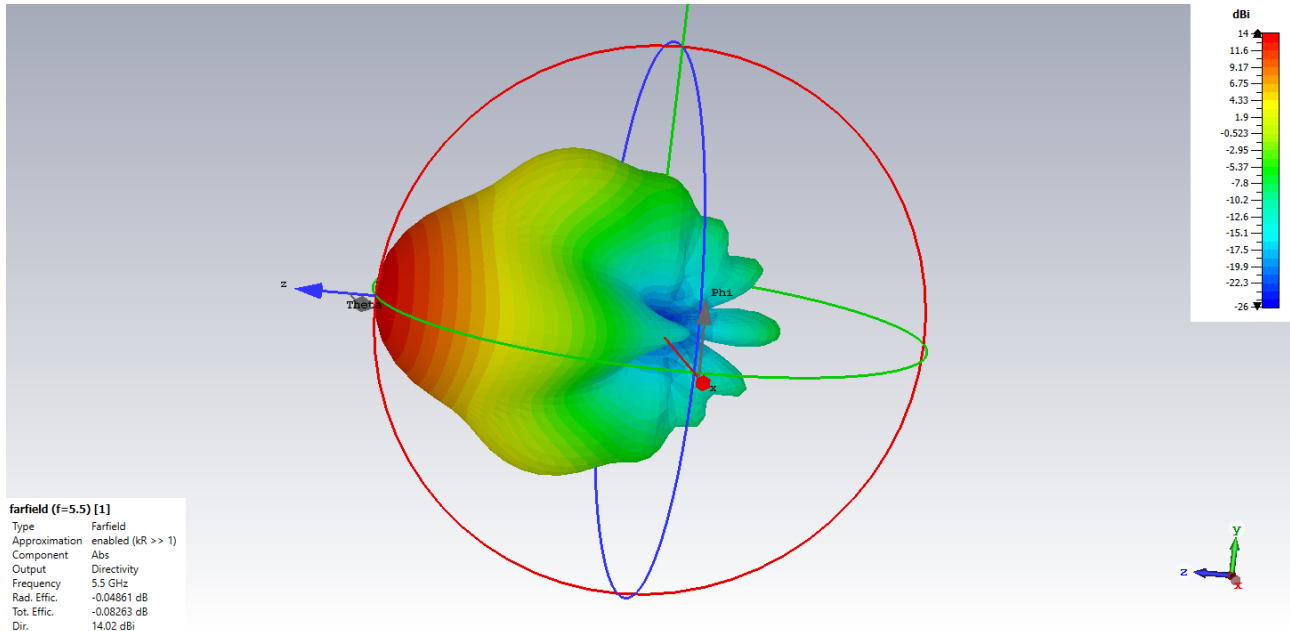


Figure 3.16: The 3D radiation pattern at 5.5 GHz.

and their characteristics (e.g., moisture content and sugar concentration) .

### 3.2.2 The Predictive Model

The moisture predictive model is shown in equation 3.10, where the independent variables are moisture content ( $M$ ), sugar ( $S$ ), and frequency ( $f$ ), and the dependent variable is  $\kappa$ . In the equation,  $\{\alpha, \beta$  and  $\zeta\}$  are the regression coefficients for  $\{M, S$ , and  $f\}$ , respectively, and  $\mu$  is the  $y$ -intercept. The monotonic relationship - discussed in §3.1 - between the dependent variable ( $\kappa$ ) against the independent variables ( $M, S$ , and  $f$ ) of the moisture predictive model encourages us to consider linear regression as a fitting model for our data.

$$\kappa = \alpha M + \beta S + \zeta f + \mu \quad (3.10)$$

From equation 3.10, the moisture content ( $M$ ) at frequency ( $f$ ) is calculated as in equation 3.11, and the final moisture content value ( $\bar{M}$ ) is taken to be the mean moisture content value of all tested frequencies ( $f_{\text{all}}$ ) as in equation 3.12.

$$M = \frac{-1}{\alpha}(\beta S + \zeta f + \mu - \kappa) \quad (3.11)$$

$$\overline{M} = \frac{1}{f_{\text{all}}} \sum_{i=1}^{f_{\text{all}}} M_i \quad (3.12)$$

### 3.2.3 SING's Free Space Transmission Technique

As mentioned in §2.1, the free-space transmission technique works by placing the object of interest in a container between two antennas; the Attenuation Factor ( $A$ ) and Phase Shift ( $\phi$ ) are used to compute  $\varepsilon^*$ . Since  $A$  and  $\kappa$  have a monotonic relationship - as explained in §3.1 -, any change to  $A$  is reflected on the value of  $\varepsilon^*$ , and consequently, on  $\kappa$ . Therefore, to measure  $\varepsilon^*$  accurately, the attenuation ( $A$ ) and the phase shift ( $\phi$ ) should be consistent regardless of the object's orientation (i.e., regardless of which part of the object is facing the antennas). A container is used to enforce consistency of  $A$  and  $\phi$ , among other reasons. Unfortunately, this consistency does not apply for grape clusters since clusters are non-uniform geometrically. To illustrate, we perform experiments on four grape clusters with different moisture contents through the experiment setup mentioned in §3.2.1. The purpose of the experiments is to emphasize the inconsistency in both  $A$  and  $\phi$  at different angles of the clusters. Figures 3.17 and 3.18 report the results for  $A$  and  $\phi$  for a cluster with moisture content = 380 ml at multiple frequencies between 5.1 and 5.9 GHz and equidistant angles between 0 and  $2\pi$ . The figures for the remaining three clusters and other frequencies are plotted in appendix A, §A.3. The figures - plotted here and in §A.3 - show that  $A$  and  $\phi$  are inconsistent and are dependent on which part of the cluster is facing the transmission antenna. As a precaution, we performed the experiments in an electromagnetic chamber to ensure that the inconsistency in  $A$  and  $\phi$  is the sole responsibility of the clusters. This inconsistency leads us to conclude,

**Hypothesis 3.2.** *The attenuation ( $A$ ) and the phase shift ( $\phi$ ) of a grape cluster is dependent on the orientation of the cluster with respect to the incident plane wave.*

To explain 3.2 mathematically, we refer to equations 3.13 and 3.14. For a specific transmission frequency, equation 3.13 shows that  $A$  is dependent on  $\kappa$  and  $d$  (i.e., the travelled distance by waves).  $\kappa$  - similar to  $\varepsilon^*$  - is a characteristic of dielectric materials such as grape clusters. A cluster as a whole has a specific  $\varepsilon^*$ , and by extension, a specific  $\kappa$ . Since a cluster is geometrically

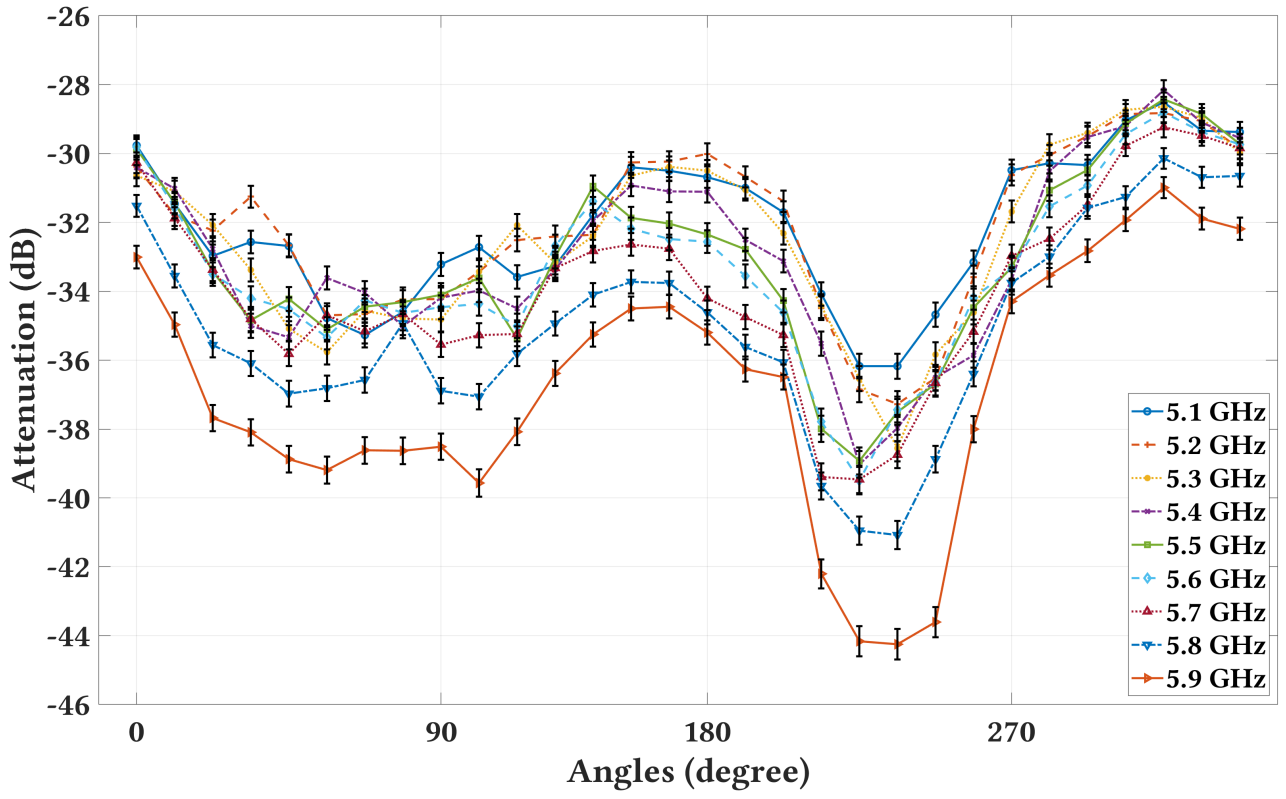


Figure 3.17: The attenuation  $\{A\}$  in dB at  $\{5.1, 5.2, 5.3, \dots, \text{and } 5.9 \text{ GHz}\}$  for a cluster with moisture content = 380 ml at 30 equidistant angles between 0 and  $2\pi$ .

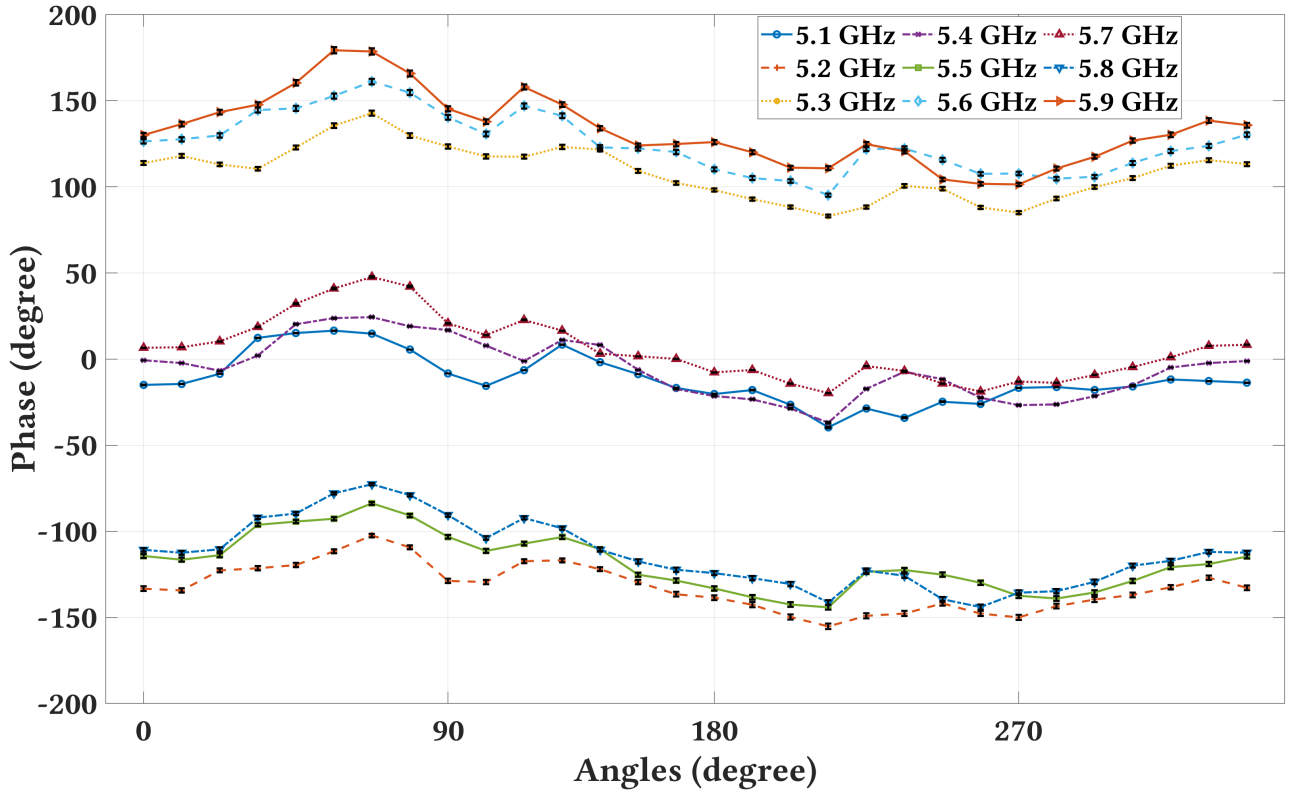


Figure 3.18: The phase shift  $\{\phi\}$  in degree at  $\{5.1, 5.2, 5.3, \dots, \text{and } 5.9 \text{ GHz}\}$  for a cluster with moisture content = 380 ml at 30 equidistant angles between 0 and  $2\pi$ .

non-uniform, different sides of a cluster will have different thicknesses. Therefore, the travelled distance by waves inside the cluster depends on which side is facing the waves. Now, for a specific transmission frequency and a specific  $\kappa$ ,  $A$  depends on  $d$ , which depends on the cluster's orientation. Thus,  $A$  is dependent on a cluster's orientation. The same argument applies for  $\phi$ , where equation 3.14 ([32]) shows that  $\phi$  is dependent on a cluster's permittivity and thickness ( $\rho$ ) for a specific transmission frequency. From before, the cluster as a whole has a specific permittivity, and  $\rho$  depends on the cluster's orientation. Thus,  $\phi$  is also dependent on a cluster's orientation.

$$A = e^{-2\frac{\pi}{\lambda}\kappa d} \quad \text{from Eq.3.5} \quad (3.13)$$

$$\phi = \frac{2\pi}{\lambda}\rho\sqrt{\epsilon'} \quad (3.14)$$

As a consequence of hypothesis 3.2, it is insufficient to compute  $\epsilon^*$  for non-uniform objects such as grape clusters by relying on measurements from a single angle. Thus, we introduce in the next section our technique to accurately calculate  $\epsilon^*$ .

### 3.2.4 Calculating $\epsilon^*$ and $\kappa$

As a consequence of hypothesis 3.2, SING computes  $\epsilon^*$ , and subsequently  $\kappa$ , by measuring  $A$  and  $\phi$  at multiple angles of the cluster. Measuring multiple angles is accomplished by either rotating the antennas, rotating the cluster, or placing multiple  $(T_x, R_x)$ -pairs around the cluster. In this paper, we choose to rotate the cluster for convenience of measurements. However, we note that we can substitute the rotation of the cluster conveniently by the other two options in real-world deployments, as we discuss this in Chapter 5.

As a result of measuring the cluster from multiple angles through the VNA (§3.2.1), we obtain

the following two S-parameters arrays,

$$S_{11}^{\Theta} = \{S_{11}^{\theta_1}, S_{11}^{\theta_2}, \dots, S_{11}^{\theta_m}\} \quad (3.15)$$

$$S_{21}^{\Theta} = \{S_{21}^{\theta_1}, S_{21}^{\theta_2}, \dots, S_{21}^{\theta_m}\} \quad (3.16)$$

where  $\{\theta_i \in \{\theta_1, \theta_2, \dots, \theta_m\}\}$  is the angle  $i$  of the cluster facing  $T_x$ , and  $\theta_m$  is the last angle before the cluster completes a  $2\pi$  rotation. In the current setup of SING (§3.2.1),  $m = 30$ . From the two arrays (3.15 and 3.16), we obtain the transmission coefficient array  $\{\tau_{\Theta} = \{\tau_{\theta_1}, \tau_{\theta_2}, \dots, \tau_{\theta_m}\}\}$  as in equations {3.17, ..., 3.19}.

$$X_{\theta_i} = \frac{(S_{11}^{\theta_i})^2 - (S_{21}^{\theta_i})^2 + 1}{2S_{11}^{\theta_i}} \quad (3.17)$$

$$\Gamma_{\theta_i} = X_{\theta_i} \pm \sqrt{X_{\theta_i}^2 - 1}, \quad \text{where } |\Gamma_{\theta_i}| < 1 \text{ is required} \quad (3.18)$$

$$\tau_{\theta_i} = \frac{S_{11}^{\theta_i} + S_{21}^{\theta_i} - \Gamma_{\theta_i}}{1 - (S_{11}^{\theta_i} + S_{21}^{\theta_i})\Gamma_{\theta_i}} \quad (3.19)$$

From  $\tau_{\Theta}$ , SING computes  $\varepsilon^*$ , and subsequently  $\kappa$ , through equations {3.20, ..., 3.30}, where  $d = d_{\{T_x - R_x\}}$  is the euclidean distance between the transmitter ( $T_x$ ) and the receiver ( $R_x$ ).

$$\bar{\tau}_{\Theta} = \frac{1}{m} \sum_{i=1}^m \tau_{\theta_i} \quad (3.20)$$

$$\bar{\tau}_{\Theta} = e^{(-\bar{\gamma}_{\Theta}d)} = e^{-(\bar{\alpha}_{\Theta} + j\bar{\beta}_{\Theta})d} = e^{(-\bar{\alpha}_{\Theta}d)} . e^{(-j\bar{\beta}_{\Theta}d)} \quad (3.21)$$

$$\bar{\tau}_{\Theta} = e^{(-\bar{\alpha}_{\Theta}d)} [\cos(\bar{\beta}_{\Theta}d) - j\sin(\bar{\beta}_{\Theta}d)] \quad (3.22)$$

$$\bar{\tau}_{\text{real}_{\Theta}} = e^{(-\bar{\alpha}_{\Theta}d)} . \cos(\bar{\beta}_{\Theta}d) \quad (3.23)$$

$$\bar{\tau}_{\text{imag}_{\Theta}} = -e^{(-\bar{\alpha}_{\Theta}d)} . \sin(\bar{\beta}_{\Theta}d) \quad (3.24)$$

Note that the values for  $\bar{\tau}_{\text{real}_{\Theta}}$  and  $\bar{\tau}_{\text{imag}_{\Theta}}$  represent the transmission coefficient for everything between  $T_x$  and  $R_x$  (i.e. Air-Grapes-Air). In order to isolate the transmission coefficient of

grapes ( $\bar{\tau}_{\Theta}^{\{G\}}$ ), we refer to equations {3.25,3.26}, where G stands for the cluster of grapes.

$$\bar{\tau}_{\Theta} = e^{(-\bar{\gamma}^{\{Air\}} \cdot (d - \bar{\rho}_{\Theta}^{\{G\}}))} \cdot e^{(-\bar{\gamma}_{\Theta}^{\{G\}} \cdot \bar{\rho}_{\Theta}^{\{G\}})} \quad (3.25)$$

$$\bar{\tau}_{\Theta}^{\{G\}} = e^{(-\bar{\gamma}_{\Theta}^{\{G\}} \cdot \bar{\rho}_{\Theta}^{\{G\}})} = \frac{\bar{\tau}_{\Theta}}{e^{(-\bar{\gamma}^{\{Air\}} \cdot (d - \bar{\rho}_{\Theta}^{\{G\}}))}} \quad (3.26)$$

The value for  $-\bar{\gamma}^{\{Air\}}$  is obtained by performing an experiment with a clear Line-of-Sight between  $T_x$  and  $R_x$  at distance  $d$  to obtain  $\bar{\tau}_{\Theta}^{\{Air\}}$ . Then, solve for  $-\bar{\gamma}^{\{Air\}}$  as in equations 3.27.

$$\begin{aligned} \bar{\tau}_{\Theta}^{\{Air\}} &= e^{(-\bar{\gamma}^{\{Air\}} \cdot d)} \quad \text{from Eq.3.1} \\ \ln(\bar{\tau}_{\Theta}^{\{Air\}}) &= -\bar{\gamma}^{\{Air\}} \cdot d \\ -\bar{\gamma}^{\{Air\}} &= \frac{\ln(\bar{\tau}_{\Theta}^{\{Air\}})}{d} \end{aligned} \quad (3.27)$$

The value  $\bar{\rho}_{\Theta}^{\{G\}}$  in equations 3.25 and 3.26 represents the mean ‘relative’ thickness of the cluster, and it will be discussed in more details in §3.2.5. Now that we have the values for  $\bar{\tau}_{\text{real}_{\Theta}}^{\{G\}}$  and  $\bar{\tau}_{\text{imag}_{\Theta}}^{\{G\}}$ , we calculate the values for  $\bar{\alpha}_{\Theta}^{\{G\}}$  and  $\bar{\beta}_{\Theta}^{\{G\}}$  as in equations 3.28 and 3.29.

$$\bar{\alpha}_{\Theta}^{\{G\}} = \frac{1}{\bar{\rho}_{\Theta}^{\{G\}}} \ln\left(\frac{\pm 1}{|\bar{\tau}_{\Theta}^{\{G\}}|}\right) \quad \text{where } \bar{\alpha}_{\Theta}^{\{G\}} > 0 \text{ is required} \quad (3.28)$$

$$\bar{\beta}_{\Theta}^{\{G\}} = \frac{2}{\bar{\rho}_{\Theta}^{\{G\}}} \text{atan}\left(\frac{\bar{\tau}_{\text{real}_{\Theta}}^{\{G\}} \pm |\bar{\tau}_{\Theta}^{\{G\}}|}{\bar{\tau}_{\text{imag}_{\Theta}}^{\{G\}}}\right) \quad \text{where } \{3.23, 3.24\} \text{ must be met} \quad (3.29)$$

Now that we have  $\bar{\alpha}_{\Theta}^{\{G\}}$  and  $\bar{\beta}_{\Theta}^{\{G\}}$ , we calculate  $\varepsilon^*$  as in equation 3.30.

$$\varepsilon^* = \left( \frac{\lambda(\bar{\alpha}_{\Theta}^{\{G\}} + j\bar{\beta}_{\Theta}^{\{G\}})}{j2\pi} \right)^2 \quad (3.30)$$

From equation 3.30, the value of  $\kappa$  is calculated as in equation 3.4, §3.1. Finally, it is worth mentioning that individual grapes in a cluster may have different moisture levels. For example, outer grapes may contain less water than inner grapes due to direct exposure to sunlight. Thus, we compute  $\varepsilon^*$  by computing the average value of the transmission coefficients ( $\bar{\tau}$ ) of all scanned angles as presented in equations {3.20, ..., 3.30}.

In figure 3.19, we summarize the procedure mentioned above, which we refer to hereinafter as **SING procedure**.

### 3.2.5 Calculating $\rho$

As mentioned in equations {3.25 , 3.26, 3.28, 3.29}, §3.2.4,  $\bar{\rho}_{\Theta}^{\{G\}}$  is the mean ‘relative’ thickness of grape clusters. This value is different from the physical thickness of grape clusters. The physical thickness yields a correct  $\varepsilon^*$  only if all the transmitted waves pass through the sample before reaching the receiving antenna. Hence, pouring the sample into a large container - usually three times bigger than the transverse dimension of the 3 dB of the transmitted antenna [59] - in the free-space transmission technique. However, including the physical thickness in calculating  $\varepsilon^*$  introduces two problems. First, containers employed in the free-space transmission technique are geometrically uniform, thus, the thickness is easily defined. Grape clusters, on the other hand, are geometrically non-uniform, thus, their thickness is not easily defined. For the sake of argument, let us assume that we were able to define an approach, from which, the thickness is obtained, there is still another problem to solve. This problem is related to the size of grape clusters. Grape clusters are relatively small. Therefore, to obtain a correct  $\varepsilon^*$  value, we must employ antennas with a laser-sharp beamwidth to ensure all the transmitted waves pass through the clusters before reaching the receiving antenna. Dish antennas can achieve an extremely narrow beamwidth [33]. However, they are heavy, bulky, and unsuitable for mobile applications such as in vineyards, where antennas should move around to scan thousands of grape clusters.

From above, we conclude that we cannot compute  $\varepsilon^*$  correctly by using the physical thickness of the grape cluster. Thus, we regard the value of  $\bar{\rho}_{\Theta}^{\{G\}}$  from equation {3.25, 3.26, 3.28, 3.29}, §3.2.4 as the mean ‘relative’ thickness of a grape cluster. Without containers or dish antennas, the interaction between waves and grape clusters will depend highly on antennas’ beamwidth. By changing the beamwidth, waves intercepted by the receiving antenna having interacted with the cluster will be different. Thus, the word ‘relative’ refers to  $\rho$  (i.e., cluster’s thickness) as

being relative to antennas' beamwidth.

To obtain the relative thickness ( $\rho_{\Theta}^{\{G\}}$ ), we analyze the relationship between grape clusters thickness and the transmitted waves. In other words, we analyze the relationship between  $\rho_{\Theta}^{\{G\}}$  and  $\tau_{\Theta}^{\{G\}}$ . To do so, we refer to equations 3.31.

$$\begin{aligned}
 \tau &= e^{-j\frac{2\pi}{\lambda}\sqrt{\varepsilon^*}d} && \text{from Eq.3.2} \\
 \tau_{\Theta}^{\{G\}} &= e^{-j\frac{2\pi}{\lambda}\sqrt{\varepsilon^*}\rho_{\Theta}^{\{G\}}} && \text{for a grape cluster} \\
 \bar{\tau}_{\Theta}^{\{G\}} &= e^{-j\frac{2\pi}{\lambda}\sqrt{\varepsilon^*}\bar{\rho}_{\Theta}^{\{G\}}} && \text{incorporating the mean value for } \tau_{\Theta}^{\{G\}} \text{ and } \rho_{\Theta}^{\{G\}} \\
 \ln(\bar{\tau}_{\Theta}^{\{G\}}) &= -j\frac{2\pi}{\lambda}\sqrt{\varepsilon^*}\bar{\rho}_{\Theta}^{\{G\}} \\
 \ln(\bar{\tau}_{\Theta}^{\{G\}}) &= -j\frac{2\pi f}{c}\sqrt{\varepsilon^*}\bar{\rho}_{\Theta}^{\{G\}} && \text{substituting } \lambda \text{ by } \frac{c}{f} \text{ where } c \text{ is the speed of light}
 \end{aligned} \tag{3.31}$$

Since a grape cluster has a specific  $\varepsilon^*$ , equations 3.31 emphasizes the relationship between  $\tau_{\Theta}^{\{G\}}$  and  $\rho_{\Theta}^{\{G\}}$  for a specific transmission frequency ( $f$ ). Thus, we build a regression model to calculate  $\rho_{\Theta}^{\{G\}}$  for a given  $\tau_{\Theta}^{\{G\}}$  and  $f$ . Equation 3.32 represents the regression model, which we refer to as the thickness regression model.  $\bar{\tau}_{\Theta}^{\{G\}}$  and the frequency are the independent variables;  $\bar{\rho}_{\Theta}^{\{G\}}$  is the dependent variable.  $v$ ,  $\psi$  are the regression coefficients, and  $\omega$  is the y-intercept.

$$\bar{\rho}_{\Theta}^{\{G\}} = v|\bar{\tau}_{\Theta}^{\{G\}}| + \psi f + \omega \tag{3.32}$$

In the regression model, we substitute  $\bar{\tau}_{\Theta}^{\{G\}}$  by its absolute value (i.e.,  $|\bar{\tau}_{\Theta}^{\{G\}}|$ ) because  $\bar{\rho}_{\Theta}^{\{G\}}$  is a real number, whereas  $\bar{\tau}_{\Theta}^{\{G\}}$  is a complex number. Thus, equation 3.32 has  $|\bar{\tau}_{\Theta}^{\{G\}}|$  instead of  $\bar{\tau}_{\Theta}^{\{G\}}$ . We calculate  $\bar{\tau}_{\Theta}^{\{G\}}$  as in equations {3.17, ..., 3.26} and calculate  $\bar{\rho}_{\Theta}^{\{G\}}$  through equations 3.33.

$$\begin{aligned}
 \gamma^{\{G\}} &= \alpha^{\{G\}} + j\beta^{\{G\}} = \frac{-j2\pi}{\lambda}\sqrt{\varepsilon^*} && \text{from [116]} \\
 \alpha^{\{G\}} &= \text{Real}\left\{\frac{-j2\pi}{\lambda}\sqrt{\varepsilon^*}\right\} && \alpha^{\{G\}} \text{ is the real part of the complex number} \\
 \rho_{\Theta}^{\{G\}} &= \frac{1}{\alpha^{\{G\}}}\ln\left(\frac{\pm 1}{|\tau_{\Theta}^{\{G\}}|}\right)
 \end{aligned} \tag{3.33}$$



The value of  $\sqrt{\varepsilon^*}$  is obtained by measuring sucrose solutions - through the dielectric properties kit [2] - with the same water-sugar concentration as the grape clusters considered for the training set of the thickness regression model. It is worth noting that the thickness regression model (3.32) is calibrated to the current settings of SING, where the antennas' beamwidth is  $32.1^\circ$  (a gain of 14 dBi). Thus, when the setting changes, the model needs to be trained again to reflect the new changes.

### 3.2.6 The impact of diffraction on SING accuracy

As mentioned in §3.2.5, the free-space transmission technique requires a container three times bigger than the transverse dimension of the 3 dB of the transmitted antenna [59]. A key reason for this is to avoid the effect of diffraction. Diffraction occurs when a signal is *bent* around edges, and in some cases, this results in multiple instances of the signal reaching the receiving antenna. In other words, received signals did not necessarily travel through the object of interest, rather they could have been diffracted around its edges. Figure 3.20 depicts how diffraction - if it exists - may occur at the edges of a grape cluster. From the figure we emphasize that diffraction affects mainly the transmitted waves, and consequently, the transmission coefficient ( $\tau$ ). Since in SING we compute  $\varepsilon^*$  through the transmission coefficient ( $\tau$ ), we dedicate the section to investigate the diffraction effect on the accuracy of computing  $\varepsilon^*$ .

To investigate the diffraction effect, we run four simulations following the simulation setup in §3.2.1. The simulations are:

- CLoS: a Clear Line-of-Sight (CLoS) between the transmitter ( $T_x$ ) and the receiver ( $R_x$ ) as in figure 3.21.
- Small container: a container smaller than three times the  $T_x$  3 dB transverse dimension. The container is filled with water and placed between  $T_x$  and  $R_x$  as in figure 3.22.
- Large container: a container larger than three times the  $T_x$  3 dB transverse dimension. The container is filled with water and placed between  $T_x$  and  $R_x$  as in figure 3.23.

- Grape cluster: a grape cluster between  $T_x$  and  $R_x$  as in figure 3.24.

In the second and third simulations, the container has the same depth, but different width and height. Otherwise, all other parameters such as the distance between the antennas and the antennas type are the same in all four simulations. The transmitted signal in the simulations is an impulse signal and is shown in figure 3.25. We choose the impulse signal because it emphasises - graphically - the features in time-domain figures more clearly than the default signal in high frequencies CST simulations (i.e. the Gaussian signal).

Figure 3.26 shows the results for the first three simulations: *CLoS*, *Small container*, and *Large container* subplots. The *CLoS* is the first subplot and it represents the received time-domain signal for the *Clear Line of Sight* (CLoS) simulation. The second is the *Small container*, which represents the received time-domain signal for the *Small container* simulation. The third subplot is the *Large container*, which represents the received time-domain signal for the *Large container* simulation. The CLoS subplot shows a single version of the impulse signal because no objects exist between the transmitter ( $T_x$ ) and the receiver ( $R_x$ ) to alter the signals path. However, the Small container and Large container subplots show the original and multiple delayed versions of the impulse signal because a container exists in both simulations between  $T_x$  and  $R_x$ .

The container will impact the incident signals in three aspects. First, the signals will slow down because they will travel from a medium with a lower refractive index (i.e., air) to a medium with a higher refractive index (i.e., water) [61]. Second, some signals will bounce back and forth between the container's edges. This generates reflected signals (i.e., reflected back to  $T_x$ ), transmitted signals without bouncing off the edges (i.e., from  $T_x$  to the container to  $R_x$ ), and signals that bounce off one or more times before reaching  $R_x$ . Third, the signals' amplitude will decrease for a reason similar to that of the first aspect. The Small container and Large container subplots emphasize the three aspects. We notice the original signal in the dashed box in both subplots is slightly delayed compared to the signal in the CLoS subplot. This corresponds to the first aspect. For the second aspect, we observe the multiple subsequent -

delayed - versions of the original signal. Contrary to the CLoS subplot, where only the original signal appears. The third aspect is illustrated by the lower amplitude of the signals in the second and third subplots compared to the first subplot.

After examining the signals in the subplots, the only signal left is the signal in the solid box in the Small container simulation subplot (i.e., the second subplot). This signal is the diffracted signal, and we know that because of the following reasons. First, the signal arrives simultaneously compared to the signal in the first subplot because both signals do not travel through the container. The slight difference in time between the two signals - as emphasized by the vertical line between the two subplots - is because the diffracted signal travel through a longer path (i.e. from  $T_x$  to  $R_x$  through the container's edges). Second, the absence of the diffracted signal in the Large container subplot. As mentioned at the beginning of this section, a container three times larger than  $T_x$  3 dB transverse dimension should eliminate the diffraction effect [59]. Finally, the amplitude of the diffracted signal is significantly lower than the signal in the CLoS subplot. This is because the former arrives at  $R_x$  from the antenna's side, whereas the latter arrives from the center. The horn antenna we design for the simulation performs the best when receiving the signals from the center [33]. However, the performance degrades when the signals angle of arrival deviates from the center [33].

After illustrating the diffraction effect on containers, we investigate the diffraction effect on grapes. To do so, we refer to [103], where the authors state that the diffraction effect is more prominent around sharp edges. Thus, spherically shaped objects such as grapes may not exhibit diffraction. To further investigate this, we refer to the fourth simulation; the Grape cluster simulation (figure 3.24). The results of the simulation is presented in figure 3.27. In the figure we introduce two subplots: the first is the received time-domain signal for the Clear Line of Sight (CLoS) simulation (i.e., the first simulation), and the second is the received time-domain signal of the grape cluster simulation (the fourth simulation). The second subplots shows the original signal similar to the first subplot, albeit slightly delayed, as demonstrated by the vertical line in the figure. The delay occurs as a results of the signal travelling from a

low refractive index medium (i.e., air) to a higher refractive index medium (i.e., grapes). More interestingly, the second subplot does not exhibit any traces of diffracted signals. Thus, the diffraction effect, an artefact of using containers smaller than three times the  $T_x$  3 dB transverse dimension, is not an issue with grape clusters, and consequently, does not affect SING accuracy.

### 3.2.7 The impact of foliage on SING accuracy

As mentioned earlier, the accuracy of SING is dependent on the accuracy of computing  $\varepsilon^*$ , which is dependent on measuring the S-parameters ( $S_{11}$  and  $S_{21}$ ) as in equations {3.17, ..., 3.30}, §3.2. Since foliage (i.e., leaves) typically cover grape clusters in a vineyard, we dedicate the section to investigate the effect of foliage on  $S_{11}$  and  $S_{21}$ .

We run simulations where we place a grape cluster (figure 3.28) with leaves between the transmitter  $T_x$  and the receiver  $R_x$ . In the simulations, we measure the S-parameters (i.e.,  $S_{11}$  and  $S_{21}$ ) from multiple angles by rotating the cluster by  $\frac{\pi}{4}$ . The simulation setup is the same as in §3.2.1. At each angle, we measure the S-parameters with and without leaves and compare between their results. The objective is to investigate if there is a difference in the S-parameters measurements, and if yes, how significant? Figures 3.29, 3.30, 3.31, and 3.32 report the results for  $\{0, \frac{\pi}{2}, \pi, \frac{3\pi}{2}\}$ , respectively. The results for the rest of the angles are reported in appendix A, §A.4.

From the figures, we notice how similar the S-parameters measurements are with and without the leaves. In fact, the maximum difference between the  $S_{11}$  of both cases is **0.067**, and the  $S_{21}$  is **0.34**. Thus, foliage does not affect S-parameters measurements significantly, and by extension, does not affect SING accuracy.

This concludes the discussion about SING methodology and the chapter. In the chapter, we presented SING and emphasized the feasibility of SING to estimate the moisture content inside

grapes. We accomplished that by investigating the relationship between the grapes' dielectric properties and the moisture content inside the grapes. Particularly, we presented how the extinction coefficient ( $\kappa$ ) is related to the dielectric properties ( $\varepsilon^*$ ). From there, we highlighted through detailed analytical analysis and thorough experimentation the relationship between  $\kappa$  and the three independent variables in the moisture content predictive model (§3.2.2, Eq. 3.10). The moisture content predictive model maps  $\varepsilon^*$ , through  $\kappa$ , along with sugar and frequency to the moisture content. Afterwards, we emphasized the reasons why the traditional free-space technique is unable to compute reliably the dielectric properties of geometrically non-uniformed objects such as grape clusters. Then, we presented our novel technique to compute the dielectric properties of grape clusters in §3.2.4. In our technique, we eliminate the need for a container to compute the thickness of grape clusters ( $\bar{\rho}_{\Theta}^{\{G\}}$ ). Instead, we introduced the concept of “relative thickness” in §3.2.5, from which we resolve the value of  $\bar{\rho}_{\Theta}^{\{G\}}$  required by our technique.

At the end of the chapter, we discussed different factors that may affect the accuracy of our technique, namely, the foliage and signals diffraction. We learned that our technique is resilient to both factors due to SING frequencies (i.e., the 5 GHz band). In the next chapter, we analyze SING performance and present the results.

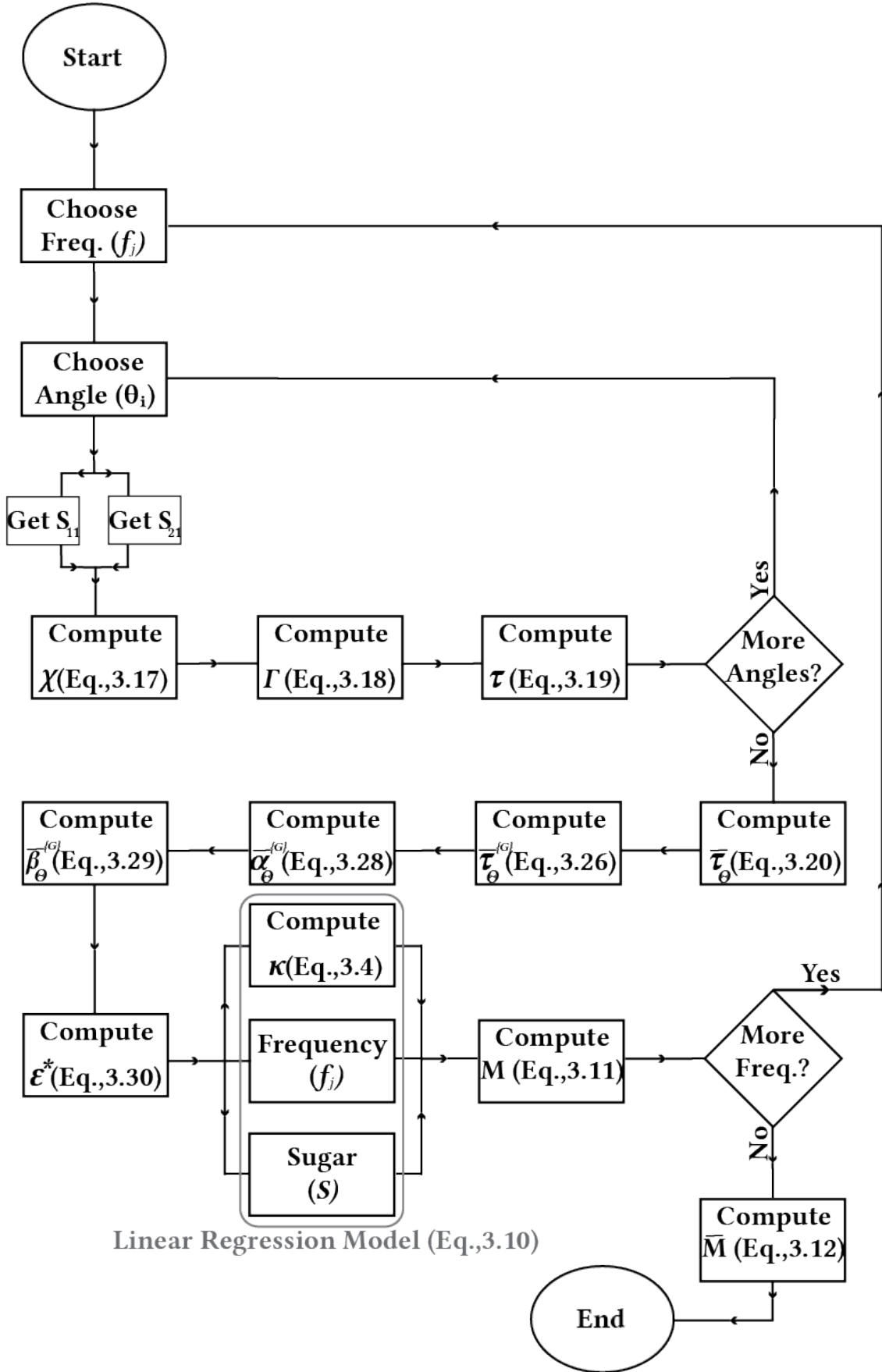


Figure 3.19: Summary of SING Procedure

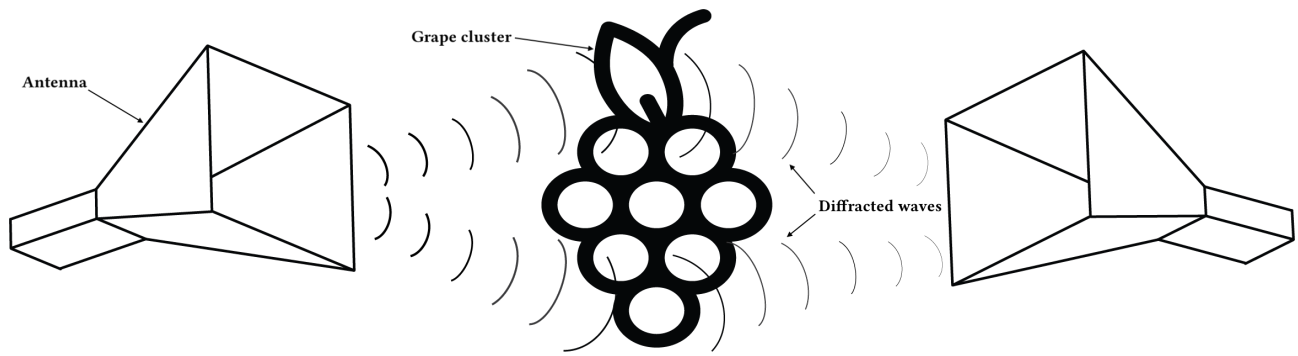


Figure 3.20: An illustration of the potential diffracted waves around the edges of a grape cluster.

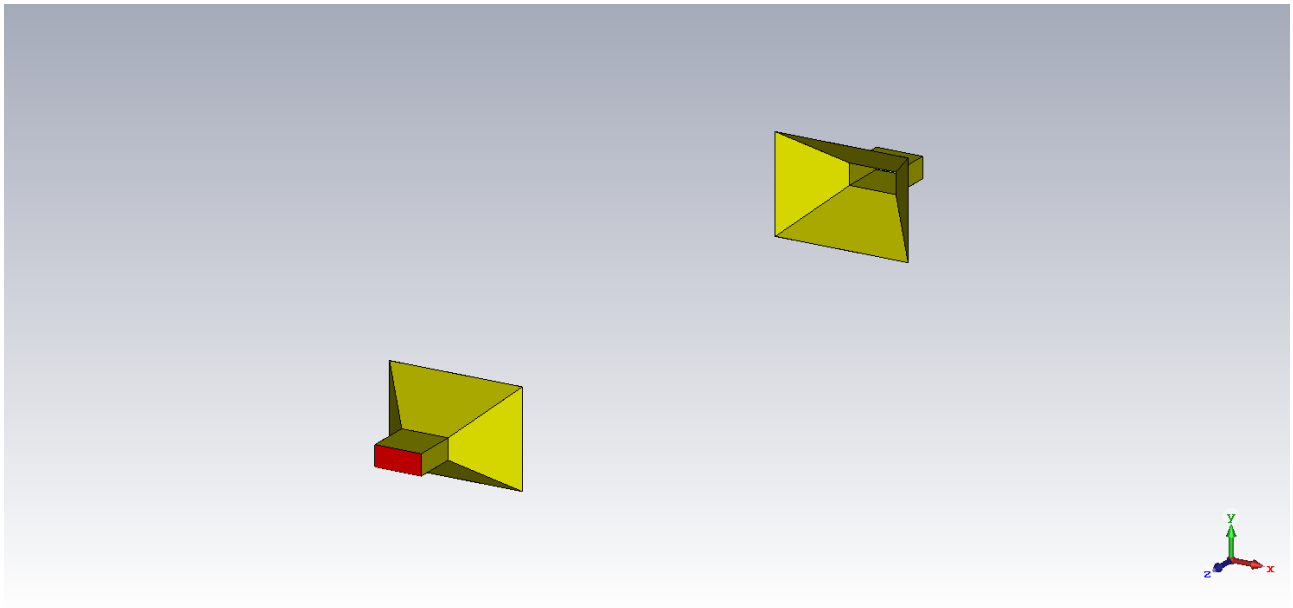


Figure 3.21: Clear Line of Sight (CLOS) simulation setup

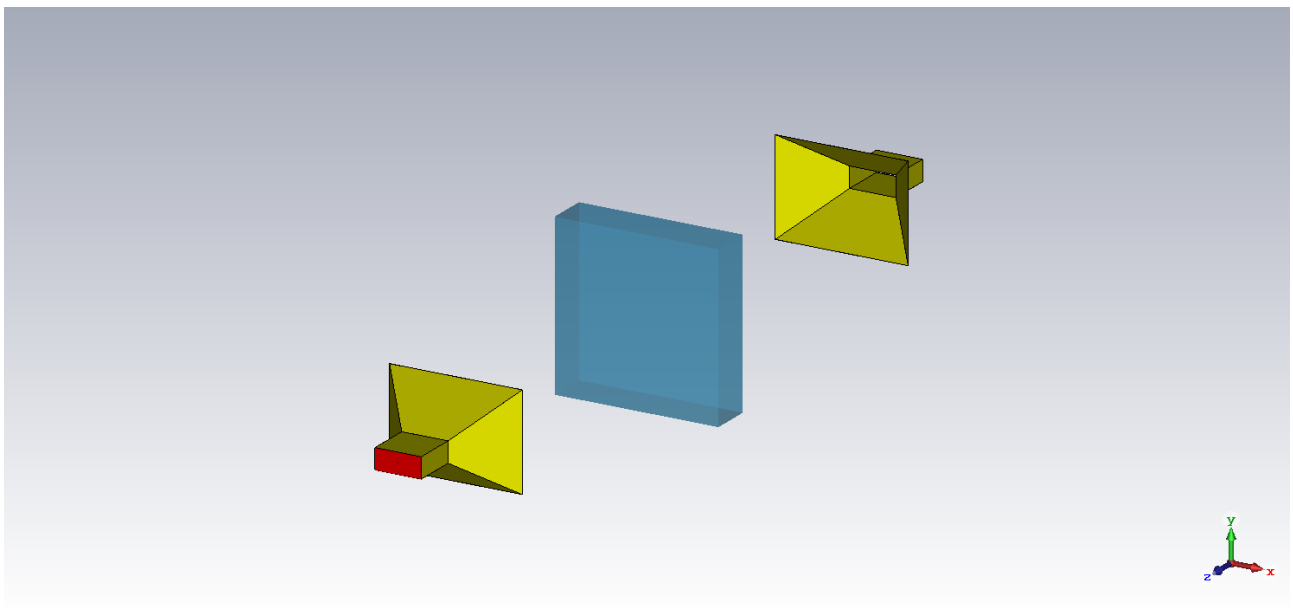


Figure 3.22: Small container simulation setup.

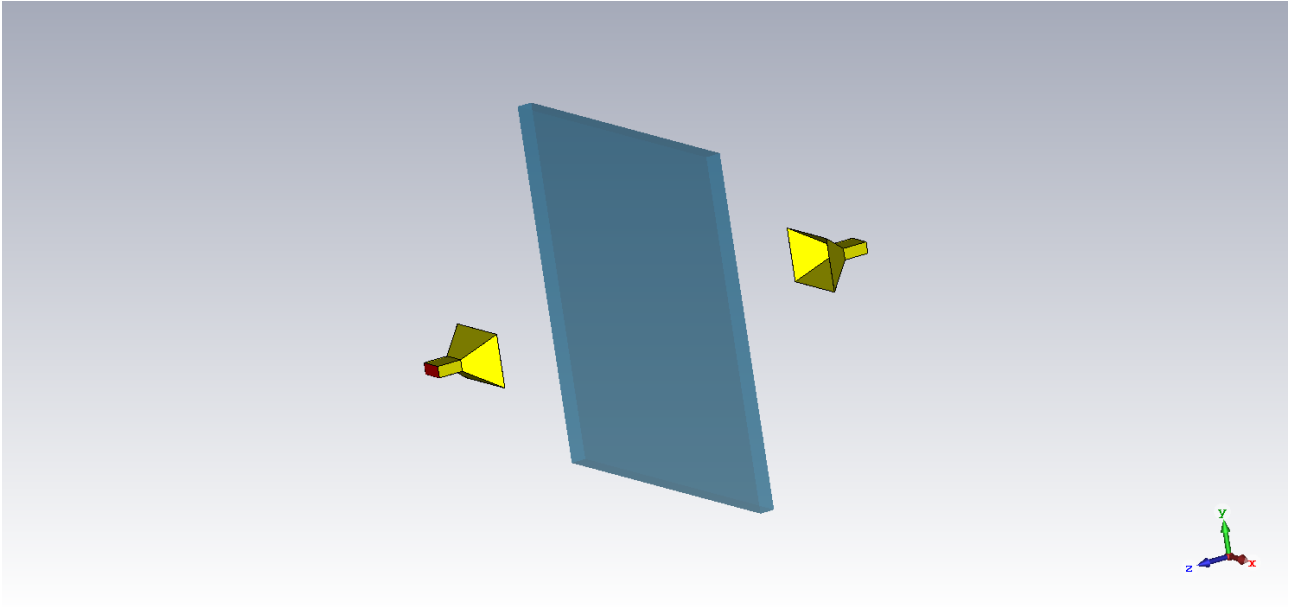


Figure 3.23: Large container simulation setup.

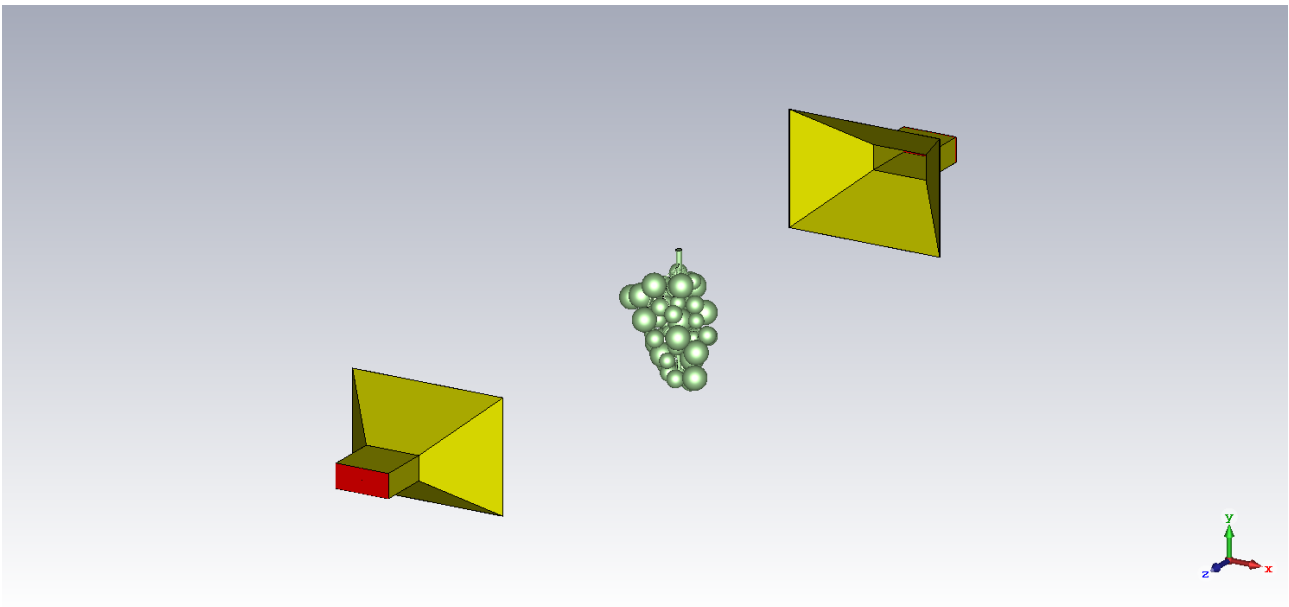


Figure 3.24: The grapes simulation through CST Microwave studio.



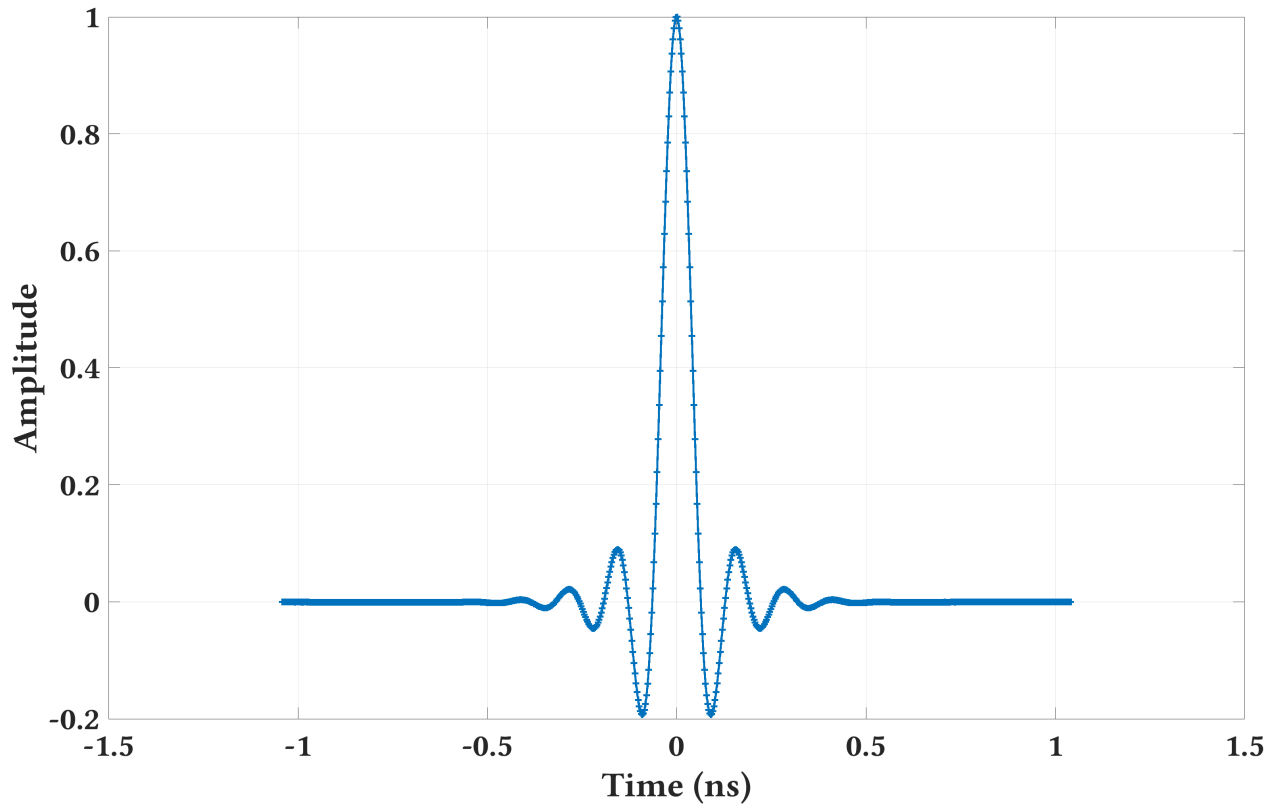


Figure 3.25: Impulse - normalized - simulation signal

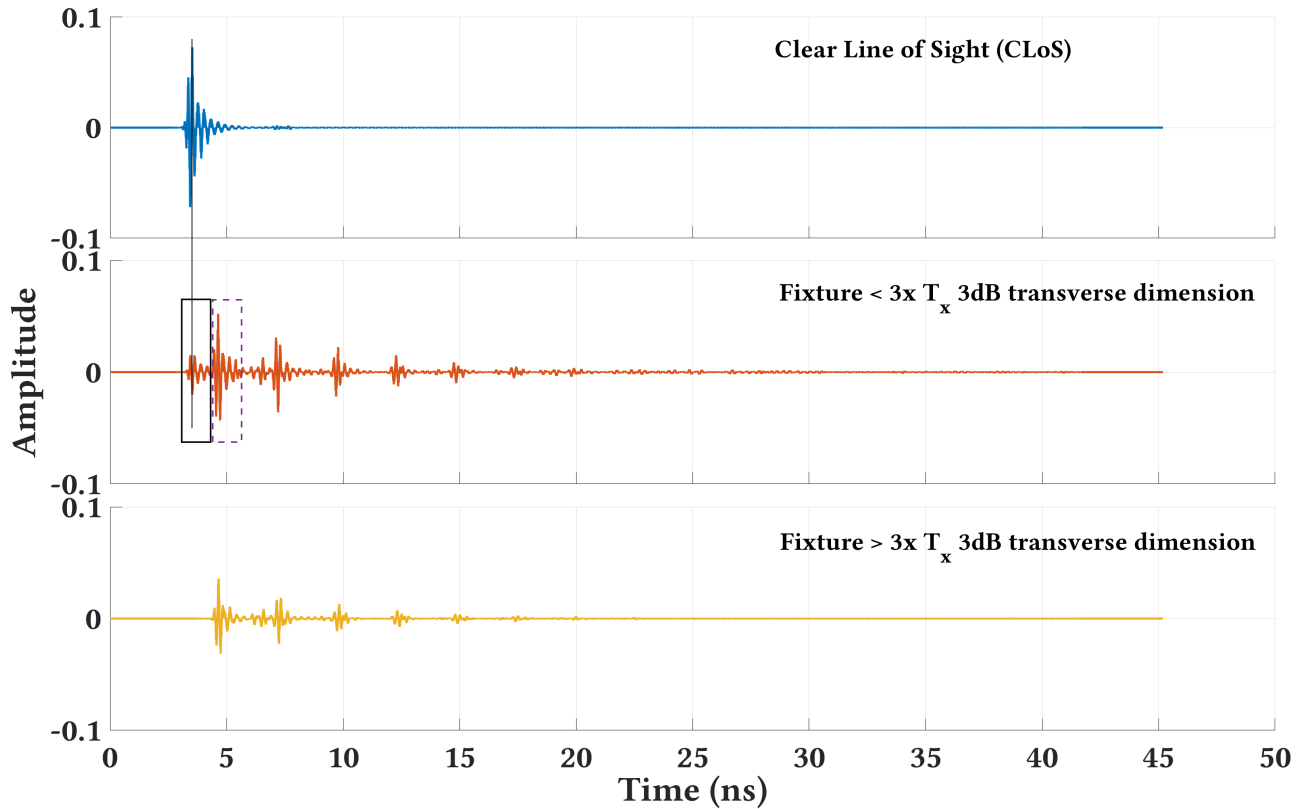


Figure 3.26: The received time-domain signal at  $R_x$  for CLoS, Small container, and Large container simulations. The x-axis is time in ns and the y-axis is the amplitude normalized to the input impulse signal.

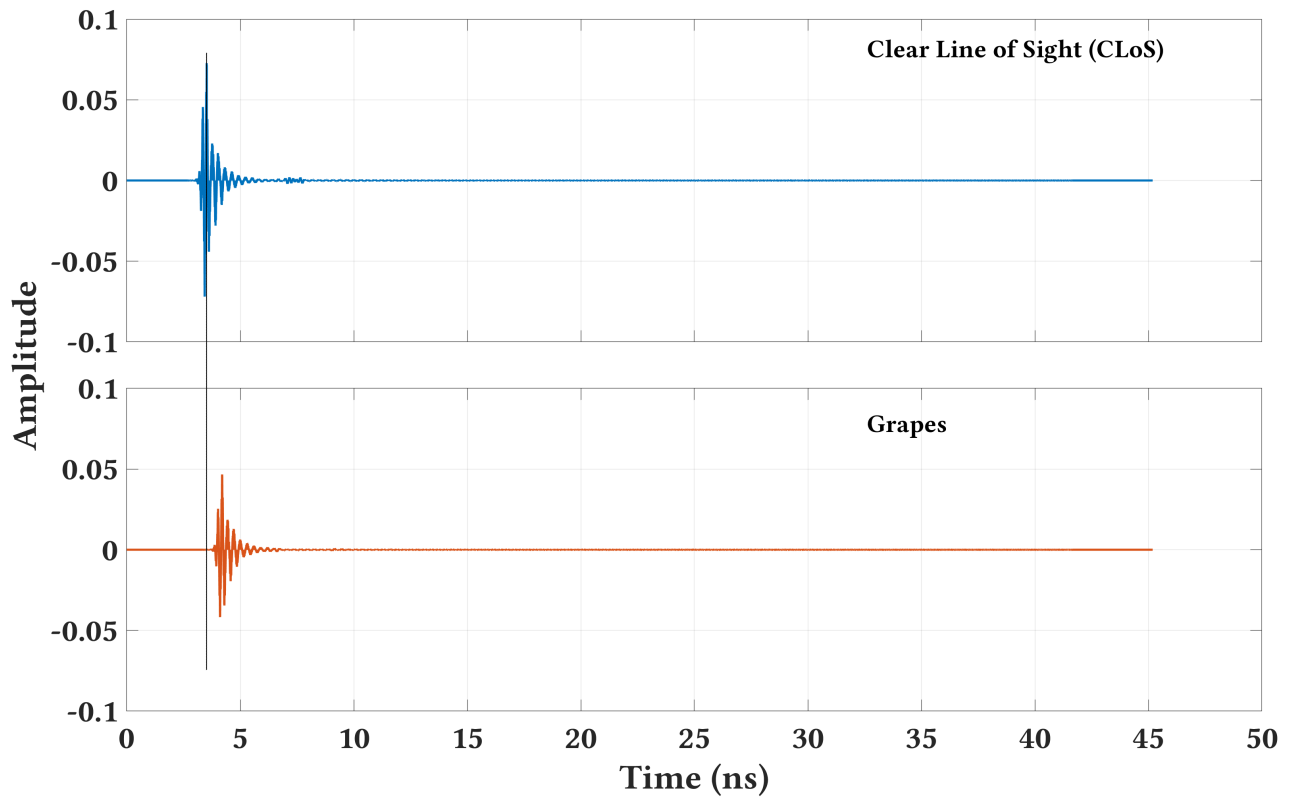


Figure 3.27: The received time-domain signal at  $R_x$  for the clear line of sight (CLOS) and a grape cluster simulations. The x-axis is time in ns and the y-axis is the amplitude normalized to the input impulse signal.

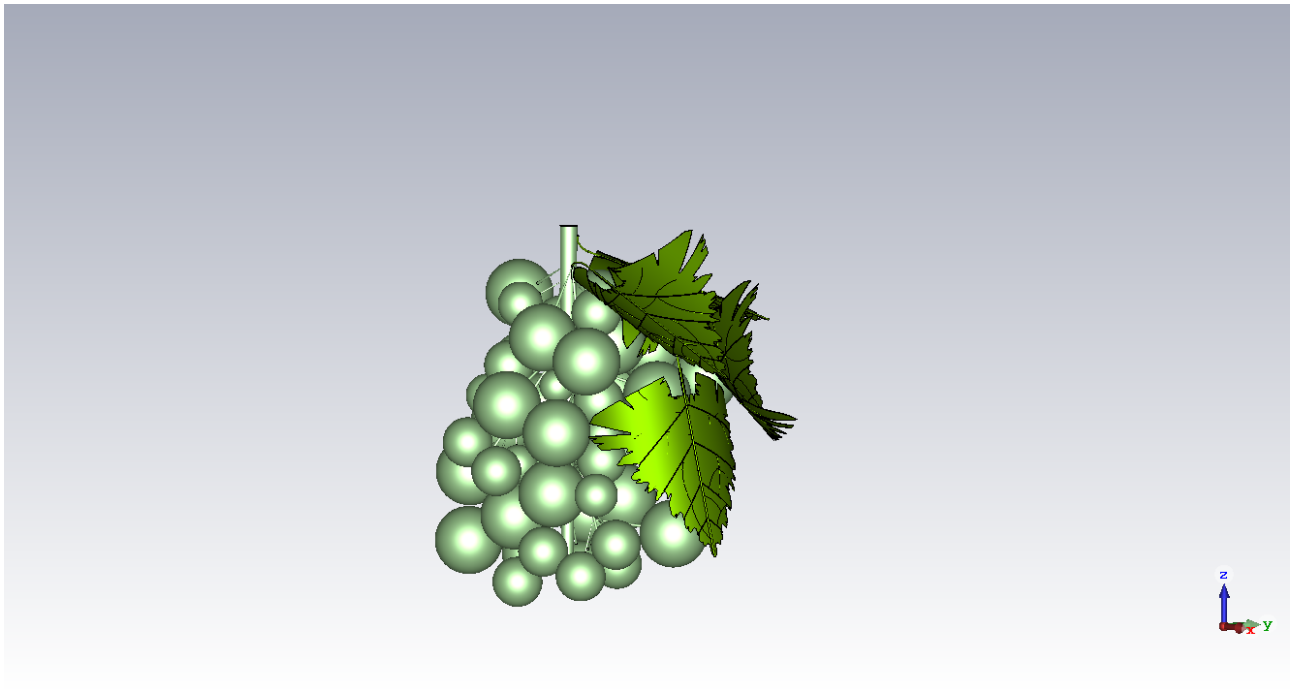


Figure 3.28: CST simulation of a cluster with leaves

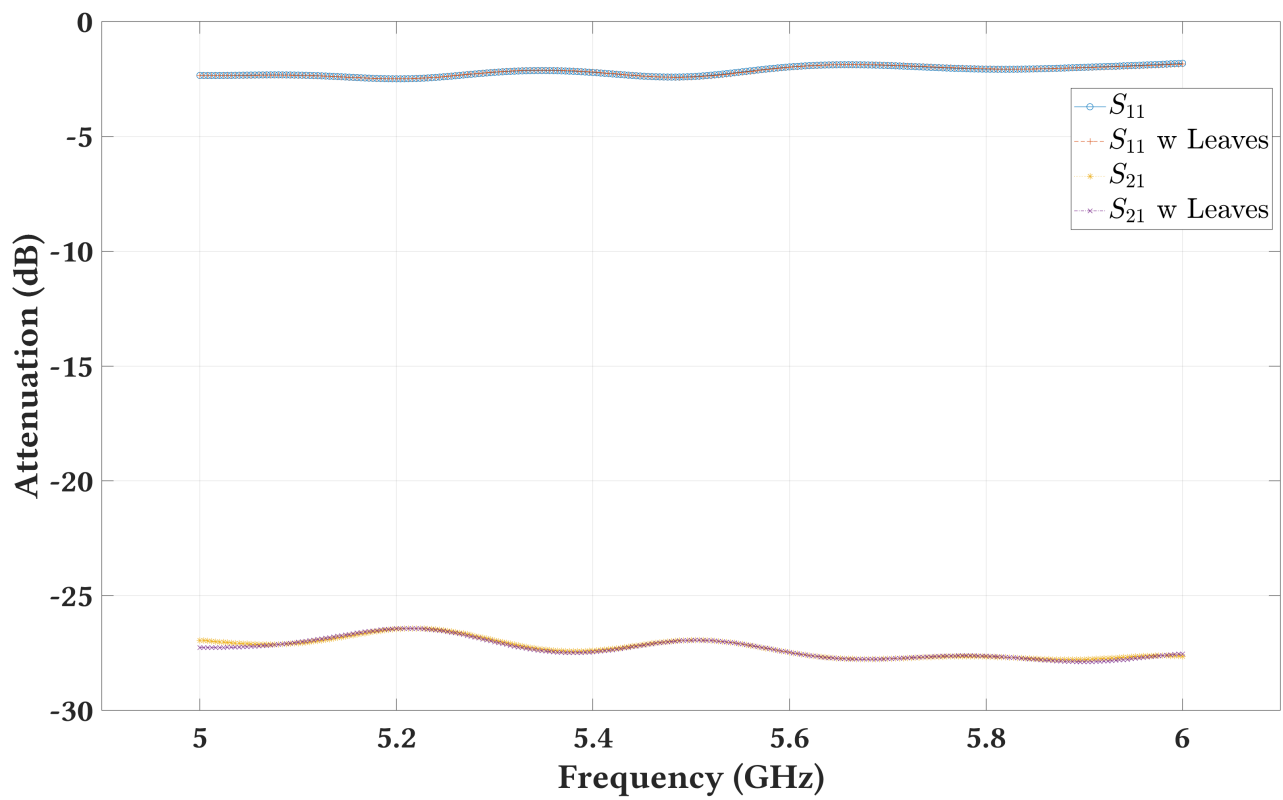


Figure 3.29: The  $S_{11}$  and  $S_{21}$  measurements with leaves (i.e., w Leaves) and without leaves at angle 0.

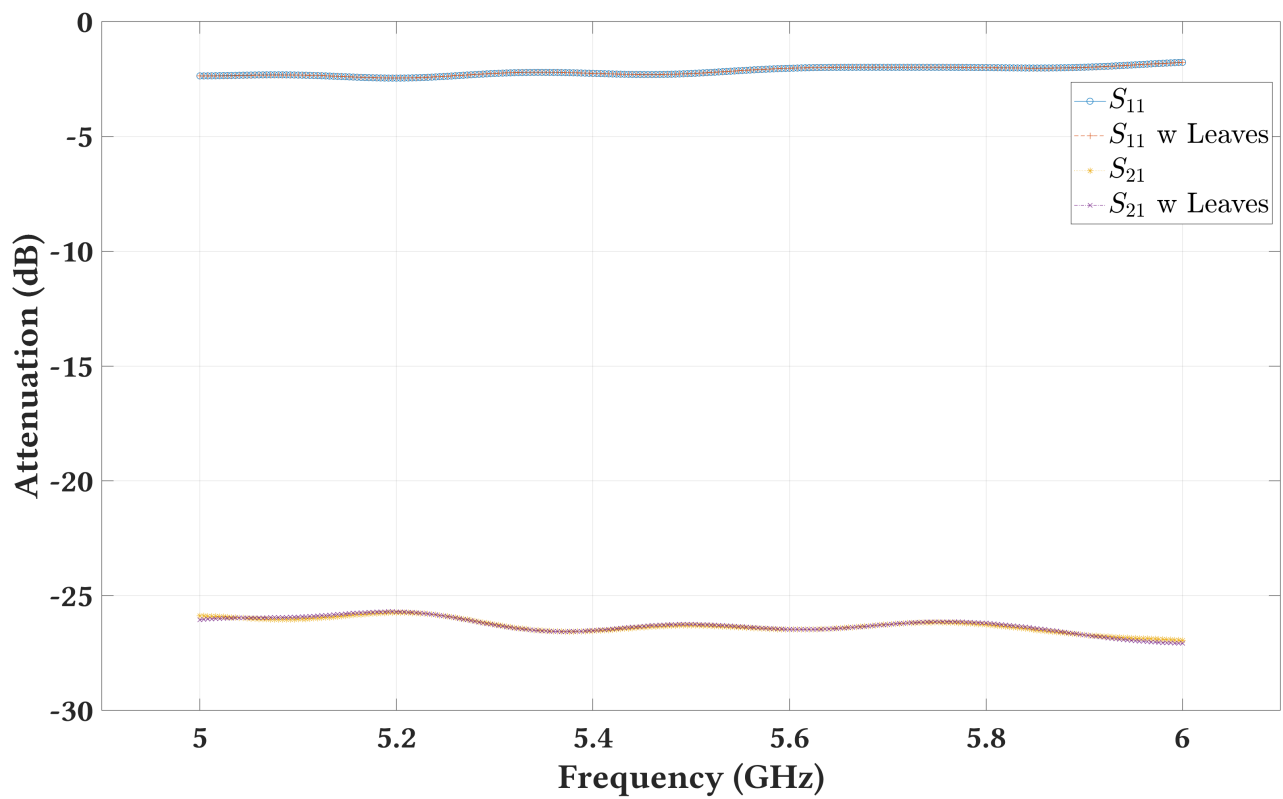


Figure 3.30: The  $S_{11}$  and  $S_{21}$  measurements with leaves (i.e., w Leaves) and without leaves at angle  $\frac{\pi}{2}$ .

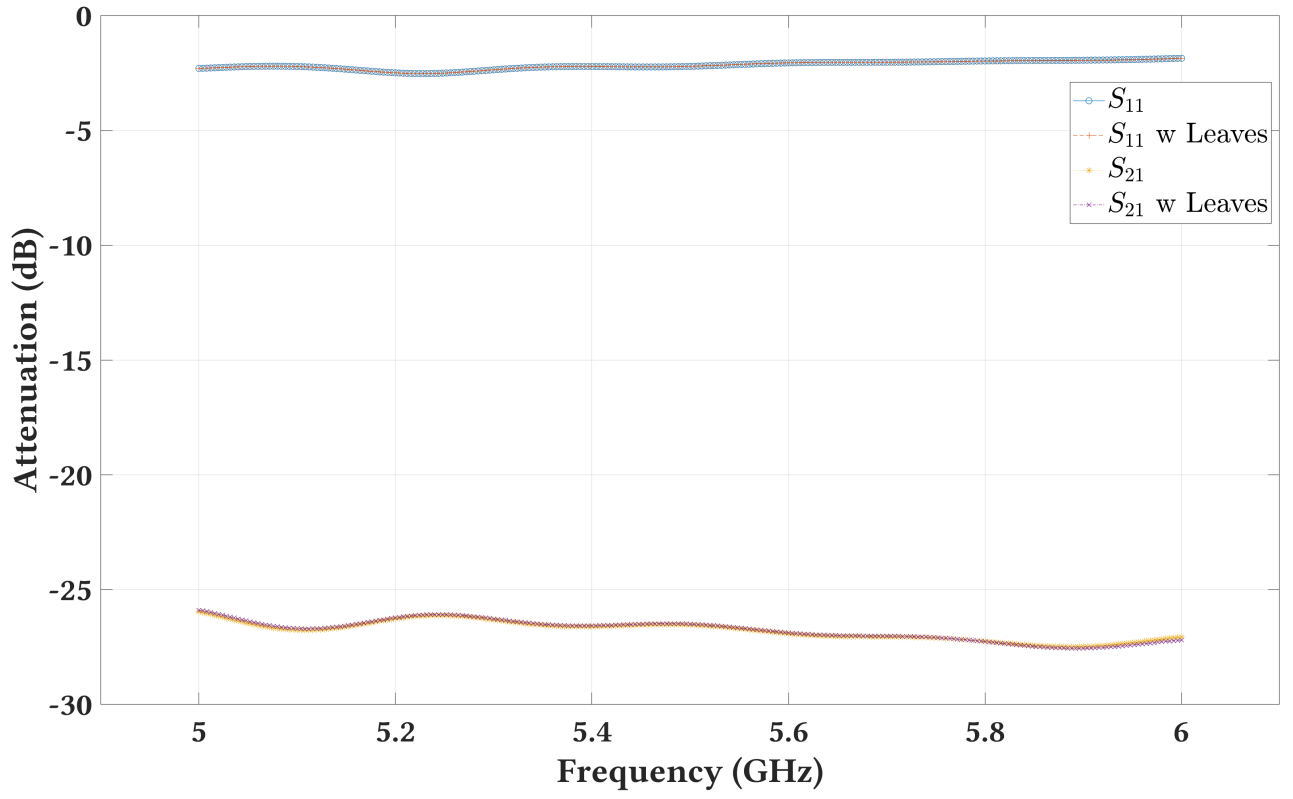


Figure 3.31: The  $S_{11}$  and  $S_{21}$  measurements with leaves (i.e., w Leaves) and without leaves at angle  $\pi$ .

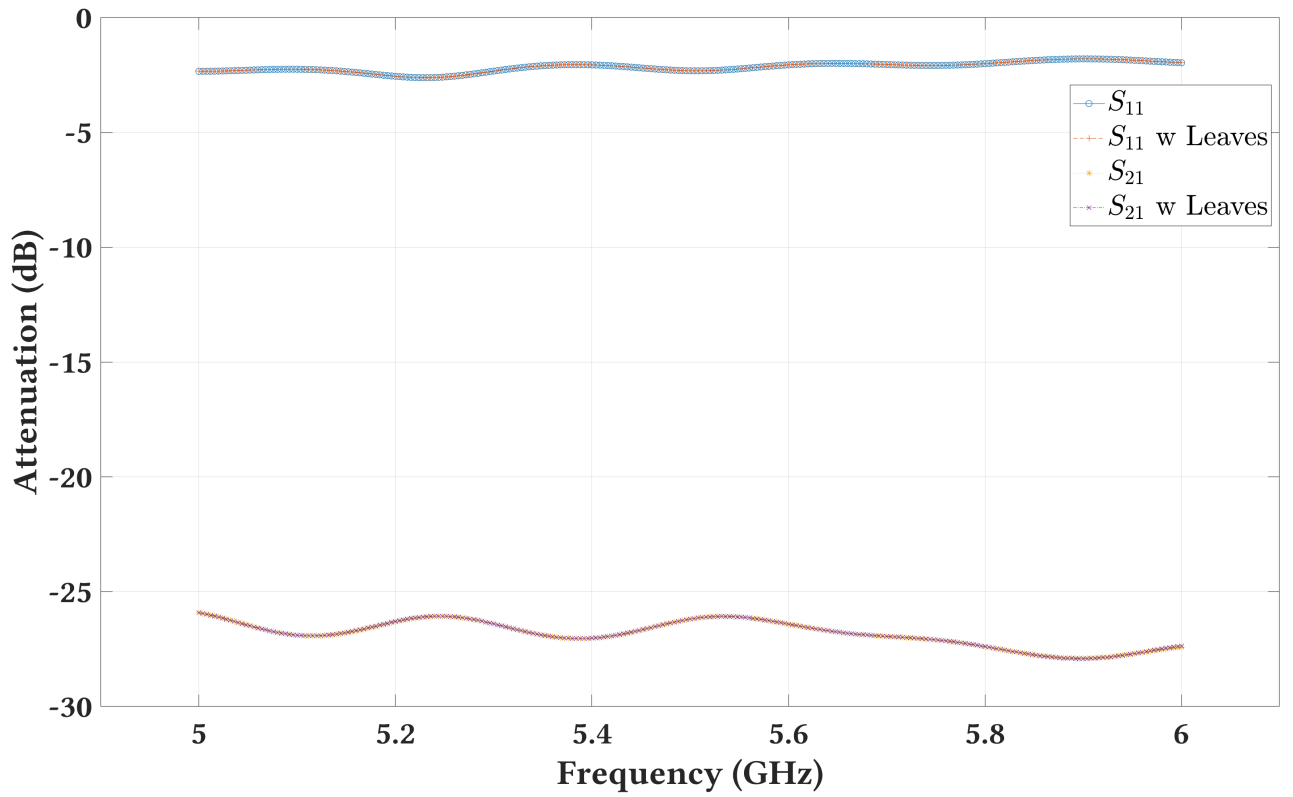


Figure 3.32: The  $S_{11}$  and  $S_{21}$  measurements with leaves (i.e., w Leaves) and without leaves at angle  $\frac{3\pi}{2}$ .

# Chapter 4

## SING Results

In this chapter, we discuss SING performance and present the results in section 4.1, and conclude the discussion about SING in section 4.2.

### 4.1 Results and Discussion

In this section, we discuss SING performance and present the results. Specifically, we start with section 4.1.1, where we discuss the training and validation sets for the moisture (Eq. 3.10, §3.2.2) and thickness (Eq. 3.32, §3.2.5) regression models introduced in the previous chapter. Since SING employs multiple angles to present accurate estimations of moisture content in grape clusters, we dedicate section 4.1.2 to investigate the concept of multiple angles in more details. Afterwards, we discuss SING performance and present the results in section 4.1.3.

#### 4.1.1 Moisture and Thickness Regression Models

Both the training and validation sets for the moisture (Eq. 3.10) and thickness (Eq. 3.32) regression models are obtained by performing experiments on nine grape clusters and simulations on six others; a total of 15 clusters. For the real clusters, we obtain the ground truth of the moisture content and sugar weight through the Air-drying technique and a refractometer,

respectively. Regarding the moisture content, Air-drying a well-known method to estimate the moisture content inside fruits [138]. It works by measuring a fruit weight before and after air-drying them to evaporate the moisture inside. The difference in weight is the amount of moisture inside the fruit. Regarding the sugar weight, We obtain the sugar weight by using a refractometer and an analytical balance. A refractometer (e.g., Kern 32BA Analog Refractometer [13]) is a device used to measure sugar concentration (Brix°) in a fluid by measuring its refractive index [13]. To obtain the sugar weight, first, we measure a grape weight ( $G_w$ ) using the analytical balance. Then, we squeeze a few drops of juice from the grape into the refractometer's prism to measure the sugar concentration ( $G_{sc}$ ) as a percentage. Finally, the sugar weight ( $S$ ) is calculated as in equation 4.1.

$$S = G_w \cdot \frac{G_{sc}}{100} \quad (4.1)$$

Due to the small number of clusters, we consider Cross-Validation (CV) as a method to verify the effectiveness of both regression models [46]. Specifically, we perform k-fold CV by separating the data-set into k equally sized groups. One group is for validation, and the remaining k-1 groups are for training. Since we have 15 clusters, we can separate the clusters into 3 or 5 equally sized groups. Thus, we perform both 3-Fold and 5-Fold CVs. For the 3-Fold CV, we can generate a maximum of 3003 possible training sets from the 15 clusters. Similarly, a maximum of 455 possible training sets can be generated for the 5-Fold CV. We train the moisture and thickness regression models using the training sets generated for both the 3-Fold and 5-Fold CVs to obtain the  $R^2$  value for each regression model; a total of 3458 regression models.

### Cross Validation on the Moisture Regression Model

Figures 4.1 and 4.2 show the  $R^2$  values resulting from the 3-Fold and 5-Fold CVs for the moisture regression model (Eq. 3.10, §3.2.2). Specifically, both figures show the  $R^2$  value distribution resulting from the 3-Fold and 5-Fold CVs, respectively. For each  $R^2$  value, we round the value to the nearest integer to present a meaningful analysis of the values. In fact,

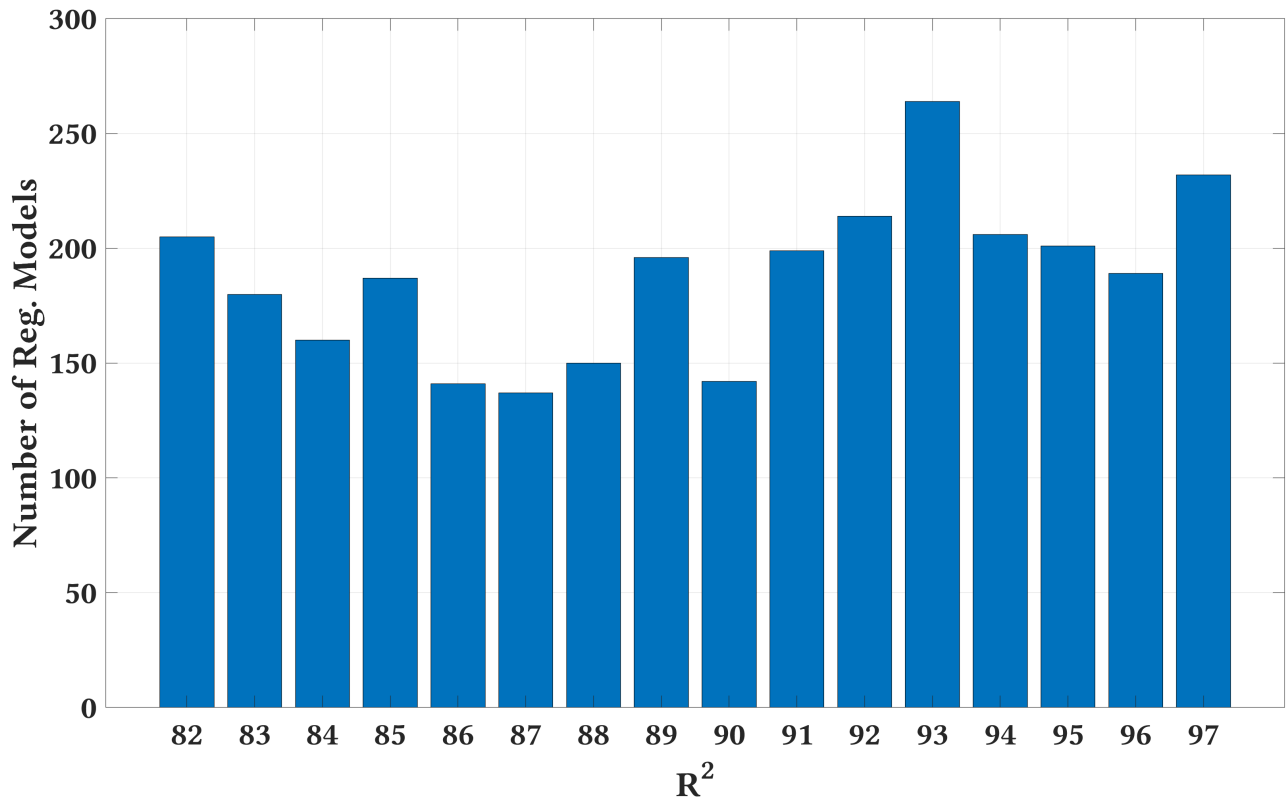


Figure 4.1: The  $R^2$  value for each moisture regression model employed in the 3-Fold CV. The x-axis shows the  $R^2$  values, and the y-axis shows the number of regression models at each  $R^2$  value.

when analyzing both figures, we were searching for a common trait between regression models with high  $R^2$  value. An interesting trait we found is that regression models with  $R^2 \geq 90\%$  have a higher ratio of real clusters to simulation clusters in their training sets than regression models with  $R^2 < 90\%$ . 90% is the mean values in both figures as illustrated later in table 4.1. Put differently, the ratio of real clusters to simulation clusters in the former regression models is 1.6 and 1.7 for the 3-Fold and 5-Fold CVs, respectively. On the other hand, the ratio drops to 1.4 for both CVs in the latter regression models. This 1.4 ratio is also lower than the original ratio of real clusters (nine clusters) to simulation clusters (six clusters), which is 1.5. This observation emphasizes the importance of employing real clusters when training SING. Fortunately, one possible deployment ground for SING is vineyards, where harvested clusters can be used to train the model.

Since we have a high number of regression models (3458 regression models), it is infeasible to verify the performance of SING through all of them. Thus, we need to choose a single regression

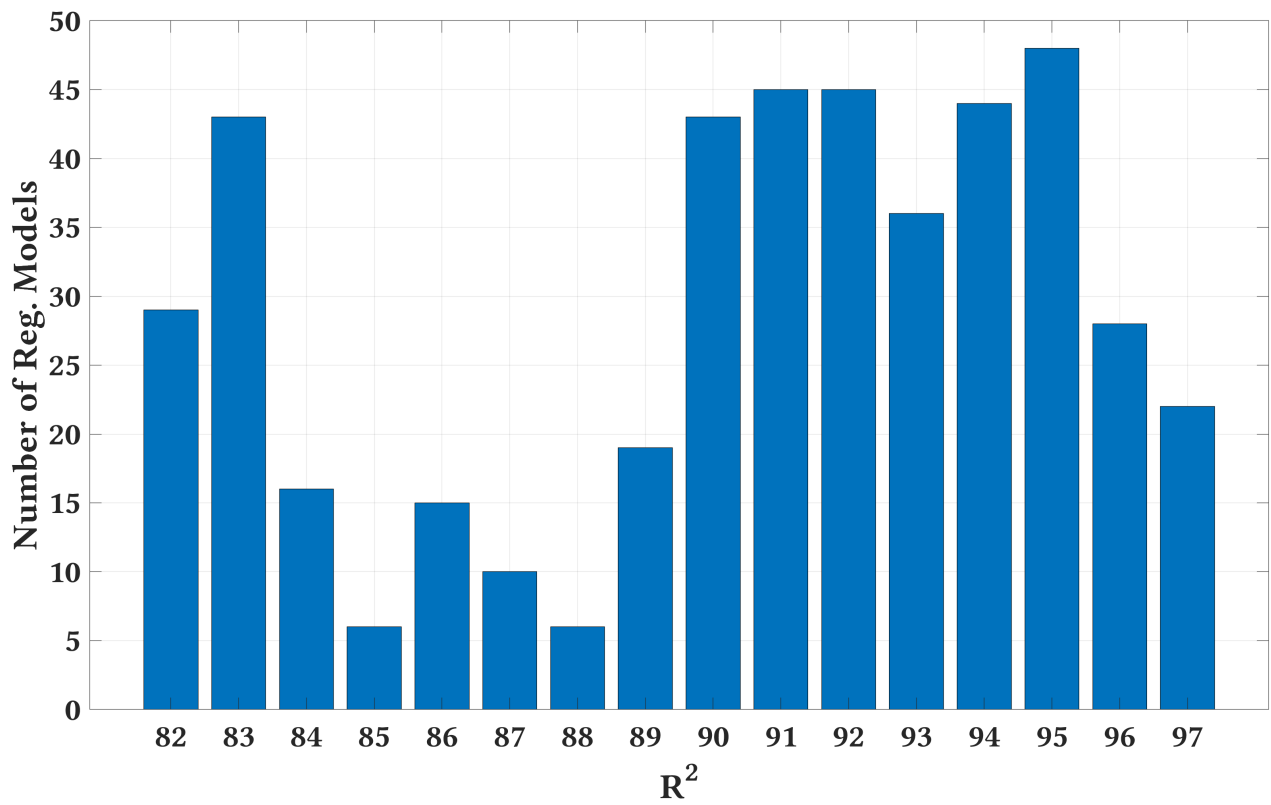


Figure 4.2: The  $R^2$  value for each moisture regression model employed in the 5-Fold CV. The x-axis shows the  $R^2$  values, and the y-axis shows the number of regression models at each  $R^2$  value.



	Mean	Median	Standard Deviation	Minimum	Maximum
3-Fold CV	89.9	91	4.7	82	97
5-Fold CV	90.4	91	4.6	82	97

Table 4.1: Different Statistical measures of the  $R^2$  value for the 3-Fold and 5-Fold CVs. The values are obtained from figures 4.1 and 4.2.

Table 4.2: The moisture regression model information (equations 3.10, §3.2.2).

Variable/Feature	Regression coefficient	Variance Inflation Factor
Moisture ( $M$ )	$-5.144 \times 10^{-4}$	1.005
Sugar ( $S$ )	$7.338 \times 10^{-4}$	1.005
Frequency ( $f$ )	$2.159 \times 10^{-10}$	1

model to verify the performance of SING. The candidate regression model should be robust - according to the  $R^2$  value - to swapping clusters between the training and validation sets. Naturally, such a regression mode should have a  $R^2$  value close to the mean value. According to table 4.1, the mean value from figures 4.1 and 4.2 is 90%. Thus, the candidate regression model should be a regression model where  $R^2 \approx 90\%$ .

A total of 185 regression models with  $R^2 \approx 90\%$ . From those, 142 regression models are for the 3-Fold CV, and the rest 43 are for the 5-Fold. We discard the latter regression models because the former have more clusters in the validation set than the latter; 5 clusters in the validation set for the 3-Fold CV comparing to 3 clusters for the 5-Fold CV. This criteria is to verify the performance of SING on more clusters. As a result, we have a total of 142 regression models left. From those, we focus on regression models with real clusters only in the validation set. Since we intend to deploy SING in a vineyard, we believe it is more informative to validate the performance of SING on real clusters only. From the 142 regression models, only 3 of them contain real clusters only in their validation set. Any regression model out of the 3 is a candidate regression model. We choose one of them and report its information in table 4.2. The  $y$ -intercept value ( $\mu$ ) of the model is  $4.684 \times 10^{-1}$ . The training set clusters of the regression model are presented in table 4.3, and the set contains 216,144 data points. Similarly, the validation set clusters are presented in table 4.4, and the set contains 240,150 data points.

From table 4.2, the Variance Inflation Factor (VIF) quantifies the severity of the multicollinearity between independent variables in linear regression models [50]. A score of 1, which is the

Table 4.3: The training set clusters information

Cluster	Moisture (ml)	Sugar (g)
Cluster I	369	88.1
Cluster II	157	38.08
Cluster III	95	22.28
Cluster IV	150	37.63
Cluster V	92	14.3
Cluster VI	89	27.7
Cluster VII	125	19.5
Cluster VIII	122	32.5
Cluster IX	153	23.9
Cluster X	150	40

Table 4.4: The validation set clusters information

Cluster	Moisture (ml)	Sugar (g)
Cluster I	233	53.17
Cluster II	380	82.84
Cluster III	282	69.82
Cluster IV	215	53.14
Cluster V	103	26.5

lowest score in VIF, means that an independent variable is uncorrelated with the other independent variables [50]. In other words, the regression model is more reliable [50]. In the moisture regression model, the low scores of VIF support our choice of linear regression as a fitting model for our data.

### Cross Validation on the Thickness Regression Model

Figures 4.3 and 4.4 show the  $R^2$  values resulting from the 3-Fold and 5-Fold CVs for the thickness regression models (Eq. 3.32, §3.2.5). Similar to figures 4.1 and 4.2, figures 4.3 and 4.4 present the  $R^2$  value distribution resulting from the 3-Fold and 5-Fold CVs, respectively. Contrary to figures 4.1 and 4.2, we do not round the  $R^2$  values to the nearest integer in figures 4.3 and 4.4 because all  $R^2$  values = 99%. We also present in table 4.5 different statistical measures of the regression models in figures 4.3 and 4.4.

For the sake of consistency, We employ the same training and validations sets (table 4.3 and 4.4, respectively) for the thickness regression model. Table 4.6 shows the regression model

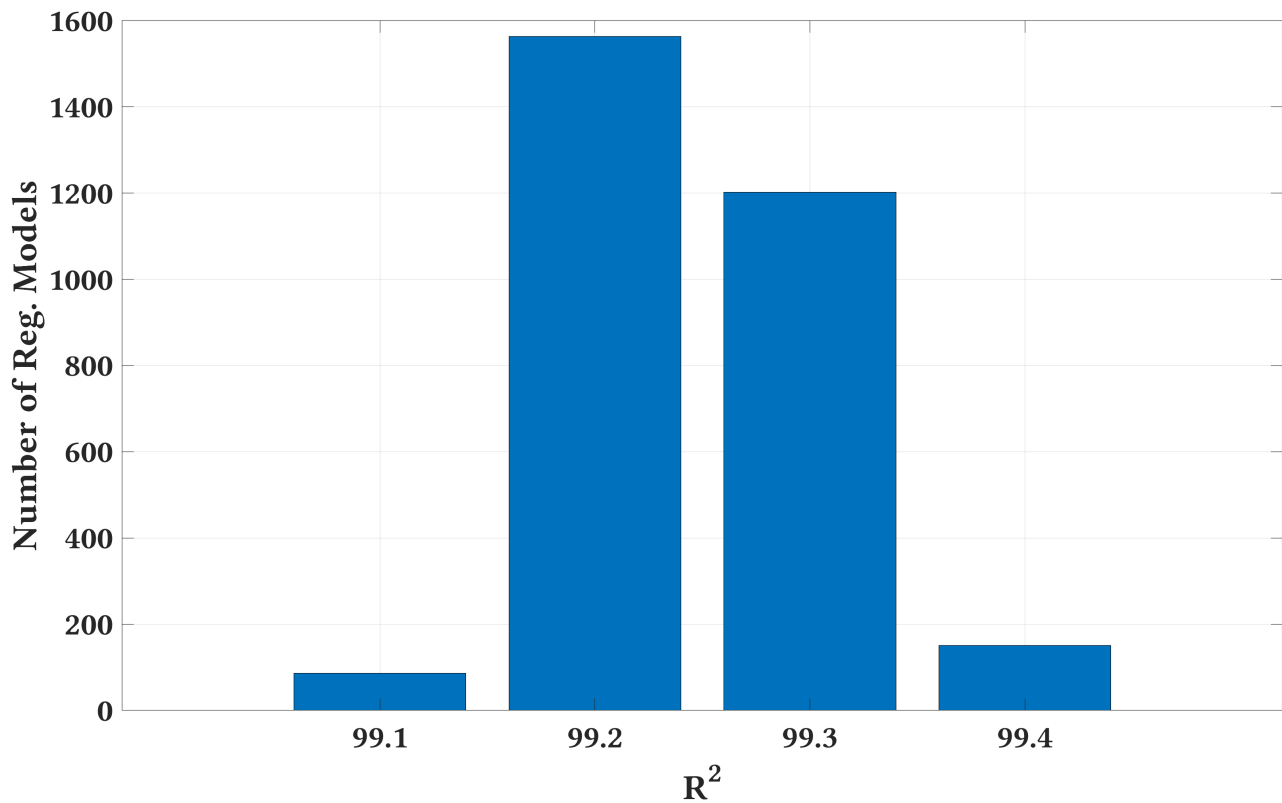


Figure 4.3: The  $R^2$  value for each thickness regression model employed in the 3-Fold CV. The x-axis shows the  $R^2$  values, and the y-axis shows the number of regression models at each  $R^2$  value.

	Mean	Median	Standard Deviation	Minimum	Maximum
3-Fold CV	99.23	99.2	0.05	99.1	99.4
5-Fold CV	99.25	99.2	0.06	99.1	99.4

Table 4.5: Different Statistical measures of the  $R^2$  value for the 3-Fold and 5-Fold CVs. The values are obtained from figures 4.3 and 4.4.

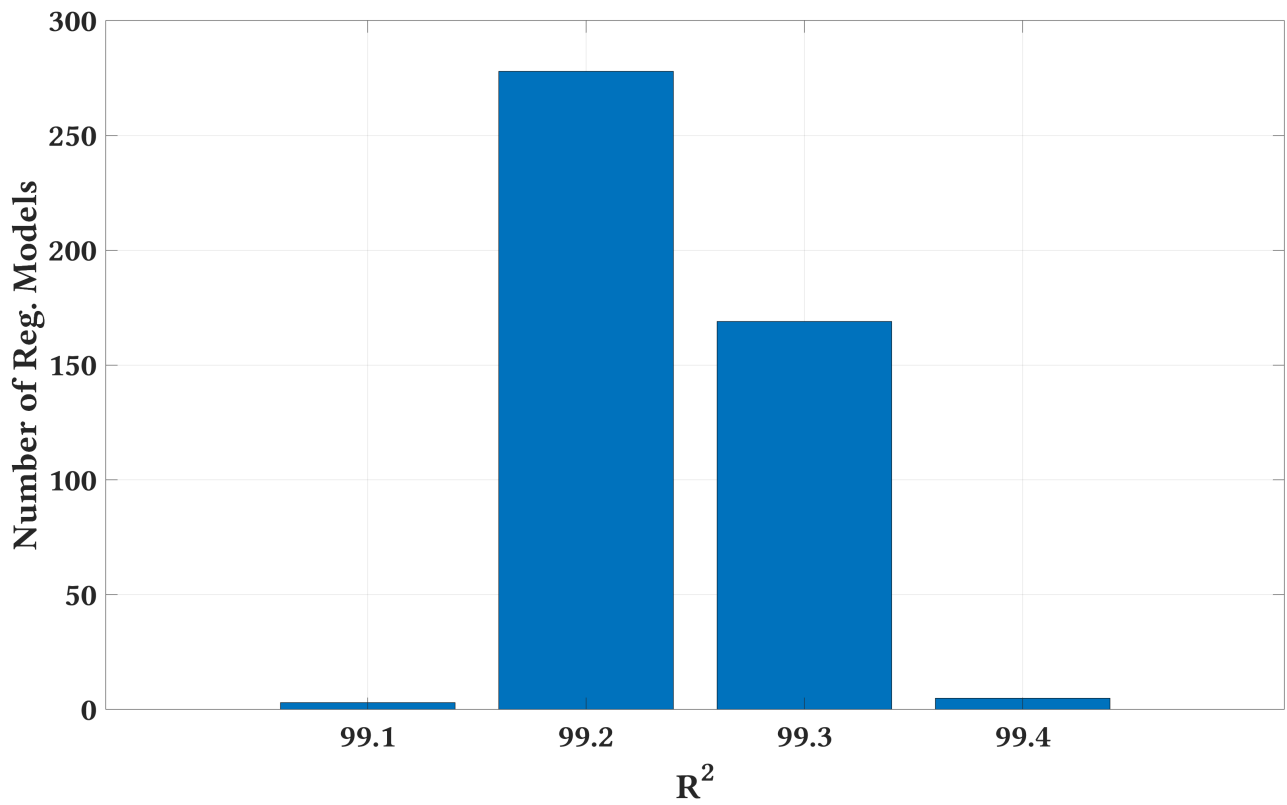


Figure 4.4: The  $R^2$  value for each thickness regression model employed in the 5-Fold CV. The x-axis shows the  $R^2$  values, and the y-axis shows the number of regression models at each  $R^2$  value.

Table 4.6: The thickness regression model information (Eq.3.32, §3.2.5).

Variable/Feature	Regression coefficient	Variance Inflation Factor
Transmission coefficient ( $ \bar{\tau}_{\Theta}^{\{G\}} $ )	-0.0657	1.009
Frequency ( $f$ )	-0.1431	1.009

information. The  $y$ -intercept value ( $\mu$ ) of the model is 0.768 and the coefficient of determination ( $R^2$ ) is 0.993. Similar to the moisture regression model, the low VIF scores support our choice of linear regression as a fitting model for our data.

After discussing the moisture and thickness regression models, we discuss SING performance and aspects related to SING performance in the following sections.

#### 4.1.2 SING's Angle Combinations

SING measures moisture content in grape clusters through scanning the clusters from multiple angles. In this section, we discuss the notion of multiple angles in more details, and formulate the following question: how many angles are required by SING to yield the best performance? To answer the question, we introduce the term *angle set*. An angle set is a group of angles from which SING scans a grape cluster. For example, if we have an angle set that contains the following angles  $S = \{0, \frac{\pi}{2}, \pi, \frac{3\pi}{2}\}$ , then SING scans a grape cluster from those angles. To assess the angle sets effect on SING performance, we examine SING performance through different angle sets using the validation set (table 4.4, §4.1.1). For each angle set, we run SING through that set and solve equation 4.2. In the equation, we calculate  $\text{offset}_i$ , which represents the total difference in moisture content between SING and the ground truth when using an angle set  $S_i$ .  $\text{offset}_i$  is a useful metric for yield estimation applications, where SING performance is assessed by considering the whole yield rather than individual grape clusters. In equation 4.2, the whole yield is represented by the value  $\text{Truth}_{\text{total}}$ , which in our case represents the total moisture content for the grape clusters in the validation set (table 4.4, §4.1.1).  $N$  is the number of angle sets, and  $M$  is the number of grape clusters.  $\text{SING}_{i,j}$  is SING moisture measurement for an angle set  $i$  and a grape cluster  $j$ , whereas  $\text{Truth}_j$  is the ground truth moisture content for a

grape cluster  $j$ . We multiply  $\text{offset}_i$  by 100 to obtain the results as percentage.

$$\forall i \in N, \text{offset}_i = \left\{ \frac{1}{\text{Truth}_{\text{total}}} \sum_{j=1}^M |\text{SING}_{i,j} - \text{Truth}_j| \right\} \times 100 \quad (4.2)$$

From equation 4.2, the angle set with the minimum  $\text{offset}_i$  value yields the best performance for SING. In the next section we discuss and present the results for running SING with different angle sets.

### 4.1.3 SING's Performance

In this section, we present and analyze SING performance by employing SING on the validation set from table 4.4, §4.1.1. Recall from §3.2.1 that we measure real clusters from 30 angles. From the 30 angles, we can obtain  $2^{30} - 1$  distinct angle sets. Specifically, we can obtain 107,374,182,3 angle sets. It is infeasible to examine SING performance through all the angle sets. However, it is possible to examine different aspects of SING using only a subset of those angle sets. Thus, we choose a total of 11353 angle sets from all angle set categories. An Angle Set Category ( $S^i$ ) is a collection of angle sets with the same number of angles ( $i$ ) in each set. For example,  $S^2$  represents all angle sets that have exactly two angles. Since we can measure SING at 30 angles, we can compose the following angle set categories:  $\{S^1, S^2, S^3, \dots, S^{30}\}$ . The 11535 angle sets contain angle sets from each angle set category.

We discuss SING performance through the following categories:

- A: The relationship between SING accuracy and the number of scanned angles. In this category, we investigate how efficient SING approach is in achieving reliable estimations by scanning grape clusters from multiple angles.
- B: The relationship between SING accuracy and scanning from randomly or specifically

chosen angles. In this category, we investigate how tolerant SING is - in terms of accuracy - to scanning from random angles rather than specifically chosen angles.

- C: The relationship between SING accuracy and scanning from a single segment of a grape cluster or multiple segments. This category investigates the importance of scanning a grape cluster from multiple segments rather than a single segment. We explain further the meaning of “segment” in this category.
- D: The relationship between SING accuracy and scanning from few or many angles at the same segment. This category discusses SING performance when scanning from a single or few angles rather than many angles for a specific segment.

The data in the figures in this section is the result of running SING with different angle sets to obtain - for each angle set - the *offset* values discussed in §4.1.2. To best represent the results, we plot the figures using three statistical metrics: the mean, median, and standard deviation. The first two metrics are chosen to represent the central tendency of the data, with the median being less affected by outliers and skewed data [123]. The standard deviation is chosen to examine SING performance consistency at each angle set category.

#### A: The number of scanned angles

In this criteria, we investigate how varying the number of angles may affect SING accuracy. To do so, we refer to figure 4.5. The figure reports the results at each angle set category ( $S^i$ ). In the figure, the value of each bar is the mean offset value for the corresponding angle set category. The error bars represent the standard deviation values. The figure shows clearly that increasing the number of angles enhances SING accuracy. These results promote the essence of SING; scanning grape clusters from multiple angles to improve accuracy. In fact, this direct relationship between increasing the number of angles and improving SING accuracy is also illustrated in figure 4.6. The figure emphasizes the positive effect of increasing the number of angles on SING accuracy. For example,  $S^1$  has an  $\approx 18\%$  increase in offset value comparing to the

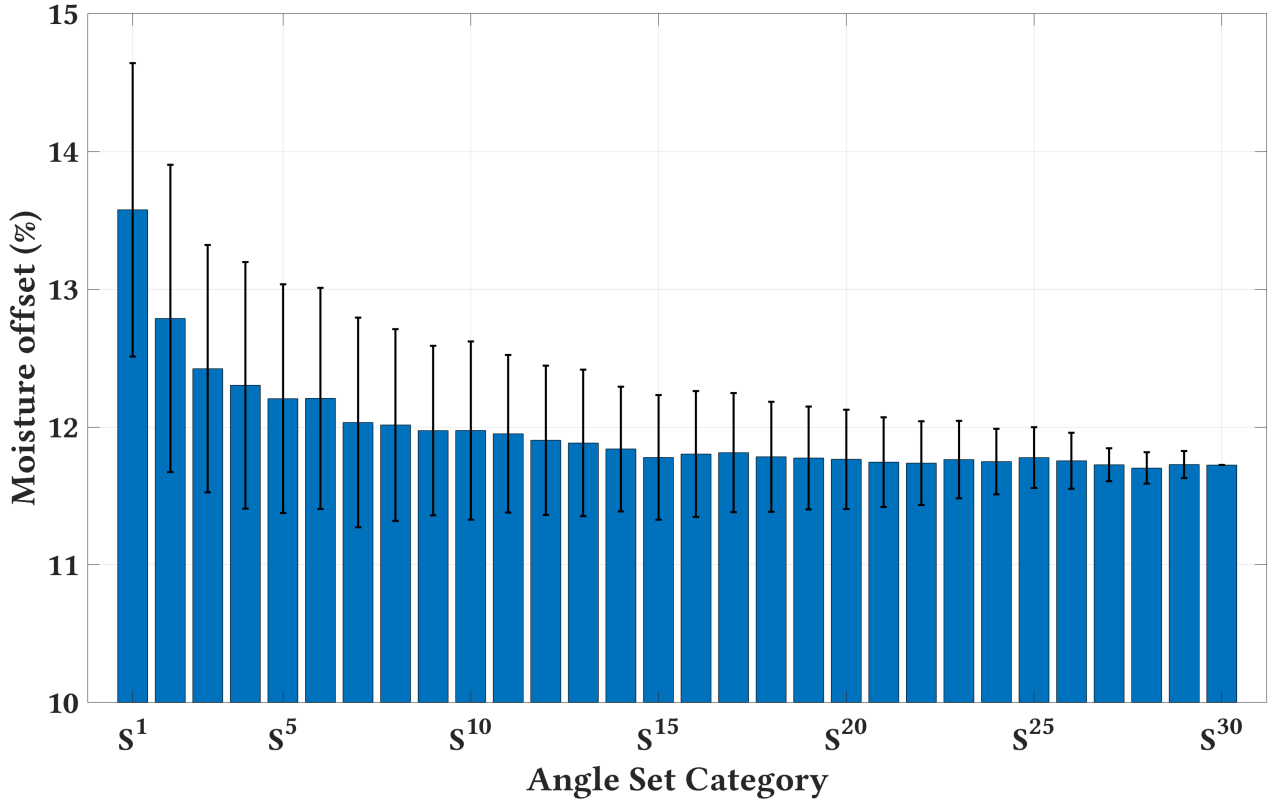


Figure 4.5: The mean offset value (%) for each category set.

offset value of  $S^{30}$ . Evidently, this offset gap is constantly decreasing until we reach  $\approx 0\%$  at  $S^{29}$ .

Another observation from figure 4.5 is related to the consistency of SING measurements. This is best illustrated by the standard deviation values (i.e., the error bars in the figure) and figure 4.7. Figure 4.7 reports the standard deviation values at each angle set category, except for  $S^{30}$ , which has a single angle set. Both, the error bars in figure 4.5 and figure 4.7 emphasize the consistency of SING measurements as the number of angles increases. In fact, the standard deviation value of  $S^2$  is one order of magnitude larger than the standard deviation value of  $S^{29}$ .

## B: Random against Specific angles

Here we discuss the performance of SING using angle sets with random angles against specific angles. An angle set with specific angles is an angle set where the angles are equally separated. We refer to those angle sets as *equidistant*. Any other angle set that are not equidistant is



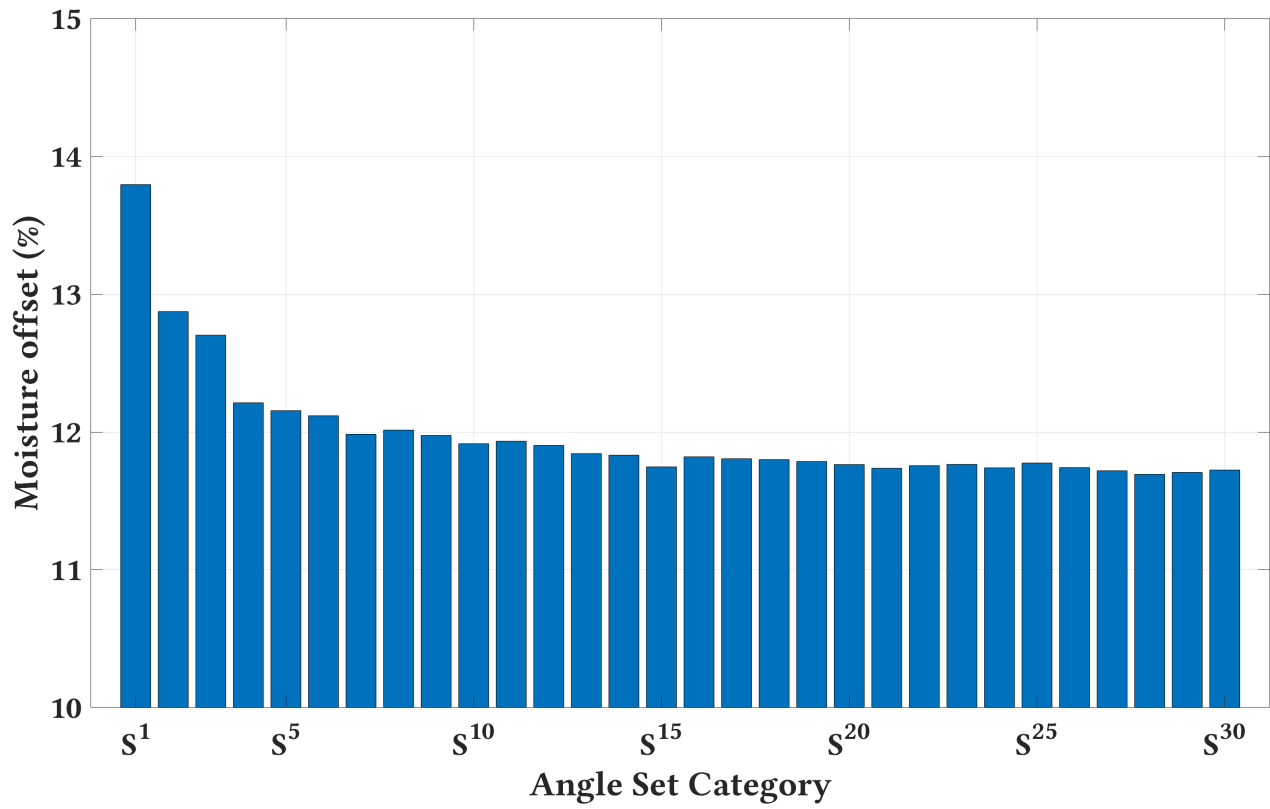


Figure 4.6: The median offset value (%) for each category set.

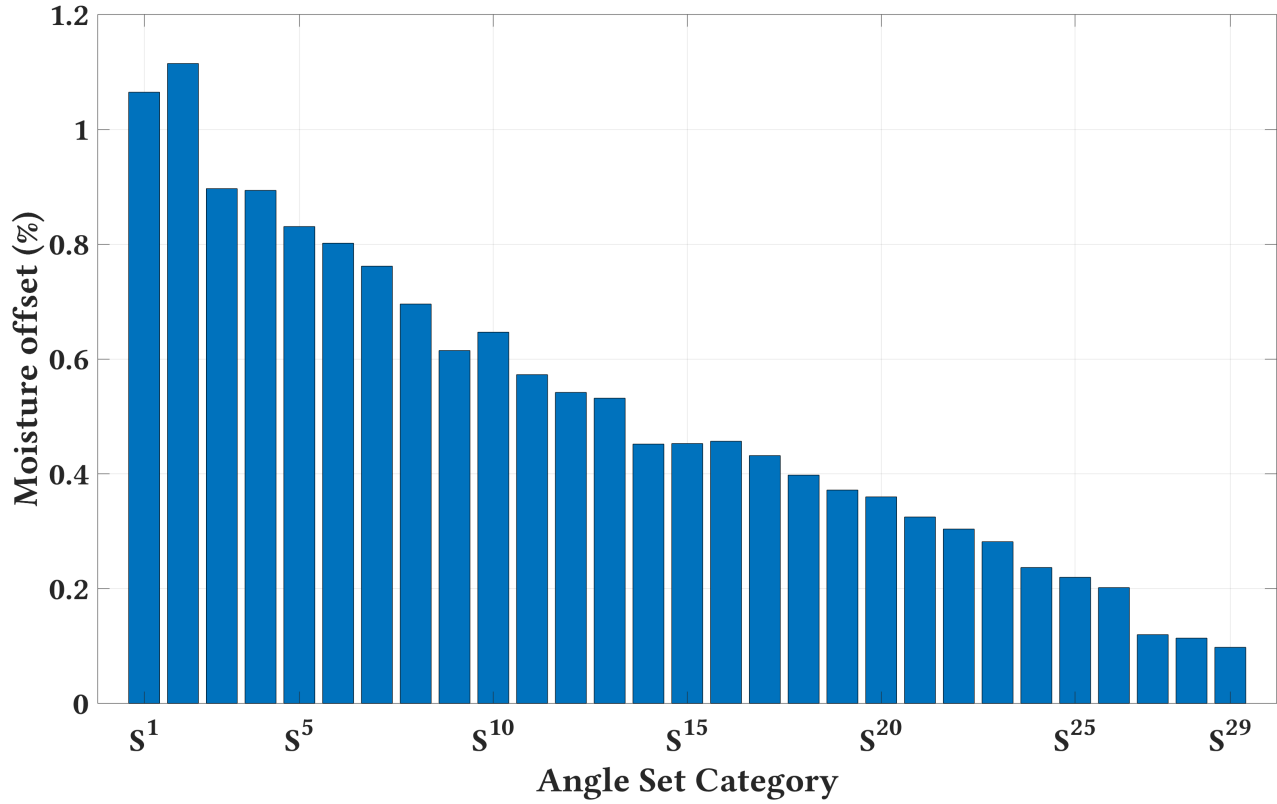


Figure 4.7: The standard deviation value for each category set.

referred to as *random*. For example,  $S_i^4 = \{0, \frac{\pi}{2}, \pi, \frac{3\pi}{2}\}$  is an equidistant angle set because all the angles are separated by  $\frac{\pi}{2}$ . In contrast,  $S_j^4 = \{0, \frac{\pi}{4}, \pi, \frac{3\pi}{2}, 2\pi\}$  is a random angle set because the angles are not equally separated. Thus, in here we investigate how the performance of an equidistant angle set such as  $S_i^4$  compares to the performance of a random angle set such as  $S_j^4$ .

For each angle set category, we run SING with all possible equidistant angle sets from  $S^3$  to  $S^{29}$  - a total of 946 angle sets - against random angle sets. We exclude  $S^1$  and  $S^2$  because the minimum number of angles required to categorize an angle set as equidistant is three. We also exclude  $S^{30}$  because it has a single angle set. We also run SING on all random angle sets in the sample we have mentioned at the beginning of the section (i.e., the sample of 11353 angle sets). Figures 4.8 and 4.9 show the mean and median values for the equidistant and random angle sets at each angle set category. The error bars in the former figure is the standard deviation values. The results show that scanning from equidistant angles is not a requirement for SING to generate accurate estimations. In fact, the performance of random angle sets is slightly better than equidistant angle sets at almost every angle set category. This highlight SING ability to provide accurate estimations in spite of angles locations. This outcome, we believe, is related to the shape of grape clusters. Since grape clusters are geometrically non-uniform, choosing to scan from random or specific angles is not as important as scanning from multiple angles as illustrated before in figures 4.5, 4.6, and in the figures here especially in the random scanned angles.

### C: Single against Multiple segments

From before, we have shown that scanning from multiple angles is crucial for SING accuracy. In here, we discuss the location of those angles. Specifically, we investigate how SING accuracy is affected by scanning multiple angles of a grape cluster from either a single side or multiple sides. To do so, we divide - virtually - a grape cluster into different segments. Since we scan a grape cluster from 30 angles, we can equally divide the cluster into two, three, five, six, ten, or fifteen segments. In the two-segment category, we have fifteen angles in each segment;  $\{0^\circ, 12^\circ,$

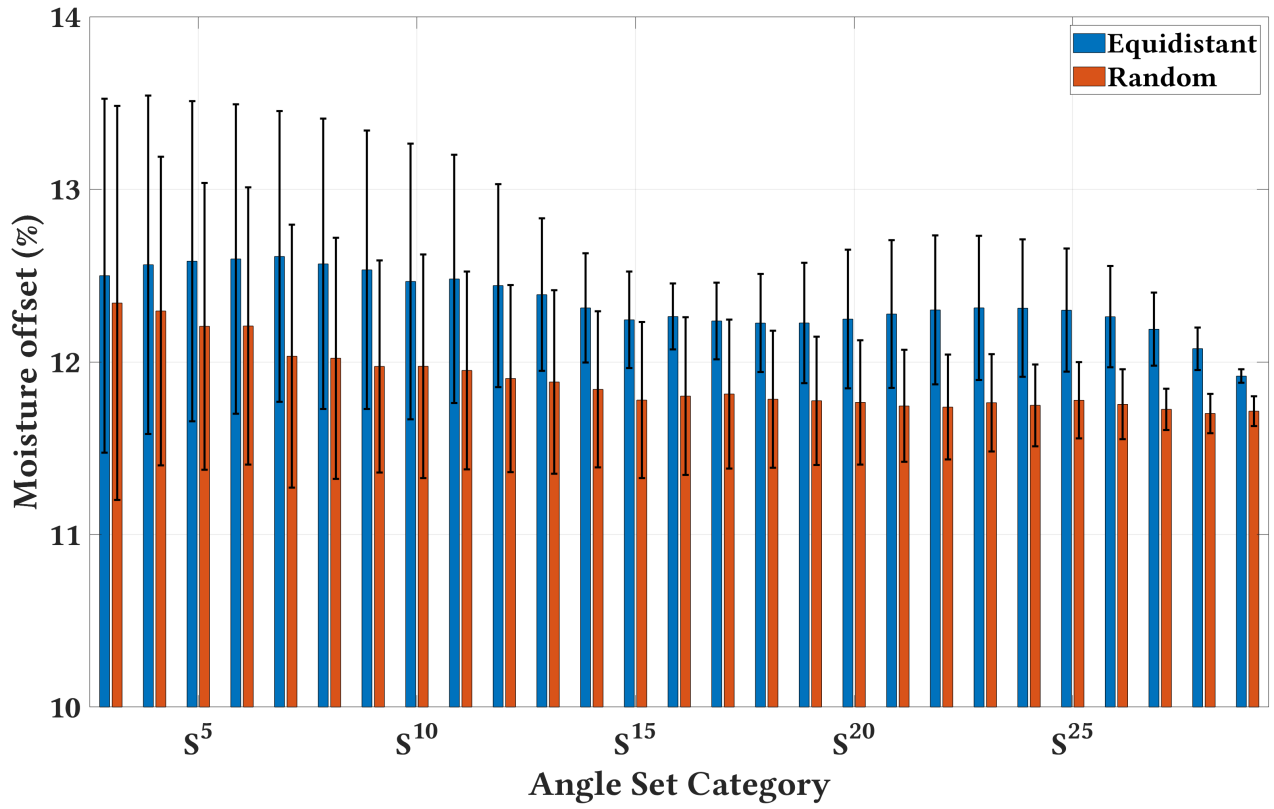


Figure 4.8: The mean offset values (%) for equidistant against random scanned angles for each angle set category.

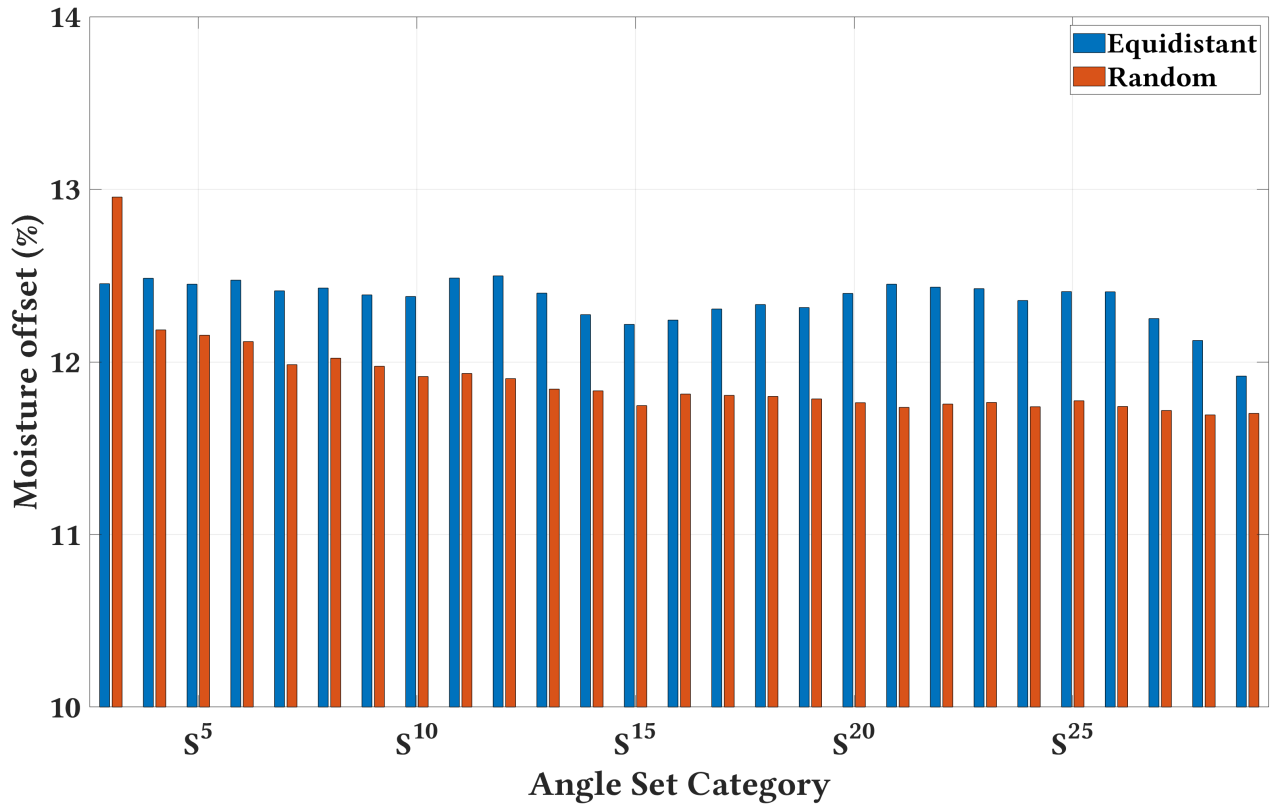


Figure 4.9: The median offset values (%) for equidistant against random scanned angles for each angle set category at the *all* frequency set.

...,  $168^\circ$ } in the first segment, and  $\{180^\circ, 192^\circ, \dots, 348^\circ\}$  in the second segment. In the three-segment category, we have 10 angles in each segment;  $\{0^\circ, 12^\circ, \dots, 108^\circ\}$  in the first segment,  $\{120^\circ, 132^\circ, \dots, 228^\circ\}$  in the second segment, and  $\{240^\circ, 252^\circ, \dots, 348^\circ\}$  in the third segment. The same applies to the other segment categories (i.e., the five, six, ten, and fifteen-segment).

For each segment category, we assign an angle set to the corresponding segment based on the angles in that angle set. For example,  $S_i^4 = \{0^\circ, 12^\circ, 24^\circ, 36^\circ\}$  belongs to the first segment (i.e.,  $\{1\}$ ) in the two, three, five, and six-segment categories because all four angles (i.e.  $0^\circ, 12^\circ, 24^\circ, 36^\circ$ ) are in the first segment of the mentioned segment categories. However, in the ten-segment category,  $S_i^4$  belongs to the  $\{1,2\}$  segment because the first three angles (i.e.,  $0^\circ, 12^\circ, 24^\circ$ ) are in the first segment, and the last angle (i.e.,  $36^\circ$ ) is in the second segment. Similarly, in the fifteen-segment category,  $S_i^4$  also belongs to the  $\{1,2\}$  segment because the first two angles are in the first segment, and the last two angles are in the second segment. We apply the same classification to all angle sets.

After classifying the angle sets, we compare the performance of SING when scanning a grape cluster from a single segment against multiple segments for each segment category. Since we have more than one single-segment and multiple-segment in each segment category, we group all angle sets that belong to *single-segment* into one group and all angle sets that belong to *multiple-segment* into another group. For example, in the three-segment category, we have three single-segment ( $\{1\}$ ,  $\{2\}$ , and  $\{3\}$ ) and four multiple-segment ( $\{1,2\}$ ,  $\{1,3\}$ ,  $\{2,3\}$ , and  $\{1,2,3\}$ ). In this case, we group all angle sets in  $\{1\}$ ,  $\{2\}$ ,  $\{3\}$  into the single-segment group, and all angle sets in  $\{1,2\}$ ,  $\{1,3\}$ ,  $\{2,3\}$ ,  $\{1,2,3\}$  into the multiple-segment group. After dividing the angle sets into those two groups, we compute the mean and median offsets for both groups. The same applies to the other segment categories. Note that an angle set in a segment category belongs only to one segment.

Figure 4.10 reports the mean offset values of the single-segment against multiple-segment. The

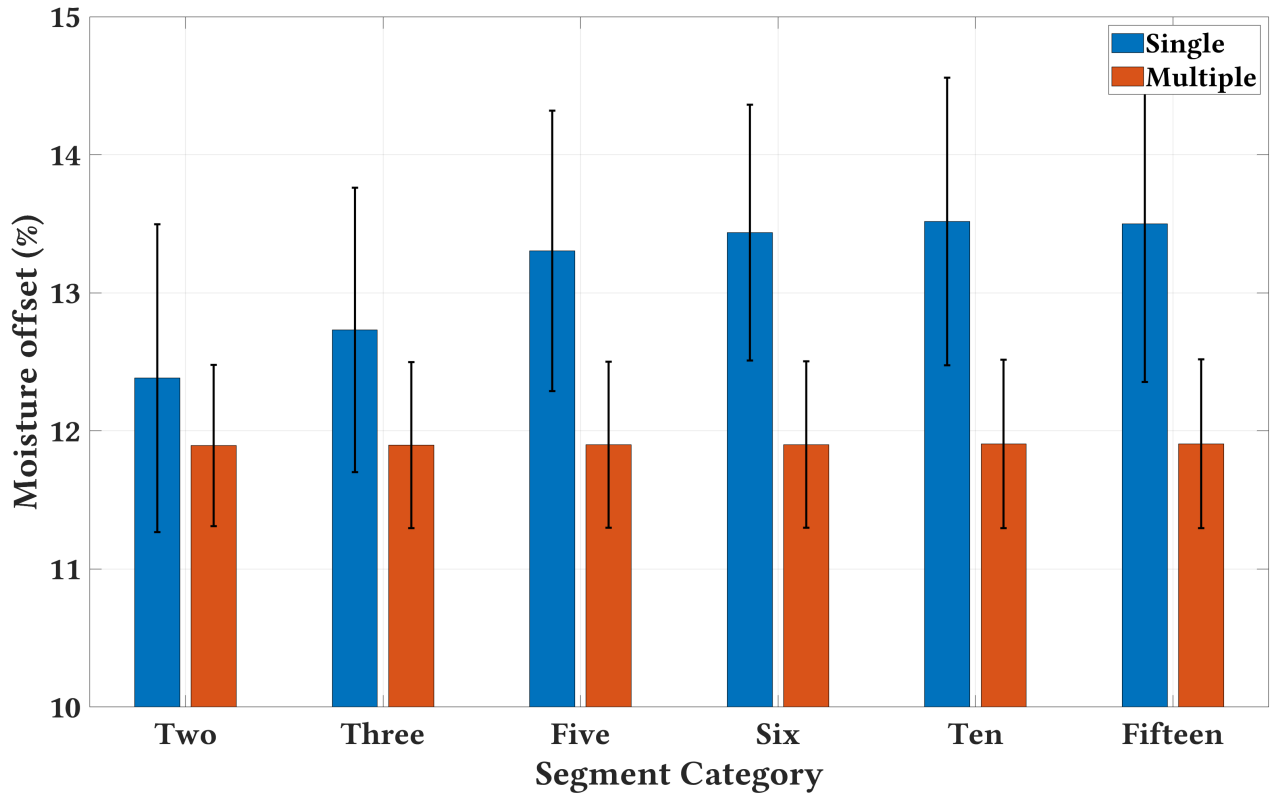


Figure 4.10: The mean offset values of the single-segment and multiple-segment.

error bars in the figures represent the standard deviation values. Figure 4.11 report the median offset values.

In all the figures, the multiple-segment outperforms the single-segment, thus, emphasizing the importance of scanning a grape cluster from multiple segments rather than a single segment. Scanning a grape cluster from multiple segments provides more information for SING about the cluster dielectric properties ( $\varepsilon^*$ ). This increases the chances of SING to estimate correctly  $\varepsilon^*$ , and by extension, the moisture content. Whereas scanning from a single segment only provides information about that segment in particular and not the cluster as a whole. The figures also show how similar the performance of the multiple-segment across all category sets, which emphasizes once again how crucial the scanning from multiple segments is to SING accuracy. The performance of the single-segment and multiple-segment can also be explained through the number of scanned angles, which we discussed earlier in the section. Recall that SING performs better when the number of angle increases. Thus, we examine the number of angles for each segment category in both the single-segment and multiple-segment in figures

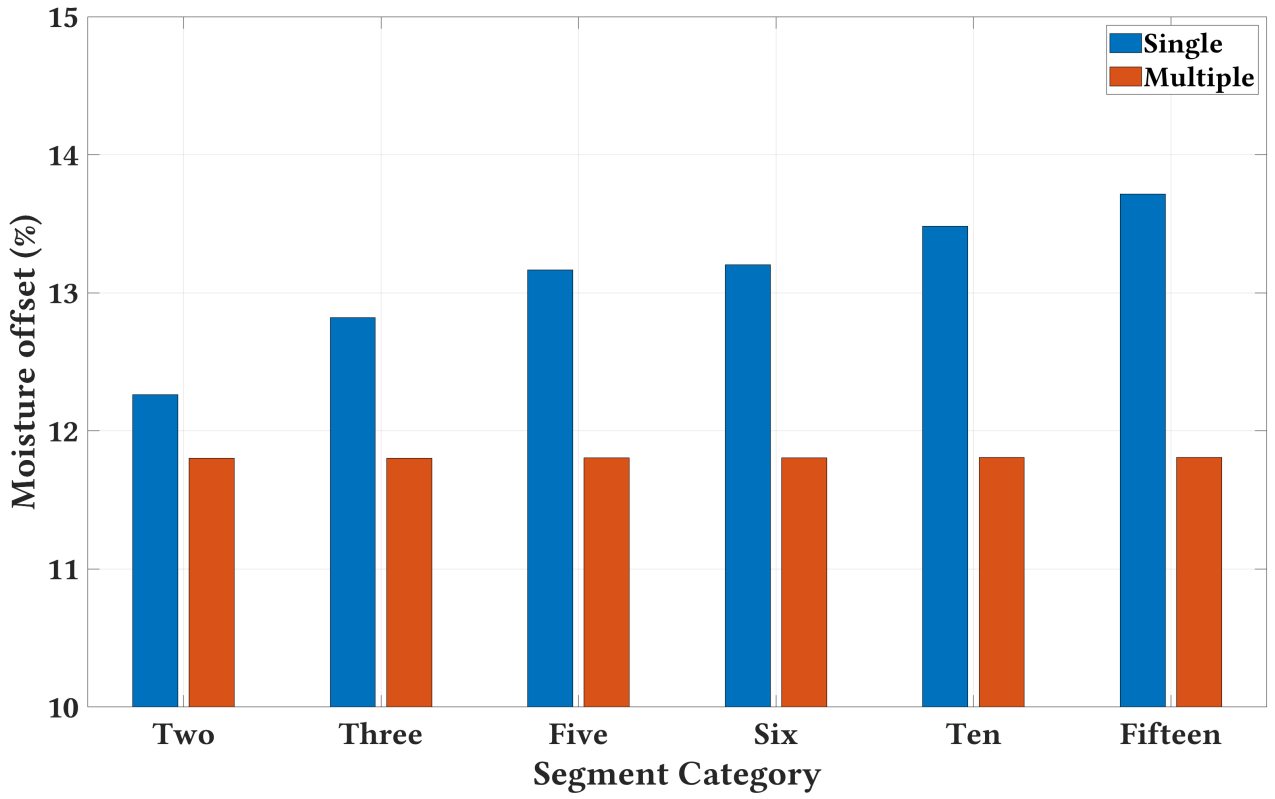


Figure 4.11: The median offset values of the single-segment and multiple-segment.

4.12 and 4.13, respectively.

### Single-Segment

In figure 4.12, the fifteen-segment in the single-segment group is composed only of two angle set categories,  $S^1$  and  $S^2$ . Specifically, 30 angle sets from  $S^1$  and 12 angle sets from  $S^2$ . The ten-segment is composed of 30  $S^1$ , 21  $S^2$ , and 1  $S^3$ . The ten-segment category outperforms the fifteen-segment category in figures 4.10 and 4.11 because the former has more angles in higher angle set categories than the latter. In a similar vein, the two-segment category outperforms the rest in the single-segment group because it has more angles in higher angle set categories than the rest. Evident by the  $S^8$ , which only exists in the two-segment category.

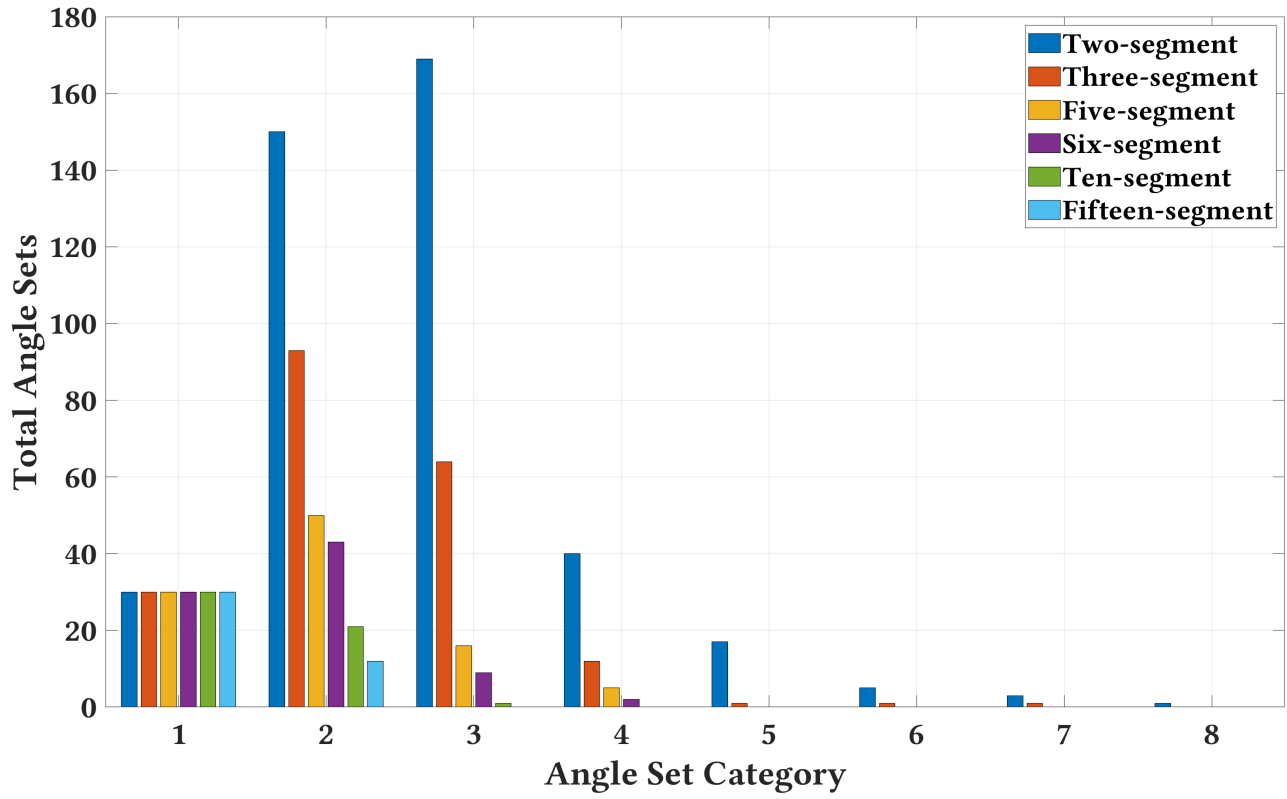


Figure 4.12: The total number of angle sets at each angle set category for each segment category in the single-segment group.

#### 4.1.4 Multiple-Segment

In the multiple-segment group represented by figure 4.13, all segment categories are composed of angle set categories from  $S^2$  to  $S^{30}$ . The number of angle sets in high angle set categories (especially from  $S^6$  onward) are almost identical across all segment categories. This explains the similar performance of the segment categories in the figures 4.10 and 4.11.

The results in figures 4.12 and 4.13 prove once again the efficiency of SING approach to scan grape clusters from multiple angles to provide reliable estimations. Since we have established that, the following criteria examines in more details the minimum number of angles required by SING to provide such reliable estimations.

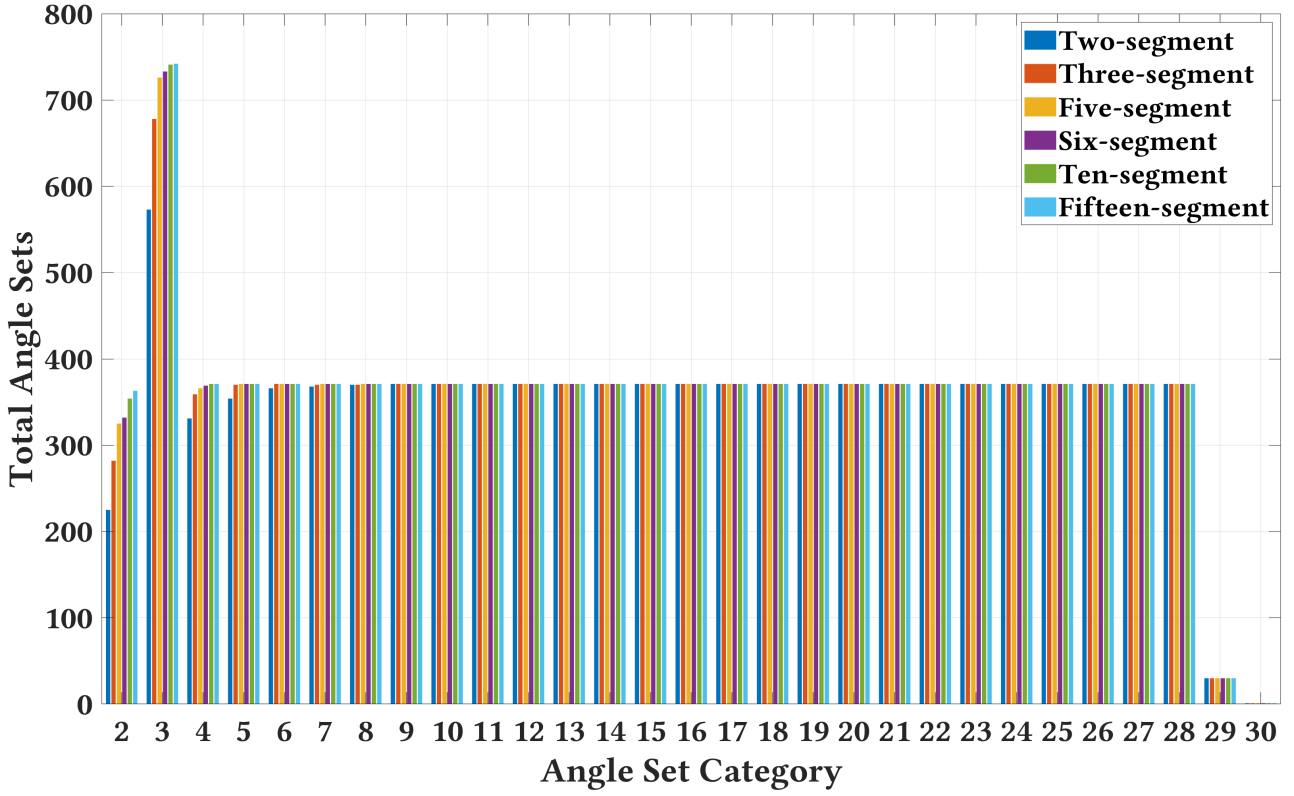


Figure 4.13: The total number of angle sets at each angle set category for each segment category in the multiple-segment group.

#### D: Minimum against Maximum number of angles

Here we discuss SING performance when scanning from the minimum (i.e., *Min*) or maximum (i.e., *Max*) number of angles at the same segment and segment category. *Min* and *Max* refer to angle sets with the minimum and maximum number of angles in a given segment, respectively. For example, assume that we have the following angle sets  $S_i^1 = \{0^\circ\}$ ,  $S_j^1 = \{12^\circ\}$ ,  $S_k^2 = \{0^\circ, 12^\circ\}$ , and  $S_l^3 = \{0^\circ, 12^\circ, 24^\circ\}$ , which all belong to the same segment and segment category. In this case,  $S_i^1$  and  $S_j^1$  are considered *Min* because both angle sets have the minimum number of angles (i.e., one angle) comparing to  $S_k^2$  and  $S_l^3$ , which have more angles (i.e., two and three angles, respectively). Consequently,  $S_l^3$  is considered *Max* because it has the maximum number of angles. Naturally, there may exist a segment where the difference between *Min* and *Max* is as small as one angle. For example, a segment may have two angle sets,  $S^{15}$  and  $S^{16}$ . In this case,  $S^{15}$  is *Min* and  $S^{16}$  is *Max* although the difference is just one angle.



Segment Category	All segments	Eligible segments	Eligible segments (%)
Two-segment	3	3	100
Three-segment	7	7	100
Five-segment	31	31	100
Six-segment	63	63	100
Ten-segment	944	662	70
Fifteen-segment	4660	671	14

Table 4.7: All and eligible segments in each segment category

The purpose of this category is to determine, for a given segment, if SING is required to scan from the maximum number of angles to yield reliable estimations, or to scan from the minimum number of angles and still yield reliable estimations. Put differently, can SING yield similar performance using angle sets such as  $S_i^1$  and  $S_j^1$  instead of  $S_l^3$  given that all those angle sets belong to the same segment and segment category? Similar to before, we compute the mean and median offsets for both groups (i.e.  $Min$  and  $Max$ ), for each segment and segment category. Note that we exclude any segment that only have identical angle sets because we cannot divide the angle sets into the two groups mentioned above. Table 4.7 shows the total number of segments and the number of eligible segments in each segment category. An eligible segment is a segment that has both  $Min$  and  $Max$ .

Figures 4.14, 4.15, 4.16, 4.17, 4.18, and 4.19 show the results for the two-segment, three-segment, five-segment, six-segment, ten-segment, and fifteen-segment category, respectively. Due to the high number of segments in the last three segment categories, we plot only the first 50 segments. We also plot the results only for the mean offset values. The median offset values are plotted in appendix B, §B.1. From the figures, we notice how similar the performance of SING through both the  $Min$  and  $Max$  groups. Specifically, scanning from  $Min$  generated lower offset values than scanning from  $Max$  in  $\approx 48\%$  of the segments (i.e., 2088 segments). The rest 52% (i.e., 2223) is won by  $Max$ .

Figure 4.20 shows the distribution of the wins for each segment category. In the two-segment, scanning from  $Max$  completely outperforms scanning from  $Min$ . The three-segment and five-

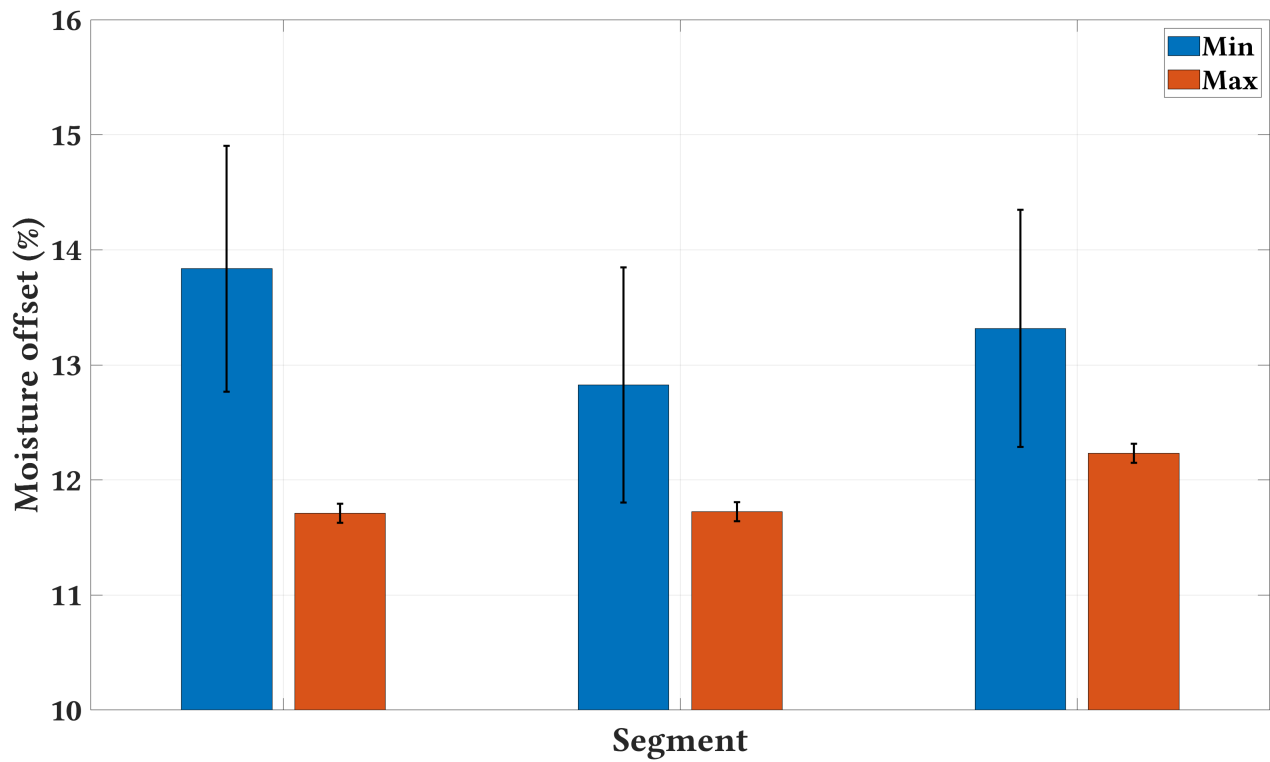


Figure 4.14: The mean offset of the two-segment *Min* against *Max* for the *All* frequency set.

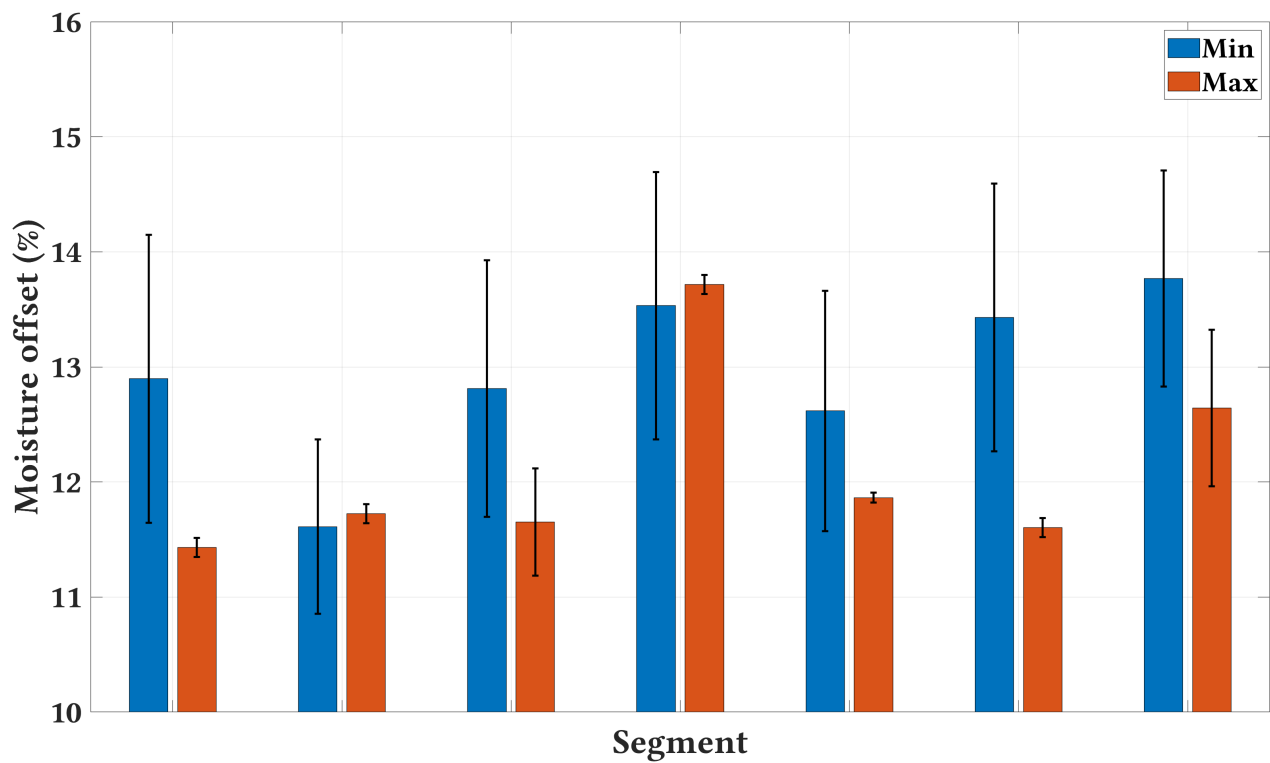


Figure 4.15: The mean offset of the three-segment *Min* against *Max* for the *All* frequency set.

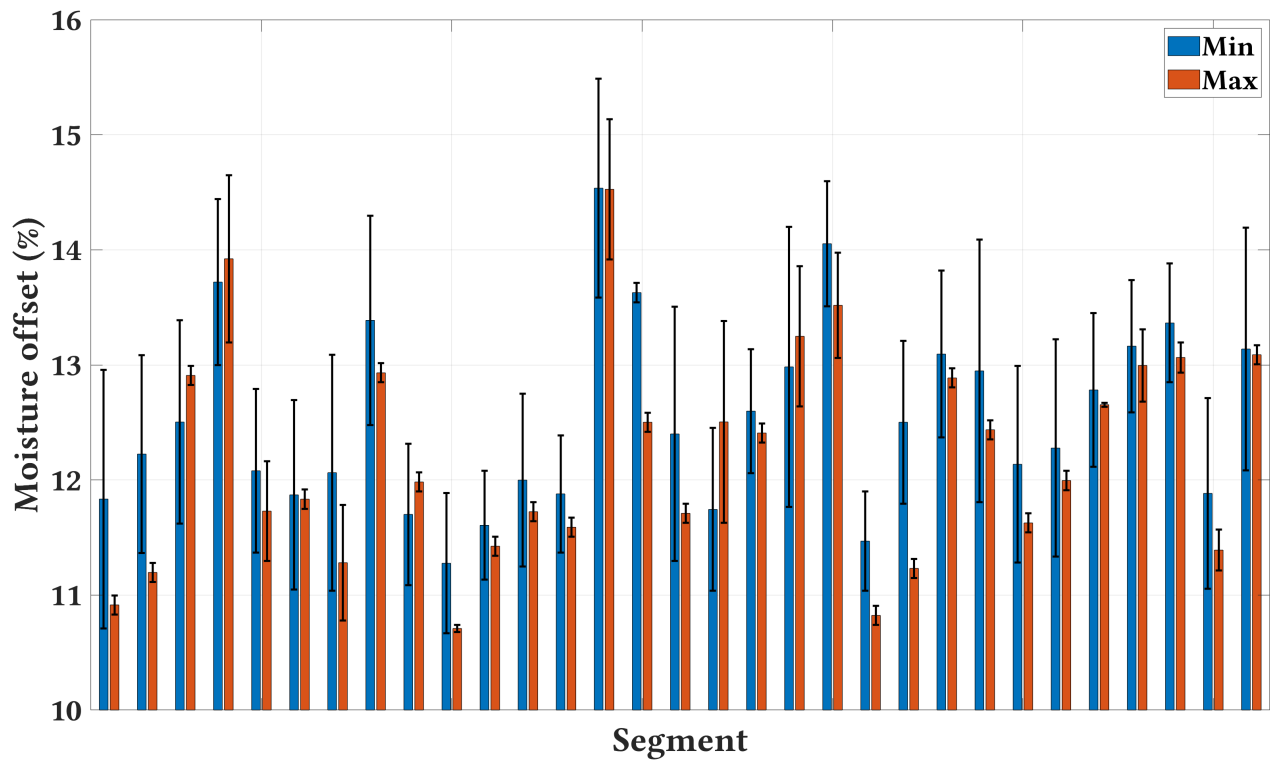


Figure 4.16: The mean offset of the five-segment *Min* against *Max* for the *All* frequency set.

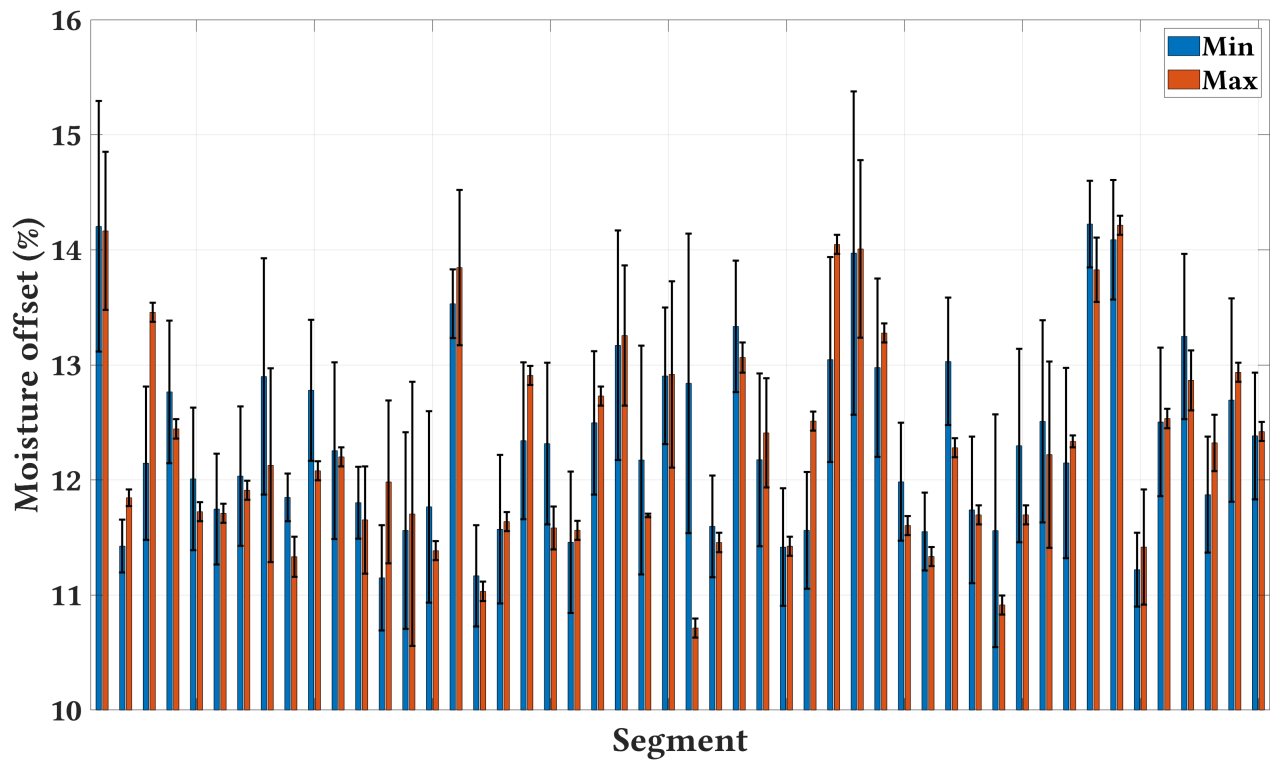


Figure 4.17: The mean offset of the six-segment *Min* against *Max* for the *All* frequency set.

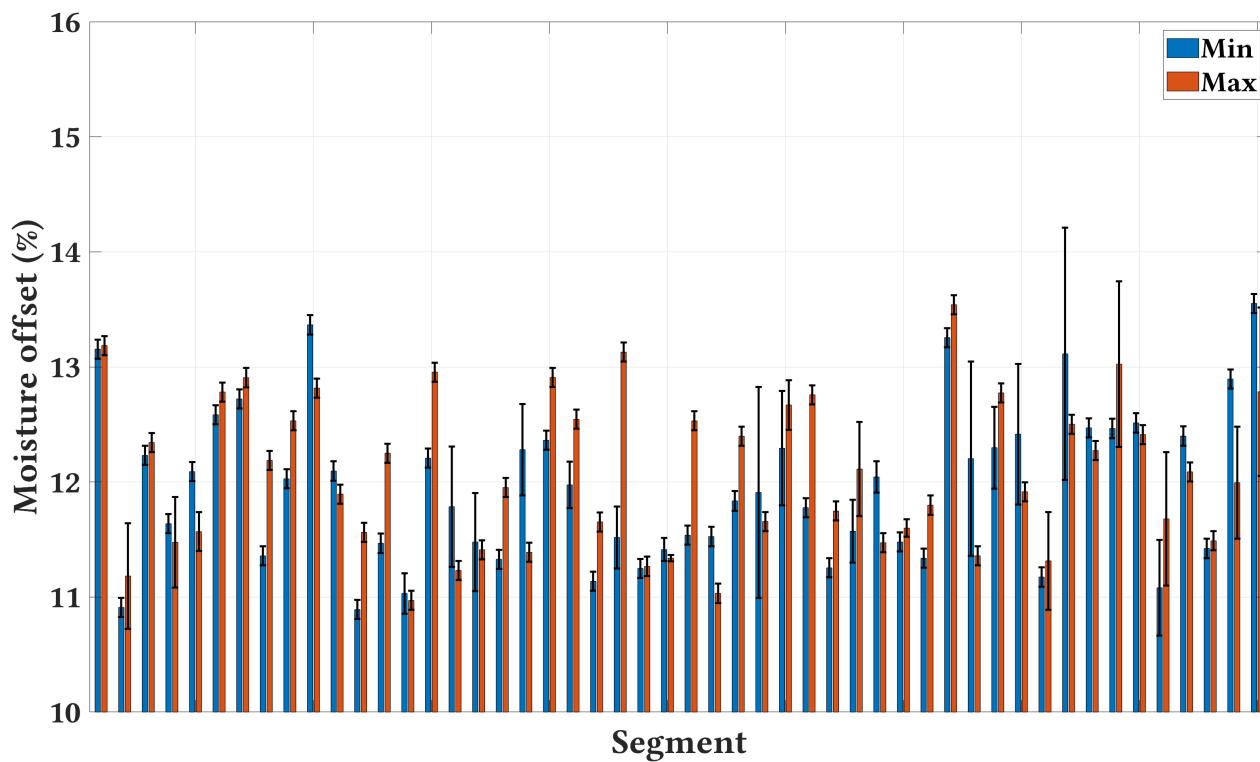


Figure 4.18: The mean offset of the ten-segment *Min* against *Max* for the *All* frequency set.

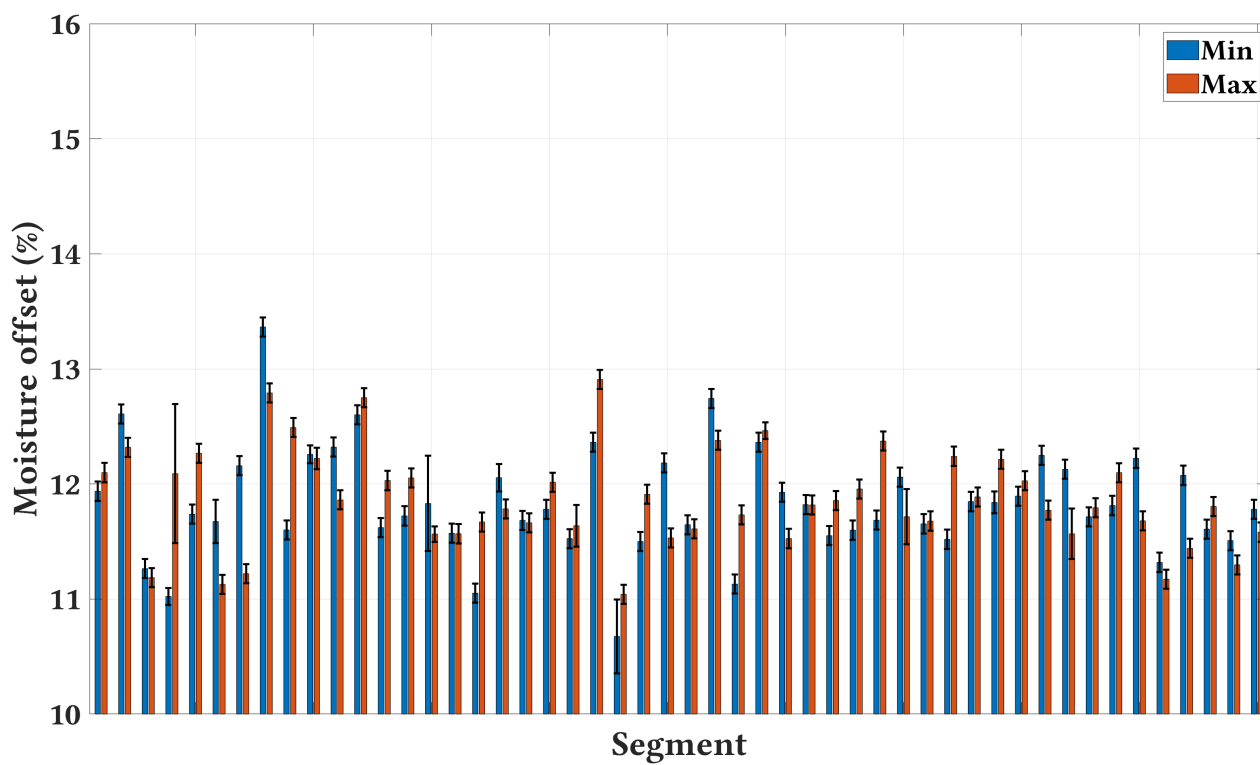


Figure 4.19: The mean offset of the fifteen-segment *Min* against *Max* for the *All* frequency set.

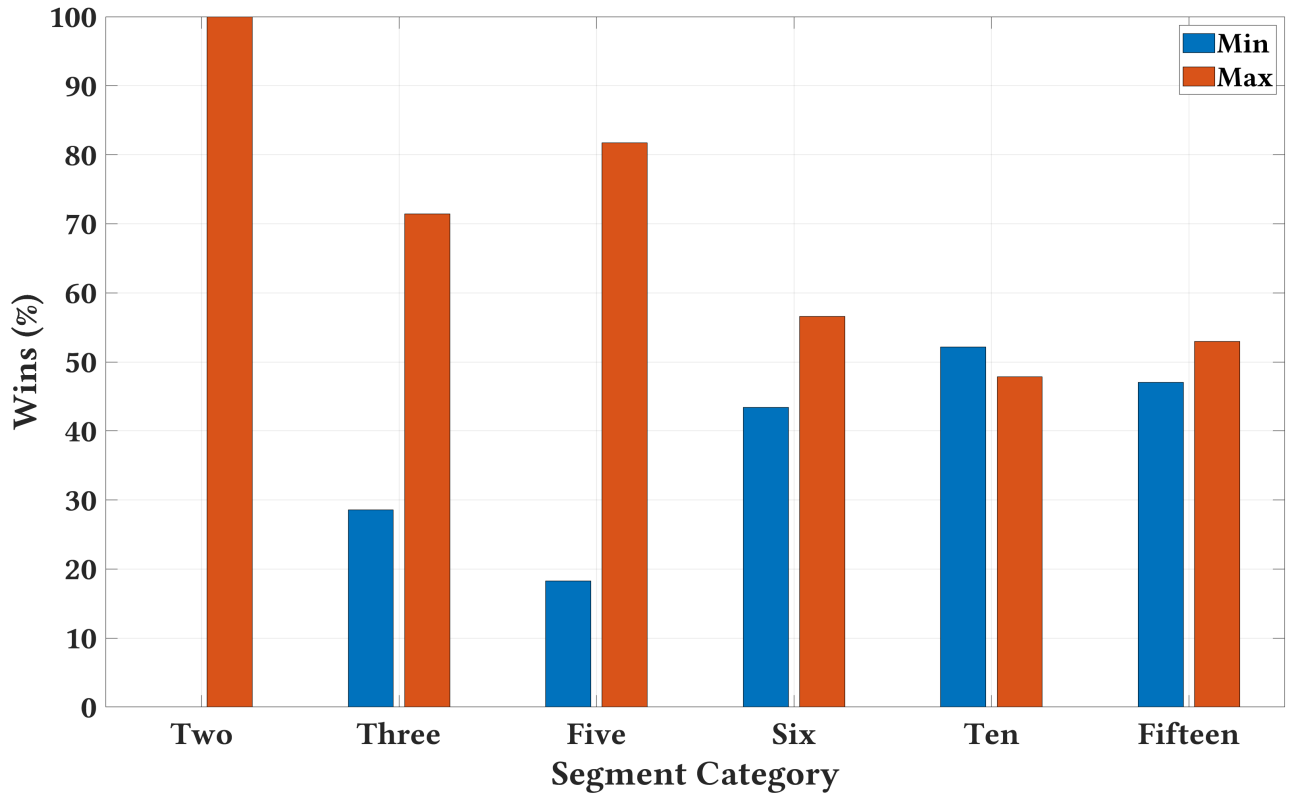


Figure 4.20: The wins (%) for each segment category.

segment follow in the footsteps of the two-segment but to a lesser extent. At six-segment, ten-segment, and fifteen-segment, scanning from *Min* or *Max* yield similar results.

Those results - once again - comply with the main strength of SING; scanning from multiple angles to provide reliable estimations. To explain, in the segment category where *Max* are significantly better than *Min* (i.e., the two-segment, three-segment, and five-segment categories), the segments are sufficiently large with respect to the number of angles in a segment. Therefore, segments encompass both high and low angle sets. A High angle set is an angle set with many angles such as  $S^{28}$ , whereas a low angle set is an angle set with few angles such as  $S^2$ . As we have emphasized throughout this section, running SING with a high number of angles (i.e., high angle sets) provides more accurate estimations than with a low number of angles (i.e., low angle sets). Thus, in most segments in the two-segment, three-segment, and five-segment categories, high angle sets and low angle sets coexist. Since high and low angle sets coexist, the high angle sets are considered as *Max*. SING performs better with high angle sets, thus,

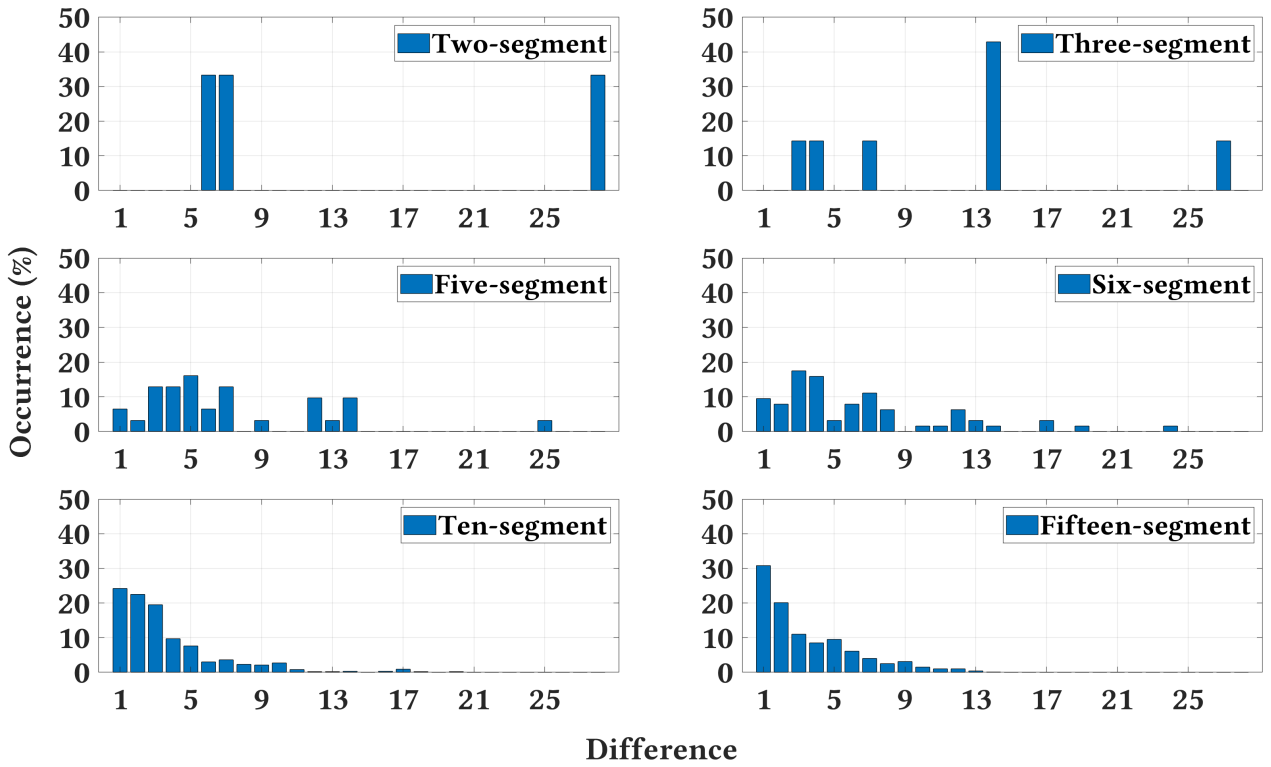


Figure 4.21: The difference in the number of angles between *Min* and *Max* and the occurrence (%) of such difference across all segments in each segment category.

*Max* outperforms *Min* in the mentioned segment category.

In the six-segment, ten-segment, and fifteen-segment categories where SING accuracy is indifferent - to some extent - to scanning from *Min* or *Max*, the segments are relatively small, which reduces the chances of high and low angle sets to coexist. Thus, in many segments in those segment categories, both *Min* and *Max* are represented by either high angle sets or low angle sets but not both. Figure 4.21 summarizes the discussion above. The figure shows for every segment in each segment category the *difference* - in number of angles - between *Max* and *Min*, and the *occurrence* (%) of such difference across all segments. For example, the two-segment category consists of three segments. The difference between *Min* and *Max* for the three segments is 6, 7, and 28 angles, and the occurrence is  $\approx 33\%$  for each difference.

From the figure, the two-segment category has a minimum difference of 6 angles, sufficient

enough for *Max* to outperform *Min*. Consequently, the difference of 7 and 28 angles are also sufficient for *Max* to outperform *Min*. Each difference occurred one time, thus, the occurrence does not affect the two-segment category. In the three-segment category, however, a difference of 14 and 27 angles occurring in  $\approx 43\%$  and  $\approx 14\%$  of the segments, respectively, explains the performance advantage of *Max* over *Min*. In a similar vein,  $\approx 60\%$  of the segments have a difference of five angles or more in the five-segment category. Again, this explains the performance difference between *Min* and *Max* towards the latter. On the other hand, the six-segment category shows a performance similarity between *Min* and *Max* evident by the fact that  $\approx 50\%$  of the segments have a difference less than five angles. The ten-segment category is the only segment category where *Min* outperforms *Max* since  $\approx 75\%$  of the segments have a difference of four angles or less. Of the 75%, the one angle difference is responsible for 32% of them. Comparing to the ten-segment category, the wins percentage of *Min* in the fifteen-segment category is lower because fewer segments have a difference of four angles and less.

As we have mentioned before, a main feature of SING is to examine different segments of a grape cluster to provide reliable estimations. The above discussion emphasizes SING's ability to tolerate not scanning from the maximum number of angles in a segment and still provide reliable estimations.

By this we conclude the analysis of the results. From the analysis, we have learned that scanning from multiple angles at multiple segments is more critical to SING accuracy than merely increasing the number of angles or scanning from strategically chosen angles. This observation paves the way to the discussion in Chapter 5.

#### 4.1.5 Initial Vineyard testing

To get an understanding of the performance of SING in a real-world environment, we have tested SING in a vineyard (Ridgeview vineyard [24]). A vineyard is an uncontrolled environment because entities other than grapes will affect RF signals such as leaves, trunks, soil, and people,

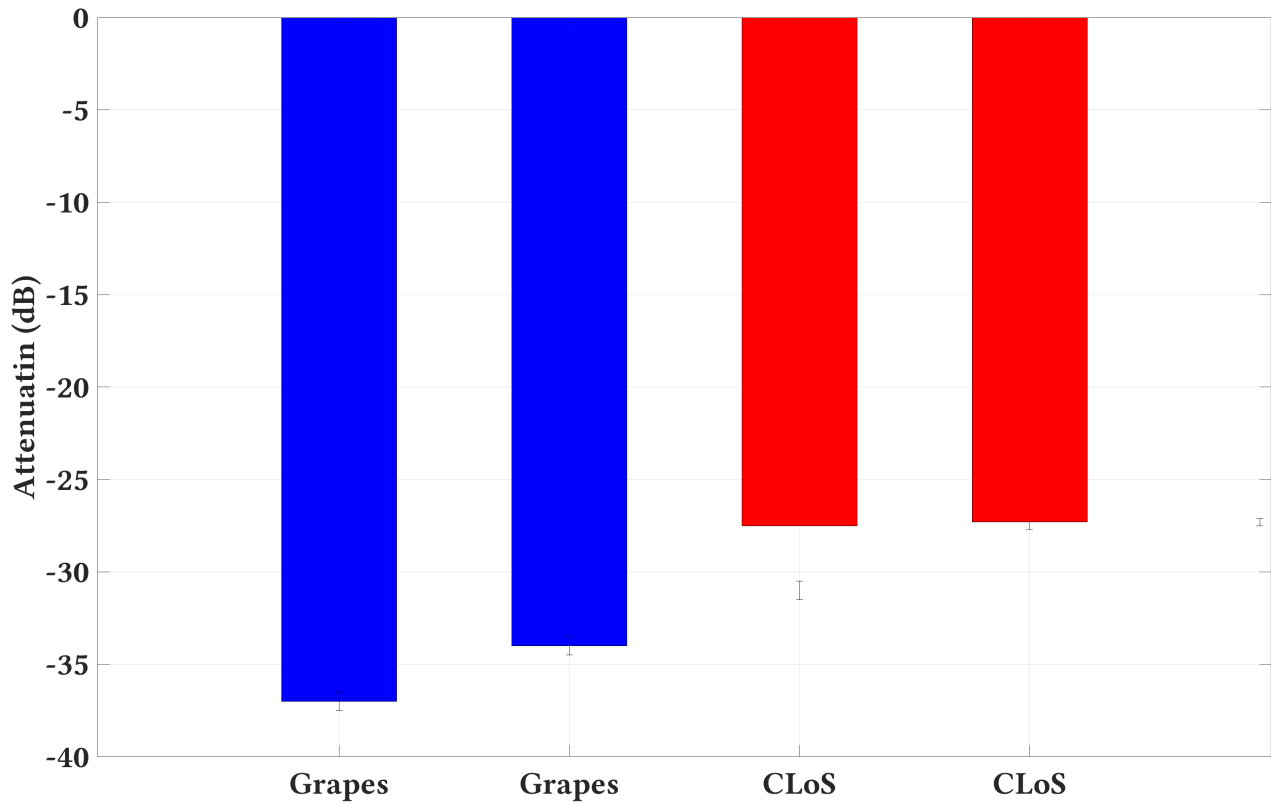


Figure 4.22: Attenuation of the signal between the transmitter and receiver in the presence of cluster of grapes against the clear line-of-sight (CLoS) in a Vineyard.

to name a few. Thus, we conducted different experiments in the vineyard to identify the extra challenges that we might encounter when deploying SING therein. In the vineyard, the sole purpose of the experiments is to examine and compare the attenuation of the signal in the presence of clusters against a clear line of sight between the transmitter and receiver. Figure 4.22 shows the results, where we measure two clusters individually - the first two bars in the figure - and CLoS at two different locations. From the results, we notice the two clusters have a minimum of 7 dB difference when compared to the CLoS readings. The difference between the clusters themselves is due to the first cluster being heavier than the second one. The outcome of the experiments mentioned above is an indication of the feasibility of deploying SING in vineyards. However, at this stage, there remains a gap between lab experiments and practical deployment, which we discuss in Chapter 5.



## 4.2 Conclusion

In many cases, the current industry practice for yield estimation is error-prone, expensive, and unresponsive to environmental changes [93, 94]. In chapter 3, we have introduced SING, a scheme that estimates the moisture content in agricultural products with focus on grapes in a non-destructive, timely manner using RF signals by measuring its dielectric properties ( $\epsilon^*$ ); this approach, to the best of our knowledge, has not been introduced before in the literature. SING calculates  $\epsilon^*$ , and consequently  $\kappa$ , in grape clusters by measuring the attenuation and the phase shift of clusters from different angles. SING is superior to that of traditional free-space transmission in its tolerance to the non-uniformity of grape clusters, its disregard of fixtures, and its applicability to real-world environments where grape clusters can be measured without removing them from the canopy; thus, continuing to grow without any disturbance.

In chapter 4, we have shown that SING senses the moisture content in various grape clusters with high accuracy ( $\approx 90\%$ ). This high accuracy provides more reliable yield estimations than traditional techniques where the yield estimations inaccuracy is as high as 40% [122]. We have also provided a detailed discussion about different factors that affect SING accuracy such as angles location and number.

In the next chapter we discuss the constraints and specifications required to transform SING from a lab based system to a system working in the fields.

# Chapter 5

## Outdoor SING

In this chapter, we discuss potential specifications and design's constraints to transform SING into a system suitable for real-world environments such as in vineyards. We start by discussing the design's constraints that we have to adhere to. Then we propose candidate designs of SING in outdoor environments. Specifically, we investigate different deployment options, different measurement devices to replace VNAs, and the responsibilities and requirements of the host computer in the design. We conclude the chapter by analyzing the power consumption and presenting an estimated overall cost of the system. Note that we refer to SING as outdoor SING throughout this chapter.

### 5.1 Outdoor SING Constraints

#### 5.1.1 The distance between the transmitter and receiver.

The distance between the transmitter and receiver must adhere to the far-field ( $D_{\text{far-field}}$ ) requirements we discussed earlier in §3.2.1. According to equation 5.1 two parameters affect that distance, the frequency ( $f$ ) and the largest antenna dimension ( $D$ ) [33].

$$D_{\text{far-field}} = \frac{2D^2}{\lambda} \tag{5.1}$$

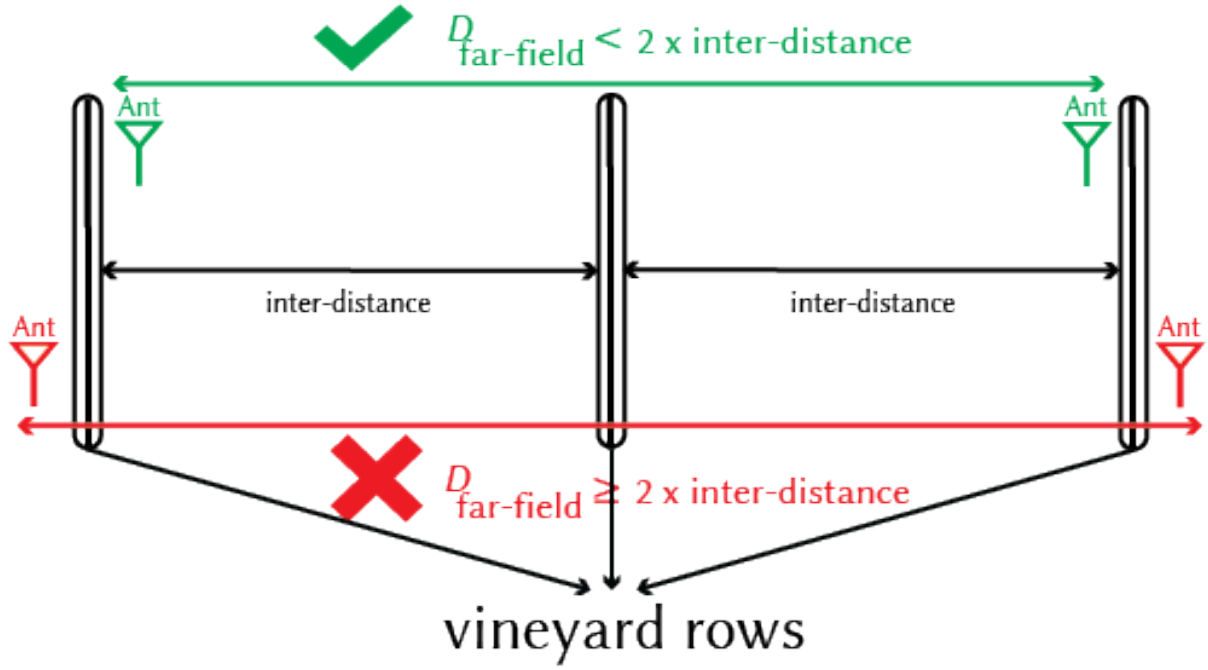


Figure 5.1: Two scenarios to illustrate the relationship between  $D_{\text{far-field}}$  and the inter-distance between a vineyard's rows.

In SING,  $f$  is fixed to the 5 GHz band, thus,  $D$  is the only variable in equation 5.1. The main criteria to choose an antenna - and by extension,  $D$  - in SING is the antenna's directivity. The directivity shapes the antenna's beamwidth, and it is decided according to the dimension (i.e., the width) of the clusters to be scanned. To explain, we scan clusters individually to obtain reliable moisture estimations. Therefore, the antenna's beamwidth should not be significantly larger than the width of the clusters. Otherwise, we may scan multiple clusters at once. Although scanning multiple clusters at once may reduce the scanning time, it is not favourable to the accuracy of SING. For those reasons, the value of  $D$  for outdoor SING should result in a far-field distance ( $D_{\text{far-field}}$ ) smaller than twice the inter-distance between vineyard rows as illustrated in figure 5.1. In the figure, the green part of the figure is the correct scenario where  $D_{\text{far-field}} < 2 \times \text{inter-distance}$ . Thus, outdoor SING scans a single cluster. The red part of the figure is the wrong scenario where outdoor SING covers multiple clusters from different rows. According to the vineyard we have visited, the inter-distance between rows are between 1 and 2 m [24]. Accordingly, a far-field distance  $< 2$  m is required. Thus, from equation 5.1,  $D$  should not exceed 24.4 cm as in equation 5.2.

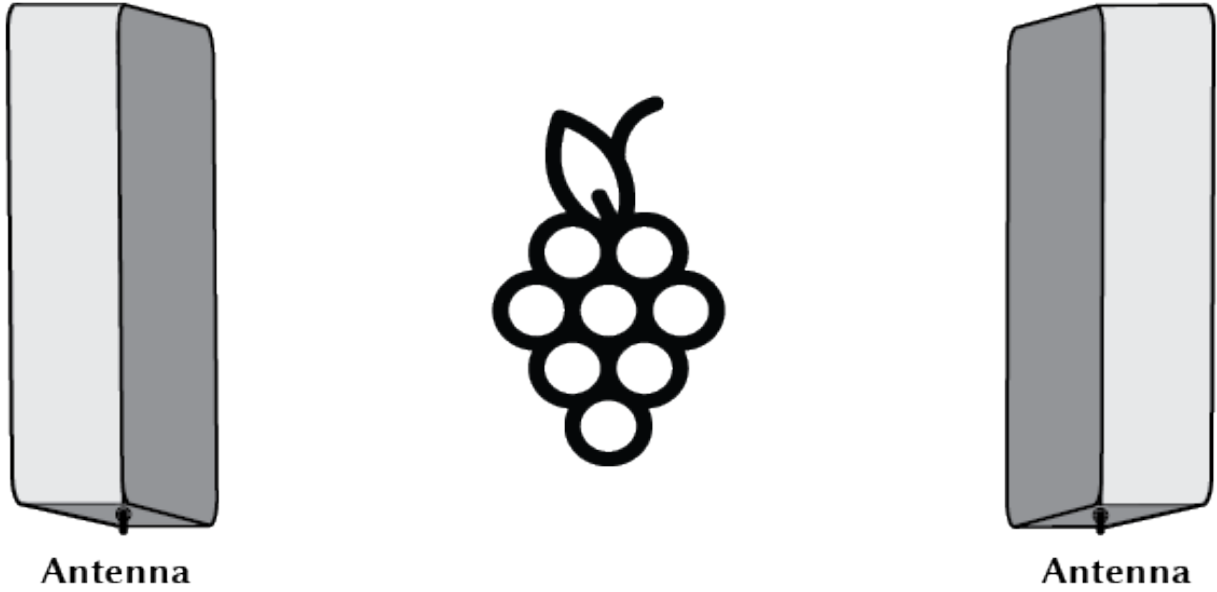


Figure 5.2: A cluster between two antennas. The preferable setup for SING.

$$\begin{aligned}
 D_{\text{far-field}} &= \frac{2D^2}{\lambda} \\
 2 &= \frac{2D^2}{0.0599} \\
 D^2 &= 0.0599 \\
 D &= 0.244 \text{ m}
 \end{aligned} \tag{5.2}$$

### 5.1.2 The placement of the antenna.

Since in SING we rely on computing the transmission coefficient ( $\tau$ ), we need to place the antennas at the opposite sides of a cluster as in figure 5.2. This will limit the deployment options as we cannot place the antennas on a single side. Thus, any viable deployment option should allow the antennas to cover a cluster from opposite sides without altering or disturbing the canopy in any way. Figure 5.3 shows two viable deployment options.



Figure 5.3: (a) Illustration of outdoor SING as a handheld device, and (b) illustration of outdoor SING as an aerial device

### 5.1.3 Multiple vs. Rotating antennas.

In SING, we scan the clusters from multiple angles by rotating the clusters. Obviously, this is infeasible in a vineyard without disturbing the canopy. Thus, we discuss two alternatives to replace the rotation of clusters. The first option is to place multiple pairs of  $T_x$ - $R_x$  around the clusters. The second option is to rotate the antennas. The former facilitates the design of outdoor SING as no rotation is required, however, the number of scanned angles is limited by the number of antenna pairs. For example, two pairs of antennas will scan a total of four angles, and three pairs will scan six angles. The second option enables outdoor SING to scan from far more angles than the first option with only a single pair of antennas. In fact, we would be able to scan from a high number of angles (e.g., 30 angles similar to §3.2.1) if we rotate the antennas with high precision. A Servo motor can achieve such a high rotation precision [11]. The downside of the second option is the added complexity of designing a mechanism for rotating the antennas.

Another matter to discuss is how accurate the scanning of angles should be? In other words, is outdoor SING required to scan the clusters precisely at specific angles, and will failing to do so might affect its performance significantly? In fact, we have discussed this in §4.1.3, and emphasized SING's ability to yield reliable estimations even when scanning at random

angles. Indeed, the primary prerequisite for SING to deliver reliable estimations is to scan a single cluster from different sides according to the results in §4.1.3. Thus, scanning a cluster at precise angles is not crucial.

## 5.2 Outdoor SING Design

### 5.2.1 Deployment options

The main objective of SING is to increase the reliability of yield prediction by measuring clusters non-intrusively throughout the vineyard. Therefore, having outdoor SING as a mobile measuring device is a necessity. Thus, we propose three deployment options for outdoor SING: as a handheld device (figure 5.3(a)), on a drone (figure 5.3(b)), or on a robot. In the first option, outdoor SING can be held by an operator that moves from one cluster to another to perform measurements. This option reduces the complexity of outdoor SING design as no drones or robots are required. However, it may lack consistency in measurements as humans are involved in the measuring process, which may require personnel training to handle the device. The second option also involves an operator that handles outdoor SING. However, it offers the convenience of operating outdoor SING from afar, moving between vineyard's rows at a higher speed, and helps in extreme weather conditions. The third option is fully automated, which should enforce consistency better than the first two options. However, it requires an algorithm to determine the location of clusters as opposed to the first two options where an operator is responsible for this job. This should increase the design complexity of SING.

In the second deployment option, outdoor SING is mounted on a drone, which may hinder the drone's ability to fly. We defer the discussion about this to §5.3. In the third deployment option, an algorithm is required to detect the location of clusters. Similar algorithms exist in previous work, specifically in [67, 93, 94]. In those works, the authors employ optical imaging to detect grapes/clusters. Thus, we can employ similar techniques to design the algorithm for

Deployment Option	Design Complexity	Cost	Antenna Rotation	Laborious/Human involvement	Suitable for extreme weather condition	Speed of navigating the field
Handheld	Low	Low	Manual	High	Low	Medium
on a Drone	Medium	Medium	Semi-Automated	Medium	Medium	High
on a Robot	High	High	Automated	Low	Medium	Low

Table 5.1: Deployment Options

the third deployment option.

Table 5.1 summarizes the advantage/disadvantage of the three deployment options. In the table, we assign three *relative* values, namely, low, medium, and high in all comparison categories except for the antenna rotation. By relative, we mean one deployment option's score is relative to the other deployment options. For example, in the speed of navigating the field category, the Drone option scores the highest, which translates to the Drone option being the fastest compared to the other two options. The Robot option has the highest cost and design complexity; however, it has the lowest human involvement. The Handheld option has the highest human involvement and it is the least suitable for extreme weather conditions. Finally, in the antenna rotation category, the Handheld option is completely manual as opposed to the Robot option where the robot is responsible for rotating the antennas. The Drone option is semi-automated as a drone rotates the antenna, however, an operator is still required to operate the drone itself.

### 5.2.2 Measurement devices

In SING, we employed a VNA to perform the S-parameters measurement. VNAs are expensive and power-hungry [52], which renders them unsuitable for outdoor deployment. An alternative to VNAs are Software Defined Radios (SDRs). SDRs are radio communication devices where components that are usually implemented in hardware, in VNAs, are instead implemented in software [119]. Components such as filters and amplifiers can be realised through mathematical models eliminating the need to implement them in hardware. With efficient power management, SDRs can survive for an extended period of time on batteries and power banks [68]. There are different commercial SDRs in the market today, from which we focus on two types: single port and multiple ports SDRs. Single port SDRs such as the HackRF One ([9]) have - as the name suggests - a single port to plug an antenna into, which reduce the design complexity and

cost. However, it cannot achieve full-duplex communication, which renders them unsuitable for a multitude of applications that require full-duplex communications. Multiple ports SDRs on the other hand can connect multiple antennas and achieve full-duplex communication at the cost of increased design complexity and power consumption. Examples of the multiple ports SDRs are BladeRF 2.0 ([6]) and LimeSDR ([15]). Table 5.2 shows a comparison between those SDRs and the HackRF One.

The SDRs in table 5.2 can be transformed to measure the S-parameters. However, doing so requires several modifications, which we discuss below:

**HackRF One.** The HackRF One is a single port SDR developed by Great Scott Gadgets to transmit and receive RF signals from 1 MHz to 6 GHz. To realise outdoor SING by employing the HackRF One, we need to measure the S-parameters using the HackRF One. Figure 5.4 illustrates a proposed design to transform the HackRF One into an SDR capable of measuring the S-parameters. In the figure, the green lines refer to the  $S_{11}$  measurements, and the red lines refer to the  $S_{21}$ . Below is a description of each component in the figure:

- **HackRF One:** Since the HackRF One is a single port SDR, we need two of them to have a  $T_x/R_x$  pair. We also need to synchronize their clocks to avoid phase synchronization problems. Fortunately, the HackRF One has a clock port that can be connected to the other HackRF One clock port to share the same clock as illustrated in the figure.
- **Frequency Synthesizer:** the role of the frequency synthesizer is to generate signals at the required frequencies (i.e., the 5 GHz band for SING). Although HackRF One can perform this task, we employ frequency synthesizers to lower the whole design's cost and power consumption.
- **Multiplexer:** A main requirement for a VNA is to measure the phase shift. This is accomplished by comparing the phase shift of the measured signals against a reference signal. Since the HackRF One has a single port, a Multiplexer enables the HackRF One



to receive both signals (i.e. measured and reference). Note that multiplexing can be achieved either by time or frequency [66].

- Directional Coupler: to enable the measurement of the  $S_{11}$  parameter as described in [63].
- RF Switch: to switch between signals received through the Directional Couple/Multiplexer path and signals received from the antenna directly to the HackRF One path. The former path is for the  $S_{11}$  measurements, whereas the latter is for the  $S_{21}$  measurements.
- Servo Motor: to rotate the antennas.
- Host Computer: to deliver power to the components and perform SING procedure (figure 3.19, §3.2.4) on the measurements.
- Battery/Power Bank: to power up the host computer and other components if needed.

The power consumption and cost of the proposed design in figure 5.4 is discussed later in §5.3. Next, we discuss the proposed design to enable S-parameters measurement through the multiple ports SDRs, namely, the BladeRF 2.0 and the LimeSDR.

**LimeSDR/BladeRF 2.0** The BladeRF 2.0 is a multiple ports SDR designed by Nuand to operate between the 47 MHz and 6 GHz [6]. BladeRF 2.0 can connect up to four antennas (two  $T_x$  and two  $R_x$ ). Equivalently, the LimeSDR - developed by Lime Microsystems [15] - can also connect up to four antennas. The LimeSDR however can only operate up to 3.8 GHz and it requires an up-converter to extend the range to 10 GHz. The up-converter in question is the LMS8001A chip developed also by Lime Microsystems. Similar to the proposed design for the HackRF One, figure 5.5 shows the required components to enable S-parameters measurement through both the BladeRF 2.0 and the LimeSDR. The green and red lines illustrate the same function as in the HackRF One design. Below is a description of the components depicted in the figure:

- LimeSDR/BladeRF 2.0: Both the LimeSDR and the BladeRF 2.0 are full-duplex multi-ports SDRs. In fact, both SDRs have two  $T_x$  chains (ports) and, similarly, two  $R_x$  chains.

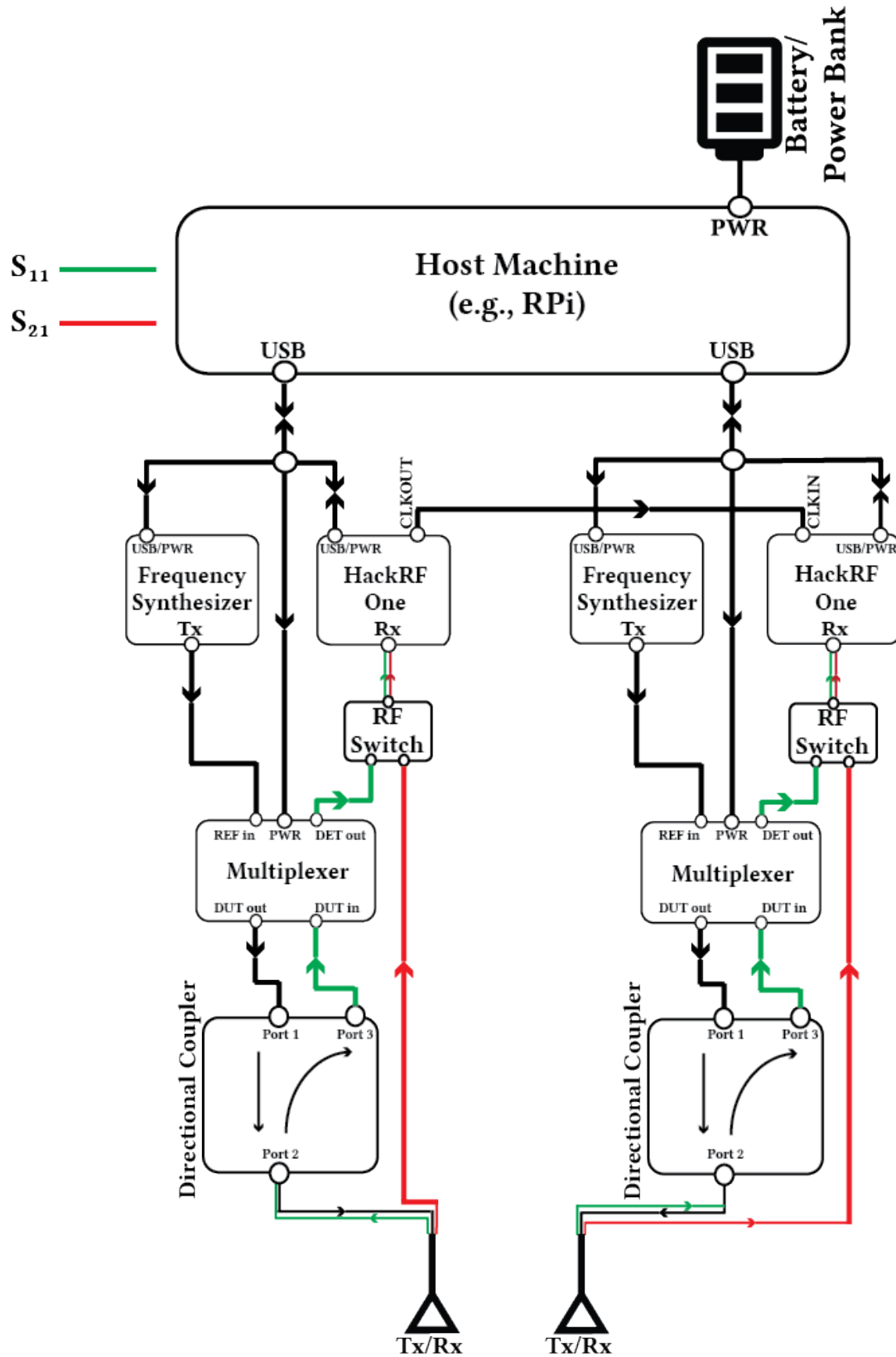


Figure 5.4: A proposed design of outdoor SING using HackRF One.

	HackRF One	BladeRF 2.0 xA5	LimeSDR
Frequency Range	1 MHz - 6 GHz	47 MHz - 6 GHz	100 KHz - 3.8 GHz (up to 10 GHz with LMS8001A [16])
RF Bandwidth	20 MHz	56 MHz	61.44 MHz
Sample Depth	8 bits	12 bits	12 bits
Sample Rate	20 MSPS	61.44 MSPS	61.44 MSPS
Transmitter Channels	1	2	2
Receivers	1	2	2
Duplex	Half	Full	Full
Interface	USB 2.0	USB 3.0	USB 3.0
Transmit Power	0 to - 10 dBm @ 4 to 6 GHz	6 dBm	0 to 10 dBm based on frequency
Price	£216	£432	£235 (without the LMS8001A up-converter)

Table 5.2: Comparison between three different types of SDRs. The values are obtained from [9, 6, 15].

Thus, we can form two  $T_x$ - $R_x$  pairs using only a single LimeSDR or BladeRF 2.0. Also, both SDRs have an on-board FPGA chip that can be utilized to perform measurements faster than the host computer. A description of both SDRs specifications is in table 5.2.

- LMS8001A: an up-converter for LimeSDR to extend the frequency range to 10 GHz [16].
- 10 dB Attenuator: to improve the impedance matching between the SDR and the directional coupler as explained in [63].
- Directional Coupler: to enable the measurement of the  $S_{11}$  parameter as described in [63].
- RF Switch: to switch between signals received through the Directional Couple/Attenuator path and signals received from the antenna directly to the SDR path. The former path is for the  $S_{11}$  measurements, whereas the latter is for the  $S_{21}$  measurements.
- Servo Motor: to rotate the antennas.
- Host Computer: to deliver power to the components and store/display the results generated by the FPGA chip.
- Battery/Power Bank: to power up the host computer and other components if needed.

We discuss later in §5.3, the design cost and power consumption of the design in figure 5.5.

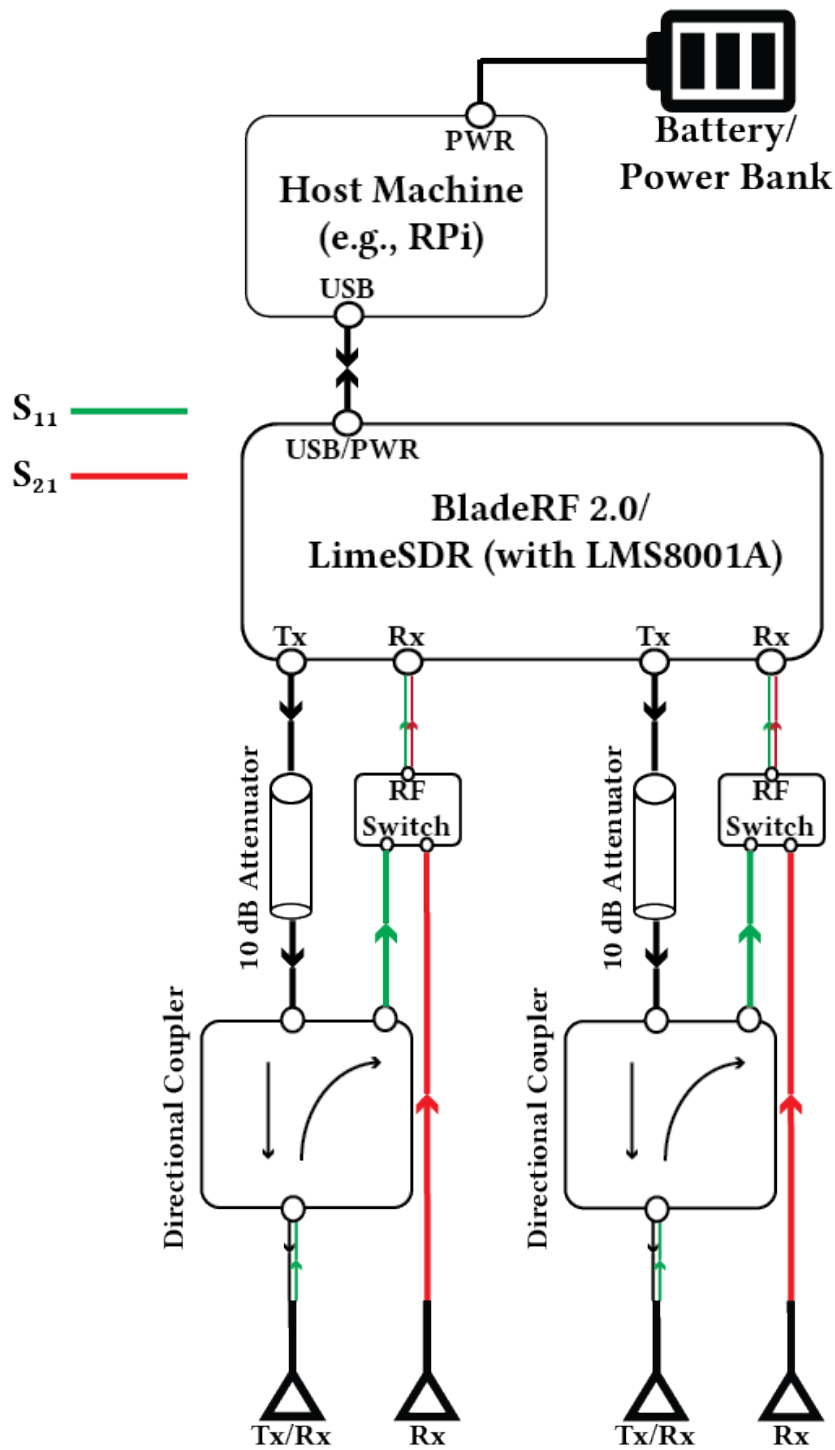


Figure 5.5: A proposed design of outdoor SING using BladeRF 2.0/LimeSDR.

### 5.2.3 Host Computer

Figures 5.4 and 5.5 illustrate proposed designs for outdoor SING. The figures show host computers that control the SDRs and, consequently, the measurement process. After discussing the SDRs in the previous section, we dedicate this section to discuss the host computers' responsibilities and requirements. The host computer responsibilities are:

- Powering up the active components in figures 5.4 and 5.5.
- Performing SING procedure (figure 3.19, §3.2.4) in the absence of an FPGA chip.
- Saving, transferring, and displaying the results (i.e., SING estimations).

Based on those responsibilities, an eligible host computer should meet the following requirements:

- Can be powered from a battery/power bank.
- Has USB 2.0 ports, although a minimum of 3.0 is recommended for a higher data rate.
- A memory card to save the S-parameters measurements and the results.
- Connectivity to transmit the measurements and results to a base station or the cloud (if needed).
- A monitor to display the results (if needed)

Among the different commercial products in the market, the Raspberry Pi family and the BeagleBone Black meet the requirements. The Raspberry Pis and the BeagleBone Black are low-cost and low-power boards and can be employed as host computers in the outdoor SING setup. The Raspberry Pis and the BeagleBone Black are not the only low-cost and low-power devices in the market today that meet the requirements mentioned above. However, they are well-documented in terms of their power consumption and cost. Thus, we choose them to analyze the role of the host computer in the outdoor SING designs in figures 5.4 and 5.5.

	Raspberry Pi 3 Model A+ (RPi3 A+)	Raspberry Pi 3 Model B+ (RPi3 B+)	Raspberry Pi 4 Model B (RPi4 B)	BeagleBone Black (BB)
CPU	1.4 GHz Quad Core ARM Cortex-A53	1.4 GHz Quad Core ARM Cortex-A53	1.5 GHz Quad Core ARM Cortex-A72	1 GHz Cortex-A8 Dual PRU
RAM	512 MB	1 GB	2/4/8 GB	512 MB
USB Ports	1x USB (2.0)	4x USB (2.0)	2x USB (2.0), 2x USB (3.0)	1x USB (2.0)
Ethernet	No	Yes	Yes	Yes
WiFi	Yes (2.4 and 5 GHz)	Yes (2.4 and 5 GHz)	Yes (2.4 and 5 GHz)	No
Bluetooth	Yes	Yes	Yes	No
Power Cons. (Idle)	240 mA	400 mA	575 mA	250 mA
Cost	£23.40	£33.90	£43.50 (2 GB), £54 (4 GB), £73.50 (8 GB)	£40.32

Table 5.3: Comparison between different host machines. The values are obtained from [20, 21, 22, 4].

In table 5.3 we show a comparison between three different Raspberry Pi boards and the BeagleBone Black board.

Now that we have explained all the components of outdoor SING in figures 5.4 and 5.5, we present a flowchart to illustrate the operation steps of outdoor SING in figure 5.6. After powering up, outdoor SING starts by locating clusters either manually or through a special algorithm as mentioned in §5.2.1. After locating a cluster, outdoor SING measures the S-parameters and saves the measurements at a specific angle. The last step is repeated for all remaining angles. After measuring the S-parameters of all angles, outdoor SING estimates the moisture of the cluster as explained in figure 3.19, §3.2.4. Outdoor SING performs the same process again for other clusters. Finally, the yield estimation is presented according to the estimations of all scanned clusters.

## 5.3 Power Consumption and Overall Cost

In this section we discuss the power consumption and overall cost of outdoor SING. Regarding the power consumption, we aim to answer the following question: how many clusters can outdoor SING scans between battery recharges? Since we have discussed three SDRs and four host computers, we perform the power consumption analysis and present the overall cost of the {SDR, Host Computer} configurations in table 5.4.

When analyzing the power consumption for each configuration, we consider the power consumption of the active components as mentioned in table 5.5. For example, in configuration C (LimeSDR, RPi3 A+), we consider the power consumption of the LimeSDR, the up-converter chip (LMS8001A), the Servo motor, and the Raspberry Pi 3 model A+.

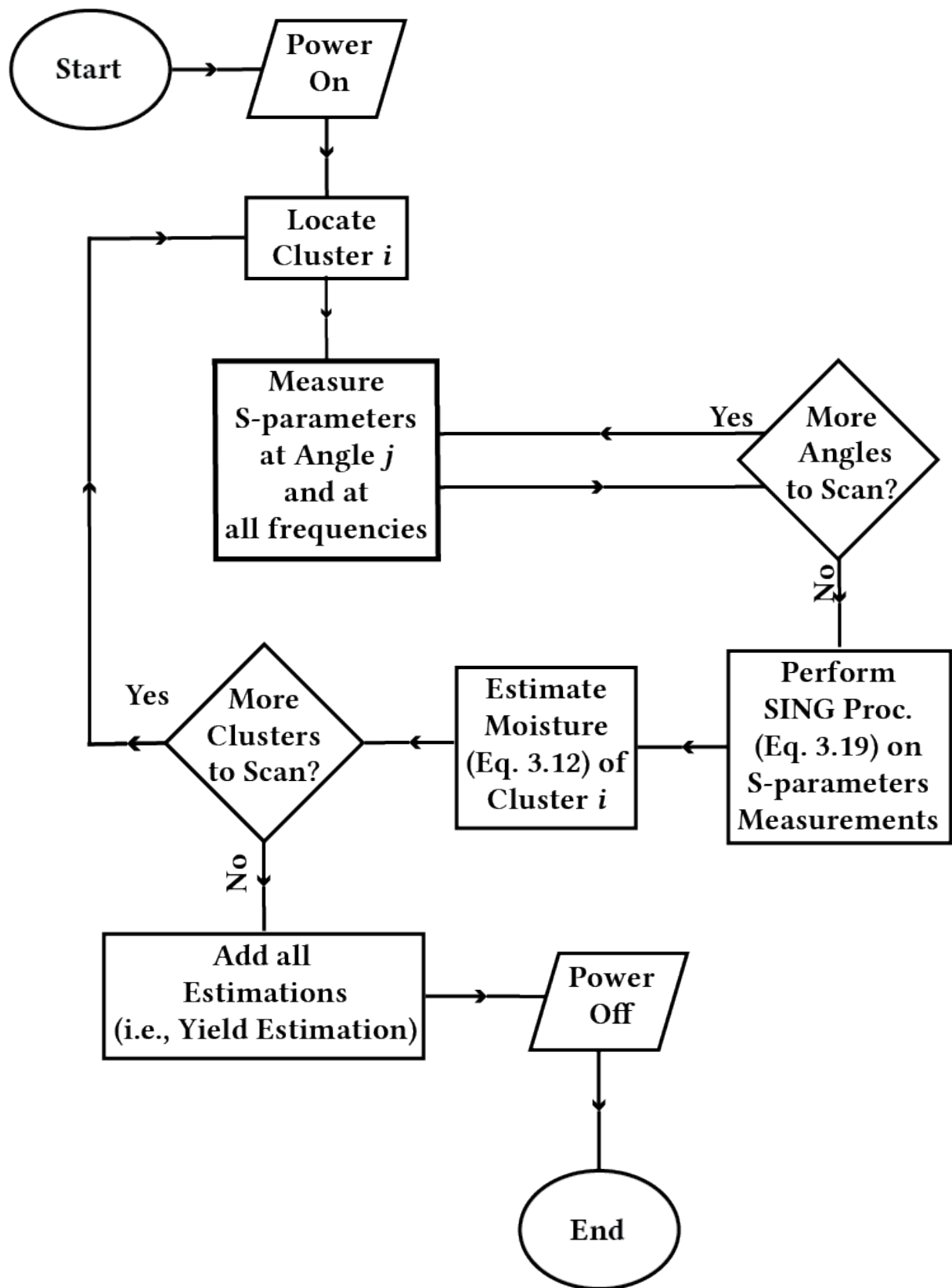


Figure 5.6: Operation flowchart of outdoor SING.

Configuration	SDR	Host Computer
A	HackRF One	Raspberry Pi 3 model A+
B		Raspberry Pi 3 model B+
C		Raspberry Pi 4 model B
D		BeagleBone Black
E	BladeRF 2.0	Raspberry Pi 3 model A+
F		Raspberry Pi 3 model B+
G		Raspberry Pi 4 model B
H		BeagleBone Black
I	LimeSDR	Raspberry Pi 3 model A+
J		Raspberry Pi 3 model B+
K		Raspberry Pi 4 model B
L		BeagleBone Black

Table 5.4: The {SDR, Host Computer} configurations

	Current (A)	Power (W)	Weight (G)
HackRF One (idle)	0.2	1	$\approx 200$
HackRF One ( $T_x$ mode)	0.44	2.2	
HackRF One ( $R_x$ mode)	0.37	1.85	
BladeRF 2.0 (idle)	0.42	2.136	$\approx 360$
BladeRF 2.0 ( $T_x/R_x$ mode)	0.67	3.362	
LimeSDR (idle)	N/A	N/A	$\approx 350$
LimeSDR ( $T_x/R_x$ mode)	0.62	3.1	
LMS8001A	0.25	1.25	N/A
Multiplexer (74HC4051)	.00008	0.0004	6
Frequency Synthesizer (STW81200)	.015	.075	0.1
Raspberry Pi 3 Model A+	.335	1.675	45
Raspberry Pi 3 Model B+	.530	2.65	45
Raspberry Pi 4 Model B	.675	3.375	46
Beaglebone Black	.390	1.95	40
Servo Motor (idle) (HS-425BB)	.150	0.75	45
Servo Motor (stall) (HS-425BB)	.8	4	

Table 5.5: Typical power consumption and weight of the active components in figures 5.4 and 5.5, and the servo motor required to rotate the antennas. The values are obtained from [10, 7, 17, 23, 5, 26, 11, 1]



	Single Scan Power Consumption	
Configuration	Current (A)	Power (W)
A	1.26	6.30
B	1.45	7.25
C	1.60	8.00
D	1.31	6.55
E	1.16	5.80
F	1.35	6.75
G	1.50	7.50
H	1.21	6.05
I	1.35	6.75
J	1.55	7.75
K	1.69	8.45
L	1.41	7.05

Table 5.6: The typical current and power consumption for each configuration.

From the values in table 5.5, the power consumption of a single scan for each configuration is presented in table 5.6.  $\text{current}_{\text{single-scan}}$  is the current consumption of scanning a single angle or two angles for configurations with HackRF One or LimeSDR/BladeRF 2.0, respectively. Since the LimeSDR and BladeRF 2.0 are full-duplex SDRs, we can scan two angles simultaneously. Table 5.6 enables us to compute the maximum (theoretical) number of scanned clusters ( $\text{cluster}_{\text{max}}$ ) between battery recharges for each configuration. To do so, we refer to equation 5.3 that computes  $\text{cluster}_{\text{max}}$  for a given number of angles per cluster ( $\text{angle}_{\text{num}}$ ), a power bank capacity ( $\text{battery}_{\text{cap}}$ ), and the time to perform a single scan ( $\text{single-scan}_{\text{sec}}$ ). Note that  $\text{operation-time}_{\text{sec}}$  is the battery operation time in seconds before requiring a recharge.

$$\begin{aligned}
\text{operation-time}_{\text{sec}} &= \frac{\text{battery}_{\text{cap}}}{\text{current}_{\text{single-scan}}} * 60^2 \\
\text{single-cluster}_{\text{sec}} &= \text{angle}_{\text{num}} * \text{single-scan}_{\text{sec}} \\
\text{cluster}_{\text{max}} &= \frac{\text{operation-time}_{\text{sec}}}{\text{single-cluster}_{\text{sec}}}
\end{aligned} \tag{5.3}$$

To present an example based on equation 5.3, we assume the following inputs:

- $\text{battery}_{\text{cap}} = 20,000 \text{ mAh}$

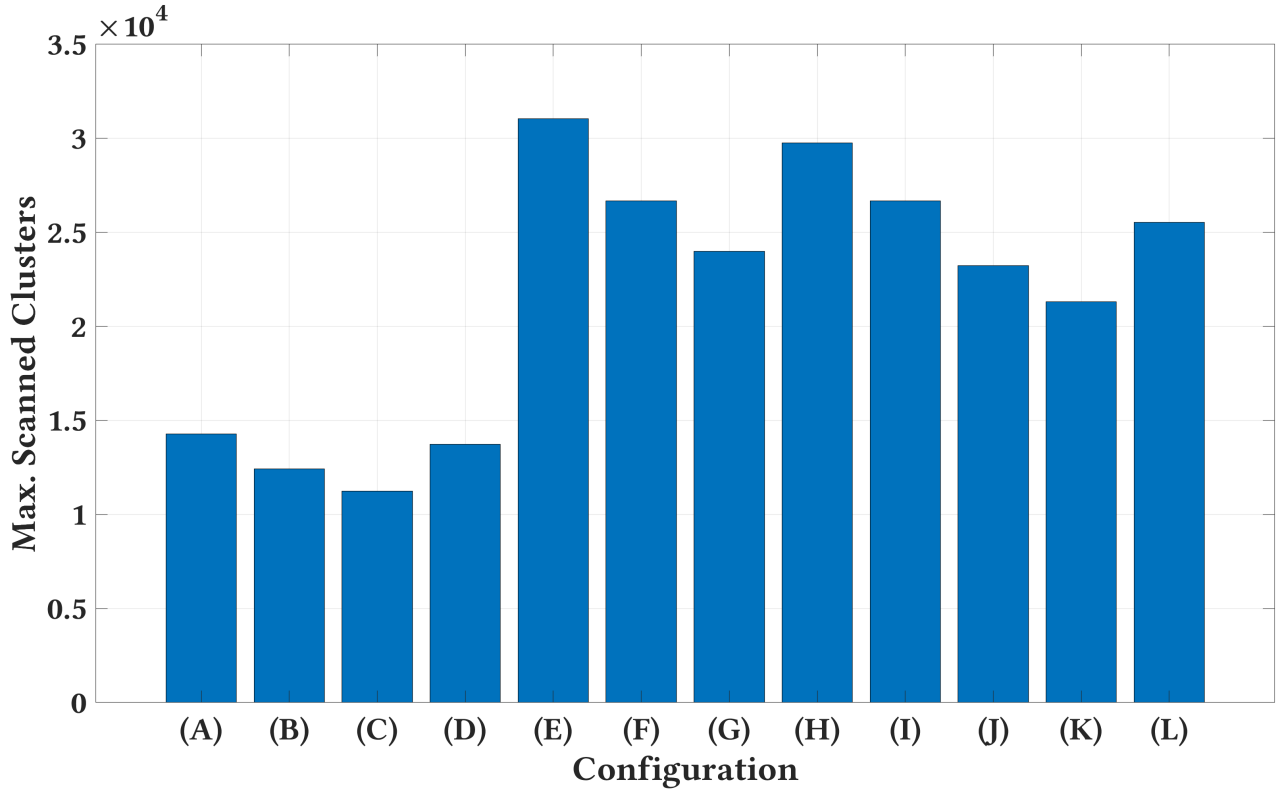


Figure 5.7: Maximum scanned clusters for each {SDR, Host Computer} configuration.

- $\text{angle}_{\text{num}} = 4$  angles.
- $\text{single-scan}_{\text{sec}} = 1$  sec

Based on those values, we present figure 5.7 that shows the theoretical  $\text{cluster}_{\text{max}}$  value of the 12 configurations mentioned in table 5.4. From the figure, we notice that BladeRF 2.0 outperforms the other two SDRs because of the  $\text{current}_{\text{single-scan}}$  lower value of the former compared to the latter as shown in table 5.6. Although HackRF One and LimeSDR alone consume less power than the BladeRF 2.0 (table 5.5), they consume more power when considering the power consumption of other components in figures 5.4 and 5.5. HackRF One performs the worst because we require two of them to measure the S-parameters as opposed to the other two SDRs. Compared to the other host computers, the Raspberry Pi 3 model A+ and the BeagleBone Black deliver more scanned clusters due to their low power consumption. Thus, configuration E (BladeRF 2.0, RPi3A+) delivers the highest  $\text{cluster}_{\text{max}}$  in the figure. Finally, the figure shows that SDRs have more impact on  $\text{cluster}_{\text{max}}$  than the host computers. This is due to the low power consumption of the host computers compared to the SDRs as evident by table 5.5.

Configuration	Cost (£)	Extra Cost (£)
A	$\approx 921$	+ Power Bank/Battery cost
B	$\approx 932$	
C (RPi4B RAM = 2 GB)	$\approx 941$	
C (RPi4B RAM = 4 GB)	$\approx 952$	
C (RPi4B RAM = 8 GB)	$\approx 971$	
D	$\approx 938$	
E	$\approx 898$	
F	$\approx 909$	
G (RPi4B RAM = 2 GB)	$\approx 918$	
G (RPi4B RAM = 4 GB)	$\approx 929$	
G (RPi4B RAM = 8 GB)	$\approx 948$	
H	$\approx 915$	+ Power Bank/Battery cost + up-converter (LMS8001A) cost
I	$\approx 701$	
J	$\approx 712$	
K (RPi4B RAM = 2 GB)	$\approx 721$	
K (RPi4B RAM = 4 GB)	$\approx 732$	
K (RPi4B RAM = 8 GB)	$\approx 751$	
L	$\approx 718$	

Table 5.7: The cost of the 12 configurations.

After discussing the power consumption, we present the overall cost of the 12 configurations in table 5.7. For the antennas, we consider the same antennas we employed in SING §3.2.1. For the LimeSDR, the cost of the up-converter (LMS8001A) is unfortunately not published yet. As can be seen from the table, the cost of each configuration is below £1000. This cost is significantly low considering the fact that VNAs can cost more than £100K [14].

Before concluding this chapter, we refer back to the discussion about the drone's ability to fly while carrying outdoor SING from §5.2.1. To further discuss this, we refer to table 5.8, which shows the potential weight of the 12 configurations. From the table, we notice that configuration G (BladeRF 2.0, RPi4B) is the heaviest. Adding the weights of the antennas and the power bank, the maximum weight for outdoor SING does not exceed 2Kg. Some of the mid-range professional commercial drones in the market can carry up to 6Kg of load [18]. This is sufficient enough to carry outdoor SING without affecting the drone's ability to fly.

This concludes the discussion about outdoor SING. In this chapter, we discussed the specifications and requirements to transform SING into a technology applicable for real-world scenarios. We proposed several designs and explained the role of each component in the design. In the

Configuration	Weight (G)	Extra Weight
A	296.0	+ Antenna's weight + Power Bank/Battery's weight
B	296.0	
C	297.0	
D	291.0	
E	456.0	
F	456.0	
G	457.0	
H	451.0	
I	446.0	
J	446.0	
K	447.0	
L	441.0	

Table 5.8: The approximate weight of the 12 configurations

end, we analyzed the power consumption and presented the overall cost of the proposed designs.

In the next chapter, we present final remarks about SING and discuss future work.

# Chapter 6

## Conclusion and Beyond

### 6.1 Thesis Summary

In this thesis, we investigated the usefulness of RF Sensing as a technology to achieve precision agriculture. Specifically, We have successfully methodized and tested SING; a model to estimate moisture content in grape clusters through RF Sensing. Before introducing SING, we started with Chapter 2, where we presented a primer on the dielectric properties and their measuring techniques. Then, we discussed related work in the field of precision agriculture, RF Sensing, realizing precision agriculture through RF Sensing. Afterwards, we showed the current practice to estimate moisture in grape clusters and estimate discussed previous work related to that. We concluded the chapter by showing a comparison between the key papers reviewed in the chapter and SING in table 2.2.

After Chapter 2, we introduced SING in Chapter 3. In that chapter, we illustrated how SING leverages the the dielectric properties of grapes to estimate their moisture content. We started the chapter by highlighting the connection between the dielectric properties ( $\epsilon^*$ ) and the extinction coefficient ( $\kappa$ ), and how to estimate the moisture content from  $\epsilon^*$  through  $\kappa$ . Also, we have successfully emphasized the monotonic relationship between  $\kappa$  and the three independent variables in the moisture predictive model (Eq. 3.2.2, §3.2) through theory and experiments.

The monotonic relationship is an important factor to promote our choice of linear regression as a model for our data. In addition, we explained through careful analysis why the 5 GHz band is suitable for SING.

After justifying the choice of the linear regression and the frequency band, the chapter continues by explaining the operation of SING. SING works by “scanning” grape clusters from different angles and employs - through careful analysis and investigation - a mathematical model that uses the output of the scanning to estimate the moisture content in clusters to a high degree of accuracy. What makes SING efficient is its tolerance to the non-uniformity of grape clusters and the simplicity of its design. Grape clusters are non-uniform - geometrically -, thus, existing moisture estimation techniques - as illustrated throughout Chapters 2 and 3 - cannot cope with the challenges imposed by such geometry. Instead, they resort to employing fixtures and destructively remove samples, such as grapes, from their natural place and pour them into the fixtures to estimate the moisture content.

The destructive nature and impracticality of using fixtures emphasize the other trait of SING; the simplicity and feasibility of its design. SING does not require fixtures as a consequence of introducing the notion of *relative thickness*. This notion allow us to forgo measuring the physical thickness of clusters - hence the use of fixtures in previous related work - and instead relate the thickness to the beamwidth of employed antennas. Thus, SING does not require the grape clusters to be removed from the canopy to estimate the moisture content correctly. In fact, SING’s is only composed of a pair of antennas, a radio frequency transceiver, and a mechanism to scan clusters from multiple angles. This design makes SING attractive for outdoor deployment (Chapter 5), where the moisture content of grape clusters can be estimated accurately and continuously in the non-invasive fashion of RF Sensing. We concluded Chapter 3 by investigating different factors that may affect SING’s accuracy. Specifically, we presented a detailed analysis of both the diffraction effect and the impact of foliage on SING’s accuracy. Regarding the former, we concluded that the accuracy is intact due to the shape of the grapes. Similarly, the latter does not affect SING’s accuracy due to SING’s operation frequency.

After introducing SING in Chapter 3, we evaluated SING’s performance in Chapter 4. In the chapter, we started by choosing training and validation sets for the moisture and thickness regression models through 3-Fold and 5-Fold Cross-Validations. Then, we introduced the term *Angle Combination*, through which we defined different criteria to evaluate SING’s performance. The criteria cover different aspects from merely increasing the number of scanned angles to choosing the location of those angles. We reached to the conclusion that scanning a cluster at different locations affects SING’s accuracy more significantly than merely increasing the number of scanned angles. We concluded the chapter by reporting preliminary results from an experiment in a vineyard.

After presenting SING in Chapter 3 and evaluating its performance in Chapter 4, a natural next step in this thesis is to deploy SING in a vineyard to assess its shortcomings and advantages. Unfortunately, the emergence of COVID-19 as a global pandemic prevented us from deploying SING in vineyards. Thus, we decided to dedicate Chapter 5 to address the requirements needed to transform SING from a lab-based system to a system working reliably out in the fields, which we refer to as *outdoor SING*. In the chapter, we highlighted some of the challenges that outdoor SING might suffer from such as the high power consumption of VNAs and the distance between the antennas. We proposed solutions for those problems and offer different design options for outdoor SING. We explained the advantages and disadvantages of each design option and describe the role of each component in those designs. We concluded the chapter by tabulating the power consumption and the cost of the different design options. We believe the work accomplished in Chapter 5 represents a roadmap to help guide the process of deploying SING into real-world scenarios.

The three chapters (i.e., Chapter 3, 4, and 5) represent the core chapters of this thesis. In the next section, we introduce different improvements and directions for SING.

## 6.2 Future of SING

Although SING is an RF Sensing technology, we believe that we can improve SING by incorporating different technologies along with RF Sensing. For example, in Chapter 2, we reviewed different work that utilize computer vision to estimate the moisture content in grapes. Although we have mentioned the drawbacks of this approach, we also recognize the potentials of utilizing images along with RF readings to improve SING. In fact, in Chapter 5, we discussed different deployment options including drones and robots (§5.2.1). Both of those devices have cameras in-board. Thus, we can re-purpose SING to benefit from computer vision along with RF Sensing. One example is related to sugar weight. To explain, in the moisture regression model (Eq.3.10, §3.2.2), one of the independent variables is the sugar weight. As we have explained in §3.2.2, the sugar's concentration (and eventually, sugar's weight) is obtained through a refractometer. On the surface, this may seem intrusive; however, viticulturists regularly take sugar measurements for quality control purposes, and those measurements can parameterize our solution [37, 85]. Nevertheless, we can relate the absorption of RF signals, shape detection algorithms through computer vision, and the heuristic data of clusters' weight [107, 125], to obtain reliable estimation of cluster's weight. From which, sugar's weight can be realized.

Moving away from grapes, we believe SING's approach is not specific to grapes. Although, some aspects of SING are indeed tailored to grapes, like how SING deals with the shape of grape clusters. However, a main feature of SING is to utilize the interaction between water and RF signals. Water is the main component in many agricultural products. We believe we can alter SING to work on those products without substantial changes to SING's methodology. Of course, different products have different characteristics that need to be considered when employing SING on them. For example, the orange rind (i.e., the outer layer of an orange) is significantly different from the grape skin. Grapes skin are thin, whereas oranges rind are thick. When dealing with the cm waves of the 5 GHz band, the thickness of the outer layers could affect the signals significantly in terms of attenuation and phase shift. However, once those characteristics are considered, we believe SING can deliver accurate moisture content



estimations similar to that of grapes.

Outside precision agriculture, we have shown that a SING-like scheme has the potentials to work in other domains such as the health domain. We believe one reason behind SING's approach versatility is the ability to "scan" an object from different angles and "stitch" those measurements together to provide a meaningful "image" of that object; similar to CT scans where a 360-degree image of an internal organ is captured to provide more information about those organs [55]. However, unlike CT scans which are created by combining a series of x-ray views [55], SING's approach relies on combining a series of *RF images* to analyze objects. By an RF image, we refer to objects response to RF signals travelling through them from a certain angle. Those images provide information about the characteristics of the objects, such as the dielectric properties that SING utilizes to infer other characteristics such as the moisture content. Thus, a future direction is to investigate how we can utilize those images captured by SING to work on other traits such as blood glucose levels in a patient.

In industry, we can exploit the RF images to monitor machines' health, for example. A deficit in a machine can be identified by recognizing abnormality in the operation of its mechanical components. For instance, a sign of malfunction in a motor can be a sudden change in its rotation speed or vibration. We can exploit the RF images to recognize patterns, especially in the phase shift, to monitor the rotation speed or vibration. Sudden and unexplained changes to those patterns may indicate a malfunction in the motor. Thus, a SING-like scheme using multiple RF images generated from multiple angles can work on industrial applications as well.

The above is some of the possible applications for SING. We realise that employing SING in some applications, such as detecting blood glucose levels, requires more effort than estimating the moisture content in a different agriculture product. However, we believe that this thesis provides enough evidence to prove the ability of SING to work on those applications as well.

# Bibliography

- [1] 8-channel analog multiplexer/demultiplexer. [https://assets.nexperia.com/documents/data-sheet/74HC\\_HCT4051.pdf](https://assets.nexperia.com/documents/data-sheet/74HC_HCT4051.pdf). Accessed: Nov 16, 2021.
- [2] Agilent 85070e dielectric probe kit 200 mhz to 50 ghz. <https://www.imperial.ac.uk/media/imperial-college/research-centres-and-groups/centre-for-bio-inspired-technology/11949699.PDF>. Accessed: Mar. 10, 2019.
- [3] Arduino uno datasheet. <https://store.arduino.cc/arduino-uno-rev3>. Accessed: Aug. 1, 2018.
- [4] Beaglebone black. <https://beagleboard.org/black>. Accessed: Nov 20, 2021.
- [5] Beaglebone black power consumption. <https://learn.adafruit.com/embedded-linux-board-comparison/power-usage>. Accessed: Dec 6, 2021.
- [6] Bladerf 2.0 micro. <https://www.nuand.com/bladerf-2-0-micro/>. Accessed: Nov 15, 2021.
- [7] Bladerf power consumption. <https://github.com/Nuand/bladeRF/wiki/bladeRF-Power-Consumption>. Accessed: Dec 3, 2021.
- [8] E8361a pna network analyzer, 10 mhz to 67 ghz. <https://literature.cdn.keysight.com/litweb/pdf/5988-7988EN.pdf?id=1000084422:epsg:dow>. Accessed: Mar. 10, 2019.
- [9] Hackrf one from great scott gadgets. <https://greatscottgadgets.com/hackrf/one/>. Accessed: Jun. 6, 2018.

- [10] Hackrf one power consumption. [https://github.com/scateu/hackrf.net/blob/master/\\_posts/2014-03-21-hackrf-one-power-consumption.md](https://github.com/scateu/hackrf.net/blob/master/_posts/2014-03-21-hackrf-one-power-consumption.md). Accessed: Dec 3, 2021.
- [11] Hs-425bb deluxe ball bearing standard servo. <https://hitecrd.com/products/servos/analog/sport-2/hs-425bb/product>. Accessed: Dec 5, 2021.
- [12] Ir 2030 – uk interface requirements 2030 - licence exempt short range devices. [https://www.ofcom.org.uk/\\_\\_data/assets/pdf\\_file/0028/84970/ir-2030.pdf](https://www.ofcom.org.uk/__data/assets/pdf_file/0028/84970/ir-2030.pdf). Accessed: Jan. 15, 2019.
- [13] Kern 32ba analog refractometer. <https://docs-emea.rs-online.com/webdocs/1686/0900766b816867a0.pdf>. Accessed: Feb. 22, 2019.
- [14] Keysight 2-port and 4-port pna-x network analyzer. <https://www.keysight.com/zz/en/assets/9018-04523/data-sheets/9018-04523.pdf>. Accessed: Aug. 1, 2020.
- [15] Limesdr. <https://limemicro.com/products/boards/limesdr/>. Accessed: Nov 16, 2021.
- [16] Limesdr lms8001a. <https://limemicro.com/products/boards/lms8001-companion/>. Accessed: Nov 16, 2021.
- [17] Limesdr power consumption. <https://discourse.myriadrf.org/t/power-consumption/448>. Accessed: Dec 3, 2021.
- [18] Matrice 600 pro. [https://dl.djicdn.com/downloads/m600pro/1208EN/Matrice\\_600\\_Pro\\_User\\_Manual\\_v1.0\\_EN\\_1208.pdf](https://dl.djicdn.com/downloads/m600pro/1208EN/Matrice_600_Pro_User_Manual_v1.0_EN_1208.pdf). Accessed: Feb 2, 2022.
- [19] Project soli- google atap. <https://atap.google.com/soli/>. Accessed: Oct. 12, 2020.
- [20] Raspberry pi 3 model a+. <https://www.raspberrypi.com/products/raspberry-pi-3-model-a-plus/>. Accessed: Nov 20, 2021.
- [21] Raspberry pi 3 model b+. <https://www.raspberrypi.com/products/raspberry-pi-3-model-b-plus/>. Accessed: Nov 20, 2021.

- [22] Raspberry pi 4 model b. <https://www.raspberrypi.com/products/raspberry-pi-4-model-b/>. Accessed: Nov 20, 2021.
- [23] Raspberry pi boards power consumption. <https://raspi.tv/2019/how-much-power-does-the-pi4b-use-power-measurements>. Accessed: Dec 6, 2021.
- [24] Ridgeview Vineyard. <http://www.ridgeview.co.uk/>.
- [25] Sencity®spot-s wifi antenna 1356.19.0022. <https://ecatalog.hubersuhner.com/media/documents/datasheet/en/pdf/84059621>. Accessed: Mar. 1, 2019.
- [26] Stw81200 wide band frac-integer-n integrated synthesizer. <https://estore.st.com/en/stw81200t-cpn.html>. Accessed: Nov 16, 2021.
- [27] H. Abdi and L. J. Williams. Principal component analysis. *Wiley interdisciplinary reviews: computational statistics*, 2(4):433–459, 2010.
- [28] F. Adib, H. Mao, Z. Kabelac, D. Katabi, and R. C. Miller. Smart homes that monitor breathing and heart rate. In *Proceedings of the 33rd annual ACM conference on human factors in computing systems*, pages 837–846, 2015.
- [29] S. Arshad, C. Feng, I. Elujide, S. Zhou, and Y. Liu. Safedrive-fi: A multimodal and device free dangerous driving recognition system using wifi. In *2018 IEEE International Conference on Communications (ICC)*, pages 1–6. IEEE, 2018.
- [30] Y. Bai, Z. Wang, K. Zheng, X. Wang, and J. Wang. Widrive: Adaptive wifi-based recognition of driver activity for real-time and safe takeover. In *2019 IEEE 39th International Conference on Distributed Computing Systems (ICDCS)*, pages 901–911. IEEE, 2019.
- [31] S. Balaghi, N. Ghal-Eh, A. Mohammadi, and H. Vega-Carrillo. A neutron scattering soil moisture measurement system with a linear response. *Applied Radiation and Isotopes*, 142:167–172, 2018.
- [32] C. A. Balanis. *Advanced engineering electromagnetics*. John Wiley & Sons, 1999.

- [33] C. A. Balanis. *Antenna theory: analysis and design*. John wiley & sons, 2016.
- [34] J. Bell. Neutron probe practice. 1987.
- [35] P. Bhadani and V. Vashisht. Soil moisture, temperature and humidity measurement using arduino. In *2019 9th International Conference on Cloud Computing, Data Science & Engineering (Confluence)*, pages 567–571. IEEE, 2019.
- [36] A. A. Bhosale. Detection of sugar content in citrus fruits by capacitance method. *Procedia Engineering*, 181:466–471, 2017.
- [37] D. Bird. *Understanding wine technology: the science of wine explained*. Board and Bench Publishing, 2011.
- [38] B. I. Bleaney, B. I. Bleaney, and B. Bleaney. *Electricity and Magnetism, Volume 2*, volume 2. Oxford University Press, 2013.
- [39] P. E. Blom and J. M. Tarara. Trellis tension monitoring improves yield estimation in vineyards. *HortScience*, 44(3):678–685, 2009.
- [40] B. Bogert. Demonstration of delay distortion correction by time-reversal techniques. *IRE Transactions on Communications Systems*, 5(3):2–7, 1957.
- [41] C.-I. Chang. *Hyperspectral imaging: techniques for spectral detection and classification*, volume 1. Springer Science & Business Media, 2003.
- [42] Y. Chen, R. Ou, Z. Li, and K. Wu. Wiface: Facial expression recognition using wi-fi signals. *IEEE Transactions on Mobile Computing*, 2020.
- [43] A. Chowdhury, T. Bera, D. Ghoshal, and B. Chakraborty. Studying the electrical impedance variations in banana ripening using electrical impedance spectroscopy (eis). In *Proceedings of the 2015 Third International Conference on Computer, Communication, Control and Information Technology (C3IT)*, pages 1–4. IEEE, 2015.
- [44] P. R. Clingeleffer, S. Martin, G. Dunn, and M. Krstic. Crop development, crop estimation and crop control to secure quality and production of major wine grape varieties: a national

- approach: final report to grape and wine research & development corporation/principal investigator, peter clingeffer;[prepared and edited by steve martin and gregory dunn]. 2001.
- [45] L. Coviello, M. Cristoforetti, G. Jurman, and C. Furlanello. Gbcnet: In-field grape berries counting for yield estimation by dilated cnns. *Applied Sciences*, 10(14):4870, 2020.
- [46] P. Dangeti. *Statistics for machine learning*. Packt Publishing Ltd, 2017.
- [47] A. Dhekne, M. Gowda, Y. Zhao, H. Hassanieh, and R. R. Choudhury. Liquid: A wireless liquid identifier. In *Proceedings of the 16th Annual International Conference on Mobile Systems, Applications, and Services*, pages 442–454, 2018.
- [48] J. Ding and R. Chandra. Towards low cost soil sensing using wi-fi. In *The 25th Annual International Conference on Mobile Computing and Networking*, pages 1–16, 2019.
- [49] J. Ding and Y. Wang. Wifi csi-based human activity recognition using deep recurrent neural network. *IEEE Access*, 7:174257–174269, 2019.
- [50] N. R. Draper and H. Smith. *Applied regression analysis*, volume 326. John Wiley & Sons, 2014.
- [51] G. M. Dunn and S. R. Martin. Yield prediction from digital image analysis: A technique with potential for vineyard assessments prior to harvest. *Australian Journal of Grape and Wine Research*, 10(3):196–198, 2004.
- [52] J. P. Dunsmore. *Handbook of microwave component measurements: with advanced VNA techniques*. John Wiley & Sons, 2020.
- [53] C. Escriba, E. G. Aviña Bravo, J. Roux, J.-Y. Fourniols, M. Contardo, P. Acco, and G. Soto-Romero. Toward smart soil sensing in v4. 0 agriculture: A new single-shape sensor for capacitive moisture and salinity measurements. *Sensors*, 20(23):6867, 2020.
- [54] D. Fan and J. Xue. The design of intelligent automatic test system for wood moisture content test. In *2010 International Conference On Computer Design and Applications*, volume 3, pages V3–314. IEEE, 2010.

- [55] T. Farncombe and K. Iniewski. *Medical imaging: technology and applications*. CRC Press, 2017.
- [56] J. F. Federici, R. L. Wample, D. Rodriguez, and S. Mukherjee. Application of terahertz gouy phase shift from curved surfaces for estimation of crop yield. *Applied Optics*, 48(7):1382–1388, 2009.
- [57] J. I. Fernandez-Golfin Seco, M. Conde García, F. Gonzalez Hernandez, M. Conde García, J. J. Fernandez-Golfin Seco, V. Baonza Merino, L. García Esteban, and J. R. Gonzalez Adrados. The influence of the moisture content on the electrical resistance of two types of cork stoppers. *Forest Systems*, 19(2):184–188, 2010.
- [58] K. Finkenzeller. *RFID handbook: fundamentals and applications in contactless smart cards, radio frequency identification and near-field communication*. John wiley & sons, 2010.
- [59] D. K. Ghodgaonkar, V. V. Varadan, and V. K. Varadan. A free-space method for measurement of dielectric constants and loss tangents at microwave frequencies. *IEEE Transactions on Instrumentation and measurement*, 38(3):789–793, 1989.
- [60] A. P. Gregory and R. Clarke. Tables of the complex permittivity of dielectric reference liquids at frequencies up to 5 ghz. 2012.
- [61] D. J. Griffiths. *Introduction to electrodynamics*. Cambridge University Press, 2017.
- [62] M. Grossetete, Y. Berthoumieu, J.-P. Da Costa, C. Germain, O. Lavialle, G. Grenier, et al. Early estimation of vineyard yield: site specific counting of berries by using a smartphone. In *International Conference of Agricultural Engineering—CIGR-AgEng*, 2012.
- [63] D. N. Grujić, P. Jovanović, and M. Savić. Using software defined radio for rf measurements. In *2017 Zooming Innovation in Consumer Electronics International Conference (ZINC)*, pages 18–21. IEEE, 2017.
- [64] B. D. Guenther. *Modern optics*. OUP Oxford, 2015.

- [65] U. Ha, S. Assana, and F. Adib. Contactless seismocardiography via deep learning radars. In *Proceedings of the 26th Annual International Conference on Mobile Computing and Networking*, pages 1–14, 2020.
- [66] S. Haykin and M. Moher. *Introduction to analog and digital communications*. Wiley, 2007.
- [67] D. Henry, H. Aubert, and T. Véronèse. Proximal radar sensors for precision viticulture. *IEEE Transactions on Geoscience and Remote Sensing*, 57(7):4624–4635, 2019.
- [68] M. Hessar, A. Najafi, V. Iyer, and S. Gollakota. Tinysdr: Low-power {SDR} platform for over-the-air programmable iot testbeds. In *17th {USENIX} Symposium on Networked Systems Design and Implementation ({NSDI} 20)*, pages 1031–1046, 2020.
- [69] D. Holslin, V. Verbinski, and L. Foster. Moisture probe using neutron moderation for puo 2 canister inspection. *Transactions of the American Nuclear Society*, 77:147–148, 1997.
- [70] F. Içier and T. Baysal. Dielectrical properties of food materials—2: Measurement techniques. *Critical reviews in food science and nutrition*, 44(6):473–478, 2004.
- [71] A. Ishimaru. *Wave propagation and scattering in random media*, volume 2. Academic press New York, 1978.
- [72] C. Jiang, J. Guo, Y. He, M. Jin, S. Li, and Y. Liu. mmvib: micrometer-level vibration measurement with mmwave radar. In *Proceedings of the 26th Annual International Conference on Mobile Computing and Networking*, pages 1–13, 2020.
- [73] Y. Jin, W.-S. Soh, and W.-C. Wong. Indoor localization with channel impulse response based fingerprint and nonparametric regression. *IEEE Transactions on Wireless Communications*, 9(3):1120–1127, 2010.
- [74] S. Julrat and S. Trabelsi. Measuring dielectric properties for sensing foreign material in peanuts. *IEEE Sensors Journal*, 19(5):1756–1766, 2018.
- [75] U. Kaatze. Complex permittivity of water as a function of frequency and temperature. *Journal of Chemical and Engineering Data*, 34(4):371–374, 1989.



- [76] C. J. Kaiser. *The capacitor handbook*. Springer Science & Business Media, 2012.
- [77] C. Kandala and S. Nelson. Measurement of moisture content in single kernels of peanuts: a nondestructive electrical method. *Transactions of the ASAE*, 33(2):567–0571, 1990.
- [78] C. V. Kandala. Moisture determination in single peanut pods by complex rf impedance measurement. *IEEE Transactions on instrumentation and measurement*, 53(6):1493–1496, 2004.
- [79] C. V. Kandala and S. O. Nelson. Rf impedance method for estimating moisture content in small samples of in-shell peanuts. *IEEE Transactions on Instrumentation and Measurement*, 56(3):938–943, 2007.
- [80] C. V. Kandala and J. Sundaram. Nondestructive measurement of moisture content using a parallel-plate capacitance sensor for grain and nuts. *IEEE Sensors Journal*, 10(7):1282–1287, 2010.
- [81] C. V. Kandala and J. Sundaram. Nondestructive moisture sensing in peanuts by nir reflectance. In *2010 IEEE Sensors Applications Symposium (SAS)*, pages 149–153. IEEE, 2010.
- [82] A. Khamis, B. Kusy, C. T. Chou, M.-L. McLaws, and W. Hu. Rfwash: a weakly supervised tracking of hand hygiene technique. In *Proceedings of the 18th Conference on Embedded Networked Sensor Systems*, pages 572–584, 2020.
- [83] M. Kotaru, K. Joshi, D. Bharadia, and S. Katti. Spotfi: Decimeter level localization using wifi. In *Proceedings of the 2015 ACM Conference on Special Interest Group on Data Communication*, pages 269–282, 2015.
- [84] P. Kurtser, O. Ringdahl, N. Rotstein, R. Berenstein, and Y. Edan. In-field grape cluster size assessment for vine yield estimation using a mobile robot and a consumer level rgb-d camera. *IEEE Robotics and Automation Letters*, 5(2):2031–2038, 2020.
- [85] B. Lewin. *Wine Myths and Reality*. Vendange Press Dover, UK, 2010.

- [86] L. Li, Z. Wen, and Z. Wang. Outlier detection and correction during the process of groundwater level monitoring base on pauta criterion with self-learning and smooth processing. In *Theory, methodology, tools and applications for modeling and simulation of Complex systems*, pages 497–503. Springer, 2016.
- [87] M. Mehdizadeh. *Microwave/RF applicators and probes: for material heating, sensing, and plasma generation*. William Andrew, 2015.
- [88] A. Meigh and B. Skipp. Gamma-ray and neutron methods of measuring soil density and moisture. *Geotechnique*, 10(3):110–126, 1960.
- [89] R. E. Mudgett. Developments in microwave food processing. *Schwartzberg, HG and Rao, MA, BioTechnology and Food Process Engineering, Marcel Dekker, New York*, pages 359–404, 1990.
- [90] C. M. O. Muvianto, K. Yuniarto, S. Ariessaputra, B. Darmawan, M. Yadnya, and A. Rachman. Detection of sugar content in mango fruit using coaxial cavity resonator. In *Proceedings International Conference on Science and Technology (ICST)*, volume 1, 2020.
- [91] S. Nelson, W. Forbus, K. Lawrence, et al. Microwave permittivities of fresh fruits and vegetables from 0.2 to 20 ghz. *Transactions of the ASAE*, 37(1):183–189, 1994.
- [92] P. Nguyen, V. Kakaraparthi, N. Bui, N. Umamahesh, N. Pham, H. Truong, Y. Guddeti, D. Bharadia, R. Han, E. Frew, et al. Dronescale: drone load estimation via remote passive rf sensing. In *Proceedings of the 18th Conference on Embedded Networked Sensor Systems*, pages 326–339, 2020.
- [93] S. Nuske, S. Achar, T. Bates, S. Narasimhan, and S. Singh. Yield estimation in vineyards by visual grape detection. In *2011 IEEE/RSJ International Conference on Intelligent Robots and Systems*, pages 2352–2358. IEEE, 2011.
- [94] S. Nuske, K. Wilshusen, S. Achar, L. Yoder, S. Narasimhan, and S. Singh. Automated visual yield estimation in vineyards. *Journal of Field Robotics*, 31(5):837–860, 2014.

- [95] F. W. Olver, D. W. Lozier, R. F. Boisvert, and C. W. Clark. *NIST handbook of mathematical functions hardback and CD-ROM*. Cambridge university press, 2010.
- [96] C. Pasquini. Near infrared spectroscopy: fundamentals, practical aspects and analytical applications. *Journal of the Brazilian chemical society*, 14:198–219, 2003.
- [97] A. Patel, J. Aparicio, N. Tas, M. Loiacono, and J. Rosca. Assessing communications technology options for smart grid applications. In *2011 IEEE International Conference on Smart Grid Communications (SmartGridComm)*, pages 126–131. IEEE, 2011.
- [98] R. R. Pethig. *Dielectrophoresis: Theory, methodology and biological applications*. John Wiley & Sons, 2017.
- [99] R. Peynman, R. Leighton, and M. Sands. The feynman lectures on physics vol. ii. 1964.
- [100] F. J. Pierce and P. Nowak. Aspects of precision agriculture. *Advances in agronomy*, 67:1–85, 1999.
- [101] J. L. Qin, D. Rundquist, A. Gitelson, M. Steele, C. Harkins, and R. Briles. A non-linear model for measuring grapevine leaf thickness by means of red-edge/near-infrared spectral reflectance. *Acta Ecologica Sinica*, 30(6):297–303, 2010.
- [102] G. Rabatel and C. Guizard. Grape berry calibration by computer vision using elliptical model fitting. In *European Conference on Precision Agriculture*, volume 6, pages 581–587, 2007.
- [103] T. S. Rappaport. Wireless communications—principles and practice, (the book end). *Microwave Journal*, 45(12):128–129, 2002.
- [104] Rohde and Schwarz. Measurement of dielectric material properties, application note, 2012.
- [105] A. Samouëlian, I. Cousin, A. Tabbagh, A. Bruand, and G. Richard. Electrical resistivity survey in soil science: a review. *Soil and Tillage research*, 83(2):173–193, 2005.

- [106] V. Semenov and Y. Mitelman. Non-destructive fruit quality control using radioelectronics: a review. In *2020 Ural Symposium on Biomedical Engineering, Radioelectronics and Information Technology (USBREIT)*, pages 0281–0284. IEEE, 2020.
- [107] E. Serrano, S. Roussel, L. Gontier, T. Dufourcq, et al. Early estimation of vineyard yield: Correlation between the volume of a vitis vinifera bunch during its growth and its weight at harvest. *FRUTIC*, 5:311–318, 2005.
- [108] C. S. Suite. <https://www.3ds.com/products-services/simulia/products/cst-studio-suite/>. Accessed: Feb. 2, 2020.
- [109] D. F. Swinehart. The beer-lambert law. *Journal of chemical education*, 39(7):333, 1962.
- [110] S. Tan, L. Zhang, Z. Wang, and J. Yang. Multitrack: Multi-user tracking and activity recognition using commodity wifi. In *Proceedings of the 2019 CHI Conference on Human Factors in Computing Systems*, pages 1–12, 2019.
- [111] S. Tan, L. Zhang, and J. Yang. Sensing fruit ripeness using wireless signals. In *2018 27th International Conference on Computer Communication and Networks (ICCCN)*, pages 1–9. IEEE, 2018.
- [112] J. Tarara, J. Ferguson, P. Blom, M. Pitts, and F. Pierce. Estimation of grapevine crop mass and yield via automated measurements of trellis tension. *Transactions of the ASAE*, 47(2):647, 2004.
- [113] J. M. Tarara, B. Chaves, L. A. Sanchez, and N. K. Dokoozlian. Use of cordon wire tension for static and dynamic prediction of grapevine yield. *American Journal of Enology and Viticulture*, 65(4):443–452, 2014.
- [114] A. Technologies. Agilent basics of measuring the dielectric properties of materials, application note, 2005.
- [115] S. Trabelsi, A. W. Kraszewski, and S. O. Nelson. Nondestructive microwave characterization for determining the bulk density and moisture content of shelled corn. *Measurement Science and Technology*, 9(9):1548, 1998.

- [116] S. Trabelsi, S. O. Nelson, and M. A. Lewis. Microwave nondestructive sensing of moisture content in shelled peanuts independent of bulk density and with temperature compensation. *Sensing and Instrumentation for Food Quality and Safety*, 3(2):114–121, 2009.
- [117] M. M. Tripathi, M. H. El Barbary, F.-Y. Yueh, J. P. Singh, P. H. Steele, and L. L. Ingram Jr. Reflection–absorption-based near infrared spectroscopy for predicting water content in bio-oil. *Sensors and Actuators B: Chemical*, 136(1):20–25, 2009.
- [118] T. Tulasidas, G. Raghavan, F. v. d. Voort, and R. Girard. Dielectric properties of grapes and sugar solutions at 2.45 ghz. *Journal of microwave power and electromagnetic energy*, 30(2):117–123, 1995.
- [119] T. Ulversoy. Software defined radio: Challenges and opportunities. *IEEE Communications Surveys & Tutorials*, 12(4):531–550, 2010.
- [120] M. Venkatesh and G. Raghavan. An overview of dielectric properties measuring techniques. *Canadian biosystems engineering*, 47(7):15–30, 2005.
- [121] J. Wang, L. Chang, S. Aggarwal, O. Abari, and S. Keshav. Soil moisture sensing with commodity rfid systems. In *Proceedings of the 18th International Conference on Mobile Systems, Applications, and Services*, pages 273–285, 2020.
- [122] WEFWEB. Exploring the role of smart technology in the future of english and welsh wine production against water and energy challenges. Technical report, *28th -29th June at Ridgeview Wine, Fragbarrow Lane, Ditchling Common, Sussex BN6 8TP*, 2017.
- [123] H. Weisberg and H. F. Weisberg. *Central tendency and variability*. Number 83. Sage, 1992.
- [124] H. Wen. *Toward Inertial-Navigation-on-Chip: The Physics and Performance Scaling of Multi-Degree-of-Freedom Resonant MEMS Gyroscopes*. Springer Nature, 2019.
- [125] J. Wolpert and E. Vilas. Estimating vineyard yields: Introduction to a simple, two-step method. *American Journal of Enology and Viticulture*, 43(4):384–388, 1992.

- [126] C. Wu, F. Zhang, Y. Fan, and K. R. Liu. Rf-based inertial measurement. In *Proceedings of the ACM Special Interest Group on Data Communication*, pages 117–129. 2019.
- [127] B. Xie, J. Xiong, X. Chen, and D. Fang. Exploring commodity rfid for contactless sub-millimeter vibration sensing. In *Proceedings of the 18th Conference on Embedded Networked Sensor Systems*, pages 15–27, 2020.
- [128] Y. Xie, Y. Zhang, J. C. Liando, and M. Li. Swan: Stitched wi-fi antennas. In *Proceedings of the 24th Annual International Conference on Mobile Computing and Networking*, pages 51–66, 2018.
- [129] S. Xu, Y. Liu, W. Hu, Y. Wu, S. Liu, Y. Wang, and C. Liu. Nondestructive detection of yellow peach quality parameters based on 3d-cnn and hyperspectral images. In *Journal of Physics: Conference Series*, volume 1682, page 012030. IOP Publishing, 2020.
- [130] W. Yang, X. Wang, A. Song, and S. Mao. Wi-wheat: Contact-free wheat moisture detection with commodity wifi. In *2018 IEEE International Conference on Communications (ICC)*, pages 1–6. IEEE, 2018.
- [131] Z. Yang, P. H. Pathak, M. Sha, T. Zhu, J. Gan, P. Hu, and P. Mohapatra. On the feasibility of estimating soluble sugar content using millimeter-wave. In *Proceedings of the International Conference on Internet of Things Design and Implementation - IoTDI '19*, page 13–24. ACM Press, 2019.
- [132] Z. Yang, P. H. Pathak, M. Sha, T. Zhu, J. Gan, P. Hu, and P. Mohapatra. On the feasibility of estimating soluble sugar content using millimeter-wave. In *Proceedings of the International Conference on Internet of Things Design and Implementation, IoTDI '19*, pages 13–24, New York, NY, USA, 2019. ACM.
- [133] S. Yue, Y. Yang, H. Wang, H. Rahul, and D. Katabi. Bodycompass: Monitoring sleep posture with wireless signals. *Proceedings of the ACM on Interactive, Mobile, Wearable and Ubiquitous Technologies*, 4(2):1–25, 2020.

- [134] Y. Zeng, D. Wu, J. Xiong, J. Liu, Z. Liu, and D. Zhang. Multisense: Enabling multi-person respiration sensing with commodity wifi. *Proceedings of the ACM on Interactive, Mobile, Wearable and Ubiquitous Technologies*, 4(3):1–29, 2020.
- [135] Y. Zeng, D. Wu, J. Xiong, E. Yi, R. Gao, and D. Zhang. Farsense: Pushing the range limit of wifi-based respiration sensing with csi ratio of two antennas. *Proceedings of the ACM on Interactive, Mobile, Wearable and Ubiquitous Technologies*, 3(3):1–26, 2019.
- [136] D. Zhang, J. Wang, J. Jang, J. Zhang, and S. Kumar. On the feasibility of wi-fi based material sensing. In *The 25th Annual International Conference on Mobile Computing and Networking*, pages 1–16, 2019.
- [137] J. Zhang, D. Du, Y. Bao, J. Wang, and Z. Wei. Development of multi-frequency swept microwave sensing system for moisture measurement of sweet corn with deep-neural-network. *IEEE Transactions on Instrumentation and Measurement*, 2020.
- [138] J. Zhang, D. Du, Y. Bao, J. Wang, and Z. Wei. Development of multi-frequency swept microwave sensing system for moisture measurement of sweet corn with deep-neural-network. *IEEE Transactions on Instrumentation and Measurement*, pages 1–1, 2020.
- [139] J. Zhang and P. Wang. Online monitoring and detecting of wood drying kilns’ parameters based on embedded system. In *2013 25th Chinese Control and Decision Conference (CCDC)*, pages 4189–4193. IEEE, 2013.
- [140] L. Zhao, S. Shang, L. Gao, X. Hu, Y. Yin, and L. Gong. Nondestructive measurement of moisture content of peanut kernels based on concentric cylindrical capacitance. *Transactions of the Chinese Society of Agricultural Engineering*, 32(9):212–218, 2016.
- [141] M. Zhao, F. Adib, and D. Katabi. Emotion recognition using wireless signals. In *Proceedings of the 22nd Annual International Conference on Mobile Computing and Networking*, pages 95–108. ACM, 2016.
- [142] Y. Zheng, Y. Zhang, K. Qian, G. Zhang, Y. Liu, C. Wu, and Z. Yang. Zero-effort cross-domain gesture recognition with wi-fi. In *Proceedings of the 17th Annual International Conference on Mobile Systems, Applications, and Services*, pages 313–325, 2019.

# Appendix A

## SING: Supplementary Figures

### A.1 The relationship between $\varepsilon^*$ and the Moisture Content

- Figure A.1 shows how  $\kappa$  reacts to changing in the moisture content at six water concentrations (i.e., 40%, 50%, ..., 90%) and 50 frequencies uniformly distributed between 5 and 6 GHz.



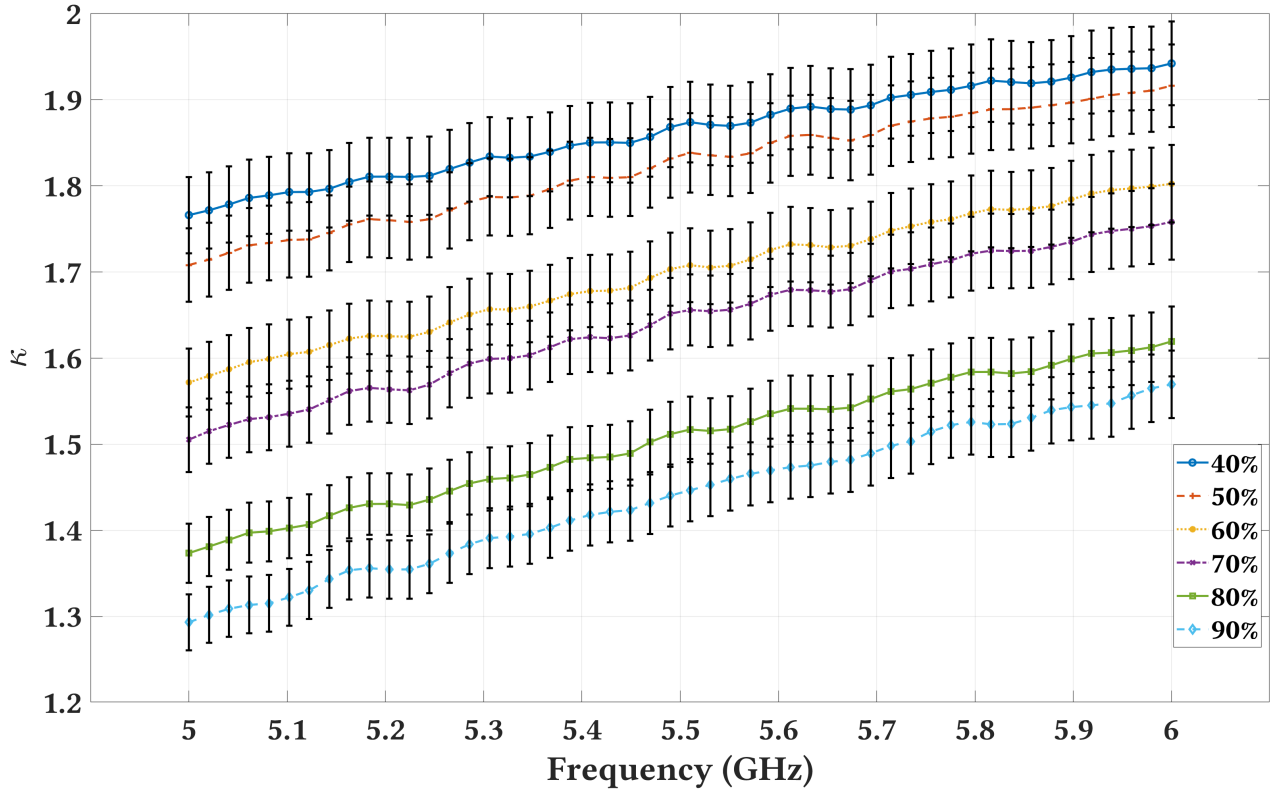


Figure A.1:  $\kappa$  against different moisture concentration (%) at 50 frequencies in  $\{5.0, 5.1, 5.2, \dots, 6.0\}$  GHz.

## A.2 Radiation Directivity and Pattern

- Figures A.2 and A.3 show the radiation directivity and the radiation pattern at 5 GHz, respectively.

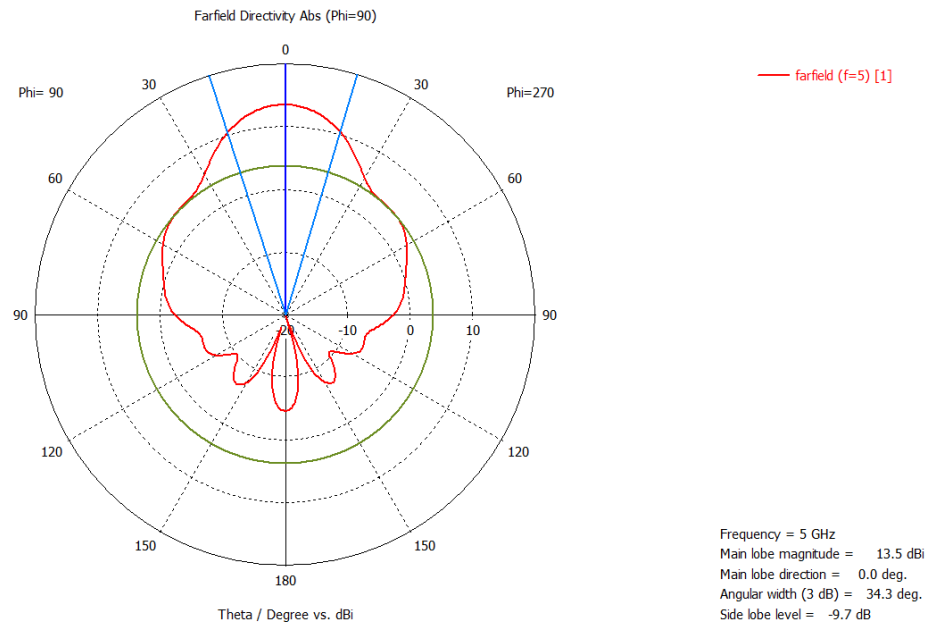


Figure A.2: Radiation directivity at 5 GHz. The red curve represents the main lobe direction, whereas the other lines/curves represent the main lobe width and the side lobe amplitude with auxiliary lines.

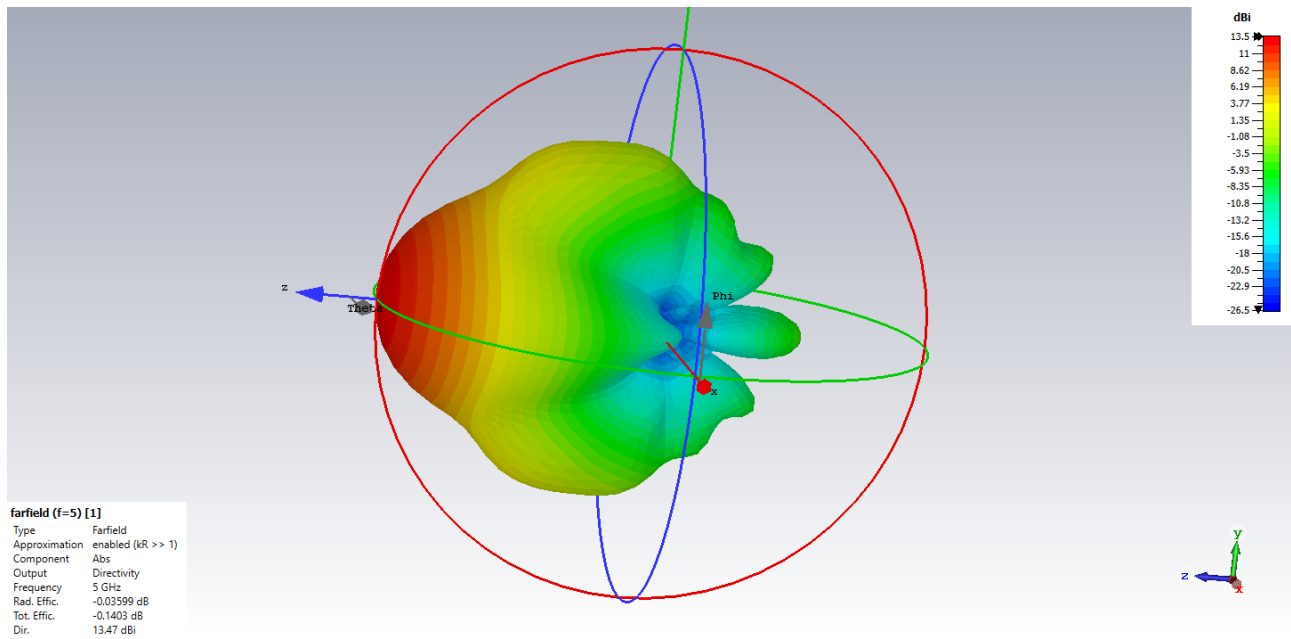


Figure A.3: The 3D radiation pattern at 5 GHz.

- Figures A.4 and A.5 show the radiation directivity and the radiation pattern at 6 GHz, respectively.

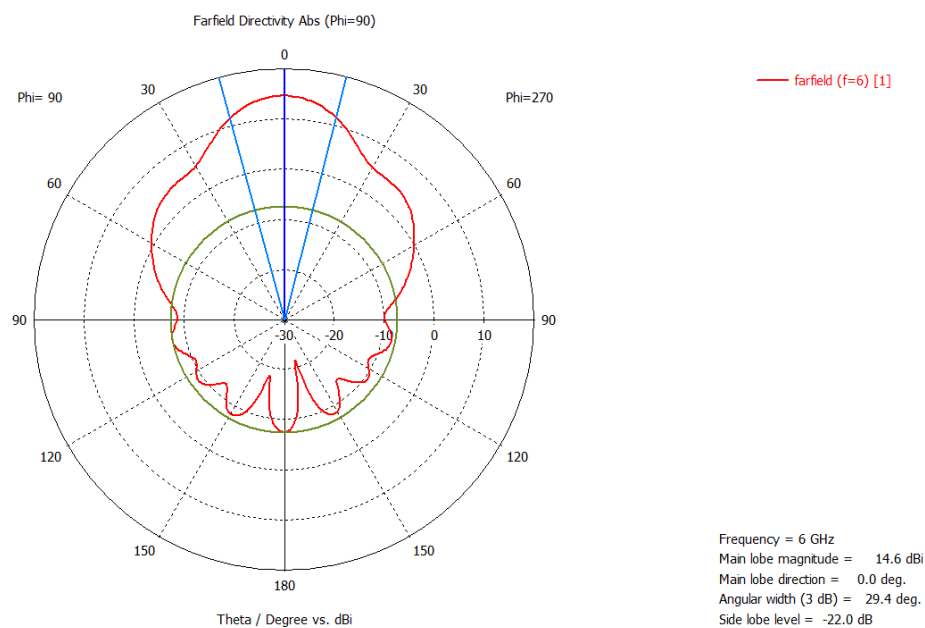


Figure A.4: Radiation directivity at 6 GHz. The red curve represents the main lobe direction, whereas the other lines/curves represent the main lobe width and the side lobe amplitude with auxiliary lines.

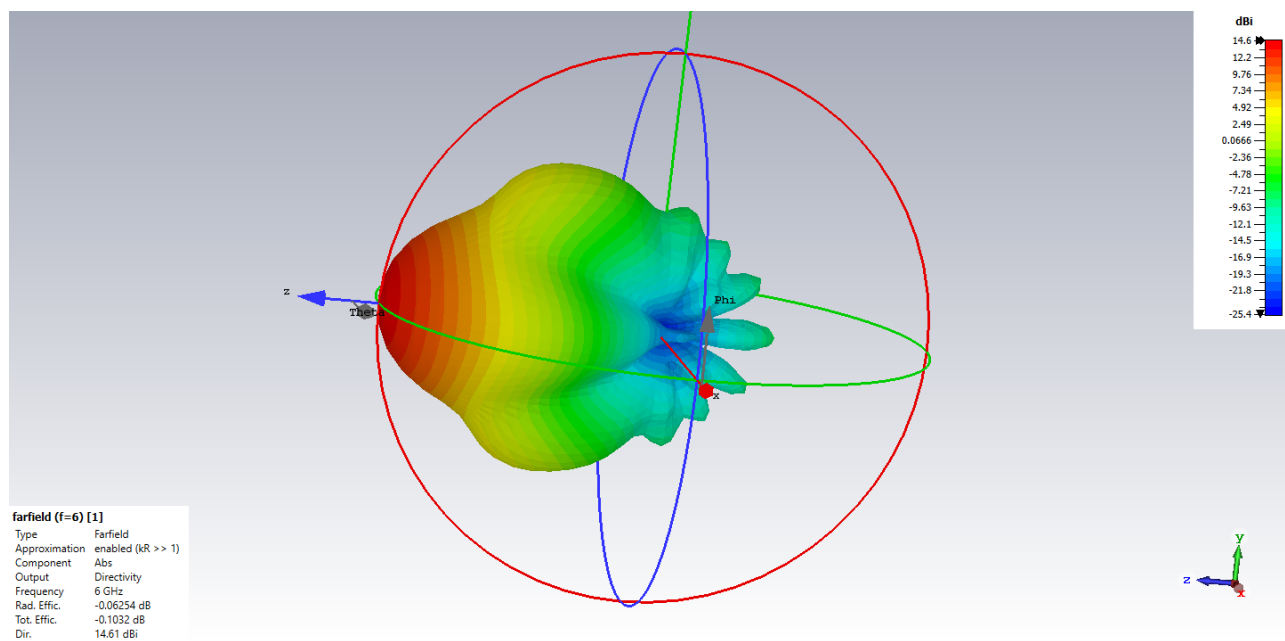


Figure A.5: The 3D radiation pattern at 6 GHz.

### A.3 Attenuation and Phase shift at multiple angles

- Figures A.6 and A.7 show the attenuation and phase shift for a cluster with moisture content = 233 ml at multiple frequencies between 5.1 and 5.9 GHz and equidistant angles between 0 and  $2\pi$ .

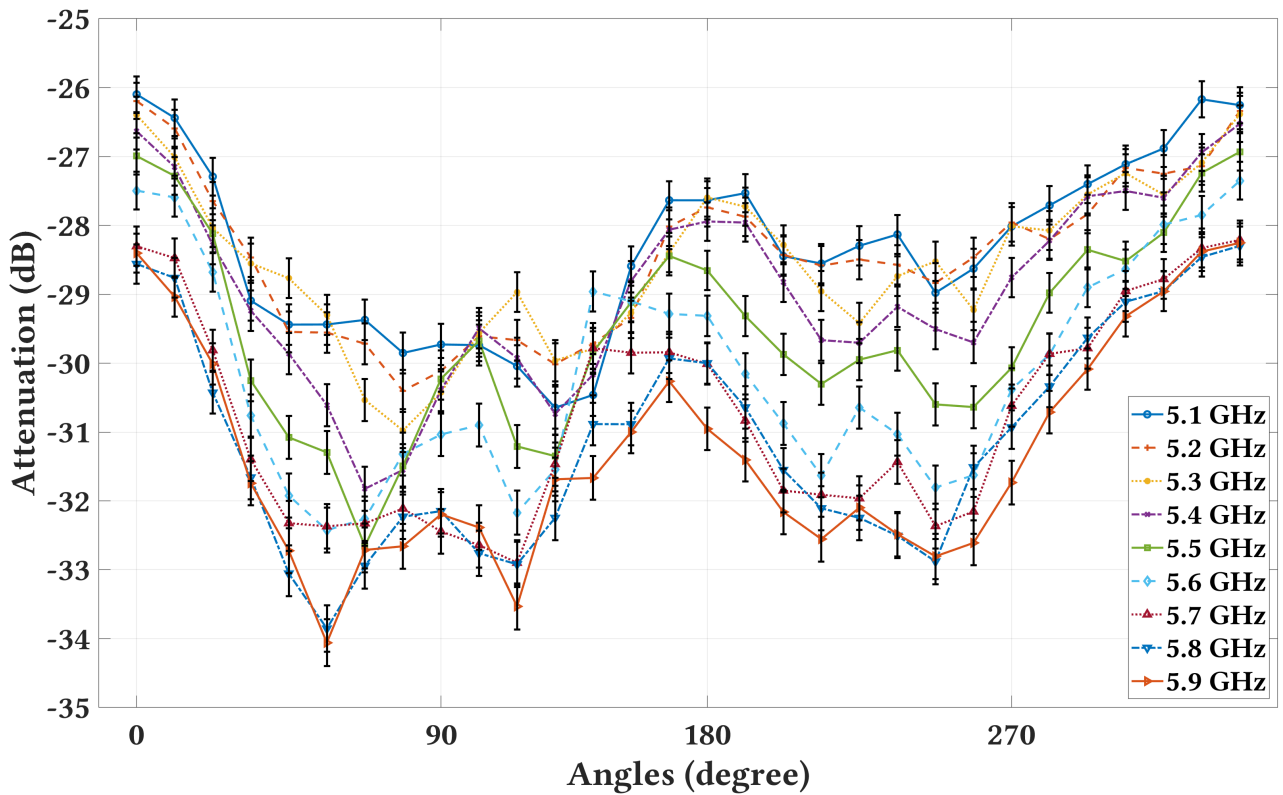


Figure A.6: The attenuation  $\{A\}$  in dB at  $\{5.1, 5.2, 5.3, \dots, \text{and } 5.9 \text{ GHz}\}$  for a cluster with moisture content = 233 ml at 30 equidistant angles between 0 and  $2\pi$ .

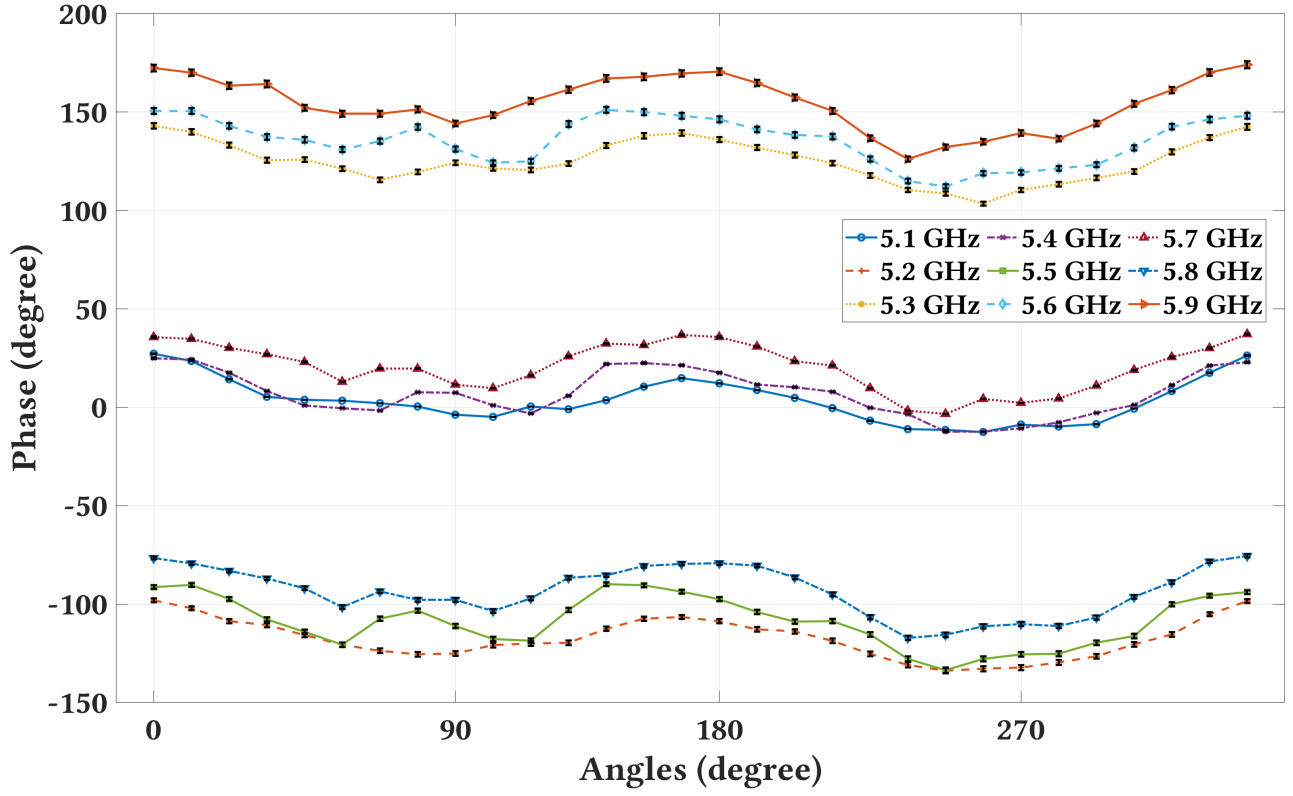


Figure A.7: The phase shift  $\{\phi\}$  in degree at  $\{5.1, 5.2, 5.3, \dots, \text{and } 5.9 \text{ GHz}\}$  for a cluster with moisture content = 233 ml at 30 equidistant angles between 0 and  $2\pi$ .

- Figures A.8 and A.9 show the attenuation and phase shift for a cluster with moisture content = 157 ml at multiple frequencies between 5.1 and 5.9 GHz and equidistant angles between 0 and  $2\pi$ .

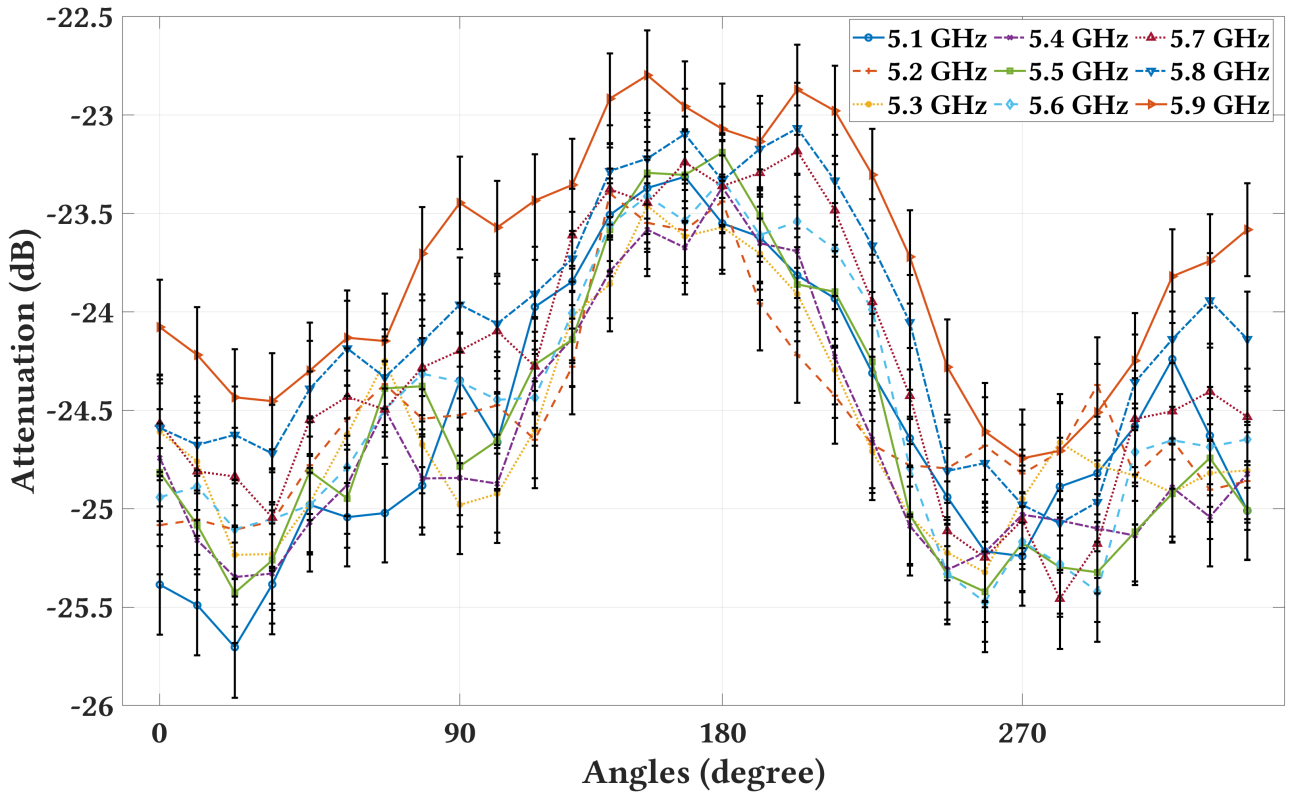


Figure A.8: The attenuation  $\{A\}$  in dB at  $\{5.1, 5.2, 5.3, \dots, \text{and } 5.9 \text{ GHz}\}$  for a cluster with moisture content = 157 ml at 30 equidistant angles between 0 and  $2\pi$ .

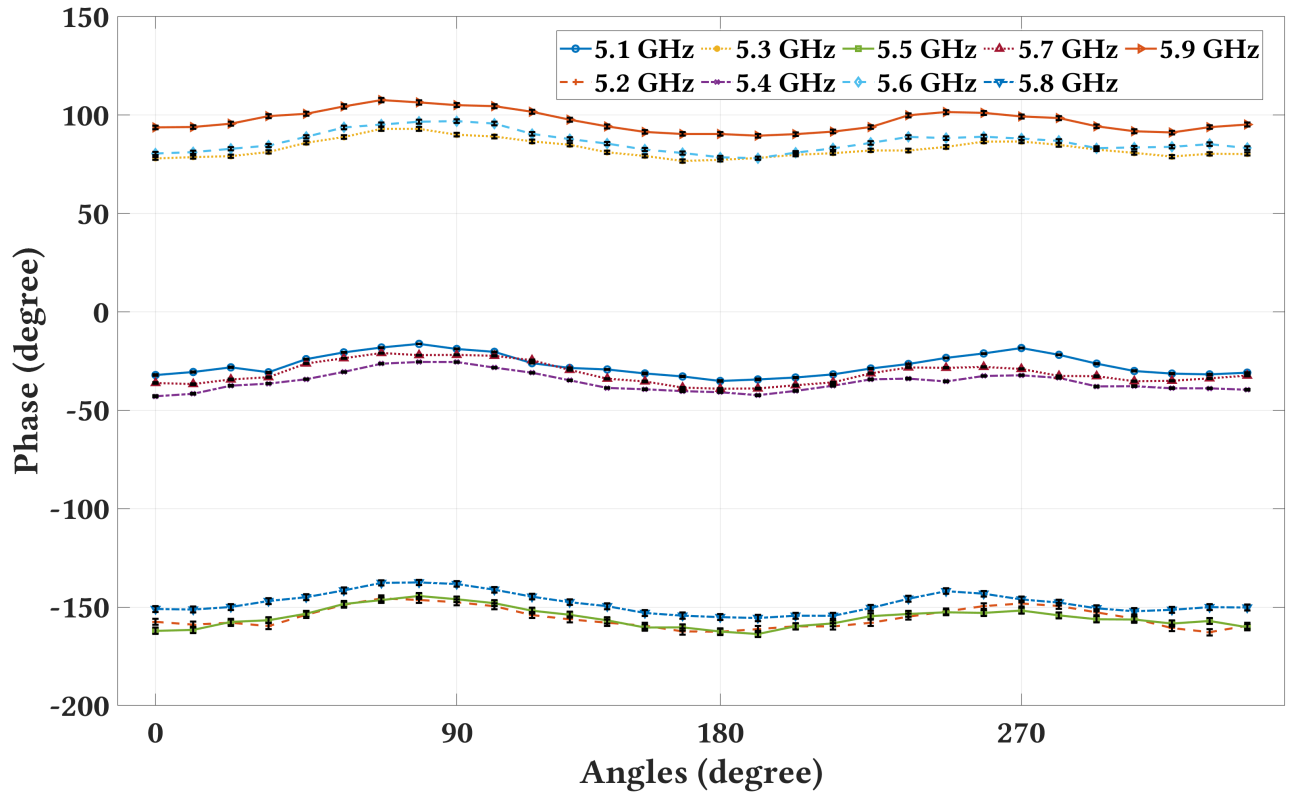


Figure A.9: The phase shift  $\{\phi\}$  in degree at  $\{5.1, 5.2, 5.3, \dots, \text{and } 5.9 \text{ GHz}\}$  for a cluster with moisture content = 157 ml at 30 equidistant angles between 0 and  $2\pi$ .

- Figures A.10 and A.11 show the attenuation and phase shift for a cluster with moisture content = 95 ml at multiple frequencies between 5.1 and 5.9 GHz and equidistant angles between 0 and  $2\pi$ .

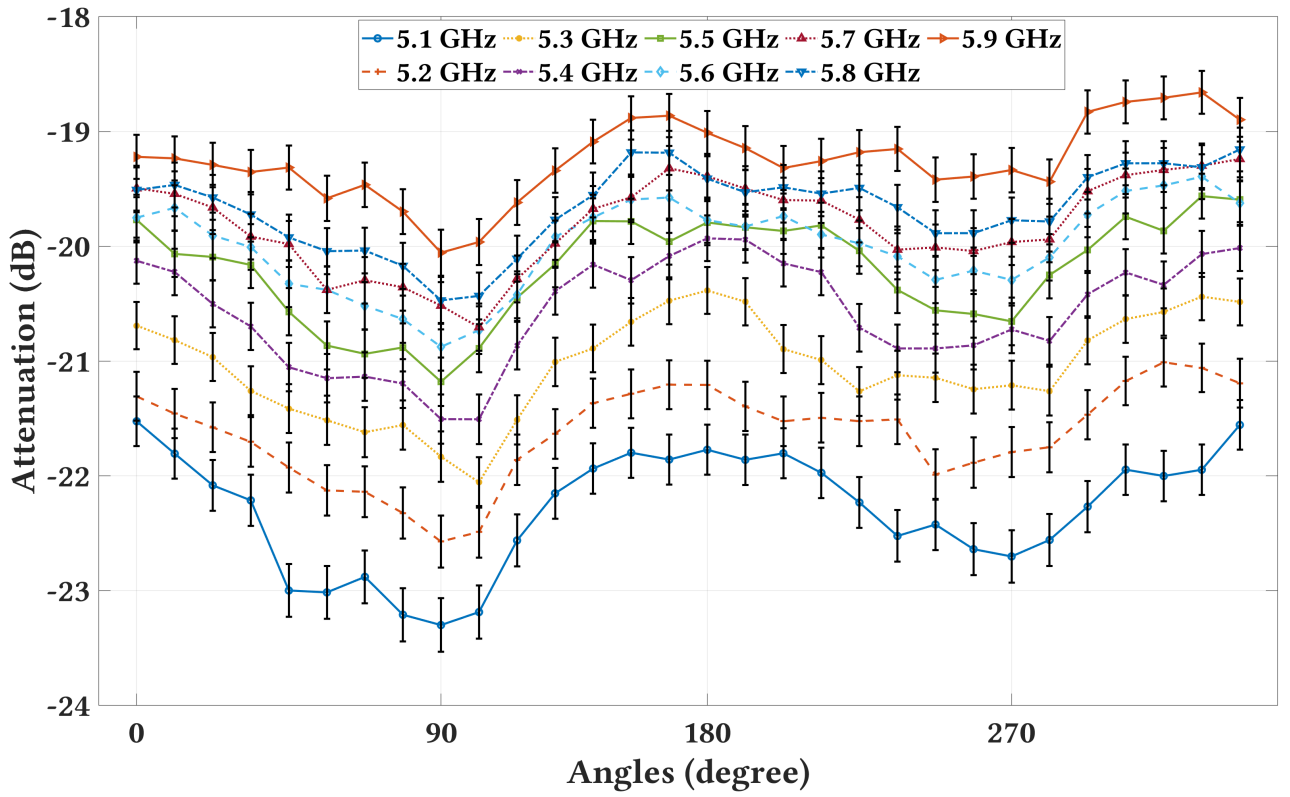


Figure A.10: The attenuation  $\{A\}$  in dB at  $\{5.1, 5.2, 5.3, \dots, \text{and } 5.9 \text{ GHz}\}$  for a cluster with moisture content = 95 ml at 30 equidistant angles between 0 and  $2\pi$ .

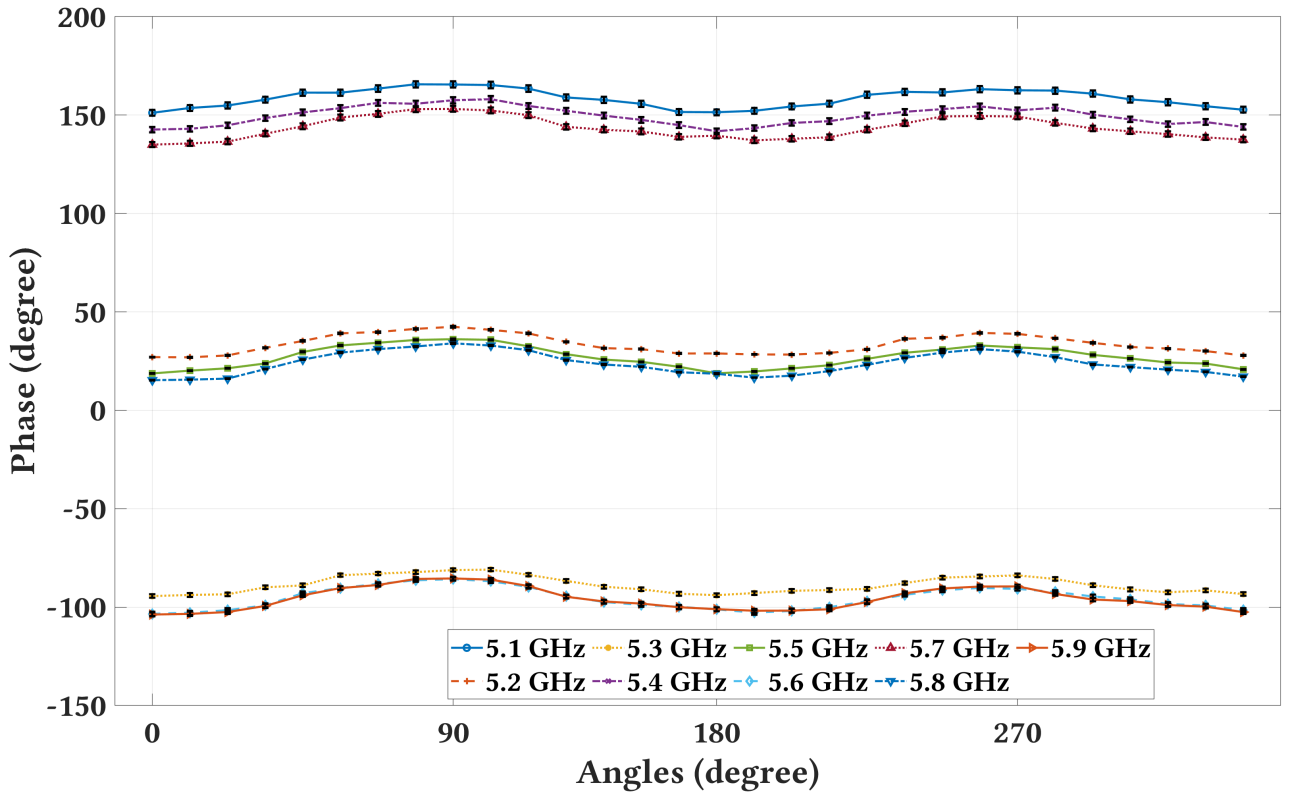


Figure A.11: The phase shift  $\{\phi\}$  in degree at  $\{5.1, 5.2, 5.3, \dots, \text{and } 5.9 \text{ GHz}\}$  for a cluster with moisture content = 95 ml at 30 equidistant angles between 0 and  $2\pi$ .

#### A.4 The impact of foliage on SING accuracy

- The S-parameters measurements with and without leaves at angle  $\frac{\pi}{4}$ .



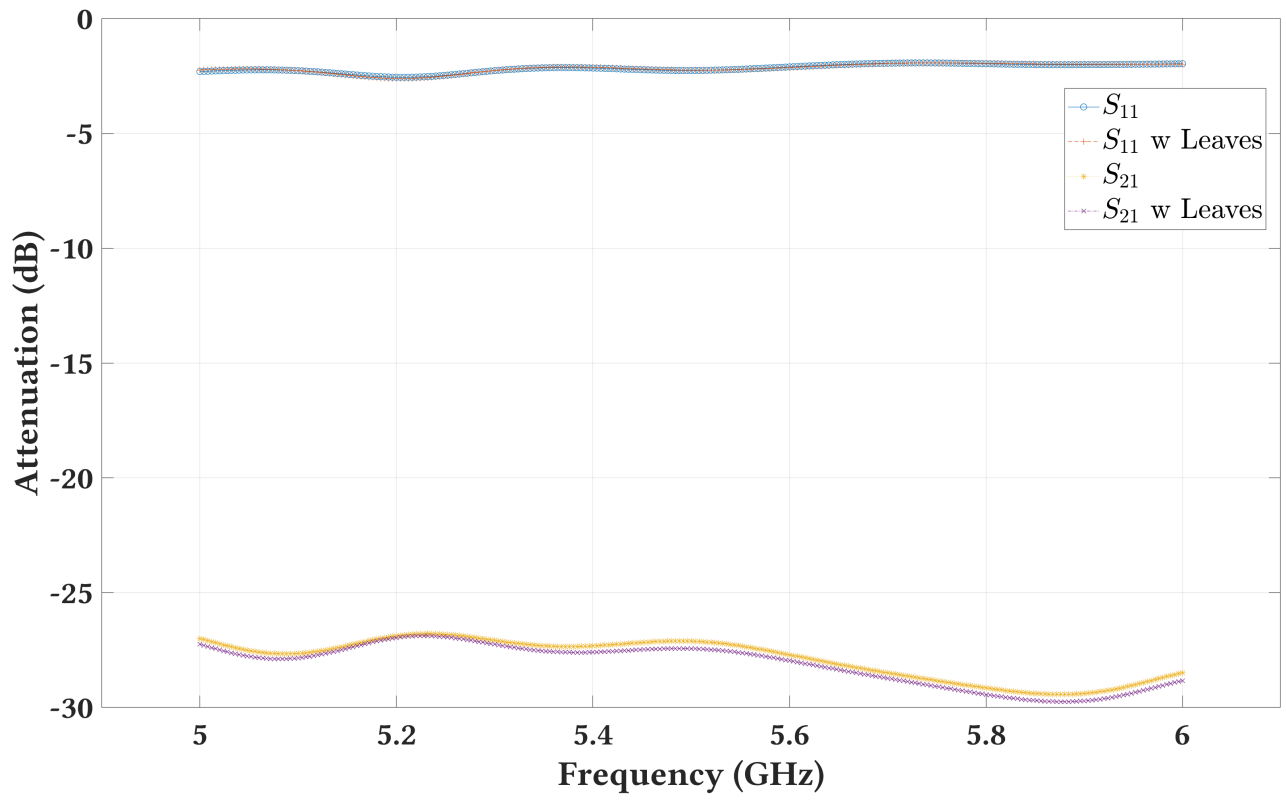


Figure A.12: The  $S_{11}$  and  $S_{21}$  measurements with leaves (i.e., w Leaves) and without leaves at angle  $\frac{\pi}{4}$ .

- The S-parameters measurements with and without leaves at angle  $\frac{3\pi}{4}$ .

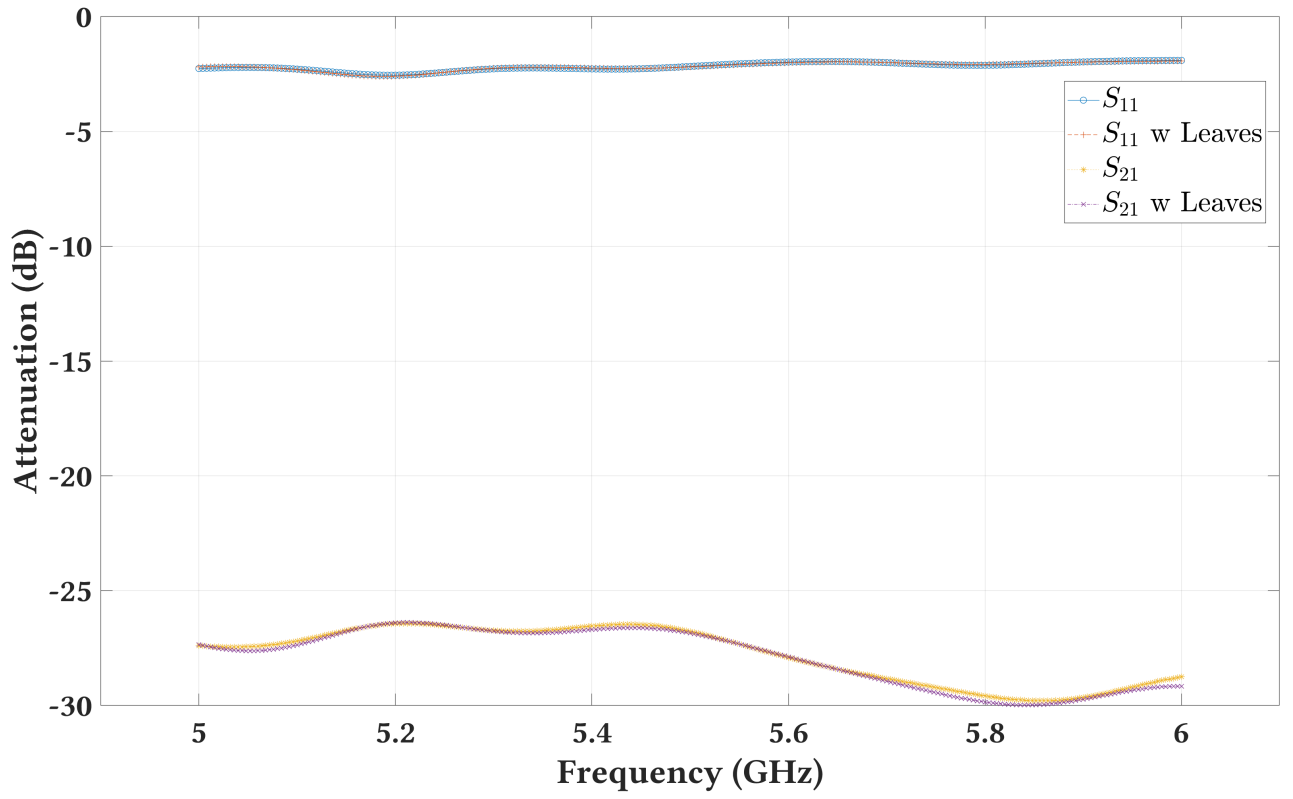


Figure A.13: The  $S_{11}$  and  $S_{21}$  measurements with leaves (i.e., w Leaves) and without leaves at angle  $\frac{3\pi}{4}$ .

- The S-parameters measurements with and without leaves at angle  $\frac{5\pi}{4}$ .

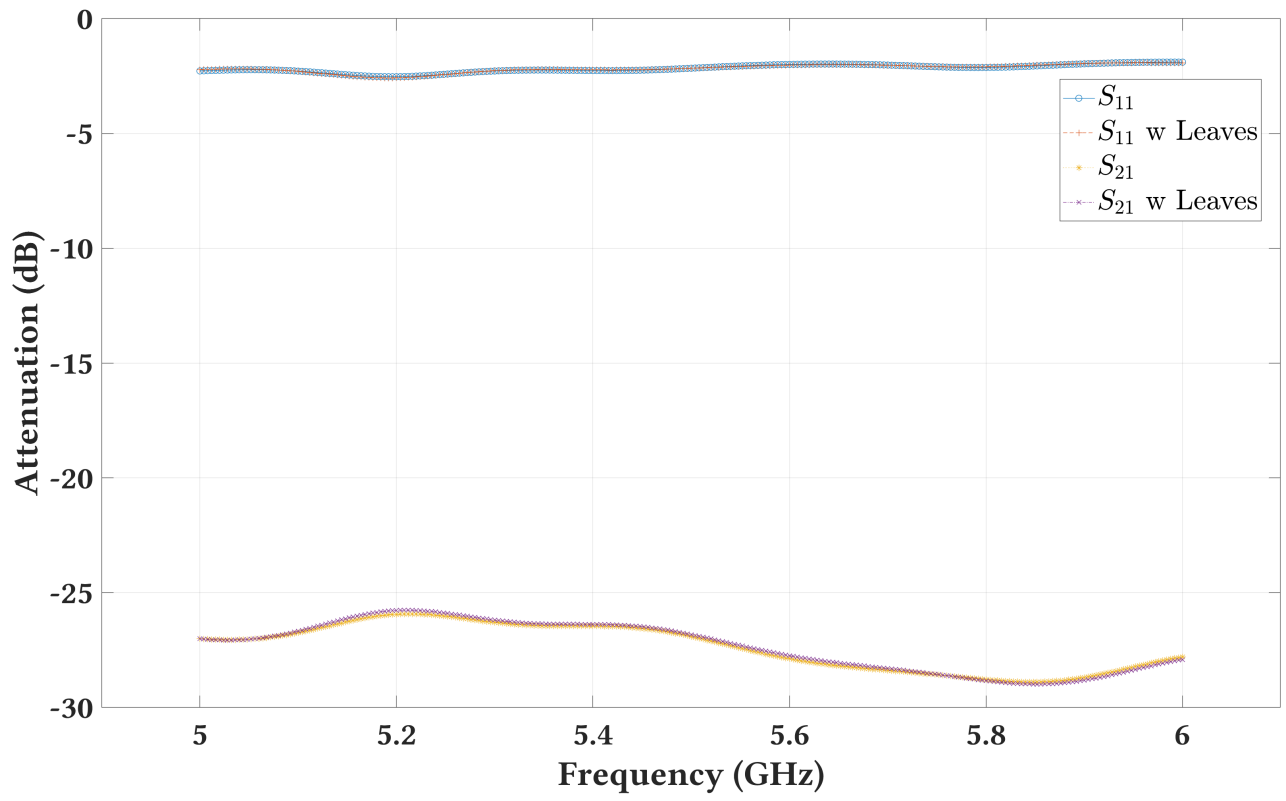


Figure A.14: The  $S_{11}$  and  $S_{21}$  measurements with leaves (i.e., w Leaves) and without leaves at angle  $\frac{5\pi}{4}$ .

- The S-parameters measurements with and without leaves at angle  $\frac{7\pi}{4}$ .

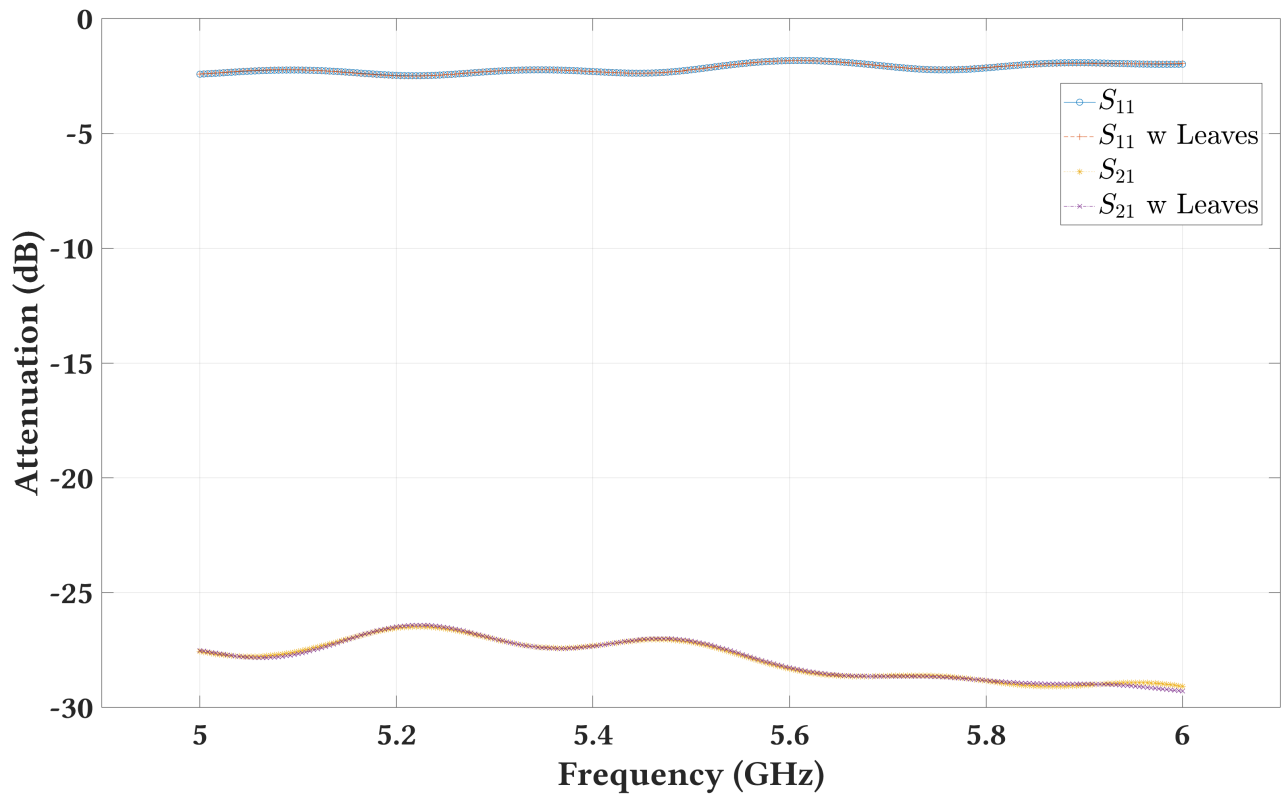


Figure A.15: The  $S_{11}$  and  $S_{21}$  measurements with leaves (i.e., w Leaves) and without leaves at angle  $\frac{7\pi}{4}$ .

# Appendix B

## SING Results: Supplementary Figures

### B.1 Minimum against Maximum number of angles

- The median offset values for the two-segment.

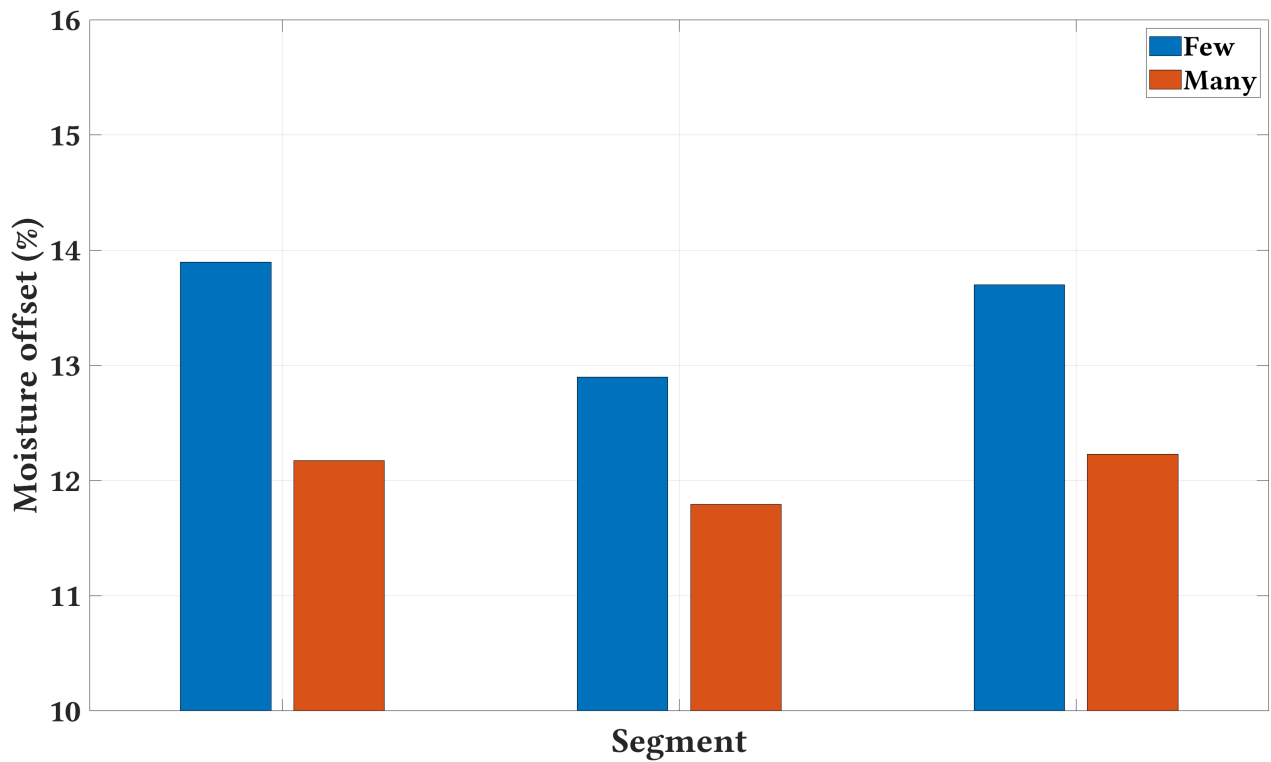


Figure B.1: The median offset of the two-segment *Min* against *Max*.

- The median offset values for the three-segment.

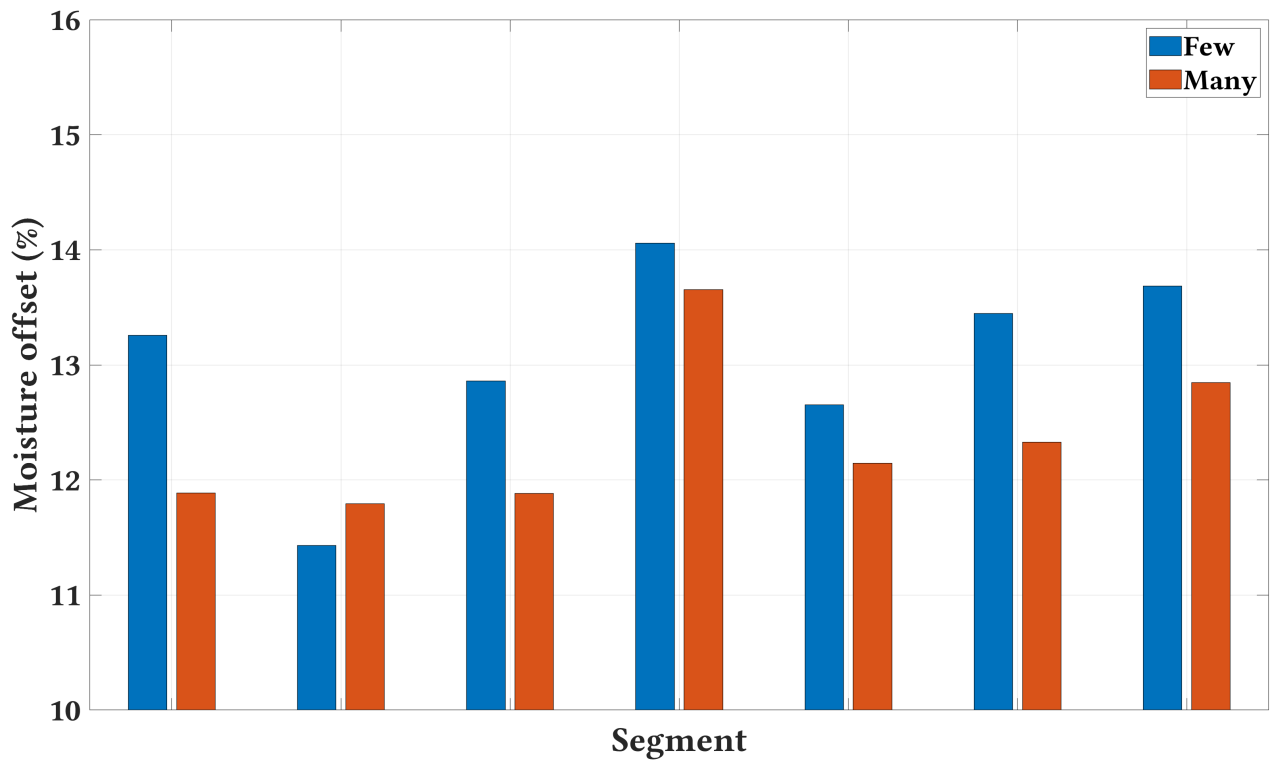


Figure B.2: The median offset of the three-segment *Min* against *Max*.

- The median offset values for the five-segment.

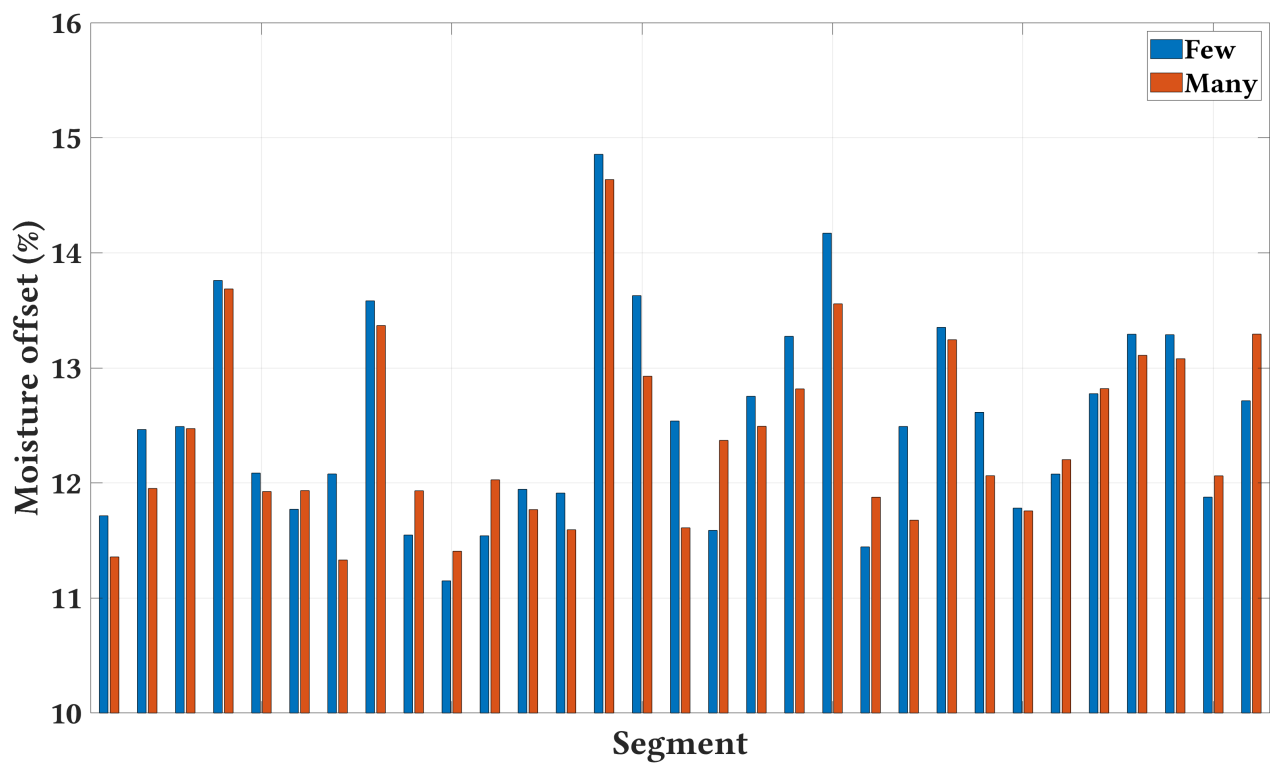


Figure B.3: The median offset of the five-segment *Min* against *Max*.

- The median offset values for the six-segment.

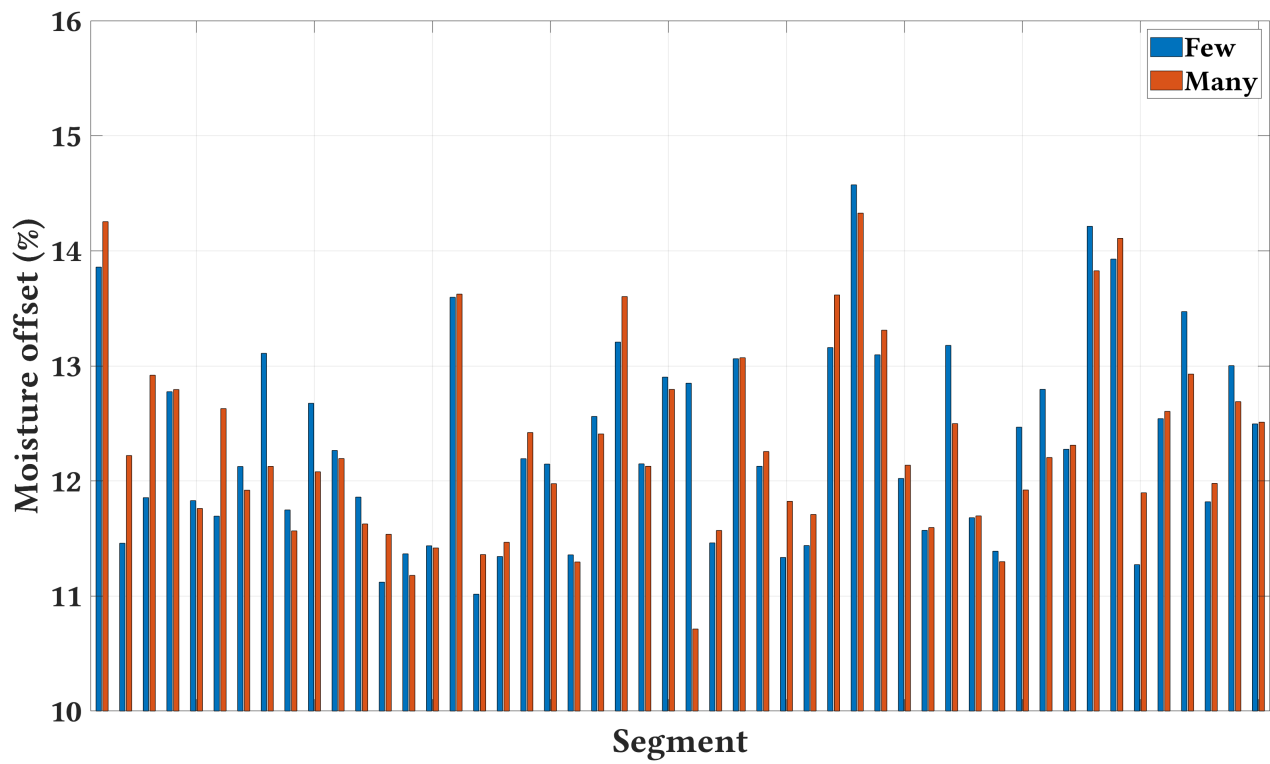


Figure B.4: The median offset of the six-segment *Min* against *Max*.

- The median offset values for the ten-segment.



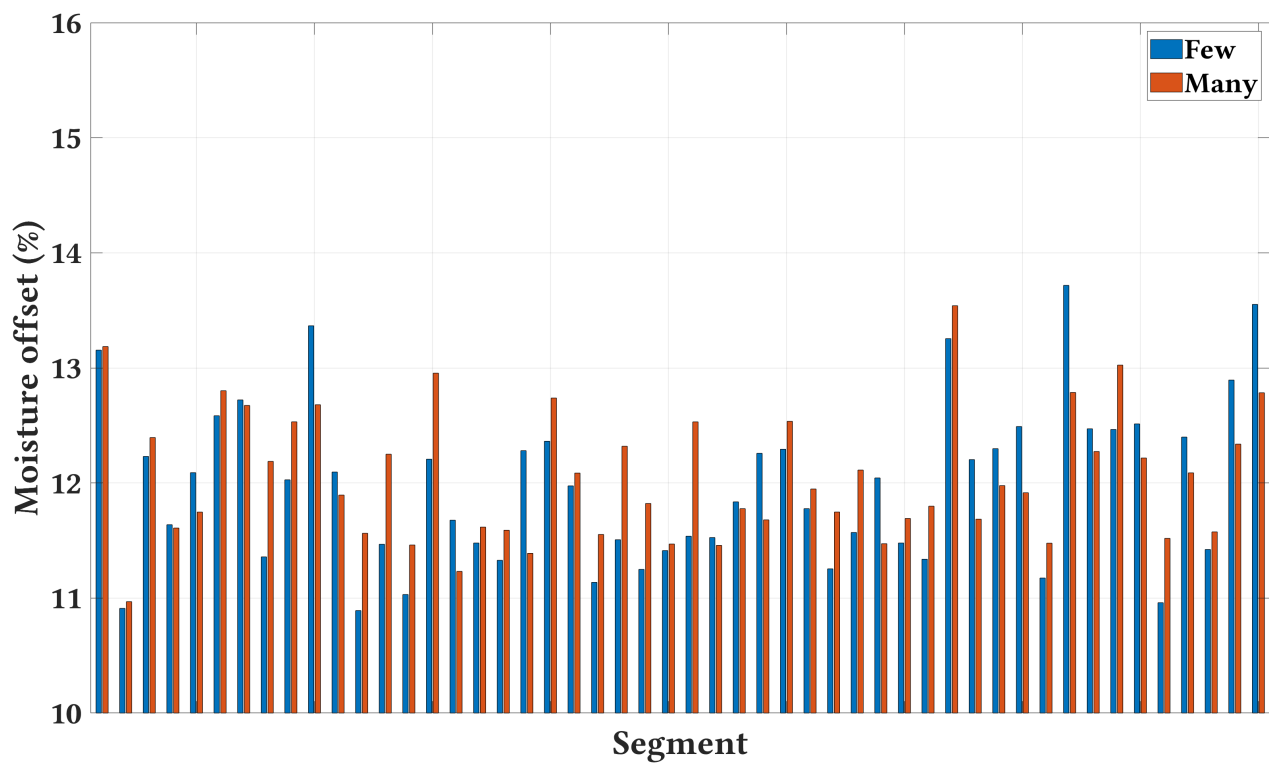


Figure B.5: The median offset of the ten-segment *Min* against *Max*.

- The median offset values for the fifteen-segment.

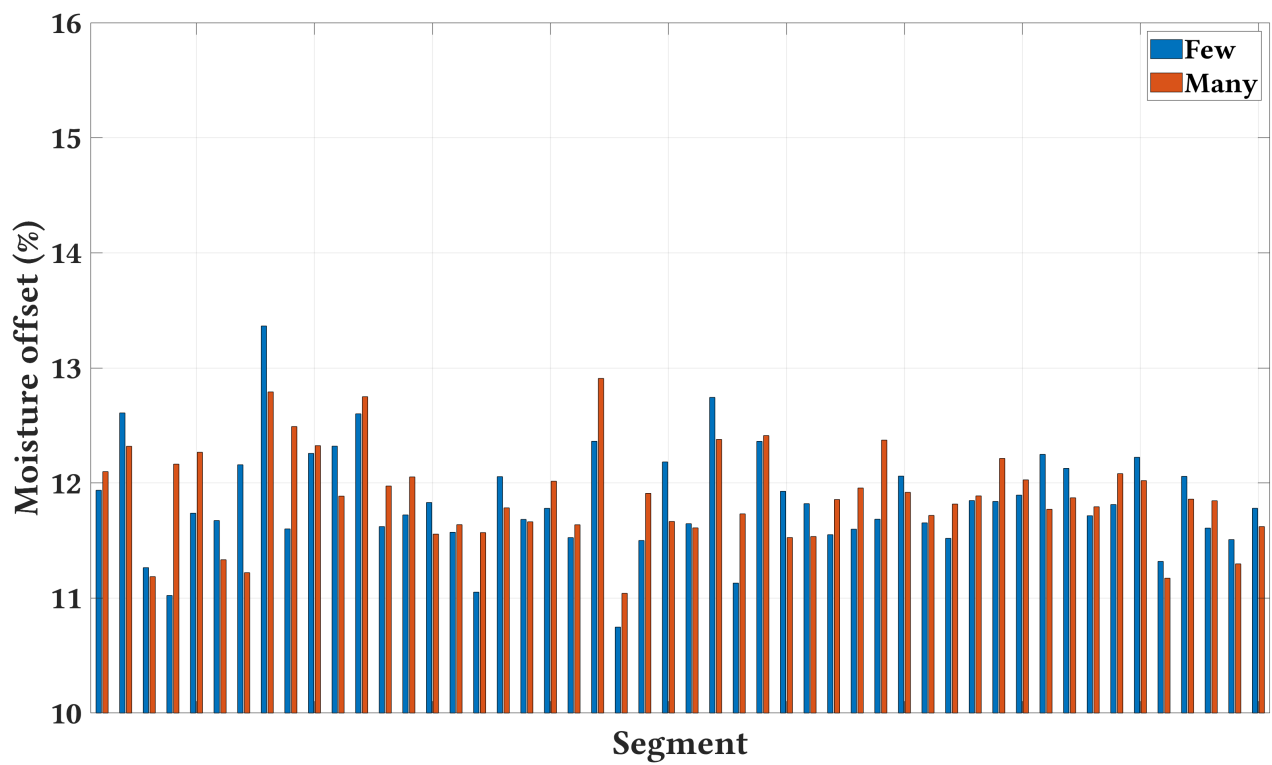


Figure B.6: The median offset of the fifteen-segment *Min* against *Max*.

# Acronyms

$A$  Attenuation Factor. 60

$E_i$  Electrical Field of the Incident wave. 39, 40

$E_t$  Electrical Field of the Transmitted wave. 39

$I_o$  EM waves Intensity. 51

$S^i$  Angle Set Category. 88

$\Gamma$  Reflection Coefficient. 7

$\eta$  Real Refractive Index. 41

$\eta^*$  Complex Refractive Index. 40

$\gamma$  Complex Propagation Constant. 40

$\kappa$  Extinction Coefficient. 40, 71, 146

$\lambda$  Transmission Frequency Wavelength. 40

$\overline{M}$  Final Moisture Content Value. 59

$\overline{\alpha}_{\Theta}^{\{\mathbf{G}\}}$  Cluster's Attenuation Constant. 64

$\overline{\beta}_{\Theta}^{\{\mathbf{G}\}}$  Cluster's Phase Constant. 64

$\overline{\gamma}^{\{\mathbf{Air}\}}$  Clear Line-of-Sight Propagation Constant. 64

$\overline{\rho}_{\Theta}^{\{\mathbf{G}\}}$  Cluster's Mean Relative Thickness. 64, 71

$\bar{\tau}_{\Theta}^{\{\mathbf{G}\}}$  Cluster's Transmission Coefficient. 64

$\bar{\tau}_{\Theta}^{\{\mathbf{Air}\}}$  Clear Line-of-Sight Transmission Coefficient. 64

$\phi$  Phase Shift. 60

$\tau$  Transmission Coefficient. 7

$\varepsilon^*$  Complex Relative Permittivity. 4, 71

$\varepsilon''$  Loss Factor. 4

$\varepsilon'$  Relative Permittivity. 4

**CLoS** Clear Line-of-Sight. 67

**CSI** Channel State Information. 14

**CV** Cross-Validation. 80

**FMCW** Frequency Modulated Continuous Wave. 14

**RF** Radio Frequencies. 2

**RFID** Radio Frequency Identification. 12

**RSS** Received Signal Strength. 12

**SDR** Software Defined Radio. 113

**VIF** Variance Inflation Factor. 83

**VNA** Vector Network Analyzer. 7